From the measurement of the $\theta 13$ mixing angle to the search for geo-neutrinos: studying electron antineutrinos with Double Chooz and Borexino

R. Roncin

Université Paris Diderot (Paris 7) Sorbonne Paris Cité
ED 560 - STEP'UP - "Sciences de la Terre de l'Environnement
et Physique de l'Univers de Paris"
Università degli Studi dell'Aquila

Thèse de Doctorat / Tesi di Dottorato
Physique des Particules / Fisica delle Particelle

From the measurement of the θ_{13} mixing angle to the search for geo-neutrinos: studying $\bar{\nu}_e$ with Double Chooz and Borexino

---

présentée par

Romain Roncin

pour l'obtention des titres de

Docteur de l'Université Paris Diderot (Paris 7) Sorbonne Paris Cité
Dottore dell'Università degli Studi dell'Aquila

Thèse dirigée par Pr Alessandra Tonazzo / Dr Francesco Villante
Laboratoire AstroParticule et Cosmologie / Laboratori Nazionali del Gran Sasso

soutenue publiquement le 29 septembre 2014 devant le jury composé de :

Dr	Jacques	Dumarchez	Président du jury
Pr	Alessandra	Tonazzo	Directrice de thèse
Dr	Francesco	Villante	Directeur de thèse
Pr	Masaki	Ishitsuka	Rapporteur
Dr	Gioacchino	Ranucci	Rapporteur
Dr	Anatael	Cabrera	Co-encadrant de thèse
Dr	Aldo	Ianni	Co-directeur de thèse

A mon papa, à ma maman,
à mon frère, à ma soeur,
à Globule et à toi, Margaux

Acknowledgments

J'ai bien conscience que les quelques pages qui vont suivre seront certainement les plus lues, au moins pour les non-anglophones, aussi je vais tenter de m'appliquer. J'ai toujours pensé qu'écrire ces pages coulerait de source. Il n'en est rien. Trouver pour chacun d'entre vous les mots justes n'est pas chose aisée. Je vais ici abandonner l'anglais pour retrouver ma bien-aimée langue maternelle. Il y a beaucoup de personnes que je voudrais remercier, je vais certainement en oublier et j'en suis par avance désolé.

Je ne suis pas certain de l'ordre protocolaire qu'il me faut respecter mais je voudrais commencer par remercier les directeurs des laboratoires dans lesquels j'ai pu étudier dans des conditions, il faut le reconnaître, optimales. Je remercie Pierre Binétruy et Stavros Katsanevas du laboratoire AstroParticule et Cosmologie (APC) ainsi que Stefano Ragazzi du Laboratori Nazionali del Gran Sasso (LNGS).

Je remercie les membres du jury d'avoir accepté d'en faire partie. Merci à Masaki Ishitsuka et Gioacchino Ranucci d'avoir accepté d'être les rapporteurs de cette thèse et à Jacques Dumarchez d'avoir présidé ce jury. Certains pourraient vous dire que je n'ai pas la mémoire des évènements mais croyez bien que le 29 septembre 2014 restera à jamais gravé dans ma mémoire.

Je voudrais continuer en remerciant mes directeurs de thèse, et ils sont nombreux ! Je remercie Aldo Ianni et Francesco Villante de m'avoir si bien accueilli et encadré au Gran Sasso. Cette expérience a été inoubliable. Je remercie ensuite Anatael Cabrera sans qui la partie light noise de cette thèse n'aurait jamais pu aboutir. Je me souviens du soulagement que j'ai éprouvé après ton coup de téléphone m'annonçant que les coupures light noise avaient été approuvées par la collaboration. Je tiens enfin à exprimer toute ma gratitude à ma directrice de thèse, Alessandra Tonazzo, qui m'a tellement apporté que j'ai bien conscience que les mots employés ici ne sont pas assez forts pour exprimer combien je te suis reconnaissant. Tu as été la directrice de thèse idéale. Depuis mon stage de L3 jusqu'à cette thèse en passant par les summer student programmes du DESY et du CERN, c'est toi qui m'a guidé au fil de toutes ces années et je t'en remercie !

Cela me permet d'enchaîner en remerciant Thomas Patzak, sans qui je n'aurais pas connu Alessandra. A l'époque de la L3, je cherchais un stage et c'est toi qui m'a orienté vers Alessandra... et Michel Cribier ! Merci Michel, merci d'être toi ! J'ai appris énormément à tes côtés

et pas seulement en physique des neutrinos ! J'aime tellement nos conversations ! A vrai dire, en écrivant ces lignes, j'ai déjà hâte que tu passes pour parler de tout et de rien. Merci Michel, merci.

Je remercie l'ensemble du groupe neutrinos de l'APC. Merci à Antoine Kouchner, Jaime Dawson, Didier Kryn, Hervé de Kerret, Michel Obolensky, Alberto Remoto et Kazuhiro Terao. Un merci particulier à Daniel Vignaud qui m'a suivi tout au long de ces trois années.

Je remercie les équipes du CEA avec qui j'ai pu échanger. Merci à David Lhuillier et Thierry Lasserre qui m'ont fait grandir. J'ai appris beaucoup à vos côtés. J'en profite également pour remercier Matthieu Vivier, Vincent Fischer et Valérian Sybille. Tu m'as beaucoup fait rire durant cette dernière année de thèse ! C'est vraiment dommage que tu ne sois pas arrivé plus tôt !

Ce qu'il y a de bien dans les collaborations comme celle de Double Chooz, c'est qu'au-delà d'être collègues, on forge des amitiés. Merci Antoine Collin ! Les meetings de collaboration vont me manquer, c'est certain ! Les shifts peut-être un peu moins, quoique, c'était quand même bien sympa, j'en garde en tout cas de bons souvenirs. Merci Guillaume Pronost ! Tu m'as vraiment beaucoup aidé avec ce boulot prenant qu'est DataMigro, surtout sur la fin ! On en aura passé des heures sur Skype, au téléphone, à Chooz et même jusqu'à Montréal à réparer, réparer et encore et toujours réparer DataMigro. Merci d'avoir été là Guillaume, j'ai toujours pu compter sur toi. Tu m'as vraiment été d'une aide précieuse.

En parlant d'aide précieuse, je remercie Pau Novella avec qui je troquais du français contre de la physique. Merci d'avoir pris le temps de relire des parties de ce manuscrit, tu m'as beaucoup appris et je t'en suis très reconnaissant. Merci à Paolo Agnes et Adrien Hourlier d'avoir réussi à me supporter dans ce bureau, surtout sur la fin. Merci à Simona Soldi avec qui je partageais toujours le premier "bonjour" en arrivant à l'APC et qui m'a aidé à affronter certains déboires liés à l'administration italienne.

A propos d'administration, je remercie Martine Laird-Bardissa, Martine Piochaud, Ludovic Davila, Marie Verleure et Sabine Tesson qui m'ont toujours apporté leur aide quand j'en avais besoin. Merci à vous tous. J'en profite également pour remercier Annette sans qui les shifts et les meetings de collaboration n'auraient pas eu la même saveur.

Je tiens maintenant à remercier Luca Agostino, Stefano Perasso et Davide Franco. Merci de m'avoir accompagné pendant ces trois années. Je me souviens Davide me remontant le moral après la publication des premiers résultats de Daya Bay, je me rappelle Stefano prenant du temps pour discuter de tout et de rien et je me rappelle Luca étant présent au quotidien, jour après jour, à partager les joies et les moments un peu plus difficiles de la thèse. Merci à tous les trois, si je garde d'aussi bons souvenirs de ces trois années, c'est sans aucun doute que vous y êtes pour quelque chose.

Je remercie tous les thésards sans qui les journées auraient été bien plus monotones. Merci à mes partenaires de UT, de QPUC et de tennis du mardi matin 8h. Je remercie les "vieux" thésards Loïc, Alexandre et Marie-Anne. Je tiens également à remercier mes amis Julian, Matthieu, Benjamin, Maïca et Alexis d'avoir réussi à me supporter tout au long de ces trois années. Je remercie mes amis du NPAC avec qui c'est toujours un plaisir d'aller boire un verre. Un grand merci à Pierre, Guillaume, Aurélien, Patrick, Flavien, Alice et Asénath. J'en profite également pour remercier Isabelle et Assina, merci d'être venues à ma soutenance.

Je tiens maintenant à remercier mes collègues du LNGS. Merci à Francesco Lombardi et Marcin Misiaszek d'avoir été là pour moi dès le premier jour. Ces quelques mois passés en Italie ont été formidables et c'est en grande partie grâce à vous et à la bonne ambiance qui régnait dans ce bureau. Je tiens également à remercier Chiara Ghiano, Yura Suvorov, Nicola Rossi et George Korga.

Ces trois années de thèse n'auraient pas eu la même saveur sans le monitorat que j'ai effectué au sein du Palais de la Découverte. Merci à Kamil Fadel et Hassan Khlifi de m'avoir accueilli et de m'avoir fait confiance. Je remercie Sigfrido Zayas et Alain de Botton d'avoir toujours su donner un éclat particulier à ces journées passées là-bas. J'adresse enfin un grand merci à Alice (encore) pour avoir été ma binôme pendant ces trois années, cette expérience au Palais de la Découverte n'aurait pas été la même sans toi.

Je remercie du fond du cœur mes amis angevins qui m'ont apporté un soutien réconfortant quand j'en avais le plus besoin et qui m'ont eux aussi beaucoup fait rire (c'est quoi theta treize ?) mais aussi réfléchir, en particulier Emilie et Meihdi. Merci à Ano, Clairette, Steph, Guillaume, Nicolas, Eléonore, Hermine, Wilfried et Maryline. Merci à Sylvain et Carole d'avoir toujours été présents et à Fanny d'être toujours à mon écoute depuis toutes ces années.

Je remercie Jean-Pierre, Françoise et Louise, ainsi que Françoise et Juliette, de s'être intéressés à mon travail et de m'avoir offert ces moments de repos à Lugon-et-l'Ile-du-Carnay, Bordeaux ou encore Lacanau. Je remercie également les grand-mères de Margaux, Suzanne et Kelly, d'avoir toujours pris de mes nouvelles.

Je remercie mon papa et ma maman qui m'ont toujours apporté leur soutien même s'ils ne devaient pas toujours comprendre ce que je faisais ! Merci du fond du cœur d'être de si bons parents ! Je remercie mon frère et ma sœur, ce manuscrit vous est en partie dédié. J'en profite également pour remercier Christelle.

En vrac, je voudrais aussi remercier Kavinsky, Daft Punk (j'en ai écrit du code sur vos chansons), Arto Paasilinna, Donald Westlake (rien de mieux que de vous lire pour se vider la tête), la dame à la gare de Tokyo qui m'a gentiment orienté dans ce labyrinthe, les dames d'easyJet qui ne m'ont jamais fait payé mes surplus de valises, les gardes italiens du Gran Sasso qui savent tellement bien prononcer mon nom de famille (Roncchhhine). Je remercie ma Peugeot 205, Titine pour les intimes, de ne pas nous avoir fait faux-bond lors de notre

descente vers le Gran Sasso, avec Margaux.

Je voudrais maintenant remercier un être cher qui nous a malheureusement quitté il y a peu, notre chat, Globule. Merci d'avoir été si tendre dans les moments difficiles de la thèse.

Je souhaiterais clore ces quelques pages en remerciant celle qui est à mes côtés depuis toutes ces années, Margaux. Merci de m'avoir supporté, de m'avoir encouragé, de m'avoir permis de me dépasser. Jour après jour tu as su croire en moi et pour tout cela je te remercie infiniment.

Contents

Introduction

You can't see them but they are everywhere
Neutrino 2014 conference

Time to read these few lines and your body will be crossed by billions of a certain type of elementary particles, the neutrinos. Neutrinos are everywhere. Nevertheless, although we are surrounded by neutrinos, we are not interacting with them so much. Neutrinos are shy particles. They are in fact the most shy particles already discovered physicists are dealing with, making their study so exciting from more than 80 years now.

Conceived by W. Pauli in 1930, named by E. Fermi in 1933, the existence of the neutrino will be finally proved by F. Reines and C.L. Cowan in 1956. Although the neutrino is probably the most abundant known particle in our Universe, it remains the least understood. Some of its properties were found to stand beyond the Standard Model of particle physics, a general framework able to predict interactions between all the known particles. Since the neutrino can change its identity as it propagates, deficits from predictions were observed when looking for a specific type of neutrino. Physicists then developed the neutrino oscillation theory, a theory which implies massive neutrinos and therefore to stand beyond the Standard Model. The measure of one of the parameters of this theory, the θ_{13} mixing angle, is the *raison d'être* of the Double Chooz experiment.

The neutrino is not simply an elementary particle, it is a messenger. The neutrino can be seen as a privileged witness of the first moments of our Universe, of the last moments of a supernova. The neutrino already helps us to better understand the Sun, to deepen the knowledge of the Earth. From the Sun to the Earth, the Borexino experiment is looking for solar neutrinos as well as geo-neutrinos and contributes to both astrophysics and geoscience.

The first chapter focuses on the history of the neutrino physics. From the neutrino birth certificate to the recent unsolved anomalies, this chapter tries to follow the evolution of the state of mind of the physicists which had to explore a new field, with all the questions and issues it can bring. This chapter ends by providing experimental observations which allow to consider the existence of possible sterile neutrinos.

The second chapter exposes the theoretical bases of the neutrino physics. The Standard Model is reviewed and surpassed in order to introduce the neutrino oscillation theory. This chapter also provides current experimental results and in particular those on neutrino masses

and neutrino oscillation parameters.

The third chapter consists of a description of the Double Chooz experiment, which aims at measuring what was defined until recently as the last unknown neutrino mixing angle, θ_{13}. Principle and design of this experiment are reviewed. Special attention is devoted to the event reconstruction. This chapter ends with a description of the backgrounds Double Chooz has to deal with.

The fourth chapter spotlights the unexpected background discovered at the very beginning of the Double Chooz data taking, the light noise. This chapter describes the strategy we developed in order to strongly discriminate light noise events. Different cross-checks which allow to validate the strategy are presented.

The fifth chapter is a reminder on the measurements of the θ_{13} mixing angle. Different data sets as well as different methods are used to provide several compatible measurements of θ_{13}. Neutrino selections are reviewed, as well as systematics errors associated to the specific data set used. From time to time, Double Chooz benefits from the possibility of measuring the background only. This peculiar configuration is discussed. Finally, the differents analyses leading to the measurement of θ_{13} are described in detail.

The sixth chapter is devoted to the Borexino experiment. After a brief overview of the success achieved by Borexino, we describe the opportunity to look for geo-neutrinos. Geo-neutrino production and signal prediction are investigated before proceeding to the selection and to the background investigation. The use of a maximum likelihood analysis is explained in order to access the signal rate of geo-neutrinos.

The seventh and last chapter describes the neutrino directionality studies which have been realized for both Double Chooz and Borexino. The motivations as well as the principle, which includes a description of the variables to be used, are first presented. We then focus on the different investigations made with the Double Chooz data sets. An important work on the vertex position reconstruction correction follows. Finally, an analysis using the Borexino neutrino candidates found in the sixth chapter is provided.

Chapter

1 Neutrinos: History and Physics

I have done something very bad today by proposing a particle that cannot be detected. It is something no theorist should ever do.
Wolfgang Pauli

Contents

Neutrinos? When speaking about neutrinos, with no clue about what it can refer to, one can first guess that this will be somewhere related to Italy. The "ino" tells us that the neutrino is something smaller than the "neutr", which will refer at some point to the neutrality.

1.1 Birth certificate

The neutrino saga started in 1914, when J. Chadwick was studying the energy spectrum of electrons emitted from β^- radioactivity processes. At that time, one should expect a two

body decay, according to the reaction:

$$ {}^{A}_{Z}\mathrm{X} \rightarrow {}_{Z+1}{}^{A}\mathrm{Y} + e^{-} \tag{1.1} $$

The α radioactivity, discovered in 1896 by H. Becquerel and the γ radioactivity, discovered in 1900 by P. Villard, lead both to discrete energy spectra because of a two body decay. The fact that the β^{-} decay produces electron with a continuous energy spectrum was not understood, leading to several theories to explain this phenomenon. Among them, L. Meitner proposed that electrons lost energy in the source before been measured. In 1927, with the use of precise calorimeters, C.D. Ellis and W.A. Wooster proved that this theory was not the one able to describe the continuous spectrum [1]. In 1924, N. Bohr proposed as a desperate remedy that the energy conservation was working only on a statistical way.

In order to save the sacrosanct energy conservation law, W. Pauli proposed, in a letter dated December 4, 1930, the postulate of a new particle he called "neutron". According to him, this particle should have the following properties:

- to be neutral
- to have a spin 1/2
- to have a mass not larger than 0.01 proton mass

This new particle has to be neutral in order to keep the charge conservation. The spin 1/2 allows to solve another issue, the spin-statistic. At that time, physicists thought that a nucleus ${}^{A}_{Z}\mathrm{X}$ was composed of A protons and $A - Z$ electrons. Protons and electrons are classified as fermions since they obey the Fermi-Dirac statistic. As a consequence, they have a spin 1/2. Photons obey the Bose-Einstein statistic and have a spin 1. The issue with this nucleus representation came from the study of ${}^{6}_{3}\mathrm{Li}$ and ${}^{14}_{7}\mathrm{N}$. Since there are 9 spin 1/2 particles in the ${}^{6}_{3}\mathrm{Li}$ nucleus and 21 spin 1/2 particles in the ${}^{14}_{7}\mathrm{N}$ nucleus, one should expect a half-integer spin for those nuclei, which is not the case. Adding spin 1/2 particles will then allow to solve the spin-statistic issue.

These properties are enough to characterize the neutrino, as it is known today. This letter can therefore be considered as the neutrino birth certificate, even if the name neutrino did not appear yet.

In early 1932, F. and I. Joliot-Curie investigated the penetrating radiation emitted after bombarding α particles on a ${}^{9}_{4}\mathrm{Be}$ target. They thought they were faced with γ but, the same year, J. Chadwick demonstrated that this radiation is composed of neutral particles with a mass comparable to that of the proton [2]. He called this particle "neutron". This new neutron, which is the one we know today, is able to solve the spin-statistic issue and lead to a new nuclear model. The same year, W. Heisenberg proposed that the nucleus is composed of Z protons and $A - Z$ neutrons. He needed then Z electrons to keep the charge conservation. The spin-statistic is correctly solved, 3 protons together with 3 neutrons for the ${}^{6}_{3}\mathrm{Li}$ and 7 protons together with 7 neutrons for the ${}^{14}_{7}\mathrm{N}$ will give integer spin for those nuclei.

Since there can not be two neutrons, one of them had to change its name. Chadwick's neutron has a mass similar to that of the proton whereas Pauli's neutron has to be much more lighter than the proton. Therefore, in October 1933, during the Solvay Conference, E. Fermi renamed Pauli's neutron the "little neutron", or in Italian, the "neutrino".

One year later, E. Fermi finalized the β-decay theory [3], transforming the process (1.1) into the correct one:

$$ {}^{A}_{Z}\mathrm{X} \rightarrow {}_{Z+1}{}^{A}\mathrm{Y} + e^{-} + \bar{\nu}_e \tag{1.2} $$

It is interesting to notice that at this time, *Nature* refused to publish the article considering it as "*too speculative*".

1.2 Chasing the different neutrino species

In 1934, it was not clear that one can observe a neutrino. H. Bethe and R. Peierls worried about the cross-section of the process where "*a neutrino hits a nucleus and a positive or negative electron is created while the neutrino disappears and the charge of the nucleus changes by 1*", which is known today as the Inverse Beta Decay (IBD) interaction. They calculated this cross-section to be lower than 10^{-44} cm^2, leading to the conclusion that "*there is no practically possible way of observing the neutrino*" [4]. Luckily, they were pessimistic.

1.2.1 $\bar{\nu}_e$, a two steps discovery

The detection of the first neutrino took place at the Savannah River Plant in 1956. A first attempt close to a Hanford nuclear reactor was made in 1953. We will explain in the third chapter why nuclear reactors are rich $\bar{\nu}_e$ factories for free. For both the Savannah River Plant and the Hanford experiments, F. Reines and C.L. Cowan relied on the detection of the $\bar{\nu}_e$ through the characteristic signature of IBD interactions:

$$ \bar{\nu}_e + p \rightarrow e^{+} + n, \tag{1.3} $$

where the positron scintillation and annihilation is followed by the neutron capture on cadmium (Cd) in their experiment.

At Hanford, six data sets were taken close to the pile, three with full power for a 10000 s live time and three with zero power for a 6000 s live time. At full power, the number of coincidence between positron scintillation and annihilation, *i.e.* "prompt" signal, and neutron capture on Cd, *i.e.* "delayed" signal, was found to be 2.55 $\pm$ 0.15 counts/min whereas it was found to be 2.14 $\pm$ 0.13 counts/min at zero power. The difference of 0.41 $\pm$ 0.20 counts/min had to be compared with the predicted 0.20 counts/min due to neutrino interactions [5]. F. Reines and C.L. Cowan were aware that this result was not sufficient to claim the detection of the neutrino, as they wrote in [6]:

"*Although a high background was experienced due to both the reactor and to cosmic radiation, it was felt that an identification of the free neutrino had probably been made.*"

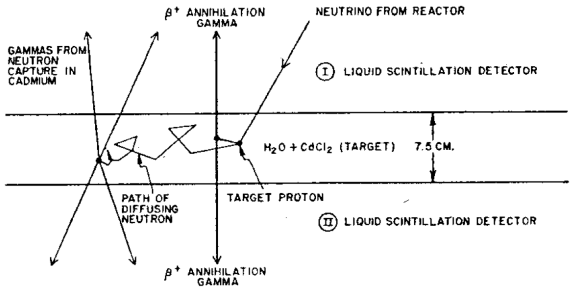

Figure 1.1: Scheme of the detection principle, from [7].

A bigger detector consisting in a "*'club sandwich' arrangement employing two targets tanks between three detector tanks*" was designed and moved to South Carolina [7]. The two $1.9 \times 1.3 \times 0.07$ m^3 targets were filled with Cd-doped water. Above and below these targets, three tanks filled with liquid scintillator were installed. The liquid scintillator was composed of triethybenzene, therphenyl and POPOP wavelength shifter. Signals were seen by 110 5-inch Dumont photomultiplier tubes. The detection principle is represented in Figure 1.1.

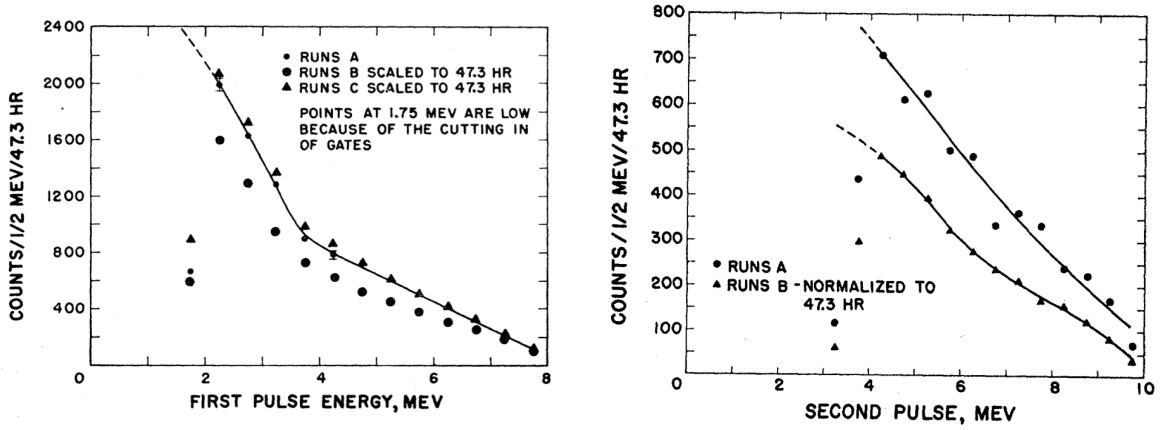

Figure 1.2: Prompt (*left*) and delayed (*right*) energy spectra for reactor-on data, *i.e.* runs A and C, and reactor-off data, *i.e.* runs B, from [8]

This experiment ran for 1371 hours with reactor-on and reactor-off periods. A flux variation was measured, depending on the reactor power, leading to the experimental proof of the existence of the neutrino. Figure 1.2 shows the flux difference for both prompt and delayed signals when the reactor was on, runs A and C, or off, runs B. This difference between on and off periods is attributed to neutrino events.

1.2.2 ν_μ discovery

An experiment which took place at the Brookhaven National Laboratory in the early 1960s can be considered as the first accelerator neutrino experiment. It was suggested independently by B. Pontecorvo [9] and M. Schwartz [10].

The goal was to observe the interaction of high-energy neutrinos with matter. Neutrinos were produced through the decay of pions and kaons, following the processes:

$$\pi^\pm \to \mu^\pm + \nu(\bar{\nu}) \tag{1.4}$$
$$K^\pm \to \mu^\pm + \nu(\bar{\nu}), \tag{1.5}$$

where pions and kaons were generated using a 15 GeV proton beam on a beryllium target. Muons were stopped within a 13.5 m thick iron shielding coming from the battleship USS Missouri [11] whereas the neutrinos interacted in a 10 ton aluminium spark chamber behind this shielding.

B. Pontecorvo pointed out the possibility that neutrinos produced in these decays are different from those produced in β-decay, as he wrote in [9]:

> "*The question discussed is the possibility of deciding, in principle, whether the neutrino emitted in the $\pi \to \mu$ decay (ν_μ) and the neutrino emitted in β decay (ν_e) are identical particles or not.*"

The detection of neutrinos can be done through the detection of electrons/positrons created in the reactions:

$$\nu + n \to p + e^- \tag{1.6}$$
$$\bar{\nu} + p \to n + e^+, \tag{1.7}$$

or through the detection of the muon/antimuon from the reactions:

$$\nu + n \to p + \mu^- \tag{1.8}$$
$$\bar{\nu} + p \to n + \mu^+ \tag{1.9}$$

34 "single tracks" events and 6 "showers" events were recorded. After checking that those single track events were not due neither to cosmic rays nor neutron produced, the physicists pointed out that those events were muons, "*as expected from neutrino interactions*" [12]. The showers events refered to electron events. The question was then to understand whether those created muons were coming from the interaction of the only neutrino species known at that time, ν_e, or whether there was another species able to produce them, ν_μ. The issue came from the fact that not as many electrons/positrons events were recorded as expected, leading to the the conclusion that "*the most plausible explanation for the absence of the electron showers, and the only one which preserves universality, is then that $\nu_\mu \neq \nu_e$*".

This experiment allowed the verification of the concept of lepton number introduced in 1953 by E.J. Konopinski and H.M. Mahmoud [13]. Indeed, the $\nu(\bar{\nu})$ created in reactions (1.4)

and (1.5) are muon-type, leading to the creation of muons when interacting in the spark chamber, according to reactions (1.8) and (1.9). Lepton numbers L_e and L_μ are conserved in all reactions, resolving the forbiddenness of the $\mu^+ \to e^+ + \gamma$ decay.

For electron-type particles, L_e is defined as:

$$L_e = \begin{cases} +1 & \text{for} \quad e^-, \nu_e \\ -1 & \text{for} \quad e^+, \bar{\nu}_e \\ 0 & \text{for} \quad \mu^-, \nu_\mu, \mu^+, \bar{\nu}_\mu, \end{cases}$$

whereas for muon-type particles, L_μ is defined as:

$$L_\mu = \begin{cases} +1 & \text{for} \quad \mu^-, \nu_\mu \\ -1 & \text{for} \quad \mu^+, \bar{\nu}_\mu \\ 0 & \text{for} \quad e^-, \nu_e, e^+, \bar{\nu}_e \end{cases}$$

A generalization to more lepton families is straightforward.

1.2.3 ν_τ, looking for the "kink"

The tau neutrino, ν_τ, is intrinsically linked to its associated lepton, the tau, τ. Whereas the electron was discovered in 1897 by J.J. Thomson, the muon in 1936 by C.D. Anderson, it was only in 1975 that the experiment lead by M. Perl at the e^+e^- collider at SLAC[1] discovered the third lepton, the τ [14]. This third lepton family brought the possible existence of a third neutino, the ν_τ.

Here again, it was an American discovery. In 2000, a collaboration of 52 physicists gathered around the DONUT[2] experiment brought out the proof of the existence of the tau neutrino [15]. Based at Fermilab, near Chicago, the DONUT experiment was looking for the interaction of a tau neutrino with a nucleus, in order to detect the created tau lepton following the reaction:

$$\nu_\tau(\bar{\nu}_\tau) + X \to \tau^-(\tau^+) + Y \tag{1.10}$$

800 GeV protons were used, created by the Tevatron accelerator. They interacted in a 1 m long tungsten beam dump, producing among various particles, D_S mesons. These D_S decay with a life time of $(500 \pm 7) \times 10^{-15}$ s, into a τ and a ν_τ for a branching fraction of (5.43 ± 0.31) %. Tau neutrinos interacted then in one of the 7 cm thick emulsion modules, placed behind magnets and various shieldings in order to absorbe or swept away undesired particles.

Following the reaction (1.10), one had to look finally for the decay of the created taus. With a life time of $(290.6 \pm 1.0) \times 10^{-15}$ s, these taus decay within 2 mm into a single charged daughter and neutrinos, leading to a "kink", a signature "*characterized by a large transverse*

[1] Stanford Linear Accelerator Center
[2] Direct Observation of the NeUtrino Tau

momentum" [15].

Four events were recorded after an exposure from April to September 1997, leading to the discovery of the third neutrino, the ν_τ.

1.2.4 How many neutrino families?

The number of neutrino families was determined at CERN in the 1990s with the use of the four LEP[3] experiments, ALEPH, DELPHI, L3 and OPAL [16]. This number concerns only neutrinos sensitive to the electroweak interaction. One can access this number by studying the different Z^0 decay modes. When the Z^0 decays into quarks or charged leptons, the width for each decay mode can be measured, leading, when summing them, to a visible decay width. *A contrario*, the Z^0 decay into neutrino-antineutrino can not be detected, leading to an invisible decay width:

$$\Gamma_{\text{inv}} = \sum_l \Gamma(Z^0 \to \nu_l + \bar{\nu}_l) \simeq N_\nu \, \Gamma(Z^0 \to \nu + \bar{\nu}), \tag{1.11}$$

where N_ν is the number of neutrino-antineutrino pairs.

Experimentally, the ratio $\Gamma_{\text{inv}}/\Gamma_{ll}$ shows a better precision than the invisible decay width alone. This is also valid for the prediction due to a reduced dependence on the unknown parameters. It allows us to determine the number of neutrino families thanks to the relation:

$$\left(\frac{\Gamma_{\text{inv}}}{\Gamma_{ll}}\right)_{\text{exp}} = N_\nu \left(\frac{\Gamma_{\nu\bar{\nu}}}{\Gamma_{ll}}\right)_{\text{th}} \tag{1.12}$$

The theoretical value for this ratio is 1.99125 ± 0.00083 whereas it has been measured to be 5.943 ± 0.016. The number of neutrino families is then:

$$N_\nu = 2.9840 \pm 0.0082, \tag{1.13}$$

in good agreement with the three lepton families observed.

1.3 Solar neutrino anomaly

The so-called solar neutrino problem came from a discrepancy between the predicted and observed rates of solar neutrino captures. It was pointed out in 1968 with the Homestake experiment in South Dakota, was confirmed by other experiments and was finally solved 34 years later with the SNO[4] experiment in Ontario.

[3] Large Electron Positron collider
[4] Sudbury Neutrino Observatory

1.3.1 The Sun, a neutrino factory

The Sun is shining because of continuous thermonuclear fusion processes in its core. Two main processes, named *pp* chain and CNO cycle, are responsible for converting protons and electrons into helium nuclei and neutrinos through the net reaction:

$$4p + 2e^- \rightarrow {}^4_2\mathrm{He} + 2\nu_e + Q, \tag{1.14}$$

where Q is the energy released defined as:

$$Q = 4m_p + 2m_e - m_{\mathrm{He}} = 26.731 \text{ MeV}, \tag{1.15}$$

where $m_{\mathrm{He}} = 2m_p + 2m_n - B(4,2)$ with $B(4,2)$ the binding energy of ${}^4_2\mathrm{He}$.

One can then estimate the solar neutrino flux on Earth:

$$\Phi_{\nu_e} = 2 \times \frac{L_\odot}{Q \times 4\pi R^2} = 6.385 \times 10^{10} \text{ cm}^{-2} \text{ s}^{-1}, \tag{1.16}$$

with $L_\odot = 3.846 \times 10^{26}$ W the Sun luminosity and $R = 149.598 \times 10^6$ km the astronomical unit taken from [11].

The *pp* chain starts converting protons into deuterium, e^+ and ν_e through the process:

$$p + p \rightarrow d + e^+ + \nu_e \qquad (pp) \tag{1.17}$$

The *pp* process is the main contribution of solar neutrinos but the maximum energy of these neutrinos makes them challenging to detect on Earth. Neutrinos can also be created through the four following processes, according to Figure 1.3:

$$p + e^- + p \rightarrow d + \nu_e \qquad (pep) \tag{1.18}$$

$${}^3_2\mathrm{He} + p \rightarrow {}^4_2\mathrm{He} + e^+ + \nu_e \qquad (hep) \tag{1.19}$$

$${}^7_4\mathrm{Be} + e^- \rightarrow {}^7_3\mathrm{Li} + \nu_e \qquad \left({}^7\mathrm{Be}\right) \tag{1.20}$$

$${}^8_5\mathrm{B} \rightarrow {}^8_4\mathrm{Be}^* + e^+ + \nu_e \qquad \left({}^8\mathrm{B}\right) \tag{1.21}$$

The number of produced elements from reactions 1.17 to 1.21 gives us the expected shapes of the neutrino spectra. For the *pep* and ^{7}Be processes, one should expect a discrete neutrino energy spectrum since there is two final products. *A contrario*, the *pp*, *hep* and ^{8}B lead to continuous spectra, as it is shown in Figure 1.4.

The CNO cycle is illustrated in Figure 1.3. It is also called Bethe-Weizsäcker cycle and provides neutrinos even if the processes involved are less dominant. Indeed, the *pp* chain dominates at temperatures below 15×10^6 K in stars with mass lower than around 1.3 $\mathrm{M}_\odot$ [17]. Since the temperature sensitivity is much larger for the CNO cycle than for the *pp* chain, the CNO cycle contributes to about only 1.5 % of the Sun luminosity [18].

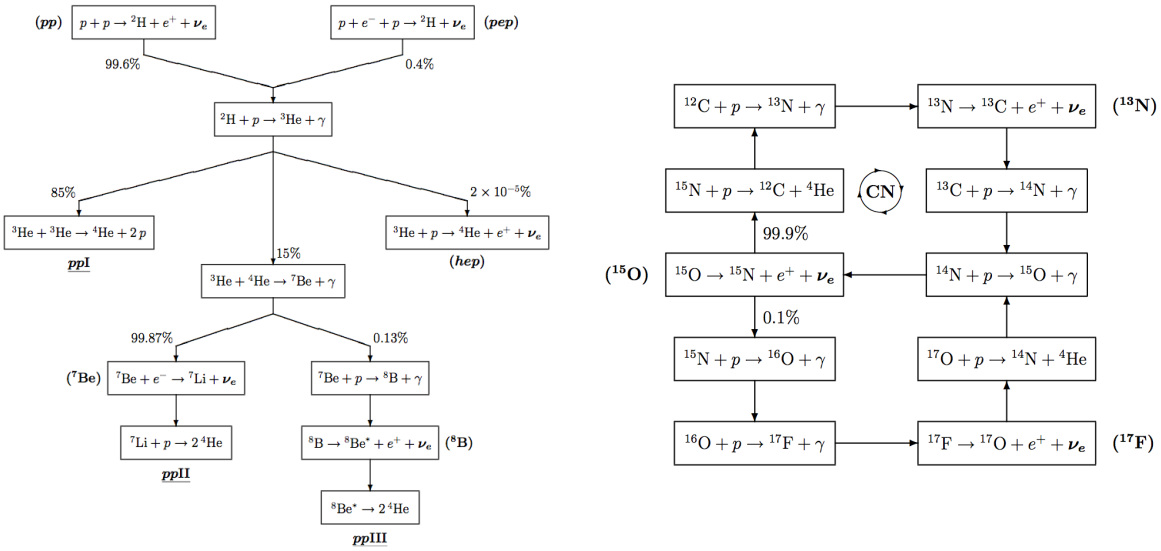

Figure 1.3: The *pp* chain (*left*) and the CNO cycle (*right*) with the generated neutrinos in bold, from [11].

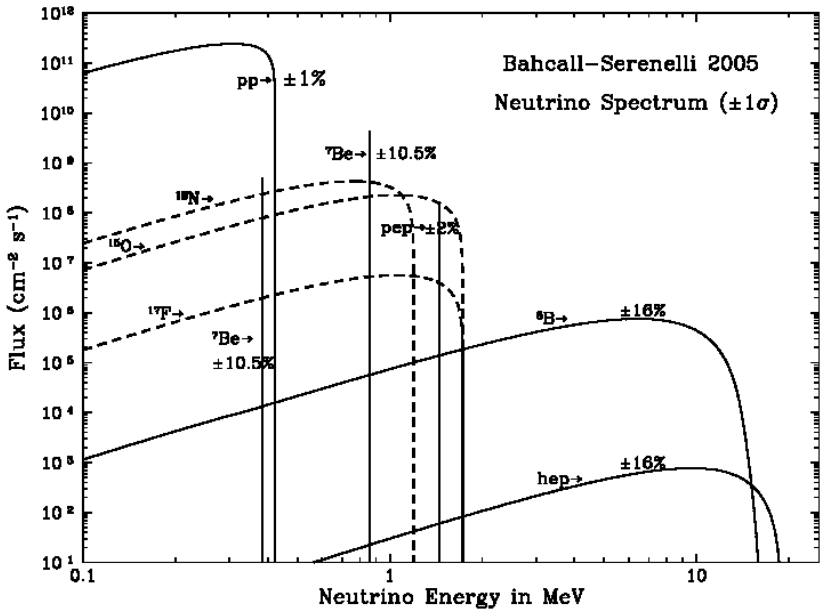

Figure 1.4: Solar neutrino energy spectrum adapted from [19] with the uncertainties from [20].

1.3.2 Chasing solar neutrinos

Radiochemical experiments

The solar neutrino anomaly started with the Homestake experiment in 1968. This experiment, led by R. Davis Jr., was looking for radioactive argon isotopes, ^{37}Ar, produced by the interaction of solar neutrinos, ν_e, on stable chlore isotopes, ^{37}Cl, through the reaction:

$$\nu_e + {}^{37}\mathrm{Cl} \rightarrow {}^{37}\mathrm{Ar} + e^- \tag{1.22}$$

The apparatus consisted of a 6.1 m diameter for 14.6 m long cylindrical tank filled with 615 tons of tetrachloroethylene, C_2Cl_4, installed in the Homestake Gold Mine in South Dakota. A 4200 m water equivalent overburden allowed the experiment to be protected from cosmic rays.

Every two months, an extraction by chemical methods of the produced ^{37}Ar was performed and subsequently counted. R. Davis Jr. and his collaborators noticed very soon after the start of the experiment that the number of ^{37}Ar was to low compared to the predictions [21]. This "surprise" gave birth to the solar neutrino anomaly, even if at that time, dependending on the Standard Solar Model (SSM) used, the observed and predicted fluxes could match. It allowed J.N. Bahcall to conclude at that time that these results "*are not in obvious conflict with the theory of stellar structure*" [22].

With more than 25 years of data, the Homestake experiment provided a ^{37}Ar production rate of $2.56 \pm 0.16\,(\mathrm{stat}) \pm 0.16\,(\mathrm{syst})$ SNU[5], about three times lower than the predictions [23]. Several tests were performed in order to verify that the detector was working properly, without finding any misbehavior.

Due to this huge discrepancy, other experiments started, such as the GALLEX[6]/GNO[7] and SAGE[8] experiments. The GALLEX/GNO experiment was located in the Laboratori Nazionali del Gran Sasso (LNGS) in Italy. The SAGE experiment is placed in the Baksan Neutrino Observatory (BNO) in Russia. They are both based on a solar neutrino interaction on ^{71}Ga instead of ^{37}Cl:

$$\nu_e + {}^{71}\mathrm{Ga} \rightarrow {}^{71}\mathrm{Ge} + e^- \tag{1.23}$$

The GALLEX/GNO experiment used 100 tons of gallium chloride $GaCl_3$, containing about 30 tons of gallium whereas the SAGE experiment opted for about 50 tons of gallium in the form of a liquid metal. Whereas the Homestake experiment had a threshold at 814 keV, the gallium experiments had a lower threshold at 233 keV, allowing them to detect solar neutrinos from the *pp* reaction (1.17).

[5] 1 Solar Neutrino Unit = 1 interaction per 10^{36} target atoms per second
[6] GALLium EXperiment
[7] Gallium Neutrino Observatory
[8] Soviet-American Gallium Experiment

The produced ^{71}Ge were extracted through chemical methods and their decay into ^{71}Ga was measured. After 10 years of running, about half of the expected signal was measured for both experiments [24, 25]:

$$69.3 \pm 4.1\,(\text{stat}) \pm 3.6\,(\text{syst})\,\text{SNU} \qquad \text{(GALLEX/GNO)} \tag{1.24}$$

$$70.8^{+5.3+3.7}_{-5.2-3.2}\,\text{SNU} \qquad \text{(SAGE)}, \tag{1.25}$$

instead of the $128\,^{+9}_{-7}$ SNU expected from the BP00 SSM [26].

Various tests were also performed, such as the introduction of ^{51}Cr sources in both experiments. It was concluded that the deficit was not due to experimental artifacts [27, 28].

Water Čerenkov experiments

The Kamiokande[9] and Super-Kamiokande experiments were also looking for solar neutrinos in order to try to solve the anomaly on a non-radiochemical base. The solar neutrino detection relies on the Čerenkov light produced by the recoil of the electron in the elastic scattering (ES) reaction:

$$\nu_\alpha + e^- \to \nu_\alpha + e^- \qquad \text{(ES)}, \tag{1.26}$$

where α stands for e, μ or τ.

Even if this reaction is sensitive to all neutrino flavors, ν_e elastic scattering dominates because of a six time higher cross-section for ν_e with respect to the ones for ν_μ and ν_τ [29].

The diffusion allowed to know the direction of the incoming neutrino, leading to the possibility of discriminating between solar neutrino events and background events. Nevertheless, since these experiments were first designed to look for nucleon decay with energy of the order of 1 GeV, they were only sensitive to the highest neutrino energy spectrum components in Figure 1.4, *i.e.* ^{8}B and *hep* components from reactions (1.19) and (1.21). A deficit was confirmed for the ^{8}B component, as shown in Table 1.1.

Deadlocked

At the dawn of the third millennium, the solar neutrino anomaly remained unsolved. Different radiochemical experiments saw deficits as well as water Čerenkov experiments which used a complete different detection method. Table 1.1 illustrates where the physicists stood before the results from the SNO experiment.

[9] Kamioka Nucleon Decay Experiment

Table 1.1: Solar neutrino flux, neutrino capture rate for ^{37}Cl and ^{71}Ga experiments from the BP00 SSM [26] and measured flux and rate for the Homestake [23], GALLEX/GNO [24], SAGE [25] and Super-Kamiokande [30] experiments. Statistical and systematic uncertainties have been added in quadrature.

Process	$\Phi_{\mathbf{BP00}}$ **(cm^{-2} s^{-1})**	$R_{\mathbf{Cl}}$ **(SNU)**	$R_{\mathbf{Ga}}$ **(SNU)**	$\Phi_{\mathbf{SK}}$ **(cm^{-2} s^{-1})**
pp	5.95×10^{10}	-	69.7	-
pep	1.40×10^{8}	0.22	2.8	-
hep	9.3×10^{3}	0.04	0.1	$< 73 \times 10^{3}$
^{7}Be	4.77×10^{9}	1.15	34.2	-
^{8}B	5.05×10^{6}	5.76	12.1	$(2.35 \pm 0.08) \times 10^{6}$
^{13}N	5.48×10^{8}	0.09	3.4	-
^{15}O	4.80×10^{8}	0.33	5.5	-
^{17}F	5.63×10^{6}	0.0	0.1	-
Total	6.54×10^{10}	$7.6^{+1.3}_{-1.1}$	128^{+9}_{-7}	-
Homestake	-	2.56 ± 0.23	-	
GALLEX/GNO	-	-	69.3 ± 5.5	
SAGE	-	-	$70.8^{+6.5}_{-6.1}$	

1.3.3 Solving the anomaly

One had to wait until 2002 and the results from the SNO experiment to be able to solve the solar neutrino anomaly [31]. Like Super-Kamiokande, SNO is a water Čerenkov experiment, sensible only to ^{8}B and *hep* components. The detector consists of a 12 m diameter sphere filled with an ultrapure heavy water (D_2O), different from the Super-Kamiokande one which is filled with ultrapure water (H_2O). Due to this outline, SNO was sensitive in one hand to the elastic scattering (ES) reaction, as Super-Kamiokande, and on another hand to the charge current (CC) reaction and to the neutral current (NC) reaction due to the interaction of the neutrinos on deuterium:

$$\nu_e + d \to p + p + e^- \qquad \text{(CC)} \tag{1.27}$$

$$\nu_\alpha + d \to p + n + \nu_\alpha \qquad \text{(NC)}, \tag{1.28}$$

where α stands for e, μ or τ.

Whereas the charged current reaction is only sensitive to ν_e, the neutral current reaction is sensitive to all neutrino flavors. If there is no other neutrino flavor involved but ν_e, then the solar neutrino flux from the charge current reaction should be of the order of the one from the neutral current reaction. SNO succeeded in measuring both Φ_{CC} and Φ_{NC}:

$$\Phi_{\mathrm{CC}} = 1.76^{+0.06}_{-0.05}\,(\mathrm{stat})\,^{+0.09}_{-0.09}\,(\mathrm{syst})\ \mathrm{cm}^{-2}\,\mathrm{s}^{-1} \tag{1.29}$$

$$\Phi_{\mathrm{NC}} = 5.09^{+0.44}_{-0.43}\,(\mathrm{stat})\,^{+0.46}_{-0.43}\,(\mathrm{syst})\ \mathrm{cm}^{-2}\,\mathrm{s}^{-1} \tag{1.30}$$

The total flux measured from the neutral current process is in agreement with the predicted value from Table 1.1. One can observe a discrepency between the Φ_{CC} and Φ_{NC} values which can be interpreted as a non-zero flux of ν_μ and ν_τ from the initial ^{8}B neutrino flux. With a change of variables, one can then deduce Φ_e and $\Phi_{\mu\tau}$:

$$\Phi_e = 1.76^{+0.05}_{-0.05}\,(\mathrm{stat})\,^{+0.09}_{-0.09}\,(\mathrm{syst})\ \mathrm{cm}^{-2}\,\mathrm{s}^{-1} \tag{1.31}$$

$$\Phi_{\mu\tau} = 3.41^{+0.45}_{-0.45}\,(\mathrm{stat})\,^{+0.48}_{-0.45}\,(\mathrm{syst})\ \mathrm{cm}^{-2}\,\mathrm{s}^{-1} \tag{1.32}$$

With a non-electron neutrino flux $5.3\,\sigma$ greater than zero, this results allowed to confirm that during their journey, some of the ν_e created through the ^{8}B process from reaction (1.21) transformed themselves into another neutrino flavor, giving a deficit of ν_e when looking only for them on Earth.

Thanks to the use of the heavy water, the SNO experiment confirmed the reliability of the SSM prediction and solved the solar neutrino anomaly. Back in 1972, B. Pontecorvo sent a fax to J.N. Bahcall telling him [32]:

> "*It would be nice if all this will end with something unexpected from the point of view of particle physics. Unfortunately, it will not be easy to demonstrate this, even if nature works that way.*"

The theory of neutrino oscillation was pointed out as the best way to resolve this anomaly. We will investigate in more details this theory in the next chapter.

1.4 Atmospheric neutrino anomaly

Atmospheric neutrinos are created from the interaction of primary cosmic rays with the Earth's atmosphere. This process gives birth to a particle zoo which contains among them pions and kaons we have already seen in the description of the ν_μ discovery. Those pions and kaons decay, producing muons and ν_μ. Those muons also decay, producing ν_e and ν_μ. We call atmospheric neutrinos the ν_e and ν_μ produced in these decays. One should expect then to measure two ν_μ for every ν_e. It is in reality a bit more complicated but stays valid for energies below 1 GeV.

Water Čerenkov experiments are looking for the leptons produced in the charge current quasi-elastic (CCQE) scattering of neutrinos in the detector, as well as single-pion and multi-pion production from both charged and neutral currents:

$$\nu_l(\bar{\nu}_l) + X \to l^-(l^+) + Y \qquad \text{(CCQE)} \tag{1.33}$$

$$\nu_l(\bar{\nu}_l) + X \to l^-(l^+) + Y + \pi^+(\pi^-) \qquad \text{(CC single-pion)} \tag{1.34}$$

$$\nu_l(\bar{\nu}_l) + X \to \nu_l(\bar{\nu}_l) + X + \pi^0 \qquad \text{(NC single-pion)}, \tag{1.35}$$

where l stands either for e or μ.

The CCQE reaction is the dominant one for energies below 1 GeV. The strength of this kind of experiments is to easily discriminate between electron-like events and muons-like events by observing the Čerenkov rings which differs from one to another. It is then of interest to look for single-ring e-like and single-ring μ-like produced by the interaction of atmospheric neutrinos in the detector.

In 1988, the Kamiokande collaboration pointed out a deficit of ν_μ when comparing with the prediction, as it can be seen in Figure 1.5. If the number of recorded e-like events was 105 ± 11 % of the estimation, it was only 59 ± 7 % for μ-like events [33]. Even if a way to explain this deficit was that "*the calculation of the atmospheric neutrino fluxes may not be correct*", this results brought a new interest and gave birth to what would be called the atmospheric neutrino anomaly.

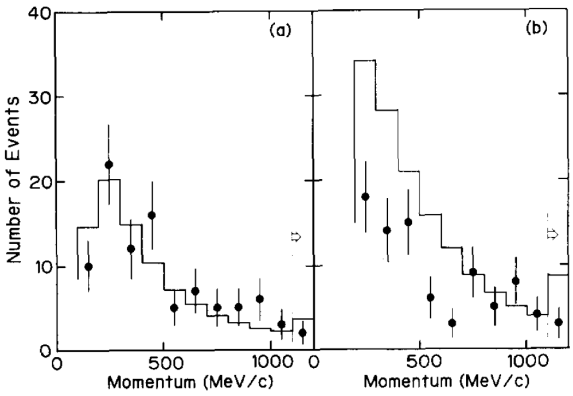

Figure 1.5: Momentum distributions for (a) e-like events and (b) μ-like events, from [33].

Several other experiments started then to investigate this deficit. In 1992, with the analysis of 610 single-ring events recorded for a total exposure of 7.7 kton year, the IMB experiment confirmed a deficit by measuring a $0.36 \pm 0.02\,(\text{stat}) \pm 0.02\,(\text{syst})$ fraction of μ-like events over all events when its simulation predicted a fraction of $0.51 \pm 0.01\,(\text{stat}) \pm 0.05\,(\text{syst})$ [34]. In 1997, with the use of an iron tracking calorimeter, the Soudan 2 experiment confirmed also a deficit. After a total exposure of 1.52 kton year, the number of e-like events corresponded to 109 ± 21 % of the estimation whereas it corresponded only to 79 ± 18 % for μ-like events [35].

In order to study the ν_μ/ν_e flux ratio, one can calculate the ratio-of-ratios R defined as:

$$R = \frac{(N_\mu/N_e)_{\text{Data}}}{(N_\mu/N_e)_{\text{MC}}}, \tag{1.36}$$

where N_μ and N_e stand respectively for μ-like and e-like events.

If both data and prediction are in agreement, one should measure $R = 1$. In 1998, the Super-Kamiokande experiment reported $R = 0.63 \pm 0.03\,(\text{stat}) \pm 0.05\,(\text{syst})$, confirming here

again a deficit of μ-like events [36].

Since neutrinos interact very weakly, atmospheric neutrinos born on the other side of the Earth should easily cross it before interacting in a detector, leading to a flight path from 20 to 12000 km. Thanks to the Čerenkov light pattern, one can then reconstruct the lepton direction which, for energies above 1 GeV, is strongly correlated to the initial incoming direction of the neutrino. The ratio of the number of upward to downward μ-like events has been measured by Super-Kamiokande to be $0.52\,^{+0.07}_{-0.06}\,(\text{stat}) \pm 0.01\,(\text{syst})$ when one should expect a value close to the unity. The same ratio for e-like events did not show any discrepancy, as it can be seen in Figure 1.6.

These misbehaviors for both the expected number of μ-like events and their angular distortion allowed the Super-Kamiokande collaboration to conclude [37]:

> "*While the zenith angle dependence of the μ-like data cannot be explained by any plausible systematic detector effect considered, the relative deficit of upward-going μ-like events from neutrinos that traveled a long distance suggests the disappearance of ν_μ via neutrino oscillations.*"

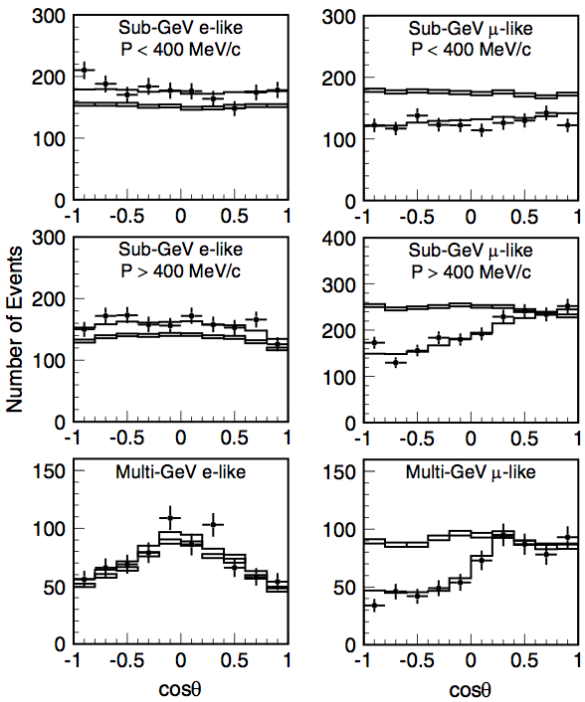

Figure 1.6: Zenithal angle distributions for fully contained single-ring e-like and single-ring μ-like events, from [38]. The points correspond to the data, the box histograms to the non-oscillation prediction and the lines to the best fit.

1.5 Unsolved anomalies

The solar and atmospheric neutrino anomalies were solved by considering a three neutrino oscillation framework, which will be reviewed in detail in the next chapter. The anomalies described in this section can not be solved through a three neutrino oscillation scenario. Up to now, they remain unsolved.

1.5.1 Reactor antineutrino anomaly

The Double Chooz experiment, which will be described in the third chapter, started taking data in April 2011 with only one detector. The final configuration implies two identical detectors located at different baselines from two nuclear reactors, in order to get rid of systematic uncertainty coming mainly from the lack of precision of the $\bar{\nu}_e$ spectra prediction. The reactor flux error is about 1.8 %, which is the main source of uncertainty for Double Chooz without a second detector [39, 40, 41, 42].

In order to reduce this error, new calculations of the $\bar{\nu}_e$ spectra coming from ^{235}U, ^{239}Pu, ^{241}Pu and ^{238}U were performed, revealing an underestimation of about 3 % [43]. A complete re-analysis of all reactor experiments at reactor-detector distance lower than 100 m followed, leading to a change in the ratio R of observed event rate to predicted rate. Whereas this ratio was 0.976 ± 0.024 before, it changed to 0.943 ± 0.023 with the new calculations. This deviation from unity at 98.6 % C.L. is called the reactor antineutrino anomaly [44].

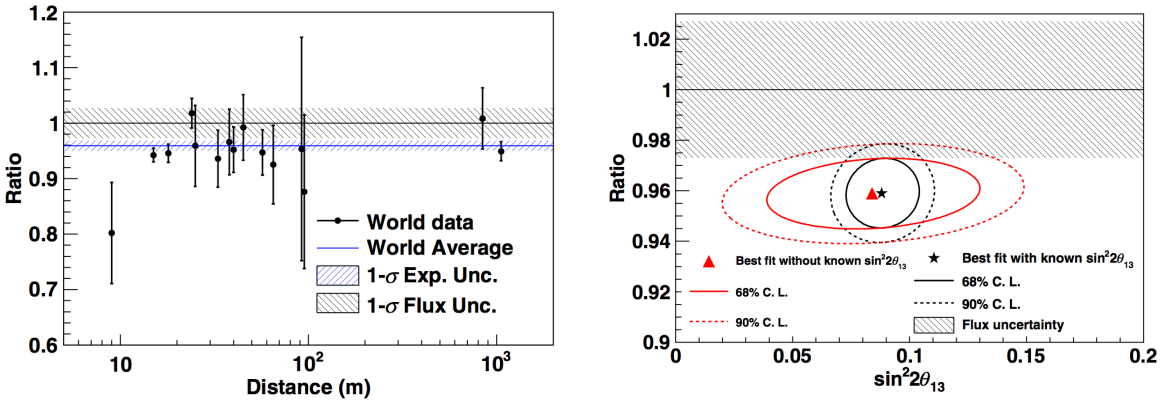

Figure 1.7: Ratio of the data to the non-oscillation prediction as a function of the distance (*left*) and $\sin^2(2\theta_{13})$ (*right*), from [45].

Recent investigations which included the precise measurement of the θ_{13} mixing angle confirmed the discrepency and determine $R = 0.959 \pm 0.009\,(\text{experiment uncertainty}) \pm 0.027\,(\text{flux systematics})$ [45]. Figure 1.7 shows the ratio of the data to the non-oscillation prediction as a function of the distance from the corresponding reactor core (*left*) and as a function of $\sin^2(2\theta_{13})$ with and without its best fit value (*right*). It was pointed out that this deficit could come from a possible "sterile" neutrino, *i.e.* that there is a non-zero probability

for an $\bar{\nu}_e$ to oscillate, at very short distance, into a hypothetical new neutrino state which remains insensitive to the electroweak interaction.

1.5.2 GALLEX and SAGE, the gallium anomaly

While the solar neutrino anomaly was not yet solved, the radiochemical gallium experiments GALLEX and SAGE exposed their detector to intense calibration sources in order to check any misbehavior which could explain the solar neutrino deficit they observed. GALLEX used two intense ^{51}Cr sources. The first one was deployed between June and October 1994 and the second one between October 1995 and February 1996. The combined value of the ratio R between the neutrino source strength and the measured one was 0.93 ± 0.08, not enough to explain the solar neutrino deficit [27]. SAGE used also a ^{51}Cr source and went to the same conclusion [28]. SAGE decided later on to expose its detector to a ^{37}Ar source. In this case, $R = 0.79^{+0.09}_{-0.10}$, nearly $2.5\,\sigma$ from unity [46].

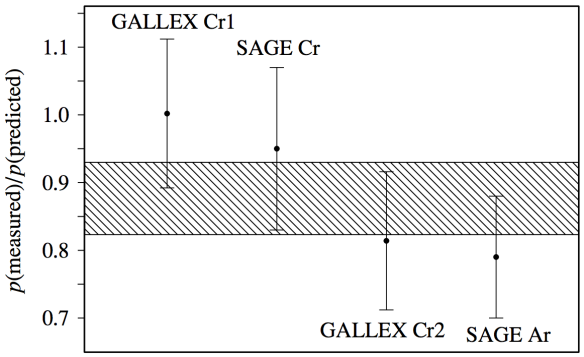

Figure 1.8: Ratio of the data to the prediction for the radiochemical gallium experiments GALLEX and SAGE, from [46]. The hashed region corresponds to the weighted average.

An average value of the two different ^{51}Cr calibration campaigns from GALLEX together with the ^{51}Cr one and the ^{37}Ar one from SAGE allowed to find a discrepency between the prediction and the observation, as it can be seen in Figure 1.8 [46]:

> "*The weighted average value of R, the ratio of measured to predicted* ^{71}Ge *production rates, is* 0.88 ± 0.05*, more than two standard deviations less than unity. Although not statistically conclusive, the combination of these experiments suggests that the predicted rates may be overestimated.*"

Another explanation comes from the possible ν_e oscillation into a sterile neutrino state, at very short distance, leading to the observed deficit.

1.5.3 LSND and MiniBooNE anomalies

The LSND[10] experiment took place at the Los Alamos Neutron Science Center from 1993 to 1998. This experiment was designed to study $\bar{\nu}_\mu \to \bar{\nu}_e$ from μ^+ decay at rest. A total excess of $87.9 \pm 22.4 \pm 6.0$ $\bar{\nu}_e$ events identified through IBD interactions were registered above the expected background [47]. This excess can be interpreted as an oscillation, although the mass-squared difference reported stands in the range $[0.2, 10\ \text{eV}^2]$, which does not correspond to the mass-squared differences of solar or atmospheric neutrinos we will review in the next chapter. This observation implies the existence of at least one sterile neutrino with a mass greater than 0.4 eV.

The MiniBooNE[11] experiment has been designed to investigate the LSND results. With a similar L/E range, MiniBooNE has been studied both $\bar{\nu}_\mu \to \bar{\nu}_e$ and $\nu_\mu \to \nu_e$ transitions. While the results for the $\bar{\nu}_\mu \to \bar{\nu}_e$ transition are fairly in agreement, the $\nu_\mu \to \nu_e$ transition has been found to be inconsistent [48]. Figure 1.9 shows the energy spectra with and without background substraction for both antineutrino and neutrino modes. A fit analysis was performed on a two-neutrino oscillation model, which shows a different behavior for antineutrino and neutrino modes.

The excess in the $\bar{\nu}_\mu \to \bar{\nu}_e$ transition being localized in the low energy part of the spectrum, the MicroBooNE experiment has been designed to investigate this specific part of the energy spectrum.

[10] Liquid Scintillator Neutrino Detector
[11] Mini Booster Neutrino Experiment

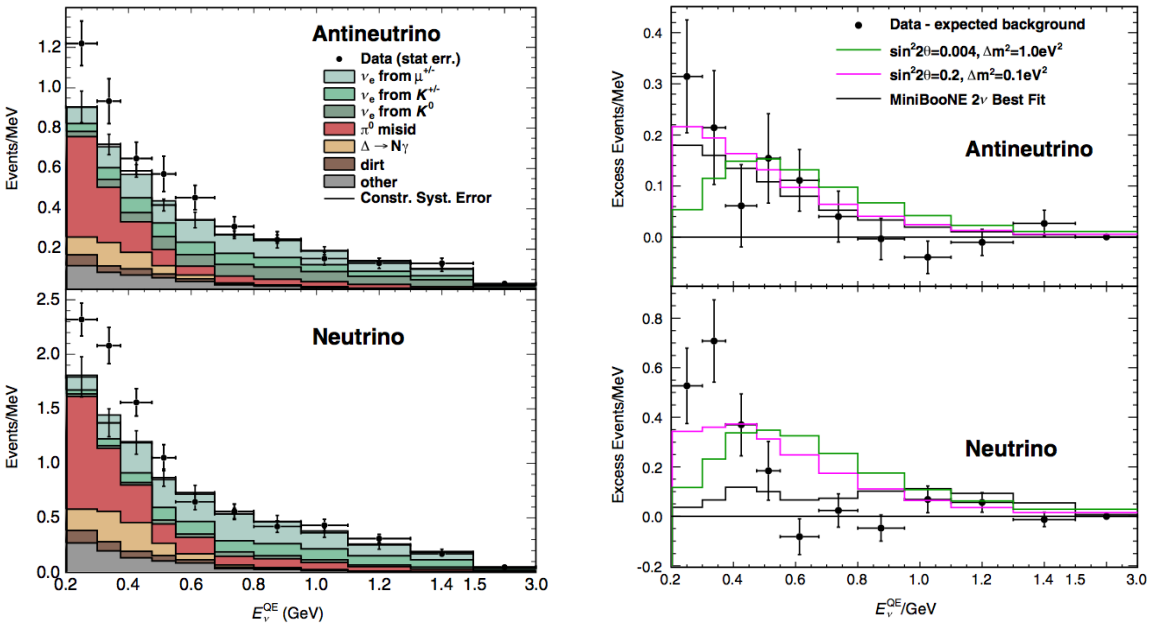

Figure 1.9: Energy spectra before (*left*) and after (*right*) background substraction for both antineutrino and neutrino modes, from [48]. Best fit for each mode as well as two fits with different sets of oscillation parameters are shown.

Chapter

2 Deepening the neutrino knowledge

There are two possible outcomes: if the result confirms the hypothesis, then you've made a measurement. If the result is contrary to the hypothesis, then you've made a discovery.
Enrico Fermi

Contents

Our understanding of neutrinos is far from being complete. Although the neutrino oscillation theory is well established, throwing out the Standard Model requirement of a massless neutrinos, physicists have still to answer key questions, such as the nature of the neutrino itself, Dirac or Majorana, or its mass.

2.1 Neutrinos within the Standard Model

The Standard Model of particle physics is a quantum field theory which aims at unifying the strong, weak and electromagnetic interactions in order to marry quantum physics together with special relativity. It allows to describe elementary particles properties and interactions between them. It derives from the Fermi theory [3] together with the Glashow-Weinberg-Salam theory [49, 50].

The Standard Model is a gauge theory based on the $\mathrm{SU(3)_C} \otimes \mathrm{SU(2)_L} \otimes \mathrm{U(1)_Y}$ local symmetry group where C, L and Y denote repectively the color, the left-handed chirality and the weak hypercharge [11]. To each group corresponds a certain number of generators, the vector gauge bosons. $\mathrm{SU(3)_C}$ owns eight generators, the gluons, which are also the force carriers of the strong interaction. $\mathrm{SU(2)_L} \otimes \mathrm{U(1)_Y}$ owns four generators. The spontaneous breaking of the $\mathrm{SU(2)_L} \otimes \mathrm{U(1)_Y}$ symmetry through the Brout-Englert-Higgs mechanism allows to generate the masses of the $W^{\pm}$ and Z^0 bosons, force carriers of the weak interaction [51, 52]. The important mass they acquired during this process is responsible for the short range of the weak interaction. The photon, γ, is finally the force carrier of the electromagnetic interaction. Weak and electromagnetic interactions were unified thanks to the Glashow-Weinberg-Salam theory of electroweak interaction [49, 50], which was able to predict the $W^{\pm}$ and Z^0 masses.

Table 2.1: Elementary properties of the fermions. Masses are taken from [29] for the quarks and charged leptons and from [53, 54, 55] for the upper limits on the masses of the neutrinos.

Fermions	**1st family**	**2nd family**	**3rd family**
Quarks	u (up)	c (charm)	t (top)
	$m_u = 2.3^{+0.7}_{-0.5}$ MeV	$m_c = 1.275 \pm 0.025$ GeV	$m_t = 173.5 \pm 0.6 \pm 0.8$ GeV
	d (down)	s (strange)	b (bottom)
	$m_d = 4.8^{+0.7}_{-0.3}$ MeV	$m_s = 95 \pm 5$ MeV	$m_b = 4.18 \pm 0.03$ GeV
Leptons	e^-	μ^-	τ^-
	$m_e = 0.511$ MeV	$m_\mu = 105.658$ MeV	$m_\tau = 1.777$ GeV
	ν_e	ν_μ	ν_τ
	$m_{\nu_e} < 2.05$ eV	$m_{\nu_\mu} < 170$ keV	$m_{\nu_\tau} < 18.2$ MeV

The Standard Model describes the fermions, which are the components of the matter, as well as the bosons, which are the force carriers. Whereas the fermions own half-integer spins, obey the Fermi-Dirac statistics and follow the Pauli exclusion principle, the bosons own integer spin and obey the Bose-Einstein statistics. The fermions can be divided into two sub-categories, the quarks and the leptons. There are three families of quarks and leptons, as it can be seen in Table 2.1. Quarks are subject to the four fundamental interactions which are the strong, weak, electromagnetism and gravitational interactions. They can not be observed directly since they are confined into hadrons, such as baryons when they are arranged with

three quarks or mesons when they form a quark/antiquark pair. Leptons do not interact through the strong interaction but are subject to the three other fundamental interactions, except for the neutrinos which do not interact through the electromagnetic interaction. The left-handed charged lepton together with the left-handed neutrino form a doublet of $SU(2)_L$. Whereas the right-handed charged lepton exists, the right-handed neutrino is not considered in the Standard Model. Up to now, there is not yet an experimental evidence for a right-handed neutrino.

2.1.1 Masses in the Standard Model: the Higgs mechanism

The masses of bosons and fermions are generated through the Higgs mechanism. The introduction of a complex scalar field $\Phi(x)$ allows to generate masses through spontaneous symmetry breaking. This field can be written through the Higgs doublet:

$$\Phi(x) \equiv \begin{pmatrix} \phi^+(x) \\ \phi^0(x) \end{pmatrix}, \tag{2.1}$$

where $\phi^+(x)$ and $\phi^0(x)$ are respectively the charged and neutral complex scalar fields.

The general potential associated to this Higgs field is given by:

$$V(\Phi) = \mu^2\Phi^\dagger\Phi + \lambda(\Phi^\dagger\Phi)^2 = \lambda\left(\Phi^\dagger\Phi + \frac{\mu^2}{2\lambda}\right)^2 - \frac{\mu^4}{4\lambda} \tag{2.2}$$

Neglecting the $\mu^4/4\lambda$ constant term, this potential has a minimum for $\Phi^\dagger\Phi = -\mu^2/2\lambda$. In order to have the spontaneous symmetry breaking, we have to consider $\mu^2 < 0$. The minimum of this potential corresponds to the vacuum. The vacuum expactation value, $\langle\Phi\rangle$, is due to the neutral complex scalar field, ϕ^0, and can be expressed as:

$$\langle\Phi\rangle = \frac{1}{\sqrt{2}}\begin{pmatrix} 0 \\ v \end{pmatrix} \qquad \text{with} \qquad v \equiv \sqrt{-\frac{\mu^2}{\lambda}} \tag{2.3}$$

The mass of the BEH[1] boson, sometimes simply called Higgs boson, is linked to v through:

$$m_{\text{BEH}} = \sqrt{2\lambda v^2} = \sqrt{-2\mu^2}, \tag{2.4}$$

which can not be predicted by the Standard Model since μ^2 has been introduced without being connected to other measurable quantities.

The existence of this boson was first postulated in 1964 by F. Englert and R. Brout and independently by P.W. Higgs [51, 52]. On July 4, 2012, the two main LHC[2] experiments, ATLAS and CMS, announced its discovery, giving the Nobel Prize the next year to P.W. Higgs and F. Englert[3] [56, 57].

[1] Brout-Englert-Higgs
[2] Large Hadron Collider
[3] R. Brout died on May 3, 2011.

The Standard Model does not provide neither a right-handed neutrino nor a mass for the neutrino. Nevertheless, it is still possible to add an extension to this model in order to give masses to the neutrinos.

2.2 Neutrino masses

The mass term arises from the Lagrangian of interaction of leptons and Higgs bosons when the symmetry is spontaneously broken [58]. It allows to connect a ψ field to its conjugate $\bar{\psi}$, leading to the Lagrangian density:

$$\mathcal{L} = -m\bar{\psi}\psi \tag{2.5}$$

The ψ field can be decomposed into a "left-handed" field, ψ_L, and a "right-handed" field, ψ_R, such that:

$$\psi = \psi_L + \psi_R \tag{2.6}$$

ψ_L and ψ_R are linked to the notions of chirality and helicity. When considering relativistic particles, the chirality almost coincides with the projection of its spin on its momentum, *i.e.* its helicity. The chirality projector P_L and P_R act on ψ such that:

$$\psi_L = P_L\psi \qquad \psi_R = P_R\psi, \tag{2.7}$$

with the following properties:

$$P_L^2 = P_L \qquad P_R^2 = P_R \qquad P_L P_R = P_R P_L = 0 \qquad P_L + P_R = 1 \tag{2.8}$$

Let us now have a look at the charge conjugation operator $\mathcal{C}$. This operator allows to change a particle into its antiparticle:

$$\psi \xrightarrow{\mathcal{C}} \psi^c = \mathcal{C}\bar{\psi}^T \tag{2.9}$$

Acting on chiral fields and neglecting phase factors, this operator allows to change a left-handed field into a right-handed field, and *vice versa*:

$$\psi_L \xrightarrow{\mathcal{C}} \psi_L^c = \mathcal{C}\bar{\psi}_L^T \equiv \psi_R \qquad \psi_R \xrightarrow{\mathcal{C}} \psi_R^c = \mathcal{C}\bar{\psi}_R^T \equiv \psi_L \tag{2.10}$$

The ψ field from equation (2.6) can then be expressed in this way:

$$\psi = \psi_L + \psi_L^c \tag{2.11}$$

2.2.1 Dirac mass term

We build a neutrino Dirac mass term by introducing the decomposed field from equation (2.6) into the Lagrangian density from equation (2.5):

$$\begin{aligned}\mathcal{L}^{\mathrm{D}} &= -M_{\mathrm{D}}(\bar{\nu}_L + \bar{\nu}_R)(\nu_L + \nu_R) \\ &= -M_{\mathrm{D}}(\bar{\nu}_L\nu_R + \bar{\nu}_R\nu_L) \\ &= -M_{\mathrm{D}}\,\bar{\nu}_R\nu_L + \text{h.c.},\end{aligned} \tag{2.12}$$

where the terms $\bar{\nu}_L\nu_L$ and $\bar{\nu}_R\nu_R$ vanish due to the chirality projector properties from equations (2.8):

$$\bar{\nu}_L\nu_L = \nu_L^\dagger\gamma^0\nu_L = \nu_L^\dagger\gamma^0 P_L\nu = \nu_L^\dagger P_R\gamma^0\nu = (P_R\nu_L)^\dagger\gamma^0\nu = (P_R P_L\nu)^\dagger\gamma^0\nu = 0, \tag{2.13}$$

where γ^0 corresponds to one of the four Dirac γ matrices.

The Dirac mass term considers both the left-handed and right-handed fields. Nevertheless, the right-handed field does not participate to any Standard Model interaction. It can be removed by using a Majorana mass term.

2.2.2 Majorana mass term

Since the left-handed field is linked to the right-handed field through the charge conjugation, we can build a neutrino Majorana mass term for the ν_L field only. This neutrino Majorana mass term can be obtained by injecting equation (2.11) into equation (2.5):

$$\begin{aligned}\mathcal{L}^{\mathrm{M}} &= -\frac{1}{2}M_{\mathrm{L}}(\overline{\nu_L} + \overline{\nu_L^c})(\nu_L + \nu_L^c)\\ &= -\frac{1}{2}M_{\mathrm{L}}(\overline{\nu_L}\nu_L^c + \overline{\nu_L^c}\nu_L)\\ &= -\frac{1}{2}M_{\mathrm{L}}\,\overline{\nu_L^c}\nu_L + \mathrm{h.c.}\end{aligned} \tag{2.14}$$

Using equation (2.10), one can express ν_L^c in terms of ν_L:

$$\overline{\nu_L^c} = (\mathcal{C}\overline{\nu_L}^T)^\dagger\gamma^0 = \nu_L^T(\gamma^0)^T\mathcal{C}^\dagger\gamma^0 = -\nu_L^T\mathcal{C}^\dagger, \tag{2.15}$$

leading to:

$$\mathcal{L}^{\mathrm{M}} = \frac{1}{2}M_{\mathrm{L}}\,\nu_L^T\mathcal{C}^\dagger\nu_L + \mathrm{h.c.} \tag{2.16}$$

Nevertheless, it is also possible to add a Majorana mass term for the ν_R field. The general neutrino Majorana mass term can then be expressed as:

$$\mathcal{L}^{\mathrm{M}} = \frac{1}{2}M_{\mathrm{L}}\,\nu_L^T\mathcal{C}^\dagger\nu_L + \frac{1}{2}M_{\mathrm{R}}\,\nu_R^T\mathcal{C}^\dagger\nu_R + \mathrm{h.c.} \tag{2.17}$$

One can directly observe from equation (2.11) that $\psi = \psi^c$ or, in other words, that a Majorana particle is its own antiparticle [59]. A charged particle can not therefore be a Majorana particle, only neutrino can be.

Neutrinoless double β decay experiments are still investigating whether the neutrino is a Majorana particle, we will talk about these experiments later on in this chapter.

2.2.3 See-saw mechanism

Let us now consider the most general neutrino mass term by combining both Dirac and Majorana mass terms. It leads to the Lagrangian density:

$$\mathcal{L}^{\mathrm{D+M}} = \frac{1}{2} M_{\mathrm{L}}\, \nu_L^T \mathcal{C}^\dagger \nu_L - M_{\mathrm{D}}\, \bar{\nu}_R \nu_L + \frac{1}{2} M_{\mathrm{R}}\, \nu_R^T \mathcal{C}^\dagger \nu_R + \mathrm{h.c.} \tag{2.18}$$

$\mathcal{L}^{\mathrm{D+M}}$ can also be written in a more compact way:

$$\mathcal{L}^{\mathrm{D+M}} = \frac{1}{2} N_L^T \mathcal{C}^\dagger \mathcal{M} N_L + \mathrm{h.c.}, \tag{2.19}$$

with N_L defined as:

$$N_L = \begin{pmatrix} \nu_L \\ \nu_R^c \end{pmatrix} \tag{2.20}$$

Since M_{D} is a non-diagonal matrix and M_{L} and M_{R} have to be symmetric, $\mathcal{M}$ can be expressed as:

$$\mathcal{M} = \begin{pmatrix} M_{\mathrm{L}} & M_{\mathrm{D}} \\ M_{\mathrm{D}}^T & M_{\mathrm{R}} \end{pmatrix} \tag{2.21}$$

$\mathcal{M}$ can then be diagonalized using an orthogonal matrix U such that:

$$\mathcal{D} = U^T \mathcal{M} U = \begin{pmatrix} m_1 & 0 \\ 0 & m_2 \end{pmatrix} \tag{2.22}$$

Playing with the traces and the determinants of these two matrices, we end with a system with two unknowns that one can easily solve in order to find the values of the neutrino mass eigenvalues m_1 and m_2:

$$m_{2,1} = \frac{M_{\mathrm{L}} + M_{\mathrm{R}}}{2} \pm \sqrt{\left(\frac{M_{\mathrm{L}} - M_{\mathrm{R}}}{2}\right)^2 + M_{\mathrm{D}}^2} \tag{2.23}$$

From this general case, we can build the so-called "see-saw" mechanism. This mechanism allows to explain why the "active" neutrinos are so light by compensating with heavy neutrinos, called "sterile" since they can not interact through the weak interaction of the Standard Model. This mechanism assumes therefore the existence of a sterile neutrino through a minimal extension of the Standard Model. From the neutrino mass eigenvalues m_1 and m_2 we have calculated earlier, $m_1 < m_2$. Assuming $M_R \gg M_D$ and $M_L = 0$, we are left with:

$$m_1 \simeq -\frac{M_{\mathrm{D}}^2}{M_{\mathrm{R}}} \qquad m_2 \simeq M_{\mathrm{R}} \tag{2.24}$$

The negative sign of m_1 can be removed by taking the physical neutrino field through the action of the γ_5 matrix [60]. Considering M_{D} to be a quark or charged lepton mass, we end with:

$$m_1 \times m_2 = M_{\mathrm{D}}^2 \tag{2.25}$$

This corresponds to the see-saw relation. It tells us that if an active neutrino of mass m_1 is so light, it is due to the presence of a heavy neutrino of mass m_2.

2.2.4 Neutrino masses from experiments

β^- decay experiments

As we have already seen in the previous chapter, the β^- decay is a radioactivity process in which an electron and an $\bar{\nu}_e$ are emitted, according to the reaction:

$$ {}^{A}_{Z}\mathrm{X} \rightarrow {}^{A}_{Z+1}\mathrm{Y} + e^- + \bar{\nu}_e \tag{2.26} $$

When neglecting the ${}^{A}_{Z+1}\mathrm{Y}$ recoil, the electron and the $\bar{\nu}_e$ share the available energy. In the case of a massless neutrino, the electron spectrum would extend up to the maximum available energy $E_e^{\max} = E_0$. *A contrario*, if the neutrino has a mass, then the electron energy spectrum will be distorted since $E_e^{\max}$ will no longer be equal to E_0. We will have in this case $E_e^{\max} = E_0 - m_{\nu_e}$, as it is shown in Figure 2.1. This kind of investigation does not rely on the nature of the neutrino, *i.e.* Dirac or Majorana.

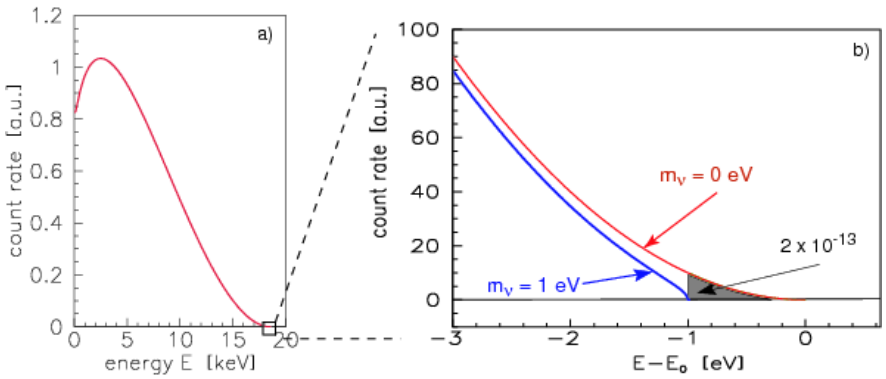

Figure 2.1: The electron energy spectrum of tritium β decay (a) with a narrow region around the endpoint (b), from [61].

The Mainz, Troitsk and upcoming KATRIN experiments are based on the tritium β decay spectroscopy. One needs a low endpoint since the neutrino mass expected is low. With an endpoint at 18.6 keV, a simple electronic shell and a half life of 12.3 years, the tritium is a good candidate.

The Mainz experiment reported in 2005 an upper limit of $m_{\nu_e} \leq 2.3$ eV at 95 % C.L. [62] and the Troitsk experiment an upper limit of $m_{\nu_e} \leq 2.12$ eV with a Bayesian approach and $m_{\nu_e} \leq 2.05$ eV with a Feldman and Cousins approach [53, 63]. The KATRIN experiment is still under construction and would have an estimated sensitivity of $m_{\nu_e} = 0.35$ eV at 90 % C.L., which is about one order of magnitude better than the previous experiments [61].

Limits were also obtained on the effective ν_μ and ν_τ masses, although less stringent. An upper limit on m_{ν_μ} was determined by studying the decay of pions in the reaction $\pi^+ \rightarrow \mu^+ + \nu_\mu$, leading to $m_{\nu_\mu} < 170$ keV [54]. Upper limit on m_{ν_τ} was derived by studying the decay of taus in the reactions $\tau^- \rightarrow 2\pi^-\pi^+\nu_\tau$ and $\tau^- \rightarrow 3\pi^-2\pi^+(\pi^0)\nu_\tau$, leading to $m_{\nu_\tau} < 18.2$ MeV [55].

Neutrinoless double β decay

Several experiments are looking for the nature of the neutrino. The principle relies on the observation of the double β decay, *i.e.* the simultaneous transformation of two neutrons into two protons in even-even nuclei for whom a simple β decay is not allowed. This process can in principle occur in two different ways:

- **Double β decay with emission of two neutrinos ($\beta\beta 2\nu$):** this reaction allows the emission of two electrons together with two neutrinos:

$$ {}^{A}_{Z}\mathrm{X} \rightarrow {}^{A}_{Z+2}\mathrm{Y} + 2e^- + 2\bar{\nu}_e \qquad (\beta\beta 2\nu) \tag{2.27} $$

  This reaction conserves the lepton number and has already been observed with typical half-lives of $10^{18}/10^{20}$ years. This reaction is possible only if the ground state of the ${}^{A}_{Z}\mathrm{X}$ nuclei has an energy larger than the ground state of the ${}^{A}_{Z+2}\mathrm{Y}$ nuclei. The inverse of the half-life can be accessed through the knowledge of the phase-space factor $G^{2\nu}(E_0, Z)$ as well as the Gamow-Teller nuclear matrix element $\left|M^{2\nu}_{GT}\right|$ through [64]:

$$ (T^{2\nu}_{1/2})^{-1} = G^{2\nu}(E_0, Z) \left|M^{2\nu}_{GT}\right|^2 \tag{2.28} $$

- **Neutrinoless double β decay ($\beta\beta 0\nu$):** this reaction allows the emission of only two electrons:

$$ {}^{A}_{Z}\mathrm{X} \rightarrow {}^{A}_{Z+2}\mathrm{Y} + 2e^- \qquad (\beta\beta 0\nu) \tag{2.29} $$

  This reaction is not allowed by the Standard Model since it violates the lepton number by two units. The inverse of the half-life requires the Gamow-Teller nuclear matrix element $\left|M^{0\nu}_{GT}\right|$ as well as the Fermi nuclear matrix element $\left|M^{0\nu}_{F}\right|$. The vector and axial vector coupling constants, g_V and g_A, are also required, such that [64]:

$$ (T^{0\nu}_{1/2})^{-1} = G^{0\nu}(E_0, Z) \left| M^{0\nu}_{GT} - \frac{g_V^2}{g_A^2} M^{0\nu}_{F} \right|^2 \langle m_\nu \rangle^2, \tag{2.30} $$

  where $\langle m_\nu \rangle$ corresponds to the effective Majorana mass and can be expressed as a combination of the neutrino mixing parameters:

$$ \langle m_\nu \rangle = \left| \sum_i U^2_{ei} m_i \right| = \left| \sum_i |U_{ei}|^2 \, e^{\alpha i} m_i \right|, \tag{2.31} $$

  where α_i correspond to the Majorana phases.

Whereas the first reaction emits two $\bar{\nu}_e$, the second one does not. It clearly violates the lepton number conservation by two units and has never been observed since W.H. Furry proposed this interpretation in 1939 [65]. He based his analysis on the fact that the neutrino can be a Majorana particle and "*plays only a transitory or virtual part*". If the neutrino is a Majorana particle, then the second reaction can occur.

Several experiments are involved in the search of a neutrinoless double β decay signal such as GERDA [66], EXO-200 [67] or KamLAND-Zen [68]. This signal can take the form of

a spectrum distortion with a possible peak at the $Q_{\beta\beta}$ value of the decay, *i.e.* the maximum energy released of the decay:

$$Q_{\beta\beta} = E_0 - 2m_e, \tag{2.32}$$

where $E_0 = M_i - M_j$ with M_i and M_j respectively the masses of the initial and final nuclei.

A neutrinoless double β decay signal has not yet been observed, with the exception that some members of the Heidelberg-Moscow experiment claimed a $3\,\sigma$ measurement of $T^{0\nu}_{1/2} = 1.19 \times 10^{25}$ years with $\langle m_{\beta\beta} \rangle = 0.44$ eV [69]. This result is strongly disfavored by the GERDA experiment which uses the same ^{76}Ge isotope and has reported $T^{0\nu}_{1/2} > 2.1 \times 10^{25}$ years [66]. The current limits on the half-lifes $T^{0\nu}_{1/2}$ of ^{76}Ge for the GERDA experiment and ^{136}Xe for the EXO-200 and KamLAND-Zen experiments are shown in Figure 2.2.

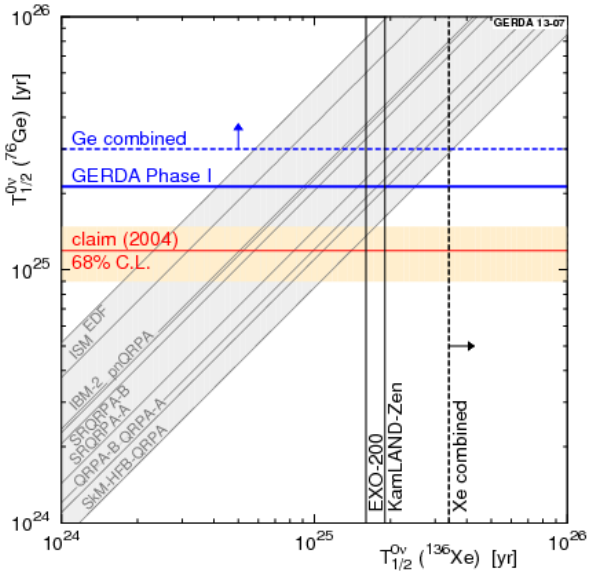

Figure 2.2: Limits on the half-lifes $T^{0\nu}_{1/2}$ of ^{76}Ge and ^{136}Xe compared with the signal claimed by the Heidelberg-Moscow experiment, from [66].

2.3 Neutrino mixing and oscillation

Neutrino oscillations are a quantum mechanical phenomenon. They allow a neutrino created with a given leptonic flavor to be measured later on with another leptonic flavor. This phenomenon requires mixing between the neutrino flavor eigenstates, ν_e, ν_μ and ν_τ, and the neutrino mass eigenstates, ν_1, ν_2 and ν_3. It requires also that the neutrinos are massive with a non-degenerative spectrum.

2.3.1 Neutrino mixing

The neutrino flavor eigenstates do not necessarily correspond to the neutrino mass eigenstates. A given flavor eigenstate ν_α can be represented as a linear combination of mass eigenstates ν_i. An unitary 3×3 complex matrix called U_{PMNS}[4] allows to link the neutrino flavor eigenstates to the neutrino mass eigenstates [70]:

$$\begin{pmatrix} \nu_e \\ \nu_\mu \\ \nu_\tau \end{pmatrix} = U_{\text{PMNS}} \begin{pmatrix} \nu_1 \\ \nu_2 \\ \nu_3 \end{pmatrix} \tag{2.33}$$

This U_{PMNS} matrix reminds us the CKM[5] matrix which acts on the quarks when they are subjects to weak interactions [71, 72]. We can write the U_{PMNS} in this way:

$$U_{\text{PMNS}} = \begin{pmatrix} U_{e1} & U_{e3} & U_{e3} \\ U_{\mu 1} & U_{\mu 3} & U_{\mu 3} \\ U_{\tau 1} & U_{\tau 3} & U_{\tau 3} \end{pmatrix} \tag{2.34}$$

This matrix can be parametrized with the use of three angles and one phase. These three angles are called neutrino mixing angles and are associated to three sectors we will develop later on in this chapter. The phase is the so-called CP-violating phase, δ. It is possible to rewrite the U_{PMNS} matrix in order to show independently the three sectors:

$$U_{\text{PMNS}} = \begin{pmatrix} 1 & 0 & 0 \\ 0 & c_{23} & s_{23} \\ 0 & -s_{23} & c_{23} \end{pmatrix} \begin{pmatrix} c_{13} & 0 & s_{13}e^{-i\delta} \\ 0 & 1 & 0 \\ -s_{13}e^{i\delta} & 0 & c_{13} \end{pmatrix} \begin{pmatrix} c_{12} & s_{12} & 0 \\ -s_{12} & c_{12} & 0 \\ 0 & 0 & 1 \end{pmatrix}, \tag{2.35}$$

where $c_{ij} = \cos\theta_{ij}$ and $s_{ij} = \sin\theta_{ij}$.

The first matrix is connected to the atmospheric sector, the second one to the θ_{13} sector and the third one to the solar sector. The three angles, θ_{12}, θ_{23} and θ_{13}, characterize the amplitudes of the oscillations whereas the CP-violating phase, δ, could explain the matter-antimatter asymmetry observed in our Universe. Considering neutrinos as Majorana particles, one should include a fourth matrix $D_{Maj} \equiv \text{diag}(1, \mathrm{e}^{i\alpha_1}, \mathrm{e}^{i\alpha_2})$, which holds two additional phases, α_1 and α_2.

2.3.2 Neutrino oscillation

The neutrino oscillation was first introduced by B. Pontecorvo in 1957 [73]. In analogy with $K^0 \leftrightarrow \bar{K}^0$ oscillations, he suggested that this phenomenon could be applied to neutrinos. As for $K^0 \leftrightarrow \bar{K}^0$ oscillations, B. Pontecorvo introduced the possibility of $\nu \leftrightarrow \bar{\nu}$ oscillations.

[4] PMNS for Pontecorvo-Maki-Nakagawa-Sakata
[5] CKM for Cabibbo-Kobayashi-Maskawa

Oscillation in vacuum

We said earlier that a given flavor state ν_α is a linear combination of mass states ν_i. It allows us to rewrite equation (2.33) as:

$$|\nu_\alpha\rangle = \sum_i U^*_{\alpha i} |\nu_i\rangle, \tag{2.36}$$

where α stands for e, μ or τ.

The mass states $|\nu_i\rangle$ are eigenstates of the following Hamiltonian:

$$\hat{H}_0 |\nu_i\rangle = E_i |\nu_i\rangle \qquad \text{with} \qquad E_i = \sqrt{p_i^2 + m_i^2}, \tag{2.37}$$

where p_i is the neutrino momentum and m_i its mass.

Let us consider a mass eigenstate $|\nu_i\rangle$. Since $|\nu_i\rangle$ are mass eigenstates, the way they propagate can be described as plane waves. From a quantum mechanical point of view, they evolve through the Schrödinger equation:

$$i\hbar \frac{\partial}{\partial t} |\nu_i(t)\rangle = \hat{H}_0 |\nu_i(t)\rangle \qquad \text{with} \qquad |\nu_i(t)\rangle = \mathrm{e}^{-iE_i t} |\nu_i\rangle, \tag{2.38}$$

where $|\nu_i\rangle$ stands for $|\nu_i(t=0)\rangle$.

Let us now describe a flavor state $|\nu_\alpha\rangle$. Since flavor and mass states are linked through the U_{PMNS} matrix, it is possible to express the evolution of $|\nu_\alpha\rangle$:

$$|\nu_\alpha(t)\rangle = \sum_i U^*_{\alpha i} \, \mathrm{e}^{-iE_i t} |\nu_i\rangle \tag{2.39}$$

We can also describe $|\nu_i\rangle$ as a function of $|\nu_\beta\rangle$:

$$|\nu_i\rangle = \sum_\beta U_{\beta i} |\nu_\beta\rangle, \tag{2.40}$$

where β stands for e, μ or τ.

When applying equation (2.40) in equation (2.39), we end with:

$$|\nu_\alpha(t)\rangle = \sum_{\beta=e,\mu,\tau} \left(\sum_i U^*_{\alpha i} \, \mathrm{e}^{-iE_i t} \, U_{\beta i} \right) |\nu_\beta\rangle \tag{2.41}$$

This is telling us that at a time $t > 0$, the initial $|\nu_\alpha\rangle$ state becomes a superposition of different flavor states. It is then possible to access the probability of transition from a $|\nu_\alpha\rangle$ state to a $|\nu_\beta\rangle$ state. We calculate the amplitude $A_{\nu_\alpha \to \nu_\beta}$ for this transition:

$$A_{\nu_\alpha \to \nu_\beta}(t) \equiv \langle \nu_\beta | \nu_\alpha(t) \rangle = \sum_i U^*_{\alpha i} U_{\beta i} \, \mathrm{e}^{-iE_i t} \tag{2.42}$$

The probability of transition depends on the amplitude and is given by:

$$P_{\nu_\alpha \to \nu_\beta}(t) = |A_{\nu_\alpha \to \nu_\beta}(t)|^2 = \sum_{i,j} U^*_{\alpha i} U_{\beta i} U^*_{\alpha j} U_{\beta j} \, \mathrm{e}^{-i(E_i - E_j)t} \tag{2.43}$$

Assuming ultrarelativistic neutrinos, *i.e.* $p_i \gg m_i$, as well as $t = L$, E_i from equation (2.37) can be rewritten as:

$$E_i \simeq E + \frac{m_i^2}{2E}, \tag{2.44}$$

which leads to:

$$P_{\nu_\alpha \to \nu_\beta}(L, E) = \sum_{i,j} U^*_{\alpha i} U_{\beta i} U_{\alpha j} U^*_{\beta j} \exp\left(-i \frac{\Delta m^2_{ij} L}{2E}\right), \tag{2.45}$$

where $\Delta m^2_{ij} \equiv m^2_i - m^2_j$.

Considering a three neutrino mixing approach leads to the introduction of three mass-squared differences:

$$\Delta m^2_{21} \equiv m^2_2 - m^2_1 \qquad \Delta m^2_{32} \equiv m^2_3 - m^2_2 \qquad \Delta m^2_{31} \equiv m^2_3 - m^2_1, \tag{2.46}$$

where two of them are independent since they can be linked through the relation:

$$\Delta m^2_{21} + \Delta m^2_{32} - \Delta m^2_{31} = 0 \tag{2.47}$$

Except for the values of these squared-mass differences which are reviewed later on in this chapter, the knowledge on the neutrino mass eigenstates is limited. The neutrino oscillation framework requires at least two eigenstates to have a non-zero mass but does not indicate the absolute scale. Two possible configurations can be considered for the mass hierarchy:

- **Normal hierarchy:** mass eigenstates are ordered in a conventional way, m_1 being the lightest eigenstate: $m_1 < m_2 \ll m_3$
- **Inverted hierarchy:** mass eigenstates are not anymore ordered in a conventional way, m_3 becoming the lightest eigenstate: $m_3 \ll m_1 < m_2$

We can express the masses as a function of the lightest eigenstate. For the normal hierarchy, we obtain:

$$\begin{cases} m_2 = \sqrt{m_1^2 + \Delta m^2_{21}} \\ m_3 = \sqrt{m_1^2 + \Delta m^2_{21} + \Delta m^2_{32}} \end{cases} \tag{2.48}$$

In the case of the inverted hierarchy, we obtain:

$$\begin{cases} m_1 = \sqrt{m_3^2 - \Delta m^2_{31}} \\ m_2 = \sqrt{m_3^2 - \Delta m^2_{31} + \Delta m^2_{21}} \end{cases} \tag{2.49}$$

Figure 2.3 shows the values of the three neutrino mass eigenstates as a function of the lightest eigenstate, for both normal and inverted hierarchies. We notice that in both schemes there is a quasi-degeneracy when the values of the three masses come closer.

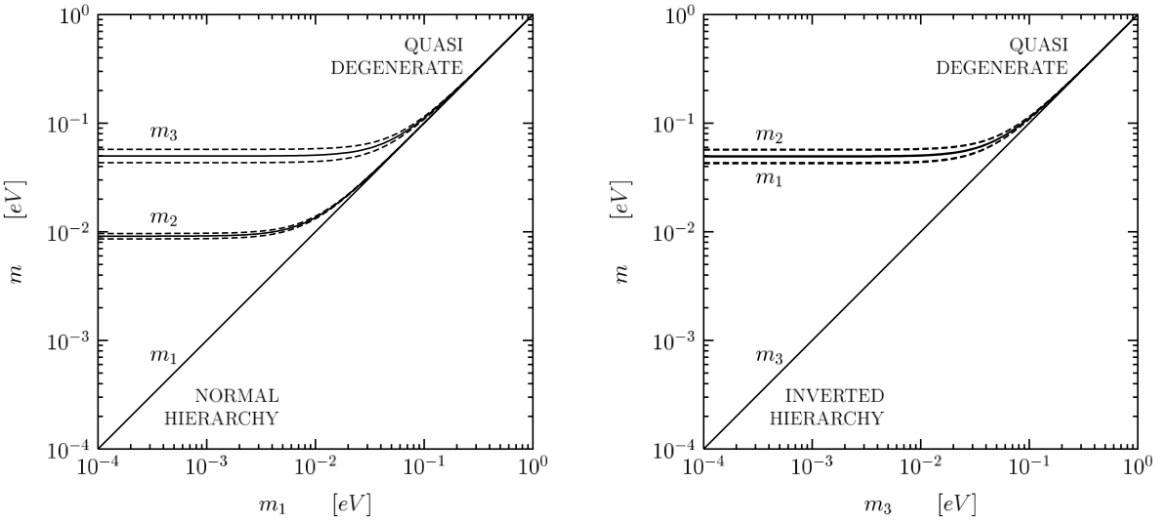

Figure 2.3: Values of the three neutrino mass eigenstates as a function of the lightest eigenstate when considering a normal hierarchy (*left*) or an inverted hierarchy (*right*), from [74].

Two flavors case The two flavors oscillation formalism represents already a good approximation for many experiments. Let us assume the oscillation of two neutrinos with flavor eigenstates $|\nu_\alpha\rangle$ and $|\nu_\beta\rangle$ and mass eigenstates $|\nu_1\rangle$ and $|\nu_2\rangle$. The flavor eigenstates do not correspond to the mass eigenstates but are a linear combination of them:

$$\begin{pmatrix} \nu_\alpha \\ \nu_\beta \end{pmatrix} = \begin{pmatrix} \cos\theta & \sin\theta \\ -\sin\theta & \cos\theta \end{pmatrix} \begin{pmatrix} \nu_1 \\ \nu_2 \end{pmatrix}, \tag{2.50}$$

which leads to:

$$\begin{cases} |\nu_\alpha\rangle = \cos\theta\,|\nu_1\rangle + \sin\theta\,|\nu_2\rangle \\ |\nu_\beta\rangle = -\sin\theta\,|\nu_1\rangle + \cos\theta\,|\nu_2\rangle \end{cases} \tag{2.51}$$

The flavor eigenstate $|\nu_\alpha\rangle$ is evolving with time:

$$|\nu_\alpha(t)\rangle = \cos\theta\,\mathrm{e}^{-iE_1 t}\,|\nu_1\rangle + \sin\theta\,\mathrm{e}^{-iE_2 t}\,|\nu_2\rangle \qquad \text{with} \qquad E_i = \sqrt{p_i^2 + m_i^2}, \tag{2.52}$$

where p_i is the neutrino momentum and m_i its mass.

The disappearance probability $P(\nu_\alpha \to \nu_\beta)$ is then given by:

$$P(\nu_\alpha \to \nu_\beta) = |\langle \nu_\beta | \nu_\alpha(t) \rangle|^2 \tag{2.53}$$

Since we are in a two flavors oscillation hypothesis, the created neutrino ν_α will be measured later on either in a ν_β state or in a ν_α state, leading to:

$$P(\nu_\alpha \to \nu_\beta) + P(\nu_\alpha \to \nu_\alpha) = 1 \tag{2.54}$$

The survival probability is then given by:

$$P(\nu_\alpha \to \nu_\alpha) = 1 - \sin^2(2\theta)\sin^2\left(\frac{\Delta m^2 L}{4E}\right), \tag{2.55}$$

which can also be written in a more usual way:

$$P(\nu_\alpha \to \nu_\alpha) = 1 - \sin^2(2\theta)\sin^2\left(1.27\,\frac{\Delta m^2(\mathrm{eV}^2)\,L(\mathrm{m})}{E(\mathrm{MeV})}\right), \tag{2.56}$$

where θ is the mixing angle considered, Δm^2 the mass-squared difference, L the distance between the source and the detector and E the $\bar{\nu}_e$ energy.

Oscillation in matter

The propagation of neutrinos in matter is different from their propagation in vacuum, causing neutrinos to oscillate in a different way. Since electrons are part of the matter while muons and taus are not, ν_e can interact with electrons through $W^\pm$ or Z^0 bosons exchange while ν_μ and ν_τ can only interact with electrons through Z^0 boson exchange. While ν_e are sensitive to both charged and neutral currents, ν_μ and ν_τ are only sensitive to neutral currents.

Considering for instance solar neutrinos which have to escape from the Sun and then travel to the Earth, the mixing will differ when being in solar matter or in vacuum. The Hamiltonian in matter, $\hat{H}_m$, differs from the Hamiltonian in vacuum we have seen earlier, $\hat{H}_0$. We can define $\hat{H}_m$ such that:

$$\hat{H}_m = \hat{H}_{int} + \hat{H}_0, \tag{2.57}$$

where $\hat{H}_{int}$ defines the interaction of neutrinos with matter.

The effective potential which describes the interaction of neutrinos with the matter through charged current is given by:

$$V = \sqrt{2}\,G_F N_e, \tag{2.58}$$

where G_F is the Fermi coupling constant and N_e the electron number density in matter.

This potential would have an opposite sign when considering antineutrinos and is small since $\sqrt{2}\,G_F \simeq 7.63 \times 10^{-14}$ eV cm$^3/\mathcal{N}_\mathrm{A}$ where $\mathcal{N}_\mathrm{A}$ is the Avogadro number. Nevertheless, this potential accounts for the effect of matter on neutrino oscillations [29]. The effect of matter on neutrino oscillations is usually called the MSW[6] effect [75, 76].

Let us consider the case of an oscillation between ν_e and ν_μ. We assume the constant electron number density, N_e, to be constant. Due to the interaction term $\hat{H}_{int}$ in equation (2.57), the eigenstates of the Hamiltonian $\hat{H}_m$ are obviously not the ones of the Hamiltonian $\hat{H}_0$. In order to maintain the representation of the eigenstates as in the case of the oscillation in vacuum, θ_m is defined such that the system described in equation (2.50) becomes:

$$\begin{pmatrix} \nu_e \\ \nu_\mu \end{pmatrix} = \begin{pmatrix} \cos\theta_m & \sin\theta_m \\ -\sin\theta_m & \cos\theta_m \end{pmatrix} \begin{pmatrix} \nu_1^m \\ \nu_2^m \end{pmatrix}, \tag{2.59}$$

[6] MSW for Mikheyev-Smirnov-Wolfenstein

which leads to:

$$\begin{cases} |\nu_e\rangle = \cos\theta_m\,|\nu_1^m\rangle + \sin\theta_m\,|\nu_2^m\rangle \\ |\nu_\mu\rangle = -\sin\theta_m\,|\nu_1^m\rangle + \cos\theta_m\,|\nu_2^m\rangle \end{cases} \tag{2.60}$$

The mixing angle θ_m in matter is then linked to the mixing angle θ in vacuum through:

$$\sin^2(2\theta_m) = \frac{\sin^2(2\theta)}{\left(\cos(2\theta) - \dfrac{L}{L_m}\right)^2 + \sin^2(2\theta)}, \tag{2.61}$$

where L is the oscillation length in vacuum and L_m a length characteristic of the motion of the neutrinos through the matter which can be written as [60]:

$$L_m = \frac{2\pi}{\sqrt{2}\,G_F N_e} \tag{2.62}$$

One can point out that there is a resonance effect when considering:

$$\frac{L}{L_m} = \cos(2\theta), \tag{2.63}$$

which leads to:

$$N_e = \frac{\Delta m^2 \cos(2\theta)}{2E\sqrt{2}\,G_F} \tag{2.64}$$

The mixing angle θ_m is maximal when this "resonance condition" is reached [76, 77], leading to the total transition between the two flavors.

2.3.3 Solar sector, Δm^2_{21} and θ_{12}

The solar neutrino anomaly mentioned in the previous chapter was finally solved by the SNO experiment in 2002 by correctly measuring all the neutrino flavors flux, while previous experiments were only sensitive to the ν_e flux. The best way to understand the lack of solar neutrinos in the Homestake, GALLEX/GNO, SAGE and Super-Kamiokande experiments relies on the oscillation of ν_e into ν_μ and ν_τ during their journey from the Sun to the Earth.

In 2008, the KamLAND[7] experiment measured the parameters relevant for the solar neutrino oscillations, Δm^2_{21} and θ_{12}, by observing $\bar{\nu}_e$ emitted from 55 nuclear reactors located at a flux-weighted average distance of 180 km. KamLAND is a 1 kton liquid scintillator experiment based at the former Kamiokande experiment site. It detects $\bar{\nu}_e$ through Inverse Beta Decay (IBD) interactions where the positron scintillation and annihilation is followed by a 2.2 MeV γ-ray from neutron capture on hydrogen. Due to the specific L/E range, the KamLAND experiment is sensitive to the solar sector and therefore to Δm^2_{21} and θ_{12} [79]:

$$\Delta m^2_{21} = 7.58^{+0.14}_{-0.13}\,(\text{stat})\,^{+0.15}_{-0.15}\,(\text{syst}) \times 10^{-5}\,\text{eV}^2 \tag{2.65}$$

$$\tan^2\theta_{12} = 0.56^{+0.10}_{-0.07}\,(\text{stat})\,^{+0.10}_{-0.06}\,(\text{syst}) \tag{2.66}$$

[7] Kamioka Liquid scintillator Anti-Neutrino Detector

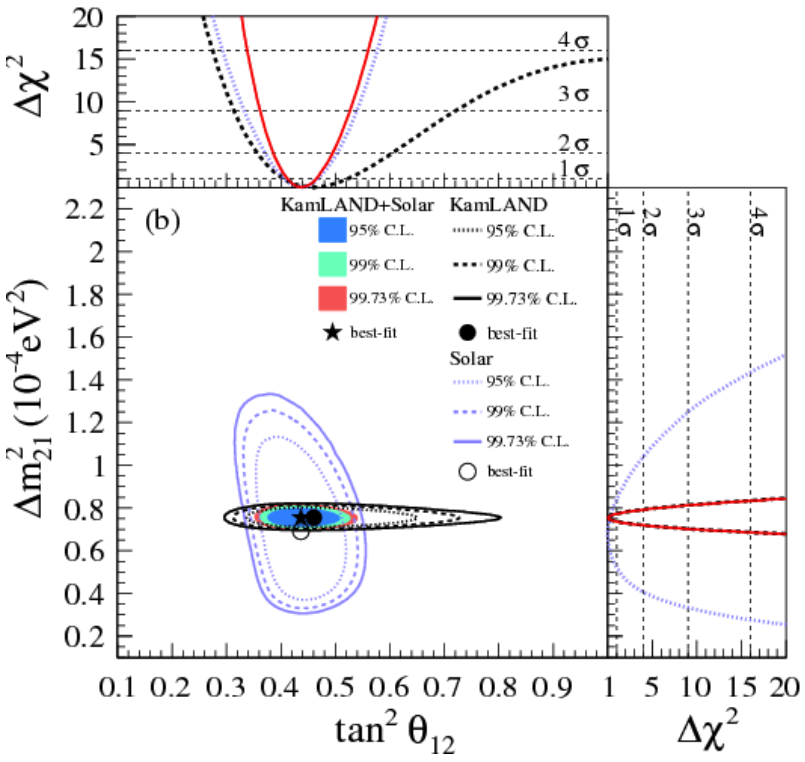

Figure 2.4: Allowed regions in the $(\tan^2\theta_{12}, \Delta m^2_{21})$ plane for KamLAND and solar neutrino experiments, from [78]. θ_{13} is constrained by accelerator and short-baseline reactor neutrino experiments. The side-panels show the $\Delta\chi^2$-profiles.

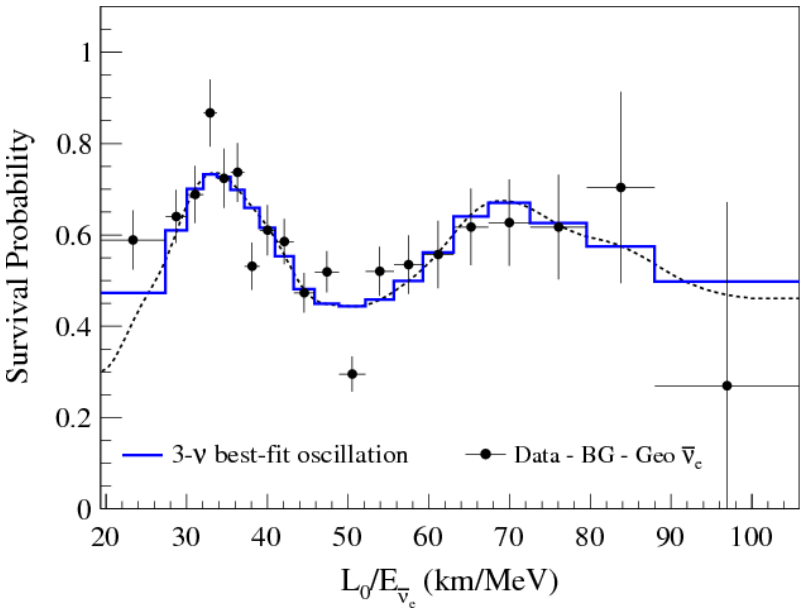

Figure 2.5: Ratio of the observed $\bar{\nu}_e$ spectrum to the non-oscillation prediction, from [78].

In 2011 and 2013, KamLAND, together with solar neutrino experiments, provided more accurate values of Δm^2_{21} and θ_{12} [80, 78]:

$$\Delta m^2_{21} = 7.53^{+0.18}_{-0.18} \times 10^{-5}\,\mathrm{eV}^2 \tag{2.67}$$

$$\tan^2\theta_{12} = 0.436^{+0.029}_{-0.025} \tag{2.68}$$

As it can be seen in Figure 2.4, KamLAND has a very good sensitivity to Δm^2_{21}, leading to the conclusion that oscillations in matter, and more precisely inside the Sun, are responsible for the ν_e deficit observed by all the solar neutrino experiments. Figure 2.5 shows the ratio of the observed $\bar{\nu}_e$ spectrum to the non-oscillation prediction.

2.3.4 Atmospheric sector, Δm^2_{32} and θ_{23}

Atmospheric and long-baseline experiments are governed by the Δm^2_{32} mass-squared difference and the θ_{23} mixing angle. The K2K and MINOS experiments started in 2006 investigating these two parameters [81, 82]. They are both long-baseline experiments and are based on the study of the flavor composition of a ν_μ beam after travelling hundreds of kilometers.

For the MINOS experiment, beams are created in the Fermilab accelerator complex and are detected 735 km away in the Soudan mine. MINOS is able to measure ν_μ and $\bar{\nu}_\mu$ interactions separately. In the case of the K2K experiment, beams were created at the KEK accelerator complex and were detected in the Super-Kamiokande detector, 250 km further.

Recently, MINOS provided accurate results on Δm^2_{32} and θ_{23} [85, 83]:

$$|\Delta m^2_{32}| = (2.28 - 2.46) \times 10^{-3}\,\mathrm{eV}^2 \tag{2.69}$$

$$\sin^2\theta_{23} = 0.35 - 0.65, \tag{2.70}$$

as well as T2K, the upgraded version of K2K [86, 84]:

$$|\Delta m^2_{32}| = (2.51 \pm 0.10) \times 10^{-3}\,\mathrm{eV}^2 \tag{2.71}$$

$$\sin^2\theta_{23} = 0.514^{+0.055}_{-0.056} \tag{2.72}$$

The sign of Δm^2_{32} is not yet known. We can then distinguish a normal hierarchy with $\Delta m^2_{32} > 0$ from an inverse hierarchy with $\Delta m^2_{32} < 0$. Figures 2.6 and 2.7 show respectively the MINOS and T2K allowed regions for the neutrino oscillation parameters $\sin^2\theta_{23}$ and Δm^2_{32}.

2.3.5 θ_{13} sector

The θ_{13} mixing angle was determined very recently by the three reactor neutrino experiments Double Chooz, Daya Bay and RENO. Since 1999, only an upper limit was achieved by the CHOOZ experiment. It was a major cornerstone since the CP-violating phase, δ, depends

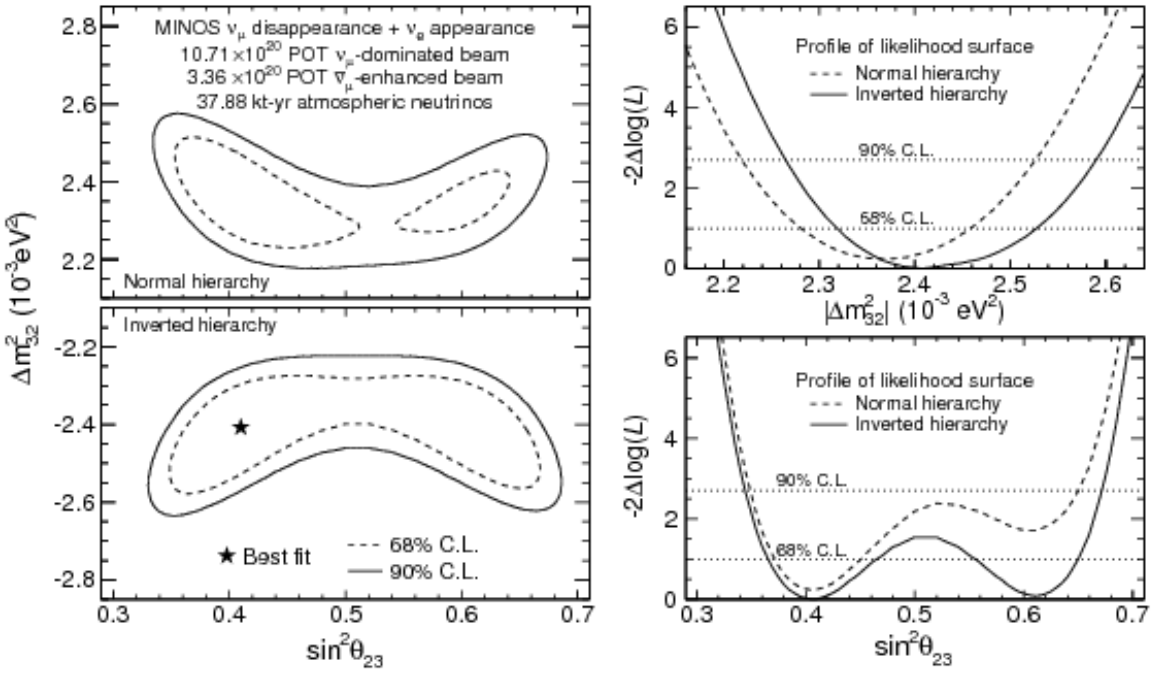

Figure 2.6: Allowed regions in the $(\sin^2\theta_{23}, \Delta m^2_{32})$ plane for MINOS, from [83].

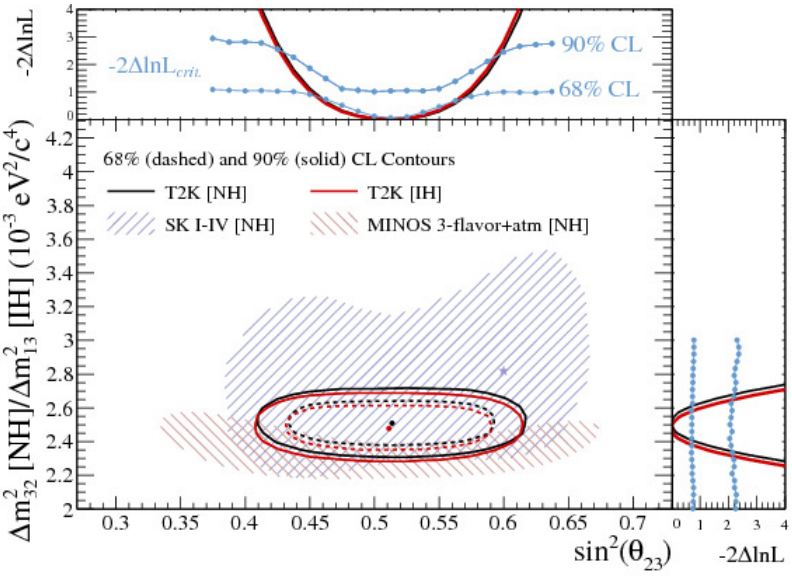

Figure 2.7: Allowed regions in the $(\sin^2\theta_{23}, \Delta m^2_{32})$ plane for T2K, from [84].

on the smallness of θ_{13}. If θ_{13} was too small, then the possibility to access δ would become harder. Both accelerator and reactor experiments are involved in the measurement of what was called the last unknown neutrino mixing angle, until 2011.

Reactor neutrino experiments

Reactor neutrino experiments looking for θ_{13} are all based on the observation of the $\bar{\nu}_e$ disappearance during their journey from their birth in the nuclear reactors to their death in the detector. One has to look then for the survival probability $P(\bar{\nu}_e \to \bar{\nu}_e)$ which depends on the neutrino mixing angle θ_{13}, on the mass-squared difference Δm^2_{31}, on the distance L and on the $\bar{\nu}_e$ energy E:

$$P(\bar{\nu}_e \to \bar{\nu}_e) \approx 1 - \sin^2(2\theta_{13}) \sin^2 \left(\frac{\Delta m^2_{31} L}{4E} \right), \tag{2.73}$$

where $L \approx 1$ km and $\langle E \rangle \approx 3$ MeV.

CHOOZ used only one detector whereas the new generation of experiments use two identical detectors in order to precisely measure a flux difference between detector(s) near the nuclear reactors and detector(s) far from them. This configuration allows to get rid of systematic errors and in particular those coming from the $\bar{\nu}_e$ production knowledge.

As for the Savannah River Plant and Hanford experiments, $\bar{\nu}_e$ are detected through IBD interactions, $\bar{\nu}_e + p \to e^+ + n$, where the positron scintillation and annihilation is followed by the neutron capture on gadolinium (Gd) or hydrogen (H). Thanks to the coincidence betwen these two signals, one can register a clear IBD signature.

We are not going to present the Double Chooz experiment since the next chapter will be entirely dedicated to it.

CHOOZ The CHOOZ experiment was the first experiment to look for θ_{13}. It was located at the exact same place as the Double Chooz far detector today. The CHOOZ detector consisted in a neutrino target filled with a Gd-doped liquid scintillator surrounded by a containment region and a veto and seen by photomultiplier tubes. CHOOZ ran from April 1997 to July 1998. The two nuclear reactors were not yet operated at the beginning of the data taking, allowing a direct measurement of the backgrounds.

Unfortunately, the liquid scintillator deteriorated after a few months, leading to the end of the experiment. With almost one year of live time, CHOOZ found no evidence for neutrino oscillation. An upper limit on θ_{13} was set at this time:

$$\sin^2(2\theta_{13}) < 0.15 \tag{2.74}$$

Figure 2.8 represents the visible energy spectrum of the prompt signals after substraction of reactor-off to reactor-on data. The ratio of the data to the non-oscillation prediction does

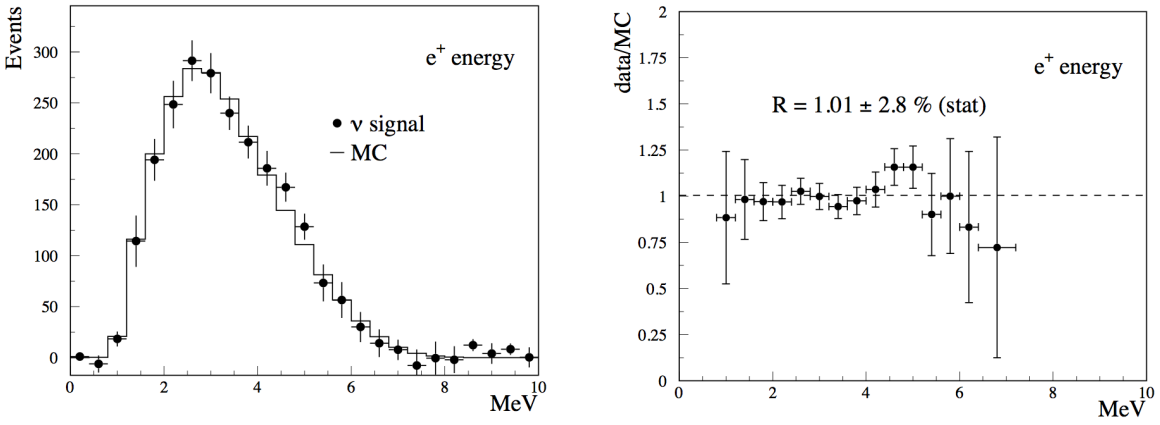

Figure 2.8: (*left*) Visible energy spectrum of the prompt signals obtained from the substraction of reactor-on and reactor-off spectra. (*right*) Ratio of the data with the MC which assumes no oscillation, from [87].

not show a spectrum distortion expected when looking for neutrino oscillation.

Daya Bay The Daya Bay experiment takes place on the southern coast of China. Eight identical detectors are installed in one far and two near experimental halls from the Daya Bay, Ling Ao and Ling Ao-II nuclear power plants. Each power plant contains two nuclear reactors which are all identical pressurized water reactors and produced a maximum of 2.9 GW thermal power.

The detectors consist of a target filled with 20 tons of Gd-doped liquid scintillator, surrounded by a γ-catcher filled with 20 tons of un-doped liquid scintillator. These two volumes are contained in acrylic vessels and form the inner detector. Around this inner detector, a stainless steel vessel filled with 37 tons of mineral oil allows to shield the inner detector from possible radiation coming from the photomultiplier tubes installed along this vessel.

The Daya Bay experiment, as the Double Chooz experiment, provided two sets of results using IBD interactions with neutron capture on Gd and H:

- **Gd-capture analysis:** Daya Bay has been able to strongly constrain θ_{13} over the last few years [89, 90, 88]. With a live time of 217 days, Daya Bay registered 41589 $\bar{\nu}_e$ candidates in the far hall and 203809 and 92912 in the near halls[8], leading to [88]:

$$\sin^2(2\theta_{13}) = 0.090^{+0.008}_{-0.009} \tag{2.75}$$

  Daya Bay has also been able to provide a direct measurement of the mass-squared difference $|\Delta m^2_{ee}|$ [88]:

$$|\Delta m^2_{ee}| = 2.59^{+0.19}_{-0.20} \times 10^{-3}\,\text{eV}^2 \tag{2.76}$$

[8]Six over eight detectors were operational at that time.

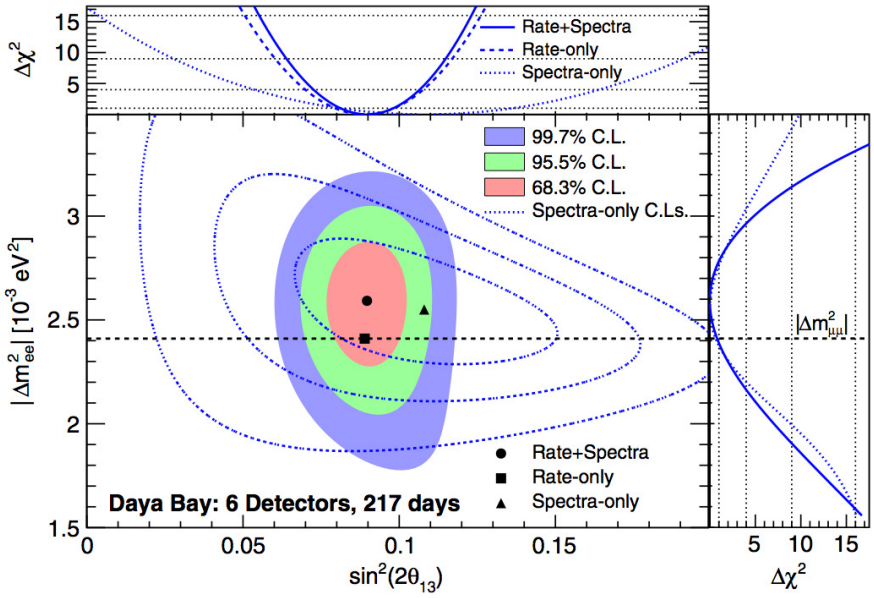

Figure 2.9: Allowed regions on $\sin^2(2\theta_{13})$ and $|\Delta m^2_{31}|$, from [88]. The 68.3 %, 95.5 % and 99.7 % C.L. are represented. The black points indicate the best fit values for differents analyses.

Figure 2.9 illustrates the allowed regions for the neutrino oscillation parameters $\sin^2(2\theta_{13})$ and $|\Delta m^2_{ee}|$. The dashed horizonthal line represents the MINOS measurement taken from [85].

- **H-capture analysis:** Daya Bay has recently developed an analysis using IBD interactions with neutron capture on H [91]. With the same live time of 217 days, they registered 62111 $\bar{\nu}_e$ candidates in the far hall and 148919 and 69083 in the near halls, leading to [91]:

$$\sin^2(2\theta_{13}) = 0.083 \pm 0.018 \tag{2.77}$$

With both Gd-capture and H-capture analyses, Daya Bay provided:

$$\sin^2(2\theta_{13}) = 0.089 \pm 0.008 \tag{2.78}$$

RENO The RENO experiment is looking for $\bar{\nu}_e$ produced by six aligned power nuclear reactors at the Yonggwang power plant in South Korea. Two identical detectors are installed at 294 and 1383 m from the reactor array center.

As for Daya Bay and Double Chooz, which initiated this strategy, the detectors consist of an innermost acrylic vessel filled with Gd-doped liquid scintillator, surrounded by a γ-catcher filled with un-doped liquid scintillator and a 70 cm thick buffer region filled with 65 tons of mineral oil which supports 354 photomultiplier tubes.

With a data taking between August 2011 and March 2012, RENO observed 17102 $\bar{\nu}_e$

candidates in the far detector and 154088 in the near detector, leading to [92]:

$$\sin^2(2\theta_{13}) = 0.113 \pm 0.013\,(\text{stat}) \pm 0.019\,(\text{syst}) \tag{2.79}$$

Figure 2.10 represents the visible energy spectrum of the prompt signals. The ratio of the data to the non-oscillation prediction shows a spectrum distortion at low energy, as expected in case of neutrino oscillation.

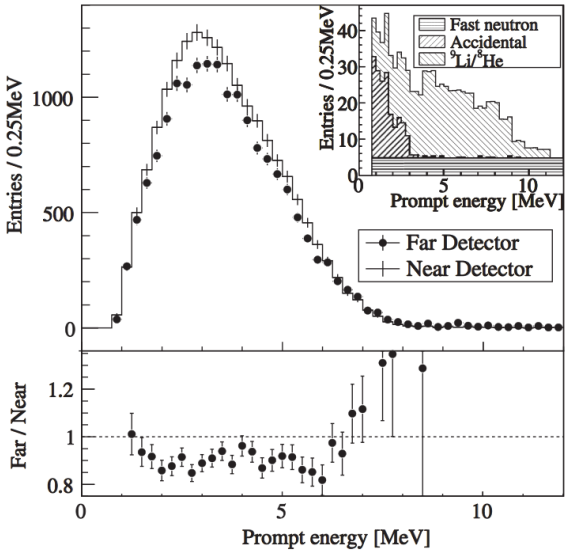

Figure 2.10: Visible energy spectrum of the prompt signals together with the ratio of the data with the MC which assumes no oscillation, from [92].

Accelerator neutrino experiments

Accelerator neutrino experiments are also sensitive to the θ_{13} mixing angle when they look for ν_e in the ν_μ beam created hundreds of kilometers away. The probability of appearance is given by:

$$P(\nu_\mu \to \nu_e) \approx \sin^2(\theta_{23}) \sin^2(2\theta_{13}) \sin^2\left(\frac{\Delta m^2_{31} L}{4E}\right) + \text{CP-violating phase, matter effect term,} \tag{2.80}$$

where L is the neutrino propagation distance and E is the neutrino energy.

The T2K experiment uses the J-PARC accelerator complex for the creation of the ν_μ beam and the Super-Kamiokande as detector. J-PARC and Super-Kamiokande are 295 km far away and the beam is willingly 2.5° off-axis in order to reduce backgrounds. Two near detectors located at 280 m from the creation point allow to investigate the beam properties.

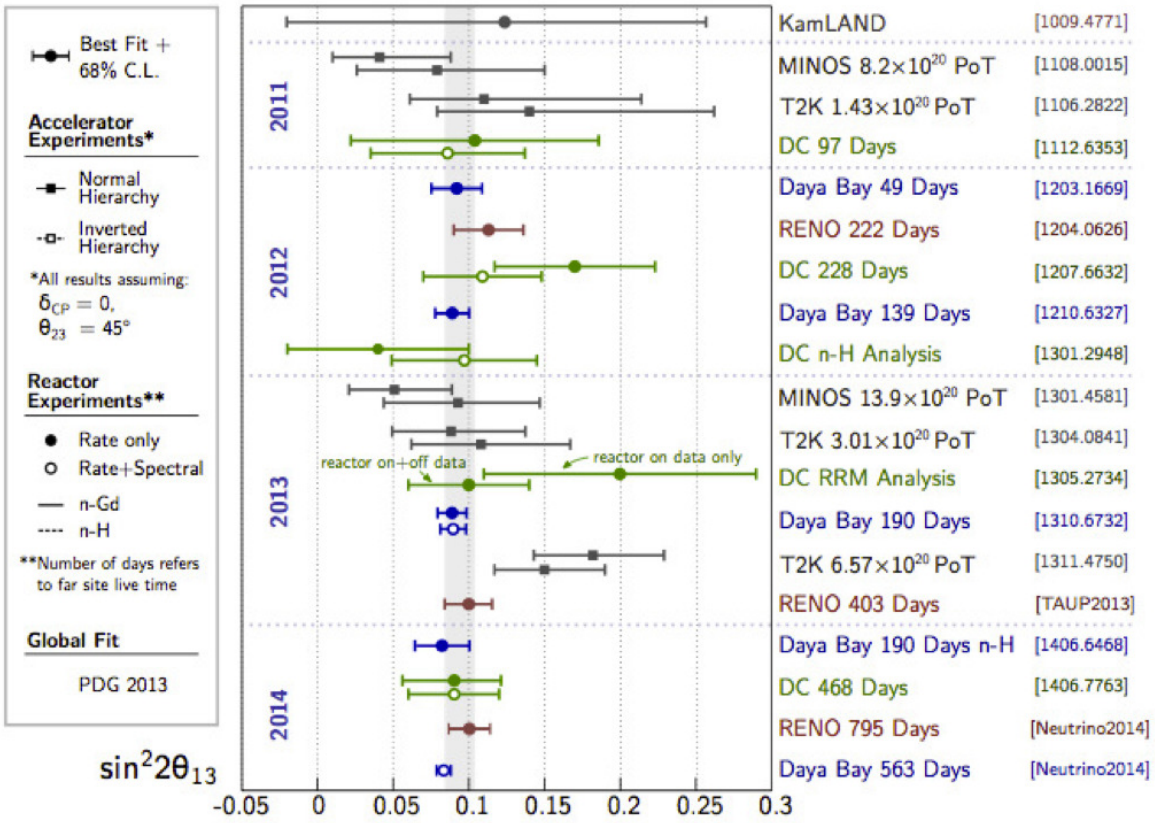

Figure 2.11: $\sin^2(2\theta_{13})$ measurements from 2011 to 2014.

In 2011, T2K was the first experiment to indicate a non-zero value of θ_{13} [93]. At the beginning of this year, T2K reported a detection of 28 ν_e candidates for 4.92 $\pm$ 0.55 background events, leading to an appearance signal with a significance of $7.3\,\sigma$. Assuming $|\Delta m^2_{32}| = 2.4 \times 10^{-3}\,\mathrm{eV}^2$, $\sin^2(\theta_{23}) = 0.5$ and $\Delta m^2_{32} > 0$ ($\Delta m^2_{32} < 0$), the best-fit value is obtained at $\delta = 0$ [94]:

$$\sin^2(2\theta_{13}) = 0.140^{+0.038}_{-0.032} \quad \left(\sin^2(2\theta_{13}) = 0.170^{+0.045}_{-0.037}\right) \tag{2.81}$$

MINOS also provided a consistent result [95]. Figure 2.11 is a summary of the $\sin^2(2\theta_{13})$ measurements done in the last few years.

2.4 Cosmological informations

Neutrinos from the earliest stages of our Universe are known as the cosmic neutrino background (CνB). Its existence has been confirmed by the composition and distribution studies of matter and energy in our Universe. Phenomenons such as primordial synthesis of elements, anisotropies of the cosmic microwave background (CMB) as well as formation of dark matter halos could find an answer from the understanding of those neutrinos. Studies on the CMB anisotropies and large scale distribution of galaxies allow to extract both a measurement on the effective number of neutrino species, N_{eff}, and an upper limit on the sum of the neutrino masses, $\sum m_\nu$.

Recent studies from the Planck satellite in combination with other observables such as Baryon Acoustic Oscillations (BAO) give [96]:

$$N_{\mathrm{eff}} = 3.30 \pm 0.27 \tag{2.82}$$

$$\sum m_\nu < 0.23\,\mathrm{eV} \text{ at } 95\% \text{ C.L.} \tag{2.83}$$

2.5 Sterile neutrinos?

Recent work on the reactor neutrino flux prediction and re-analyses of former short baseline experiments revealed the so-called reactor antineutrino anomaly we have seen in the previous chapter. This anomaly can be interpreted as the oscillation of $\bar{\nu}_e$ towards possible sterile neutrinos at very short baseline, *i.e.* of the order of a few meters. Combining both the reactor antineutrino anomaly together with the GALLEX/SAGE one helps to constrain the new possible oscillation parameters. The best fit value gives [97]:

$$\sin^2 2\theta_{14} = 0.17 \pm 0.04 \tag{2.84}$$

$$|\Delta m^2_{14}| = 2.3 \pm 0.1\,\mathrm{eV}^2 \tag{2.85}$$

Several projets using different detection techniques have been designed in order to investigate the anomaly and possibly discover a new neutrino state. Among them, the STEREO and

the SoLi∂ projects aim to evidence or discard such a short baseline oscillation near respectively the ILL research reactor (Grenoble, France) and the SCK·CEN BR2 research reactor (Mol, Belgium) by the observation of an E/L dependent distortion induced in the energy spectrum, typical of such a phenomenon.

Nuclear reactors are not the only way to look for a possible sterile neutrino. Inserting powerful radioactive sources such as chromium, ^{51}Cr, or cerium, ^{144}Ce, into detectors already built, such as Borexino, allows, in a short period of time, to test a possible new oscillation.

Chapter

3 The Double Chooz experiment

The neutrino is the smallest bit of material reality ever conceived of by man.
Frederick Reines

Contents

The Double Chooz experiment is focusing on measuring what was defined until 2011 as the last unknown neutrino mixing angle, θ_{13}. Double Chooz is a reactor neutrino oscillation experiment which studies $\bar{\nu}_e$ emitted from the two nuclear reactors of the Chooz power plant, in the French Ardennes. It aims at measuring the neutrino mixing angle θ_{13} thanks to two identical detectors located at different baselines to precisely observe the $\bar{\nu}_e$ disappearance. The Double Chooz experiment started taking data on April 13, 2011, 55 years after the first $\bar{\nu}_e$ observation by F. Reines and C. Cowan [6].

3.1 Principle

3.1.1 From the $\bar{\nu}_e$ emission...

Located in the French Ardennes, the Chooz power plant is composed of two N4 PWR[1] nuclear reactors called B1 and B2. It belongs to the French electricity company EDF. Those reactors are the most powerful nuclear reactors in France and belong, with the Civaux nuclear reactors, to the youngest generation[2]. Their construction started in 1984 and 1985 respectively and the first electricity was produced in 1996 for B1 and 1997 for B2.

The production of electricity is based on the nuclear fission of uranium (U) and plutonium (Pu). Thermal neutrons will be first captured by uranium and plutonium atoms and will allow these elements to break themselves, releasing energy and producing lighter nuclei and neutrons which can produce new fissions and therefore sustain the process, leading to a chain reaction. In order to control the rate of uranium and plutonium fissions, rods can be inserted in the core. They are made of high neutron capture cross section elements, such as boron for instance. Dropping these rods inside the core stop the chain reaction. The lighter nuclei produced by the fission reactions are unstable and neutron-rich. Their decay occur through β^- reactions which produce only $\bar{\nu}_e$. Nuclear reactors are then $\bar{\nu}_e$-rich factories "for free":

$$ {}^{A}_{Z}\mathrm{X} \rightarrow {}^{A}_{Z+1}\mathrm{Y} + e^- + \bar{\nu}_e \tag{3.1} $$

At the beginning, the nuclear fuel is composed of ^{238}U and ^{235}U. Naturally, uranium consists for 99.274 % of ^{238}U and for 0.720 % of ^{235}U with some traces of ^{234}U. These natural concentrations do not allow a nuclear reactor to work even if one can think to the Oklo natural reactor in Gabon. In the Chooz nuclear reactors, the core is composed of 205 fuel bundles containing 264 rods filled with enriched uranium, where the ^{235}U proportion is typically between 3 and 5 %. Even if the ^{238}U proportion remains greater than 95 %, this enrichment is mandatory. Indeed, whereas the ^{235}U is a "fissile" element, the ^{238}U is a "fertile" element. In other words, a fission reaction is possible with ^{235}U and do not happen with ^{238}U, apart from fast neutrons. Nevertheless, since ^{238}U is a fertile element, it means that it is able to produce fissile elements through neutron captures, following the reactions:

$$ n + {}^{238}\mathrm{U} \rightarrow {}^{239}\mathrm{U} \xrightarrow[23\ \mathrm{min}]{\beta^-} {}^{239}\mathrm{Np} \xrightarrow[2.3\ \mathrm{days}]{\beta^-} {}^{239}\mathrm{Pu}, \tag{3.2} $$

where ^{239}Pu is a fissile element which can take part in the fission process inside the core.

After two neutron captures, the ^{239}Pu can produce ^{241}Pu which is also a fissile element. The fuel composition and consequently the number of $\bar{\nu}_e$ produced from the fissions of ^{235}U, ^{238}U, ^{239}Pu and ^{241}Pu changes with time, what we call "burn-up". Whereas the number of fission from ^{235}U decreases with time and those from ^{238}U stays stable, the number of fission from ^{239}Pu and ^{241}Pu increases with time. Since Double Chooz does not have yet a near detector, the dominant uncertainty for the measurement of θ_{13} comes from the knowledge of

[1] Pressurized Water Reactor

[2] The EPR nuclear reactors in Flamanville will belong to the third generation and are under construction.

the $\bar{\nu}_e$ spectra. We have to be careful with this evolution which gives a special $\bar{\nu}_e$ spectrum at a given time.

Table 3.1: Mean energy released per fission, mean $\bar{\nu}_e$ energy and mean number of $\bar{\nu}_e$ released per fission for a given isotope from [98, 99, 100].

Isotope	$\langle E \rangle_f$ **(MeV)**	$\langle E_{\bar{\nu}_e} \rangle$ **(MeV)**	$\langle \bar{\nu}_e \rangle_f$
^{235}U	201.92 ± 0.46	5.226 ± 0.051	1.92 (1 ± 0.019)
^{238}U	209.99 ± 0.60	7.040 ± 0.326	2.38 (1 ± 0.020)
^{239}Pu	205.52 ± 0.96	3.799 ± 0.033	1.45 (1 ± 0.021)
^{241}Pu	213.60 ± 0.65	4.956 ± 0.049	1.83 (1 ± 0.019)

Table 3.1 illustrates the different properties of a given isotope. It appears that from one isotope to another, the mean $\bar{\nu}_e$ energy as well as the mean number of $\bar{\nu}_e$ released per fission change. It has to be taken into account in order to correctly predict the expected $\bar{\nu}_e$ spectra.

These spectra have been obtained from the measurement of β^- spectra of the four isotopes considered. The ^{235}U, ^{239}Pu and ^{241}Pu $\bar{\nu}_e$ spectra were measured at the ILL[3] research reactor in Grenoble, France [101, 102, 103], whereas the ^{238}U $\bar{\nu}_e$ spectrum was measured at the FRM II[4] in Garching, Germany [104]. Extrapolations below 3 MeV and above 7.5 MeV from a combination of the summation method described in [105] and an exponential-polynomial fit on the data have been performed for the ^{238}U $\bar{\nu}_e$ spectrum.

Concerning the mean cross section per fission, the Double Chooz collaboration chose to normalize it to the Bugey-4 rate measurement [106]:

$$\langle \sigma_f \rangle_R = \langle \sigma_f \rangle^{\text{Bugey}} + \sum_k \left(\alpha_k^R - \alpha_k^{\text{Bugey}} \right) \langle \sigma_f \rangle_k, \tag{3.3}$$

where k runs over the four isotopes considered and α_k stands for the fractional fission rates and R for the B1 and B2 nuclear reactors.

The second term allows to take into account the fuel difference between Bugey-4 on one side and B1 and B2 on the other side. With this correction and assuming no oscillation, we can calculate the expected number of $\bar{\nu}_e$ in the energy bin i:

$$N_i^R = \frac{\epsilon N_p P_{th}^R}{4\pi L_R^2 \langle E_f \rangle_R} \left(\frac{\langle \sigma_f \rangle_R}{\sum_k \alpha_k^R \langle \sigma_f \rangle_k} \sum_k \alpha_k^R \langle \sigma_f \rangle_k^i \right), \tag{3.4}$$

where ϵ is the detection efficiency, N_p the number of protons in the target, P_{th}^R the thermal power of the nuclear reactor considered, L_R the reactor-detector distance and $\langle E_f \rangle_R =$

[3]Institut Laue-Langevin
[4]Forschungs-Neutronenquelle Heinz Maier-Leibnitz

$\sum_k \alpha_k \langle E_f \rangle_k$ the mean energy release per fission.

The mean energy release per fission, $\langle E_f \rangle_R$, as well as the mean cross section per fission, $\langle \sigma_f \rangle_R$, are time-dependent since they vary with the evolution of the fuel composition in the reactor considered.

3.1.2 ... to their detection

Although $\bar{\nu}_e$ also interact through elastic scattering or quasi-elastic scattering, reactor neutrino experiments detect $\bar{\nu}_e$ thanks to the signature of the Inverse Beta Decay (IBD) reaction:

$$\bar{\nu}_e + p \rightarrow e^+ + n \tag{3.5}$$

Neglecting the $\bar{\nu}_e$ mass and assuming the proton to be at rest, this reaction is possible only if the $\bar{\nu}_e$ is enough energetic to produce both the positron and the neutron:

$$E_{\bar{\nu}_e}^{\text{threshold}} = \frac{(m_e + m_n)^2 - m_p^2}{2\, m_p} \simeq 1.806 \text{ MeV}, \tag{3.6}$$

where m_e, m_n and m_p are respectively the masses of the positron, the neutron and the proton taken from [29].

The $\bar{\nu}_e$ energy $E_{\bar{\nu}_e}$ is related to the positron energy E_{e^+} and can be approximated by $E_{\bar{\nu}_e} \simeq E_{e^+} + m_n - m_p$ [107]. In the detector, the visible energy E_{vis} is the sum of the positron kinetic energy together with its annihilation:

$$E_{\text{vis}} = E_{e^+} + m_e \simeq E_{\bar{\nu}_e} - m_n + m_p + m_e \simeq E_{\bar{\nu}_e} - 0.782 \text{ MeV} \tag{3.7}$$

The threshold of the IBD reaction, $E_{\bar{\nu}_e}^{\text{threshold}}$, correponds to a visible energy threshold $E_{\text{vis}}^{\text{threshold}} = 2\, m_e = 1.022$ MeV.

The expected $\bar{\nu}_e$ spectrum is illustrated in Figure 3.1 and is proportional to the product of the $\bar{\nu}_e$ flux spectrum and the IBD cross section of reaction (3.5) defined as:

$$\sigma_{\text{IBD}} = K \times (E_{\bar{\nu}_e} - \Delta)\sqrt{(E_{\bar{\nu}_e} - \Delta)^2 - m_e^2}, \tag{3.8}$$

where K is a constant directly related to the neutron lifetime and Δ the difference between the neutron and proton masses.

Since the IBD reaction produces both a positron and a neutron, one has then to look for two distinct signals, as illustrated in Figure 3.2:

1. **Prompt:** The scintillation and annihilation of the positron with an electron constitutes the prompt signal. Two 511 keV gammas will be created and after interaction in the scintillator, this signal will be detected by the photomultiplier tubes (PMTs) which are surrounding the target.

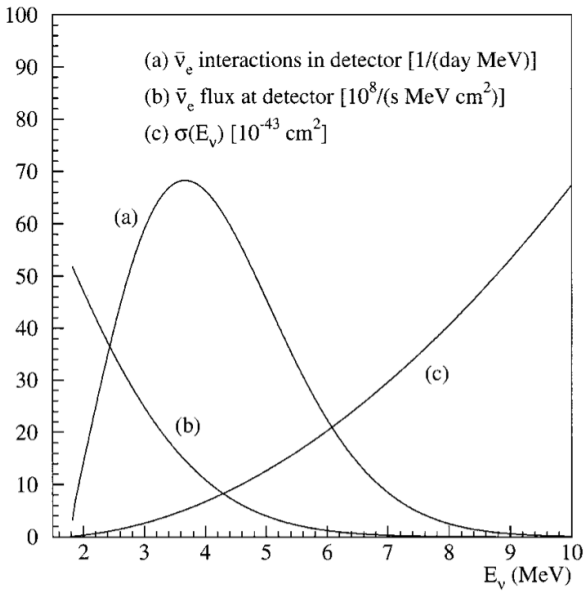

Figure 3.1: Expected $\bar{\nu}_e$ spectrum in a 12 ton fiducial mass detector located at 800 m from a 12 GW nuclear reactor (a), which is the product of the $\bar{\nu}_e$ flux spectrum (b) and the IBD cross section (c), from [108].

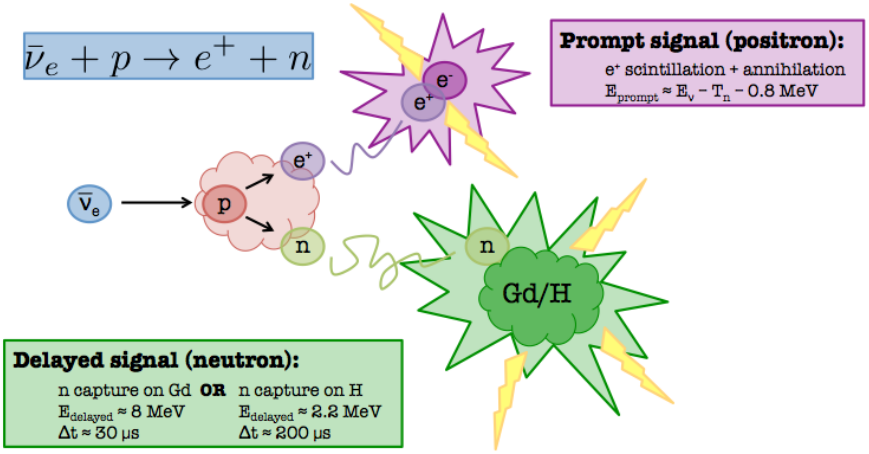

Figure 3.2: Scheme of an IBD interaction with neutron capture on Gd or H.

2. **Delayed:** The neutron capture on gadolinium (Gd) or hydrogen (H) constitutes the delayed signal. The neutron has to thermalize in the liquid scintillator before being absorbed by a high capture cross section element, such as Gd in the case of the Double Chooz experiment. A neutron capture on H is also possible. There is no need for thermalization in this case. The mean capture time when considering neutron capture on Gd is about 30 µs whereas it is about 200 µs for neutron capture on H.

3.1.3 Oscillation measurement concept

The main uncertainty in the former CHOOZ experiment comes from the $\bar{\nu}_e$ flux and spectrum at production. In order to get rid of this uncertainty, one can use two identical detectors located at different baselines from the nuclear reactors. Indeed, a detector located at a few hundred meters from the reactors will help to normalize the $\bar{\nu}_e$ flux and spectrum since the oscillation disappearance probability does not vary dramatically. *A contrario*, a detector located around 1 km from the reactors will be sensitive to the first maximum of the disappearance probability. By a relative comparison between the flux received in the "near" detector, at a few hundreds of meters, and the one received in the "far" detector, at about 1 km, it is possible to measure the disappearance, and therefore to access the value of the neutrino mixing angle θ_{13} [109].

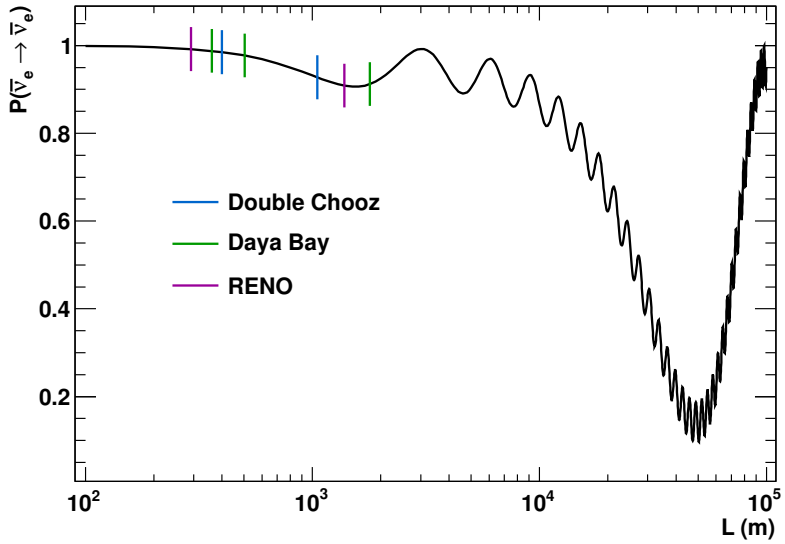

Figure 3.3: Survival probability of $\bar{\nu}_e$ assuming $E_{\bar{\nu}_e} = 3$ MeV. Mixing angles and mass square differences are taken from [110]. Double Chooz near and far detectors are placed, as well as Daya Bay and RENO ones.

This value is obtained through the neutrino survival probability formula which, in the case of a two neutrino oscillation hypothesis, can be expressed as:

$$P(\bar{\nu}_e \to \bar{\nu}_e) = 1 - \sin^2(2\theta_{13}) \sin^2 \left(1.27 \frac{\Delta m^2(\mathrm{eV}^2)\, L(\mathrm{m})}{E(\mathrm{MeV})} \right), \tag{3.9}$$

where θ_{13} is the mixing angle considered, Δm^2 the mass-squared difference, L the distance between the source and the detector and E the $\bar{\nu}_e$ energy.

This two neutrino oscillation hypothesis is valid for reactor neutrino oscillation experiment at short distance. Figure 3.3 shows the positions of the detectors for the Double Chooz, Daya Bay and RENO experiments. Whereas the near detectors are located close to the nuclear reactors, the far detectors stand in the first minimum of the survival probability.

Increasing statistics

When the CHOOZ experiment started, the two nuclear reactors of the Chooz power plant were not yet running. A two reactors-off period is something desirable in the Double Chooz experiment since it allows to understand the backgrounds [111]. Unfortunately, this two reactors-off period was too long in the case of the CHOOZ experiment, which took 40 % of its total data set in this configuration. Moreover, due to a cooling system issue, the two nuclear reactors could not run at full power at the beginning. This situation was not optimal for the CHOOZ experiment which also suffered from an instability of its detector. The attenuation length in the scintillator decreased and the transparency deteriorated. The performance of the liquid scintillator decreased with time, leading to the end of the experiment earlier than expected. The CHOOZ statistical uncertainty was measured to be 2.8 %.

Decreasing systematics

The Double Chooz experiment developed two main improvements w.r.t. the CHOOZ experiment. First of all, using two detectors located at different baselines from the reactors allows to get rid of the $\bar{\nu}_e$ production knowledge. The comparison of the observed $\bar{\nu}_e$ in the near and far detectors allows to cancel the uncertainty on the emitted $\bar{\nu}_e$. CHOOZ, as Double Chooz with the only far detector running, normalized its flux w.r.t. the measurements made in the Bugey-4 experiment, leading to a non-negligible systematic uncertainty. With two identical detectors, this systematic uncertainty is suppressed. Another improvement comes from the detector design. Finally, using a buffer, a γ-catcher and a target allows to have a fiducial volume better protected against background events. The CHOOZ systematic uncertainty was measured to be 2.7 %.

3.2 Experiment design

The two nuclear reactors of the Chooz power plant, called Chooz B, are the $\bar{\nu}_e$ sources. There are separated by about 164 m, which corresponds to a 6° angle separation when looking them from the far detector. The Double Chooz far detector has been built in one of the access galery of the previous Chooz nuclear power plant, called Chooz A. Chooz A consisted of a PWR nuclear reactor, the first running in France, from 1967 to 1991. It was built under

the hill boarding the Meuse river in order to keep the installation secret during the cold war period. This 300 meter water equivalent (m.w.e.) overbuden is of interest to protect the detector from cosmic muons and the induced background. Even if the deconstruction of Chooz A is still on-going, this access galery was available since 1996, which allowed the construction of the CHOOZ detector and which holds today the Double Chooz far detector. The Double Chooz near detector is still under construction under a smaller hill closer to Chooz B.

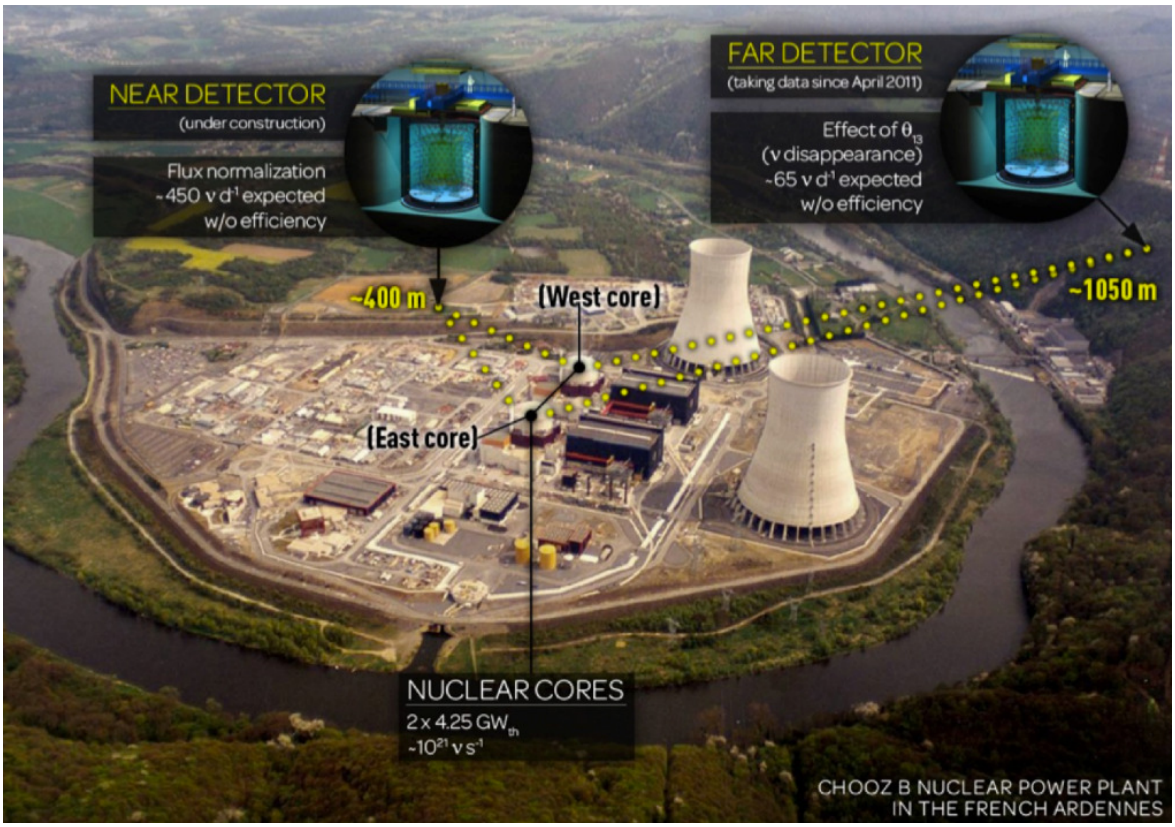

Figure 3.4: Double Chooz experimental site. The two nuclear reactors of the Chooz power plant are visible, as well as the Meuse river. The position of the near and far detectors is also indicated, from [112].

3.2.1 Detector design

A Double Chooz detector is composed of three sub-detectors. The Inner Detector (ID) allows to record the $\bar{\nu}_e$ signature. The Inner Veto (IV) is surronding it in order to detect external backgrounds which are mainly muon-induced and the Outer Veto (OV) is placed above both the ID and the IV to prevent from cosmic muon background.

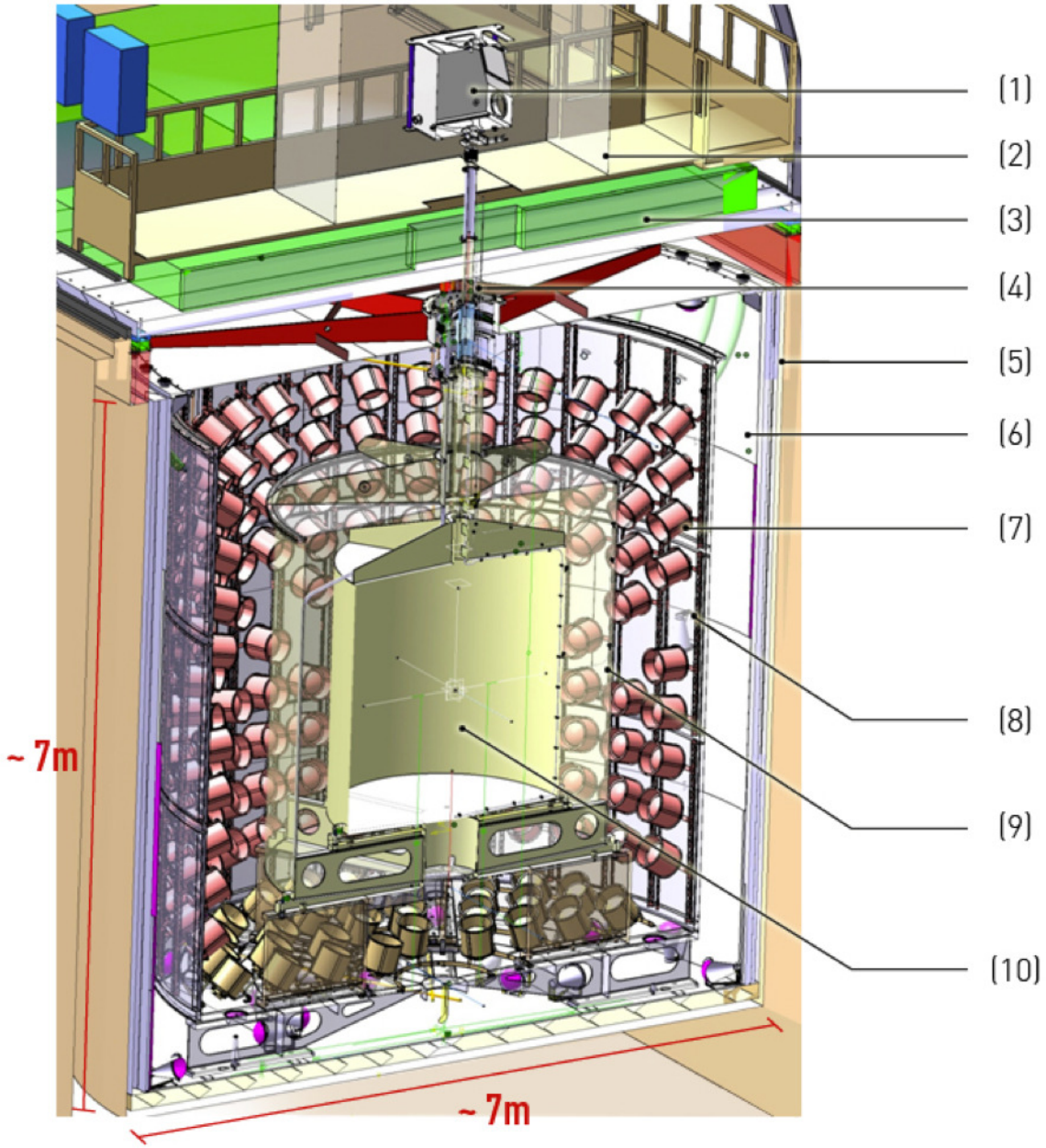

Figure 3.5: Scheme of the Double Chooz detector. (1) Glove Box (GB), (2) Clean Tent, (3) Outer Veto (OV), (4) Chimney, (5) Shielding, (6) Inner Veto (IV), (7) Inner Detector Photomultipliers (PMTs), (8) Buffer, (9) γ-catcher, (10) Target.

Inner detector (ID)

The inner detector is composed of the target in its center, surrounded by the γ-catcher itself surrounded by the buffer. Each volume is independent and the different liquids have optimal optical transmission and similar density in order not to deform the volume containers:

- **Target:** The innermost volume of the detector, which is called target, is the place where neutrino interactions with neutron capture on Gd are detected. It consists of a 1150 mm radius by 2459 mm height cylindrical acrylic vessel. This 8 mm thick vessel is filled with 10.3 m^3 of a Gd-doped liquid scintillator. It consists of 80 % of dodecane and 20 % of PXE together with 1 g/L of Gd, 7 g/L of PPO and 20 mg/L of bis-MSB. These two last components are wavelength shifters. PPO allows to reemit the scintillation light it absorbs with higher wavelengths such that the bis-MSB shifts again the light towards blue and UV wavelengths, for which the PMTs are more sensitive and the liquid more transparent. Since the CHOOZ experiment ended prematurely because of an instability of its liquid scintillator, a new type of metal loaded liquid scintillator has been developed to encapsulate the Gd atom in order to provide homogeneity and stability [113].
- **γ-catcher:** The γ-catcher is a 12 mm thick, 1708 mm radius by 3572 mm height cylindrical acrylic vessel which surrounds the target. Its 22.6 m^3 are filled with 66 % of mineral oil, 30 % of dodecane and 4 % of PXE. 2 g/L of PPO and 20 mg/L of bis-MSB are also part of this mixture. This un-doped liquid scintillator allows to contain the gammas emitted from both the positron and the neutron capture. This second acrylic vessel allows to contain the energy deposition and therefore to increase the detection efficiency. The γ-catcher light yield is tuned to provide the same photoelectrons over MeV ratio as that of the target. One has to take into account the spill-in and spill-out effects which occur between these two volumes. The spill-in consists in having the positron signal in the γ-catcher and the neutron capture in the target. *A contrario*, the spill-out is characterized by the positron signal in the target and the neutron capture in the γ-catcher. These two effects do not compensate but will become negligible when the near and far detectors will work together. This vessel is also used to detect $\bar{\nu}_e$ candidates when considering neutron capture on H.
- **Buffer:** The buffer is the last part of the inner detector. This 3 mm thick stainless steel cylindrical vessel encloses both the target and the γ-catcher. It consists of a 2760 mm radius by 5680 mm height vessel filled with 114.2 m^3 of mineral oil, which provides an optical decoupling with the inner detector. The buffer tank supports 390 10-inch Hamamatsu R7091 PMTs which collect the light which will bring information, once treated, on the energy deposition and vertex position of the collected signals [114, 115]. It allows to shield the target and γ-catcher from ^{40}K contained in the PMTs glass in the target and γ-catcher volumes. This method was first used in the Borexino experiment [116] and constitutes the main improvement with respect to the CHOOZ experiment.

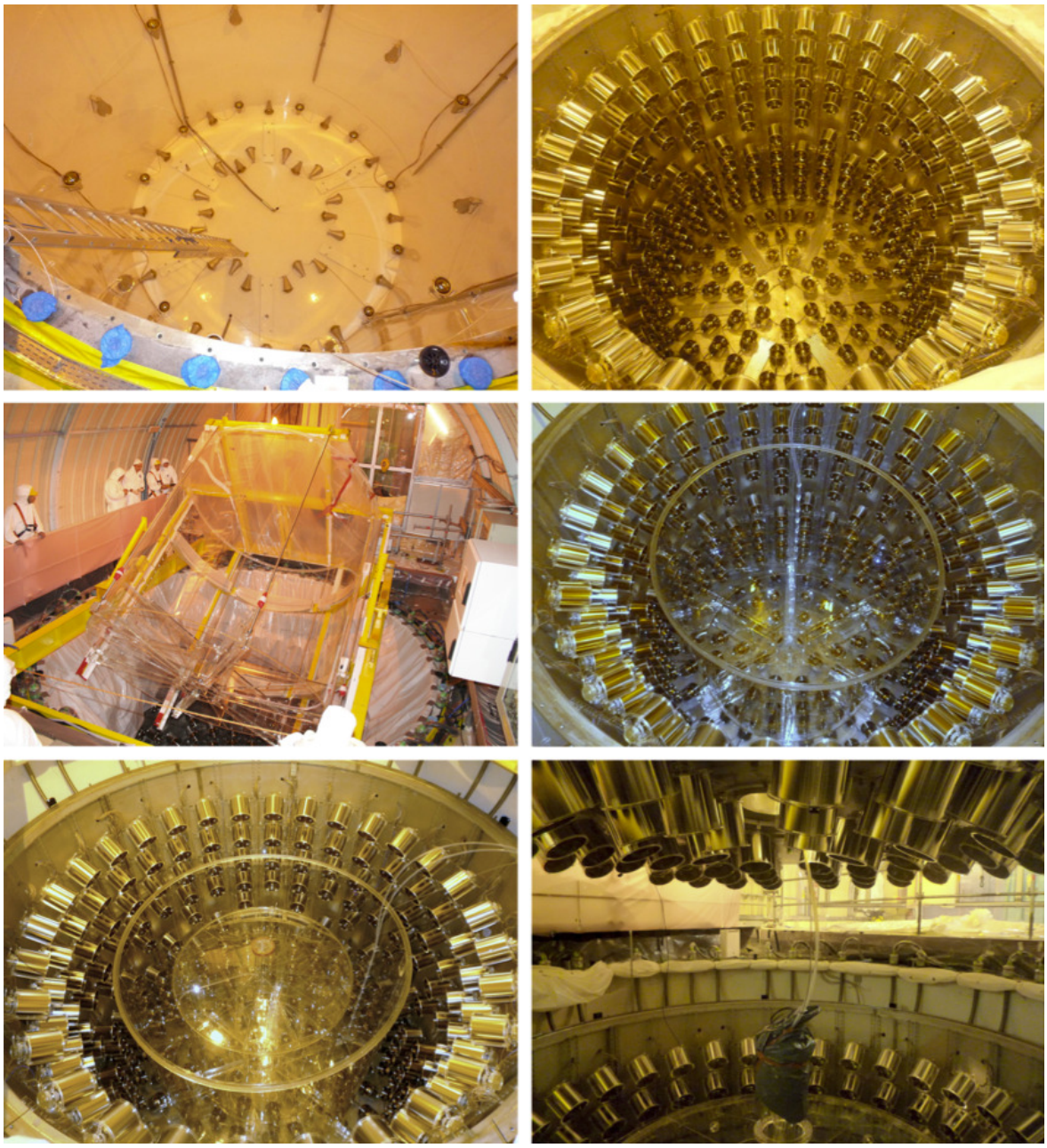

Figure 3.6: Pictures of the Double Chooz far detector at different stages of the integration, from [112]. (*top left*) Installation of the inner veto PMTs. (*top right*) Installation of the inner detector PMTs. (*middle left*) γ-catcher integration which has been a non-trivial step. (*middle right*) γ-catcher installation. (*bottom left*) Target installation. (*bottom right*) Closing of the detector.

Figure 3.7: Pictures of the Double Chooz far detector, from [112]. (*top*) Inner veto views with the special orientation of the PMTs. (*bottom*) Outer veto covering the detector with the chimney in the middle for the deployment of radioactive sources.

Inner Veto (IV)

The inner veto surrounds the inner detector and acts as a shield against radioactive and muon-induced background. It consists of a 3250 mm radius by 6830 mm height stainless steel cylindrical vessel filled with 90 m^3 of liquid scintillator composed for half of dodecane and half of linear alkylbenzene together with 2 g/L of PPO and 20 mg/L of bis-MSB. This 10 mm thick tank supports 78 8-inch Hamamatsu R1408 PMTs fixed parallel to the surface because of the confined space. In order to help the light collection, white painted walls and highly reflective VM2000 foils covering the buffer vessel have been used [117].

Table 3.2: Characteristics of the different vessels which composed the ID and the IV.

Vessel	**Radius (mm)**	**Height (mm)**	**Volume (m^3)**
Target	1150	2459	10.3
γ-catcher	1708	3572	22.6
Buffer	2760	5680	114.2
Inner Veto	3250	6830	90

Shielding

Outside the inner veto of the Double Chooz far detector, a 15 cm thick stainless steel shielding was installed in order to protect from external radioactivity. It is composed of 66 V-shaped bars, 42 for the lateral part and 12 for the bottom and top parts, which were demagnetized to prevent from PMTs signal perturbation.

Outer Veto (OV)

The outer veto is an improvement with respect to the CHOOZ experiment. It aims to identify muons which can enter or pass nearby the inner detector. It is composed of 64 plastic scintillator strips which cover an area of 13 m $\times$ 7 m above the inner detector, the inner veto and 15 cm of stainless steel shielding. Each strip measures 5 cm $\times$ 1 cm $\times$ 320 cm or 360 cm. Thanks to the crossing of the strips, the outer veto can record the (x, y) coordinates of a passing muon with a higher precision than the inner veto. In order to prevent from muons which can directly enter the inner detector through the chimney, an upper outer veto was installed above the chimney and the glove box. Working together, the inner and outer veto allow to reject more than 99.99 % of the muons crossing the inner veto.

3.2.2 Data acquisition system

For both the inner detector and the inner veto, the scintillation light produced by charged particles is seen by PMTs. This signal is transformed into a few millivolts electric signal

which is carried together with the about 1.3 kV high voltage (HV) which allows to supply the PMTs. HV-splitter circuits allow to decouple the two components. After amplification by the front end electronic (FEE) modules, digitization of the PMTs signal is done by the flash-analog-to-digital converter (FADC) electronics [118]. Figure 3.8 represents a scheme of the detector electronics.

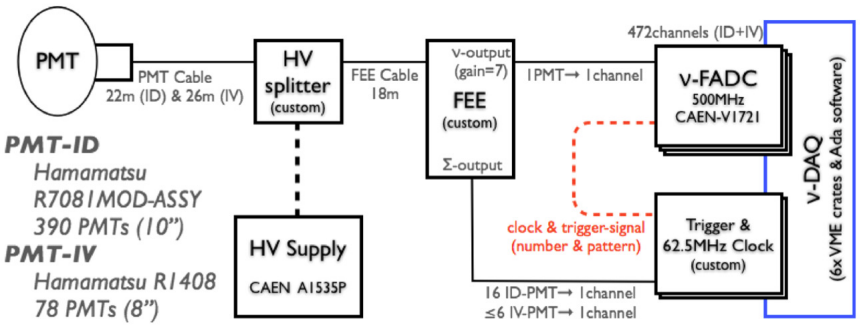

Figure 3.8: Scheme of the Double Chooz readout and DAQ systems.

ν-FADC system

The ν-FADC system has been developed in a partnership between the AstroParticule et Cosmologie (APC) laboratory and the CAEN company [119]. The system relies on 64 CAEN-Vx1721 (VME64x) waveform digitizers. Each card holds 8 channels with 8 bit resolution FADC, allowing the signal sampling at 500 MHz. This frequency corresponds to a 2 ns period and allows to save the waveforms of each PMTs. This precious tool can help to better estimate the signal arrival and can therefore help to better reconstruct the vertex position of the event considered. Each channel holds a 2 MB internal memory, separated in 1024 different area. Each of these 1024 area are themselves divided into 2048, allowing the sampling over 4096 ns. As long as the FADC does not receive any trigger signal, the digitization takes place in the same buffer region. When a trigger signal arrives, the digitization starts in the next buffer region and leaves the previous one for the readout. 1024 samples can then be recorded and kept in memory. Since the trigger rate is lower than the readout speed, the digitization index never reaches the readout index, allowing the acquisition to be free of deadtime. On the 4096 ns available, only 256 ns of the waveform is recorded. It contains more than 90 % of the light collection.

Trigger system

At the exit of the FEE, the signal coming from the PMTs is sent to the FADC but also to the trigger system. The trigger system is composed of three trigger boards (TB) and one trigger master board (TMB). Two of the trigger boards are dedicated to the ID PMTs whereas the third one stands for the IV PMTs:

- **ID trigger boards:** The ID PMTs are separated into 12 sectors containing each 32 PMTs. These 12 sectors are themselves separated into two regions, the upper part of the detector containing 6 sectors and the lower part of the detector containing the other 6 sectors. Basically, half of the PMTs from a given sector are connected to the first trigger board, TB A, and the other half to the second trigger board, TB B. The grouping has been made such that a PMT belonging to TB A is surounded by PMTs belonging to TB B, and *vice versa*. The FEE proceeds to the analog sum of the signals from a given sector by group of 16 PMTs and send it to the trigger board. Each trigger board makes the decision based on this analog sum of half of the ID PMTs. This configuration allows each trigger board to look at the same volume. The decision should then be te same.
- **IV trigger board:** Due to the geometry and the limited number of IV PMTs, the IV trigger board works differently than the ID trigger boards. The decision is in this case mainly based on the hit pattern of groups of 3 to 6 PMTs. Special attention to the event topology in the lower part of the IV allows to investigate muons which stop in the ID.
- **Trigger master board:** The trigger master board receives the decisions of the trigger boards through 8 bits words and allows the FADCs to store the event in their internal memory. It also distributes a 62.5 MHz clock signal to all the FADCs for synchronization.

3.2.3 Calibration system

Double Chooz relies on the energy deposition of events across the detector in order to build the energy spectra which will then allow to access θ_{13}. It is essential to master the knowledge of the signature of particles involved in the physics processes considered. Liquid and PMTs properties can be better characterized, even if tests were already performed during the detector installation. Calibrating the detector is therefore crucial in order to access the energy response and to carefully reconstruct the events vertices. To do so, radioactive sources as well as light injection system are used.

Radioactive sources

Up to now, four radioactive sources with different particles emission and different energies are used to calibrate the ID. The deployment of ^{137}Cs, ^{68}Ge, ^{60}Co or ^{252}Cf can be performed either using the Z-Axis Deployment System (ZADS) or the Articulated Arm[5] (AA), which brings the sources directly in the target volume, or the Guide Tube (GT), which brings the sources in the γ-catcher volume. The deployment of the sources is performed in a clean tent above the detector. When using the ZADS or the AA, operators use the Glove Box (GB) under nitrogen atmosphere and at the detector pressure.

With the emission of a 667 keV γ, the ^{137}Cs source is the less energetic source. This energy is not of interest for the $\bar{\nu}_e$ selection but remains between the trigger threshold and the inverse

[5]Not yet used.

β decay reaction threshold of 1.022 MeV according to equation (3.7). The electron capture on ^{68}Ge provides a positron which annihilates with an electron of the medium, leading to the emission of two 511 keV γ. This energy corresponds to the energy threshold of the inverse β decay reaction and helps to calibrate the trigger efficiency. The ^{60}Co source emits two γ of 1.17 MeV and 1.33 MeV in the prompt energy range of interest for the $\bar{\nu}_e$ selection whereas the delayed energy range can be studied thanks to the neutrons release from the spontaneous fission of the ^{252}Cf source.

Light injection

Light injection system emitting LED light guided through optical fibers were also installed in both the inner detector (IDLI) and the inner veto (IVLI). 46 injection points fixed on the edge of some PMTs are present in the inner detector and 96 in the inner veto. One can set the wavelength of the light to be 385 nm, 425 nm or 475 nm for the IDLI and 365 nm or 475 nm for the IVLI. The system allows either a diffuse or pencil beam mode.

Whereas the 385 nm wavelength should be totally absorbed and reemitted by the liquid scintillator, the 425 nm wavelength is partially absorbed, contraining its detection to the PMTs present on the opposite side of the detector. It allows to understand the absorption of the target and γ-catcher as well as the PMTs characteristics. The 475 nm wavelength should not excite the liquid scintillator, acting as a direct light source for the PMTs receiving the light.

3.3 Event reconstruction

3.3.1 Energy reconstruction

Energy reconstruction is one of the key of the θ_{13} measurement since it is extracted from the energy spectra comparison between the one obtained in the far detector and the Monte Carlo (MC) one, up to now. In the near future, θ_{13} will be measured by comparing the far and near detectors energy spectra. It is therefore crucial to master its knowledge.

The energy reconstruction method is based on the conversion of the total number of photoelectrons, $N_{\text{p.e.}}$, to the visible energy, E_{vis}. Correction factors for uniformity, f_u, energy scale, f_{MeV}, stability for data only, f_s, and non-linearity for MC only, f_{nl}, are also applied, as follows:

$$E_{\text{vis}} = N_{\text{p.e.}}(\rho, z, t) \times f_u^*(\rho, z) \times f_{\text{MeV}}^* \left(\times f_s^{\text{data}}(E_{\text{vis}}^0, t)\right) \left(\times f_{nl}^{\text{MC}}(E_{\text{vis}}^0)\right), \tag{3.10}$$

where (ρ, z) stands for the detector coordinates, t for the time, E_{vis}^0 for the energy once the uniformity correction has been applied and * refers to either data or MC.

$N_{\text{p.e.}}$ can be extracted by summing the amount of charge received by each PMT:

$$N_{\text{p.e.}} = \sum_i \text{p.e.}_i = \sum_i \text{q}_i \times \text{gain}_i(\text{q}_i, t), \tag{3.11}$$

where q_i is the integrated charge by pulse reconstruction for the PMT i and $\text{gain}_i(q_i, t)$ a function which converts from charge to photoelectrons and corrects for charge reconstruction non-linearity due to biased baseline estimation.

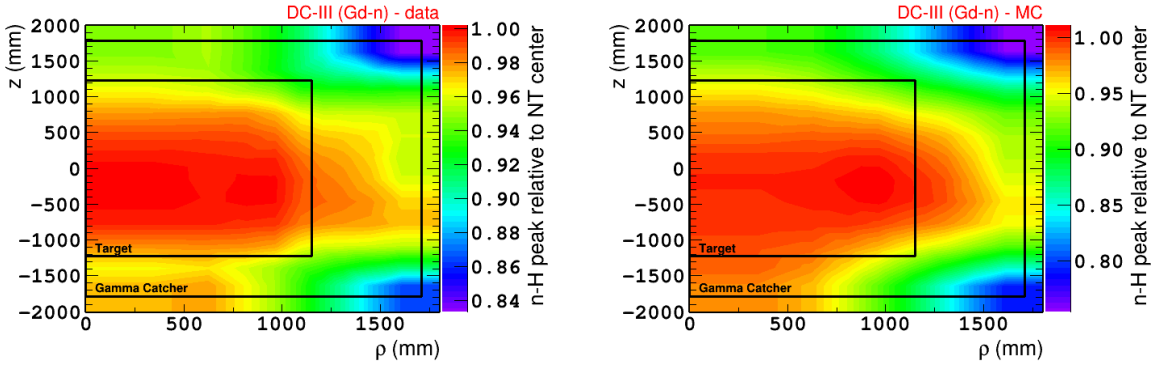

Figure 3.9: Uniformity correction maps for data (*left*) and MC (*right*) obtained by fitting the neutron capture peak on H.

Once we have $N_{\text{p.e.}}$, we need to correct it for the position dependence across the detector volume and to apply the energy scale calibration. The correction factor f_u takes into account the detector coordinates (ρ, z) of the reconstructed event and convert $N_{\text{p.e.}}$ as if the event took place in the center of the detector, *i.e.* $\rho = 0$ and $z = 0$. Figure 3.9 shows the uniformity correction maps for data and MC which were generated using spallation neutron with capture on H across both the target and γ-catcher volumes. The correction factor f_{MeV} has been studied through the neutron capture on H from a ^{252}Cf calibration source placed in the center of the detector.

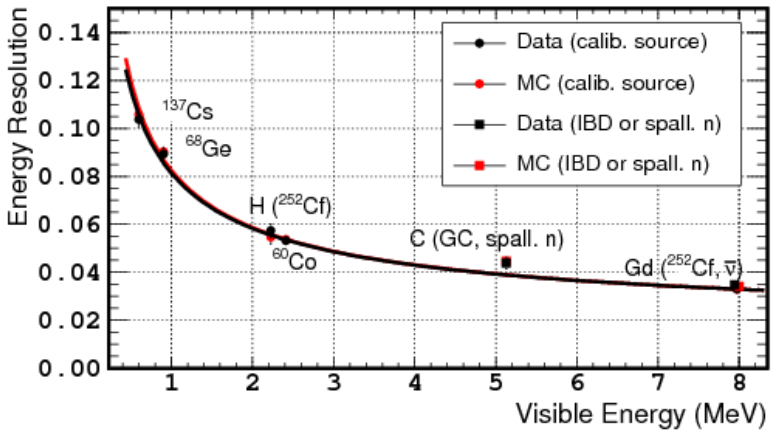

Figure 3.10: Energy resolution as a function of the visible energy for data and MC.

The evaluation of the light non-linearity has been done through the generation of MC with several different combinations of Birks quenching parameter and the light yield of the

liquid scintillator within uncertainties taken from measurements [120, 121]. Figure 3.10 shows the visible energy behavior for data and MC. The energy scale and the energy resolution are in very good agreement. Fits performed on the energy resolution show a similar behavior for both data and MC.

3.3.2 Vertex position reconstruction

The vertex position reconstruction is performed through a package with algorithms based on a charge and time maximum likelihood. Let us consider the light produced by a point-like source event $X = (x_0, y_0, z_0, t_0, \Phi)$. We assume the light intensity, Φ, to be isotropically distributed per unit of solid angle. We also assume this light to be only affected by pure attenuation when it propagates. The amount of light a PMT i located at a distance r_i from the true vertex with a quantum efficiency ϵ_i can be predicted to be [122]:

$$\mu_i = \epsilon_i \, \Phi \, \Omega_i \, \exp\left(-\frac{r_i}{\lambda}\right), \tag{3.12}$$

where Ω_i is the solid angle subtended by the PMT and λ the characteristic attenuation length.

Considering the angular response of the PMT to be $f(\cos\eta)$ with η the angle of incidence of the light with respect to the PMT normal, Ω_i can be written as:

$$\Omega_i = \pi R^2 \, \frac{f(\cos\eta)}{r_i^2}, \tag{3.13}$$

where R is the PMT radius with $R \ll r_i$ as a good approximation.

This optical model, which relies on the λ and $f(\cos\eta)$ parameters, allows to predict the amount of light seen by a given PMT. Summing over all the PMTs, it is then possible to calculate the total amount of light.

The arrival time received on the PMT i can also be predicted from the event time t_0:

$$t_i^{\text{pred}} = t_0 + \frac{r_i}{c_n}, \tag{3.14}$$

where c_n corresponds to the effective speed of light in the volume considered.

We can then define the event likelihood to be:

$$L(X) = \prod_{q_i=0} f_q(0;\mu_i) \prod_{q_i>0} f_q(q_i;\mu_i) f_t(t_i; t_i^{\text{pred}}, \mu_i), \tag{3.15}$$

where $f_q(q_i;\mu_i)$ is the probability to measure a charge q_i when expecting a charge μ_i and $f_t(t_i; t_i^{\text{pred}}, \mu_i)$ is the probability to measure a time t_i when a time t_i^{pred} and a charge μ_i are predicted.

The first product runs over PMTs which do not record any hit whereas the second one runs over PMTs which have been hit. MC are used to provided these charge and time

probabilities. They are checked using physics and calibration data. The goal then is to maximise this likelihood function, or minimize the negative log-likelihood function, in order to provide the best set of parameters $X_{\min}$:

$$\mathrm{F_V} = -\ln L(X) = -\sum_i \ln f_q(q_i; X) - \sum_{q_i>0} \ln f_t(t_i; X) \tag{3.16}$$

The vertex position reconstruction can be performed using the charge likelihood only, or the time likelihood only, or both of them. This last option allows to check the accuracy and stability of the algorithm.

3.4 Backgrounds studies

Double Chooz has to deal with several different backgrounds. The background with the highest rate is the light noise, which will be explained in the next chapter. Two other kinds of backgrounds exist, the correlated background, which is a muon-induced background, and the uncorrelated background, which does not follow a specific physical process:

- Correlated backgrounds:
  - Decays of cosmogenic isotopes such as ^{9}Li and ^{8}He created through a spallation mechanism induced by cosmic muons crossing the inner detector.
  - Fast neutrons (FN) created by cosmic muons around the detector.
  - Stopping muons (SM) which enter the detector through the chimney and decay inside the inner detector.
- Uncorrelated backgrounds:
  - Accidental coincidences of single events.

Since these backgrounds mimic the IBD signature, one has to take a special care in order to understand them. They are taking into account in the neutrino oscillation fit procedure.

3.4.1 Correlated background

^{9}Li + ^{8}He background

The so-called cosmogenic background is, after the light noise one, the main background Double Chooz has to deal with. Serious issues coming from the misunderstanding of this background have to be avoided. A special effort has then been made to correctly handle this background.

Radio-isotopes ^{9}Li and ^{8}He are created through spallation reactions induced by cosmic muons on ^{12}C contained in the liquid scintillator. There is no need to try to distinguish between ^{9}Li and ^{8}He since they have the similar behavior when considering half-life or energy spectrum. We will therefore focus on the ^{9}Li properties.

^{9}Li has a 257 ms lifetime and decays through β^- decay into unstable excited states of ^{8}Be or stable state of ^{9}Be. ^{8}Be decays then in two α particles. About half of the ^{9}Li decays is followed by the emission of a neutron, mimicking perfectly an IBD signature. With an endpoint of the β^- decay spectrum at 13.6 MeV, there is no way to distinguish between this decay and a neutrino event.

Fast neutrons

Fast neutrons are created from the interaction of cosmic muons in the surrounding rocks. The created neutrons can then enter the detector. If they manage to cross the inner veto and the buffer, these neutrons can produce a prompt-like signal due to the recoil of the proton hit by the incoming neutron and can then produce a delayed-like signal when they are captured. This background contribution can be investigated by looking at higher prompt energies where there is no more neutrino component and then extrapolating to the prompt energy range of interest.

Stopping muons

Due to the chimney we use to calibrate the detector by insering radioactive sources, it exists a path going directly from the outside of the detector to the target. Muons can therefore enter the inner detector without interacting with the inner veto nor the lower outer veto built to warn against the presence of muons. Once inside the detector, the muon looses its energy by ionization, mimicking a prompt signal, whereas the Michel electron created from the muon decay can mimic a delayed signal later on.

3.4.2 Uncorrelated background

The uncorrelated background is also called accidental background. It corresponds to a random association of a prompt-like signal together with a delayed-like signal. These two signals are not correlated. Applying cuts on the distance as well as on the time interval between the prompt and delayed signals allows to reduce the contamination but does not eliminate it. We then have to quantify the remaining amount of accidental background.

Rate and spectrum shape of accidentals are determined following an off-time window method. It consists in looking for prompt-like and delayed-like signals with a long enough time window between these two signals in order to avoid a correlation between them. The prompt and delayed signals selection follow the same criteria than the neutrino selection. Figure 3.11 shows the distance between prompt and delayed signals for data, MC and accidental sample collected in off-time coincidence windows. One can see that applying a cut on the correlation distance allows to greatly decrease the accidental background with a limited effect on the IBD signal inefficiency.

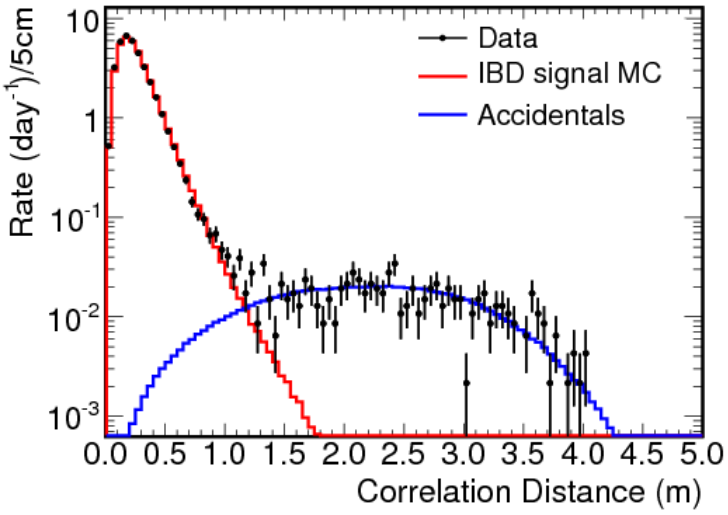

Figure 3.11: Distance between the prompt and delayed signals in the case of neutron capture on Gd. The points correspond to the data, the red line to the MC and the blue line to the accidental sample obtained through an off-time window method.

Chapter

4 Dealing with an unexpected background

I don't see the logic of rejecting data just because they seem incredible.
Fred Hoyle

Contents

Since the very beginning of the data taking, Double Chooz had to deal with an unexpected background known as "light noise" among the collaboration. This background is due to sporadic spontaneous flashes of some of the PMTs bases. Tests made in several laboratories proved the origin of the noise to be due to PMTs glowing. Investigations on the behavior of the epoxy used to cover the PMTs base in an electric field have been performed [123] and it has also been shown that reducing the PMT HV tends to reduce the light emission [124]. In order to avoid this misbehavior in the near detector, it has been decided to cover the base of the PMTs with black sheet.

4.1 Motivations

Since it is no longer possible to cover the base of the PMTs of the Double Chooz far detector, we need to provide offline analysis tools in order to discriminate between light noise

and physics events. This crucial analysis started before my thesis but the level of light noise rejection was not sufficient. I improved it and completed it to obtain what is now the "official" light noise rejection algorithm for the collaboration.

In the previous published analyses [39, 40, 41], the light noise component was handled in a different way for prompt or delayed events. For delayed events, there was also a difference when considering neutron capture on Gd or H. The strength of the set of cuts we have developed is to be the same for any kind of events considered. Both efficiency and purity have been improved.

Since both Gd and H analyses are considered in the following, we take into account events which take place in the target as well as those which take place in the γ-catcher. The only set of cuts we apply on the data are the following:

- Total charge in IV: $Q_{IV} < 30000$ charge units
- Visible energy in ID: $E_{vis} \in [0.4, 20\ MeV]$

The upper limits on both the charge collection in the IV and the visible energy in the ID allow to reject muon events. The lower limit on the visible energy in the ID has been set to 0.4 MeV since below this value the trigger efficiency remains below 100 %. One fifth of the large amount of available events[1] are used in order to be able to perform the following analysis.

4.2 Discriminating variables

Several strategies have been developed in order to get rid of light noise [125]. Since the light emission is localized in the PMT base, one PMT will first record its own light before it is spread out to the other PMTs. The inhomogeneous distribution of light noise is the key to discriminate it w.r.t. physics events. Several variables have been built in order to identify light noise events. Four of them are now used to reject light noise events.

4.2.1 PMT Time RMS variable

The PMT Time RMS variable is known among the collaboration as the $RMS(T_{start})$ variable. It corresponds to the standard deviation of the distribution of the pulse start time on each PMT, for a given event. Let us consider an $\bar{\nu}_e$-like signal taking place inside the target. Assuming an isotropic distribution of the light inside the inner detector, one should expect a small spread in the photons arrival time on PMT, *i.e.* a low $RMS(T_{start})$ value. *A contrario*, in the case of a light noise event, the PMT responsible and the PMTs around it record the event faster than the PMTs on the other side of the detector. It leads to a much larger spread in the photons arrival time on PMT, *i.e.* a higher $RMS(T_{start})$ value, w.r.t. point-like events inside the detector.

[1] 2.5 billion events

4.2.2 PMT Charge RMS variable

The PMT Charge RMS variable is also known as the RMS(Q) variable. It has been built following the same strategy as the RMS(T_{start}) variable when looking at the charge distribution among the PMTs. It corresponds to the standard deviation of the distribution of the charge on each PMT, for a given event. When building it, we first assumed that, for an $\bar{\nu}_e$-like signal taking place inside the target, the charge should be uniformly distributed on average among the PMTs. We expected then each PMT to receive more or less the same amount of charge, therefore RMS(Q) to remain low. In the case of a light noise event, since it occurs at the base of a PMT, this PMT and its neighbors should receive the largest amount of signal. The PMTs on the other side of the detector should receive less signal, leading to a more important spread in the charge distribution and consequently to a larger RMS(Q).

It appears that if the RMS(Q) variable alone is not very efficient in discriminating between physics and light noise events, together with the RMS(T_{start}) it becomes a much more powerful tool [126]. Figure 4.1 shows the PMT Charge RMS vs PMT Time RMS spectra without any light noise cuts. Two populations are distinguishable: physics events on the left, light noise events rather on the right. The following cut is established:

$$\text{RMS}(T_{start}) < 36 \text{ ns or RMS(Q)} < 464 - 8 \times \text{RMS}(T_{start}) \tag{4.1}$$

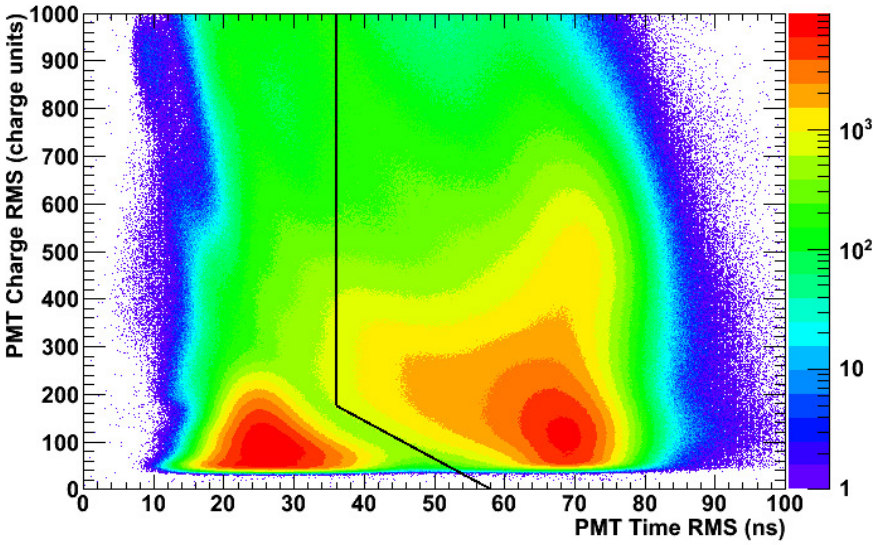

Figure 4.1: PMT Charge RMS vs PMT Time RMS spectra. No light noise cuts have been applied. The black line represents the 2D cut on the PMT Charge RMS / PMT Time RMS plan.

4.2.3 Maximum PMT Charge over Total Charge variable

The Maximum PMT Charge over Total Charge variable is also known as the Q_{max}/Q_{tot} or MQTQ variable. It corresponds to the fraction of the highest charge received by a PMT over

the total amount of charge registered for the event. Since a light noise event takes place in the PMT base, this PMT or a neighbor collects a much higher charge than the other PMTs. One should then expect a larger Q_{max}/Q_{tot} ratio for a light noise event and a smaller one for a physics event by assuming the physics event charge to be uniformly distributed among the PMTs. Physics events are selected with the Q_{max}/Q_{tot} condition:

$$Q_{max}/Q_{tot} < 0.12 \tag{4.2}$$

4.2.4 ΔQ variable

The ΔQ variable, also known as Q_{diff}, is the last light noise variable. It has been designed in order to get rid of light noise events with visible energy greater than 3 MeV. The algorithm first looks for the PMT with the highest charge received, q_{max}. PMTs within a 1 m sphere radius centered on the PMT with maximum charge are then selected in order to build the Q_{diff} variable [127]:

$$Q_{diff} = \frac{1}{N}\sum_{i}^{N}\frac{(q_{max}-q_i)^2}{q_i} \tag{4.3}$$

where N is the number of PMTs within the sphere and q_i their charge.

The signal difference between the PMT with maximum charge and its neighbors should lead to a low Q_{diff} whereas it is expected to be large in the case of a light noise event. This last cut is the high energy killer component of the light noise cuts set. Physics events are selected with the Q_{diff} condition:

$$Q_{diff} < 30000 \text{ charge units} \tag{4.4}$$

4.3 Strategy

These four variables are working together in order to reject light noise events. The official cuts used to reject those events are [128]:

- $RMS(T_{start}) < 36$ ns or $RMS(Q) < 464 - 8\times RMS(T_{start})$
- $Q_{max}/Q_{tot} < 0.12$
- $Q_{diff} < 30000$ charge units

The light noise studies we present is based on the last runs selection which extends from April 13, 2011 to January 30, 2013 for a 467.90 days total live time. Events which do not fulfill the visible energy region of interest for the $\bar{\nu}_e$ analysis, *i.e.* between 0.4 and 20 MeV, are rejected, as well as events with a charge deposition in the inner veto greater than 30000 charge units.

The so-called 2D cut is the main light noise cut. In the previous Double Chooz publications [39, 40, 41], the light noise was rejected by applying two cuts, one on the $RMS(T_{start})$ variable and another one on the Q_{max}/Q_{tot} variable. $RMS(T_{start})$ was required to be lower than 40 ns in order to reject light noise events. Even if this cut was able to correctly handle

the light noise, it appears that it also rejected low energy events. The 2D cut allows to avoid the rejection of these events by extending the cut up to 58 ns, as it can be seen in Figures 4.1 and 4.2 after applying both the Q_{max}/Q_{tot} and Q_{diff} cuts.

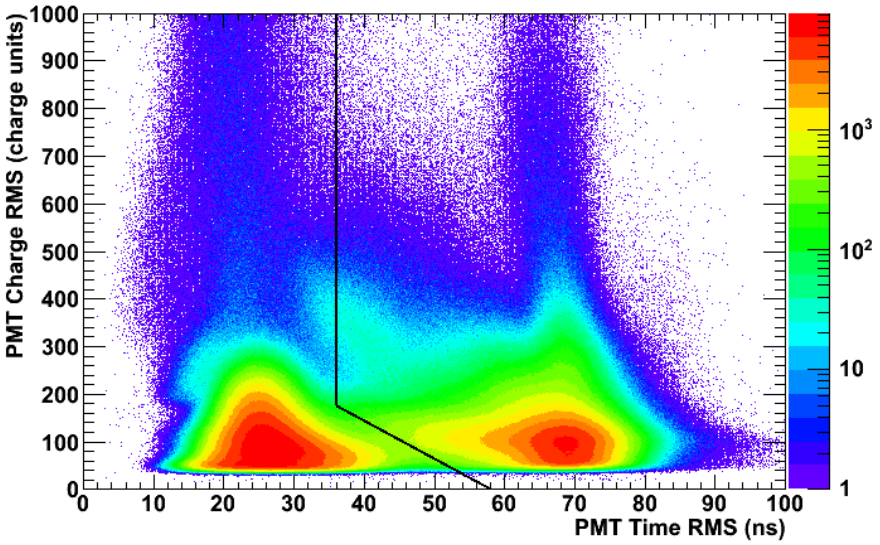

Figure 4.2: PMT Charge RMS vs PMT Time RMS spectra. Maximum PMT Charge over Total Charge and ΔQ cuts have been applied. The black line represents the 2D cut on the PMT Charge RMS / PMT Time RMS plan. Physics data belong to the left side of this line whereas light noise data belong to the right side of this line.

Figures 4.3 to 4.10 illustrate the behaviors of the four variables used to discriminate light noise events from events of interest we will call "Physics". We voluntary apply quotes since we do not know the contamination of light noise in the "Physics" sample. This sample contains physics events, as it will be demonstrated in Section 4.4, but without a pure light noise sample, we are not able to provide numbers on the contamination of light noise events in this sample.

Figures 4.3 and 4.5 show the RMS(T_{start}) and RMS(Q) spectra for both physics and light noise events. Physics events are obtained by applying the three cuts listed above. The physics spectrum evolves up to 58 ns whereas the light noise spectrum progresses in all the available range. Due to the RMS(T_{start}) cut value used in [39, 40, 41], low energy events were removed, which could have lead to a loss of detection efficiency. Since we lower the prompt visible energy to 0.5 MeV in [42] w.r.t. 0.7 MeV in [39, 40, 41], this 2D cut allows to minimize the detection inefficiency. Figures 4.4 and 4.6 show the effect of the 2D cut once both the Q_{max}/Q_{tot} and Q_{diff} cuts have been applied. This 2D cut rejects 42.5 % of the pre-selection made by the Q_{max}/Q_{tot} and Q_{diff} cuts.

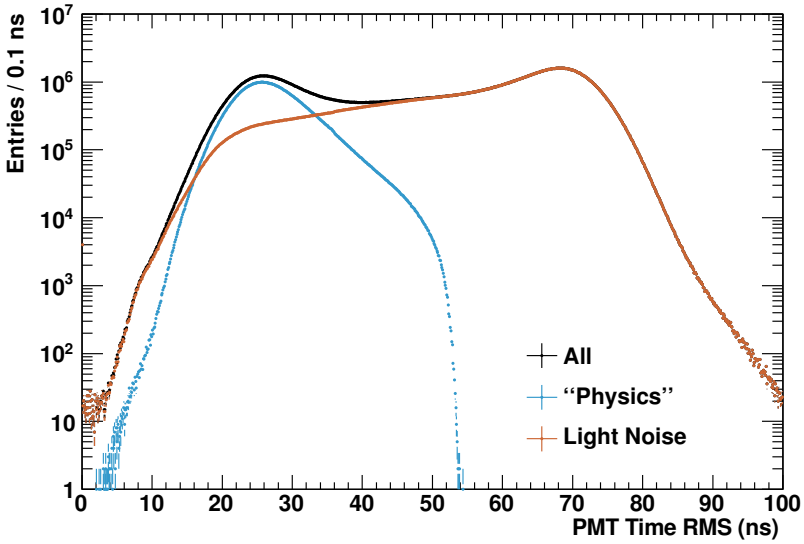

Figure 4.3: PMT Time RMS spectra. Data without any cuts are represented in black. Physics data are obtained by applying light noise cuts and are shown in blue. Light noise data are shown in orange.

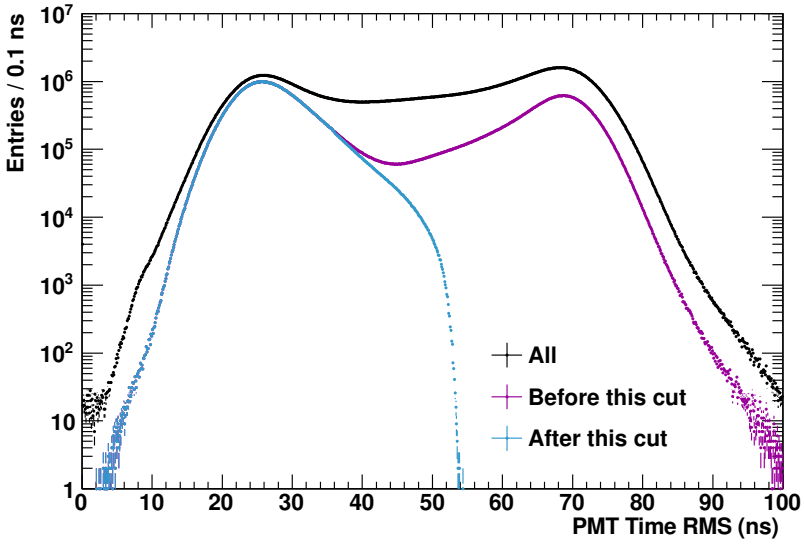

Figure 4.4: PMT Time RMS spectra. Data without any cuts are represented in black. Data when applying Maximum PMT Charge over Total Charge and ΔQ cuts are shown in magenta. These two cuts allow to keep 39.8 % of the total events. By applying then the 2D cut on the PMT Charge RMS / PMT Time RMS plan, 42.5 % of this selection is then rejected (from magenta to blue). Physics data are therefore obtained by applying all light noise cuts and are shown in blue.

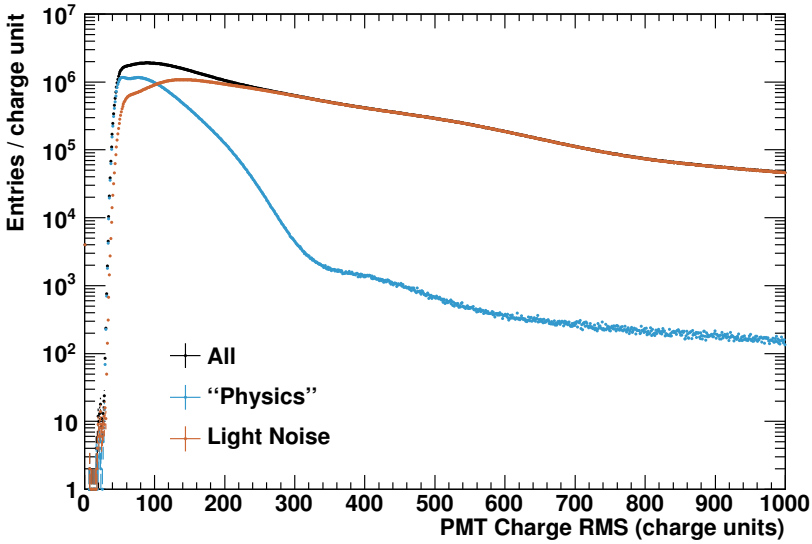

Figure 4.5: PMT Charge RMS spectra. Data without any cuts are represented in black. Physics data are obtained by applying light noise cuts and are shown in blue. Light noise data are shown in orange.

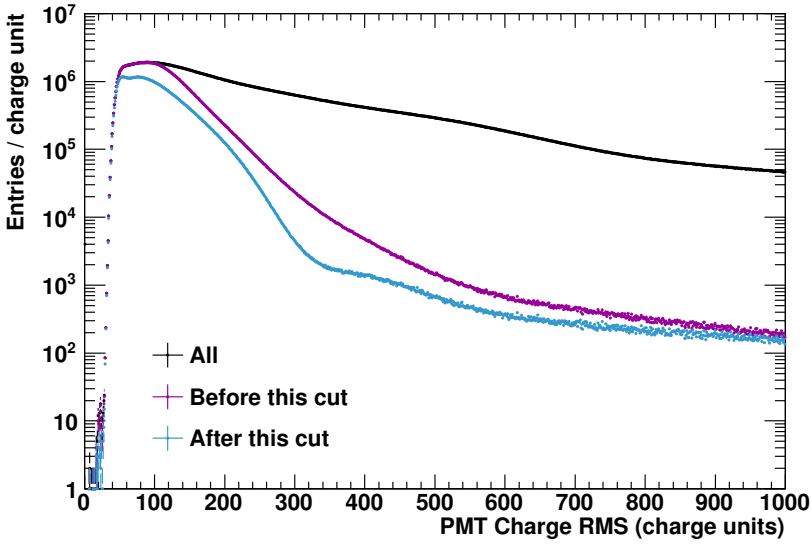

Figure 4.6: PMT Charge RMS spectra. Data without any cuts are represented in black. Data when applying Maximum PMT Charge over Total Charge and ΔQ cuts are shown in magenta. These two cuts allow to keep 39.8 % of the total events. By applying then the 2D cut on the PMT Charge RMS / PMT Time RMS plan, 42.5 % of this selection is then rejected (from magenta to blue). Physics data are therefore obtained by applying all light noise cuts and are shown in blue.

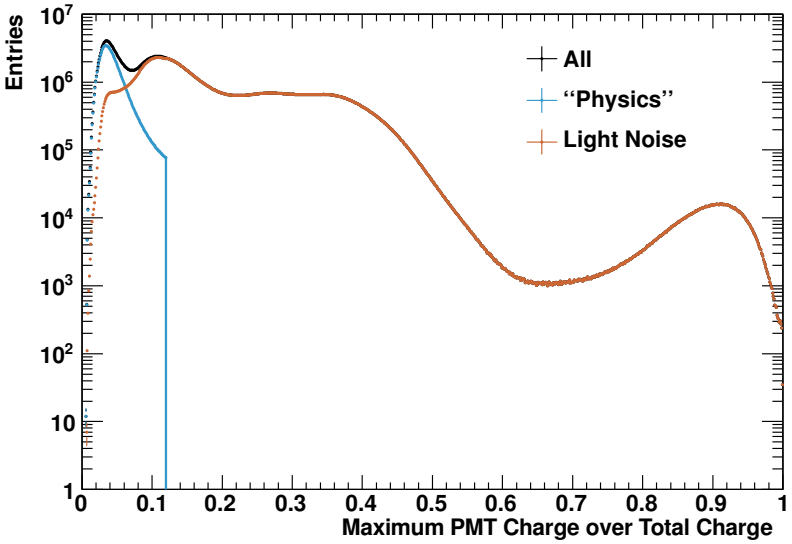

Figure 4.7: Maximum PMT Charge over Total Charge spectra. Data without any cuts are represented in black. Physics data are obtained by applying light noise cuts and are shown in blue. Light noise data are shown in orange.

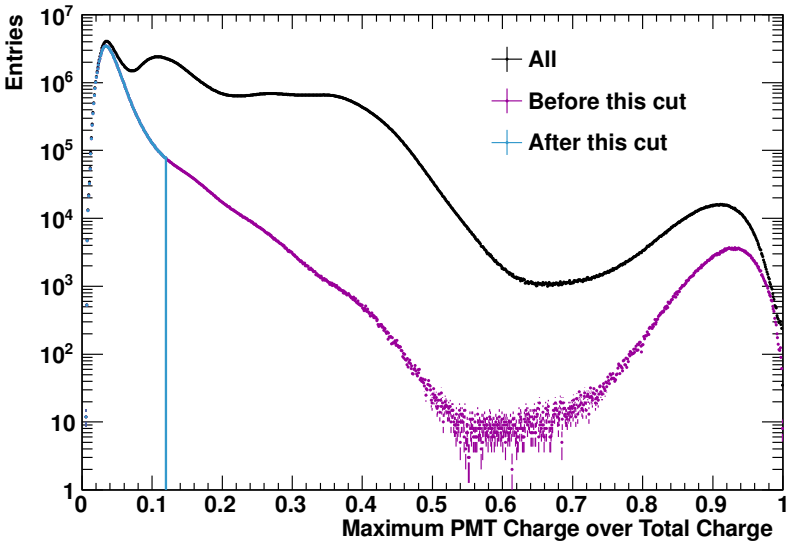

Figure 4.8: Maximum PMT Charge over Total Charge spectra. Data without any cuts are represented in black. Data when applying ΔQ cut and 2D cut on the PMT Charge RMS / PMT Time RMS plan are shown in magenta. These two cuts allow to keep 23.8 % of the total events. By applying then the Maximum PMT Charge over Total Charge cut, 3.9 % of this selection is then rejected (from magenta to blue). Physics data are therefore obtained by applying all light noise cuts and are shown in blue.

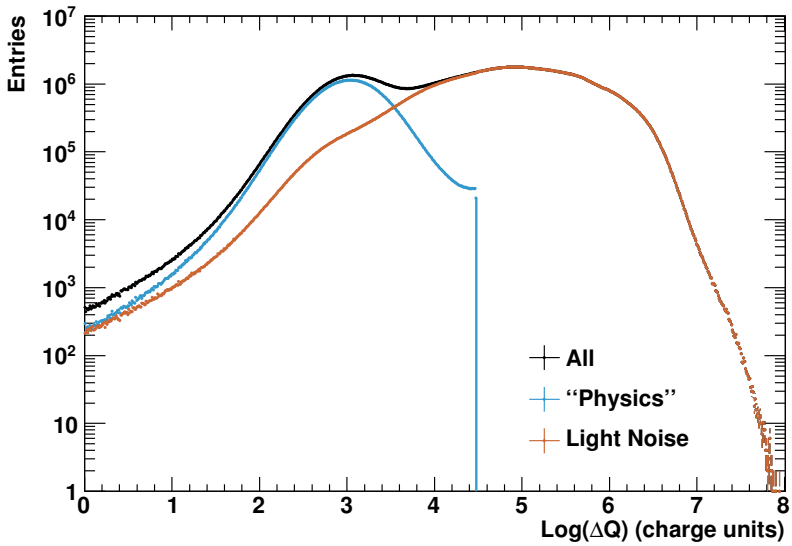

Figure 4.9: ΔQ spectra. Data without any cuts are represented in black. Physics data are obtained by applying light noise cuts and are shown in blue. Light noise data are shown in orange.

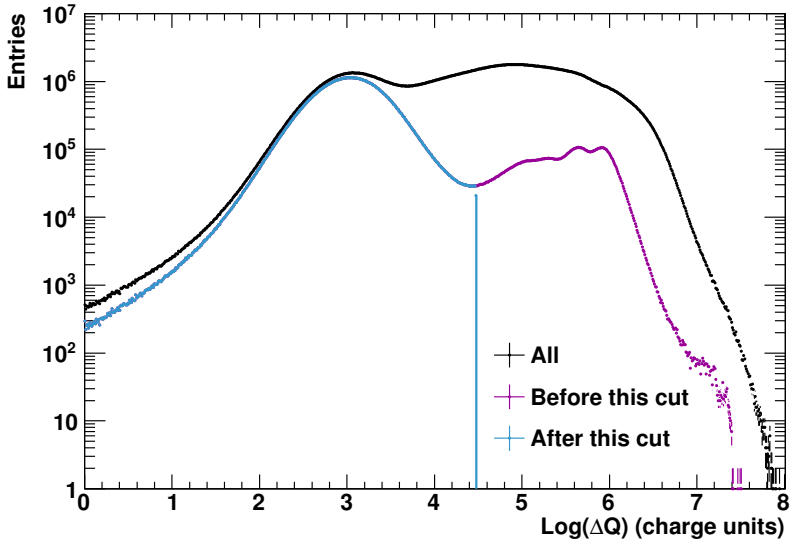

Figure 4.10: ΔQ spectra. Data without any cuts are represented in black. Data when applying Maximum PMT Charge over Total Charge cut and 2D cut on the PMT Charge RMS / PMT Time RMS plan are shown in magenta. These two cuts allow to keep 25.3 % of the total events. By applying then the ΔQ cut, 9.6 % of this selection is then rejected (from magenta to blue). Physics data are therefore obtained by applying all light noise cuts and are shown in blue.

Figure 4.7 shows the Q_{max}/Q_{tot} spectra for both physics and light noise events. This cut was relaxed to 0.12 w.r.t. the previous publications. Indeed, for the previous Gd analysis, this cut was required to be lower than 0.09 for prompt signals and lower than 0.055 for delayed signals in order to reject light noise events. For the H analysis, this cut was required to be lower than 0.09 for both prompt and delayed signals. Figure 4.8 shows the effect of the Q_{max}/Q_{tot} cut once both the 2D cut and the Q_{diff} cuts have been applied. This Q_{max}/Q_{tot} cut rejects 3.9 % of the pre-selection made by the 2D cut and the Q_{diff} cuts.

Figure 4.9 shows the Q_{diff} spectra for both physics and light noise events and Figure 4.10 shows the effect of the Q_{diff} cut once both the 2D cut and the Q_{max}/Q_{tot} cuts have been applied. This Q_{diff} cut rejects 9.6 % of the pre-selection made by the 2D cut and the Q_{max}/Q_{tot} cuts.

Applying all these light noise cuts brings out the fact that only 22.88 % of the total events are physics events. Table 4.1 summarizes the rejection power of the light noise cuts.

Table 4.1: Fraction events rejected when applying light noise cuts.

Cut	**Total rejection (cut alone)**	**Uncorrelated rejection**
$RMS(T_{start})/RMS(Q)$	67.8 %	42.5 %
Q_{max}/Q_{tot}	51.9 %	3.9 %
Q_{diff}	51.4 %	9.6 %

Figure 4.11 shows the number of hit channels when considering all the events and just the physics events. This plot suggests that it would be possible to apply an online cut in order to reduce the light noise contamination in the data. There are indeed several orders of magnitude difference between light noise and physics events when recording events which hit less than 30 channels.

We have also investigated the visible energy spectra as well as the event rate stability over time in order to confirm a good behavior of our light noise cuts. From the visible energy spectra on Figure 4.12, we can see that the Gd capture peak around 8 MeV as well as radioactive components spectra such as the ^{208}Tl around 2.6 MeV become visible once light noise events are rejected. The event rate stability is shown on Figure 4.13. Whereas the light noise rate increases since the starting of the data taking, the physics rate remains stable.

Light noise emission usually takes more than the 256 ns acquisition time window. When it lasts for a few microseconds, there is a non-trivial probability to trigger several light noise events, what we call "correlated light noise". Since light noise events are mainly low energy events, the Gd analysis does not suffer from this correlated light noise. It was not the case for the previous H analysis which had to take into account this additional background [41]. With the new set of light noise cuts, an investigation will be performed in this way.

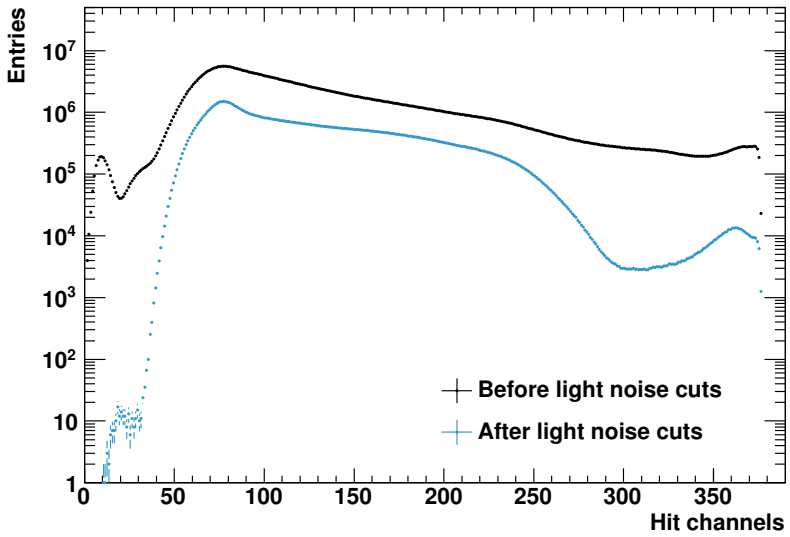

Figure 4.11: PMT Multiplicity spectra. Physics data (blue) have been obtained by applying light noise cuts on data (black).

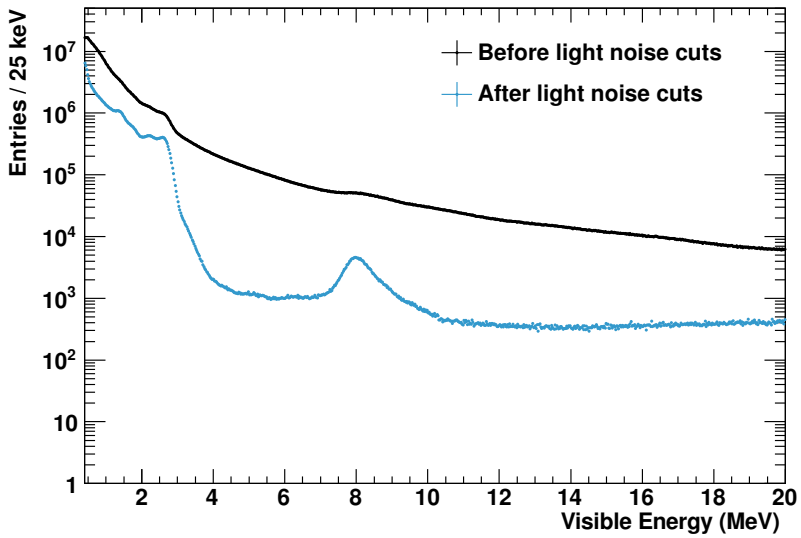

Figure 4.12: Visible energy spectra. Physics data (blue) have been obtained by applying light noise cuts on data (black).

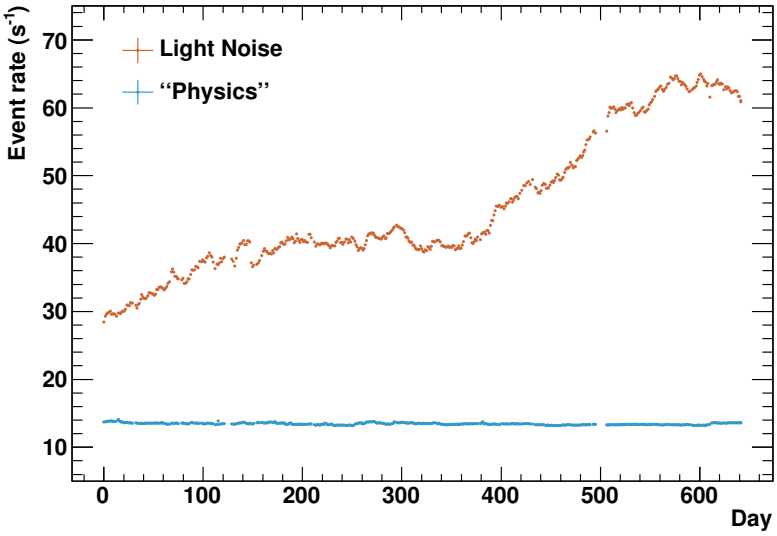

Figure 4.13: Event rate. Physics event rate (blue) and light noise event rate (orange) are shown.

4.4 Validation of the strategy

Three different investigations were handled and presented at Double Chooz meetings in order to validate the light noise strategy we developed.

4.4.1 Cross-check with calibration source

In order to validate the light noise strategy, we first investigated data taken during calibration campaigns. We focused in particular on the ^{252}Cf calibration source which was placed at different positions along the z-axis. As for general data, we applied the following set of cuts:

- Total charge in IV: $Q_{IV} < 30000$ charge units
- Visible energy in ID: $E_{vis} \in [0.4, 20$ MeV$]$

We required an additional space cut selecting only events contained in a 50 cm radius sphere around the source position.

Figure 4.14 shows the PMT Charge RMS vs PMT Time RMS spectra of ^{252}Cf calibration source along z-axis at $z = 0$ mm. We clearly see a separation between physics events on the left and light noise events on the right of the represented 2D cut. We can notice a spot around 200 charge units which corresponds to the neutron capture on Gd signal. We can also have a look at the visible energy spectra which is represented in Figure 4.15. Light noise events do not affect the Gd capture peak which stands around 8 MeV, they mainly live at very low energies. It is quite difficult to provide numbers on the inefficiency of these cuts since we do not know the light noise residual contamination.

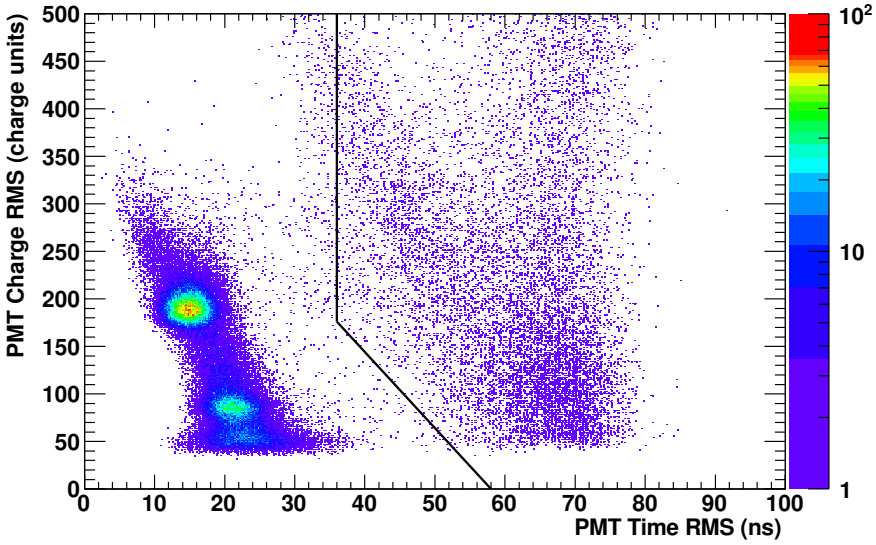

Figure 4.14: PMT Charge RMS vs PMT Time RMS spectra of ^{252}Cf calibration source along z-axis at $z = 0$ mm. No light noise cuts have been applied. The black line represents the 2D cut on the PMT Charge RMS / PMT Time RMS plan.

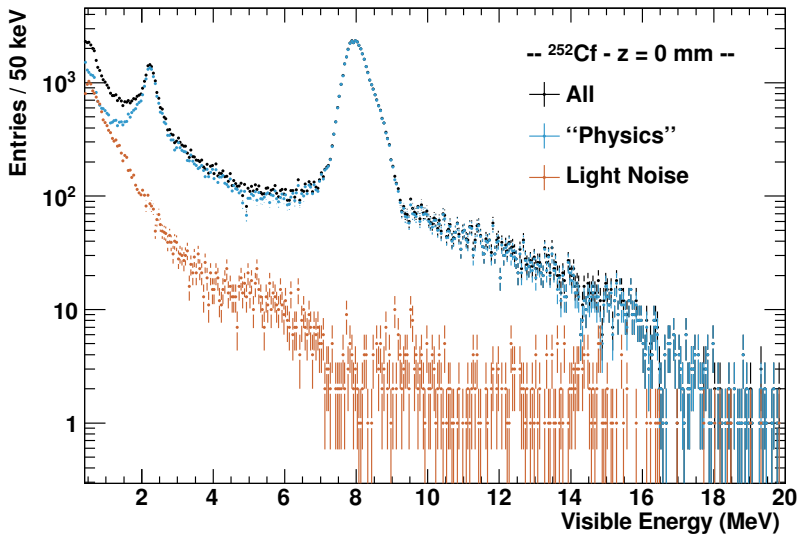

Figure 4.15: Visible energy spectra of ^{252}Cf calibration source along the z-axis at $z = 0$ mm. Physics data (blue) have been obtained by applying light noise cuts on run data (black).

4.4.2 Cross-check with MC

Using MC allows to cross-check our light noise strategy by providing inefficiency numbers. Since there is no light noise contamination, we deal only with physics events. This cross-check was done using pre-selected $\bar{\nu}_e$ candidates. This pre-selected $\bar{\nu}_e$ candidates sample fulfills the selection criteria described in Section 5.1.1 except for the ^{9}Li $+^{8}$He veto cut which was not applied. The multiplicity cut was also different, requesting no valid trigger in the 300 µs preceding and 900 µs following the prompt event, instead of 200 µs and 600 µs.

It was noticed that the MC distributions of the four light noise variables distribution were more or less shifted w.r.t. the data distributions. We applied a shift in order for the MC to match the data [129]. We ended with a negligible inefficiency of 0.01 %. Inefficiency numbers with and without shifts are provided in Table 4.2.

Table 4.2: MC inefficiency on pre-selected $\bar{\nu}_e$ candidates.

Cut	**Before shift**	**After shift**
$\mathrm{RMS(T_{start})/RMS(Q)}$	0.0000 %	0.0004 ± 0.0002 %
$\mathrm{Q_{max}/Q_{tot}}$	0.0004 ± 0.0002 %	0.0004 ± 0.0002 %
$\mathrm{Q_{diff}}$	0.0117 ± 0.0008 %	0.0118 ± 0.0008 %
Combined	0.0119 ± 0.0008 %	0.0124 ± 0.0008 %

4.4.3 Cross-check with special runs

A last step was to check whereas the light noise cuts would be able to correctly handle light noise from PMTs we know to be noisy. Since the beginning of the data taking, some PMTs were turned off in order to avoid light noise contamination on data. On September 13, 2011, dedicated runs with these PMTs turned back on were taken [130]. We used these runs to check if our cuts were able to handle the noisy PMTs issue.

Figure 4.16 shows the spatial distribution of the events for these dedicated runs before applying the light noise cuts. One can clearly see structures in the buffer, the γ-catcher and the target. It would almost be possible to identify the noisy PMTs from the position reconstruction of these structures. Figure 4.17 shows the same distributions after applying the light noise cuts. Only a few events remain reconstucted in the buffer. There is no more structure but a uniform distribution of the events. The success of the light noise cuts strategy brought the collaboration to decide to turn these PMTs back on.

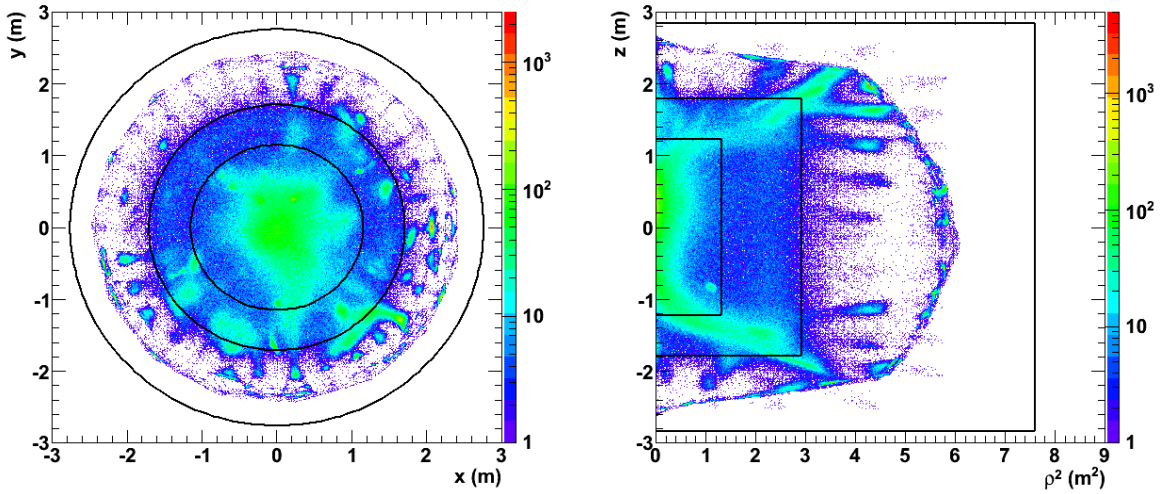

Figure 4.16: Distribution of the events on the xy plane (*left*) and on the $\rho^2 z$ plane (*right*) from the special runs dedicated to the light noise study. Light noise cuts are not applied. The black circles correspond to the target, γ-catcher and buffer.

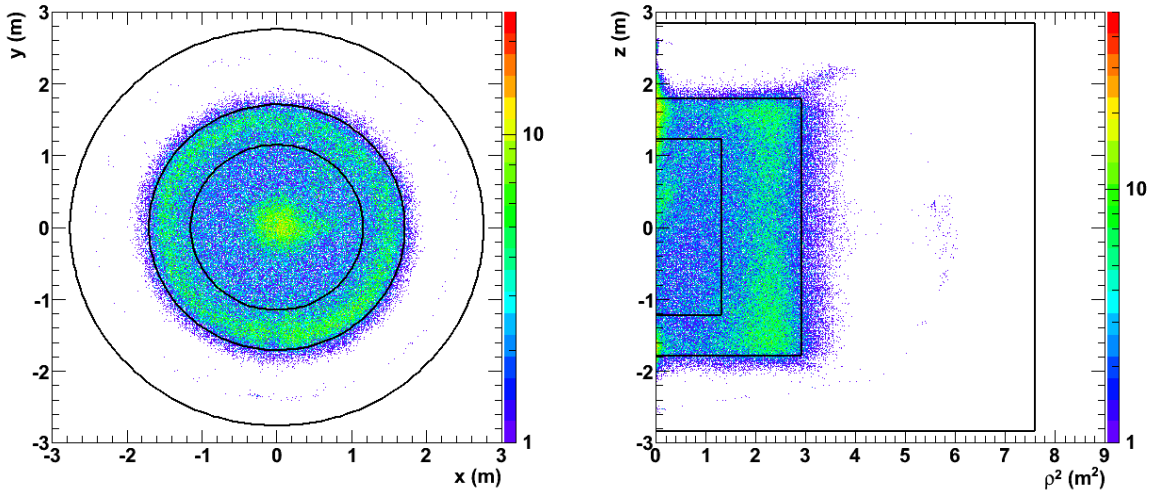

Figure 4.17: Distribution of the events on the xy plane (*left*) and on the $\rho^2 z$ plane (*right*) from the special runs dedicated to the light noise study, after applying the light noise cuts.

Chapter

5 Measuring θ_{13} with Double Chooz

Ce que tu fais en fait, c'est étudier la sexualité des neutrinos.
Bernard Roncin

Contents

Using two different data sets and three different methods, Double Chooz is able to provide several measurements of θ_{13}:

- Data sets:
  - Gd-capture sample: it corresponds to an Inverse Beta Decay (IBD) signal with neutron capture on Gd. This kind of events is limited to the target since it is the only vessel which contains Gd.
  - H-capture sample: it corresponds to an IBD signal with neutron capture on H. Both target and γ-catcher have to be considered in this case.

- Methods:
  - Rate-only analysis which focus only on the difference of the number of events between the prediction and the measurement.

- Rate and spectral shape analysis which takes into account both the rate of the $\bar{\nu}_e$ candidates as well as the spectral shape information. It brings constraints on systematic uncertainties and θ_{13}.
- Reactor Rate Modulation (RRM) which is based on a fit to the observed rate of the $\bar{\nu}_e$ candidates as a function of the prediction.

5.1 Neutrino selection

Analysis cuts differ among the data set used but a set of general cuts remains common. First of all, the events to be considered have to be valid triggers. It means that they can not be random trigger, muon events or light noise events. Events are tagged as muon events if the visible energy in the inner detector is larger than 20 MeV or if the charge collection in the inner veto is larger than 30000 charge units. A 1 ms dead time window is applied after a muon event before considering a new event, in order to reduce the cosmogenic background [131]. Light noise events are rejected by applying the cuts which were described in the previous chapter. A visible energy cut is also applied, throwing out events with a visible energy below 0.4 MeV, since the trigger efficiency is not 100 %.

5.1.1 Gd-capture sample selection

The Gd analysis looks for IBD signals with neutron capture on Gd. We run over 460.67 days of live time where at least one reactor was on and over 7.24 days of live time with two reactors off. Figure 5.1 illustrates the neutrino candidates rate per day of data taking. Prediction and observation are matching, following the nuclear reactors power history.

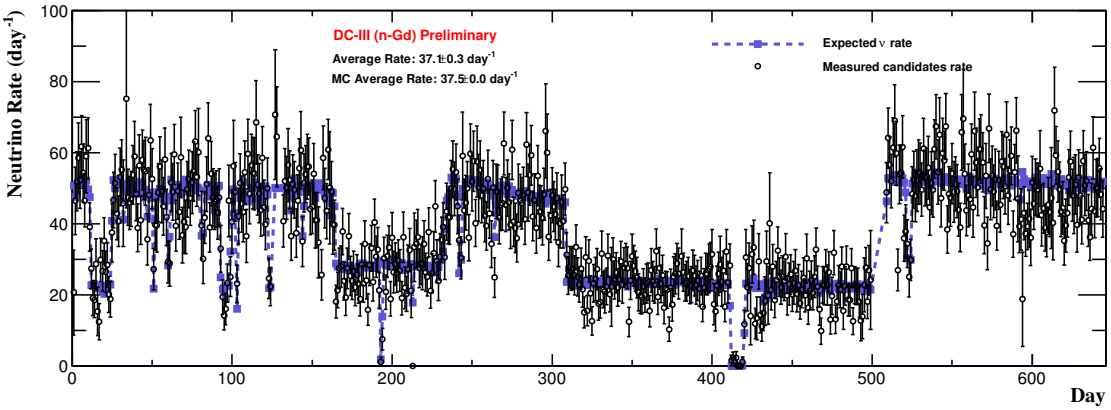

Figure 5.1: Neutrino candidates rate per day of data taking. Empty dots show data with backgrounds not subtracted whereas the dashed line shows the MC prediction.

Multiplicity cut

In order to reduce the correlated background, multiplicity cuts are applied. For the Gd analysis, it consists in rejecting candidates which hold a valid trigger in the 200 μs preceding and 600 μs following the prompt signal.

Prompt energy cut

The prompt signal corresponds to the scintillation and annihilation of the positron with an electron. The visible energy of the prompt signal has to satisfy:

- $0.5 < E_{vis} < 20$ MeV

At 0.5 MeV, the trigger efficiency is already 100 % with a negligible uncertainty [132]. This lower cut allows to keep low energy events useful for the spectrum shape whereas the upper cut allows a better constraint on the fast neutron and stopping muon (FN+SM) component [133].

Delayed energy cut

The delayed signal corresponds to the neutron capture on Gd which leads to a visible energy release of about 8 MeV. The visible energy of the delayed signal has to satisfy:

- $4 < E_{vis} < 10$ MeV

For the Gd analysis, the upper cut has been set to 10 MeV since there is a negligible contribution of IBD events above this value. The lower cut has been set by comparing signal efficiency and contamination of accidental background. Going below 4 MeV is not reasonable because of the radioactivity contamination. This lower cut allows to maximize the detection efficiency and to keep the accidental background rate below 0.1 event per day [134].

Coincidence cuts

Coincidence cuts between prompt and delayed signals are the strength of the selection. The time difference between the prompt and delayed signals is set to take into account the neutron thermalization before being captured on Gd. The capture time is around 30 μs for a neutron capture on Gd. The distance between the vertex positions of the prompt and delayed signals can also be set, which leads to the following coincidence cuts:

- $0.5 < \Delta T < 150$ μs
- $\Delta R < 100$ cm

The upper ΔT cut has been optimized in order to keep an efficiency close to 100 % [135]. It also suppress systematic uncertainty on spill-in and spill-out effects [136]. The ΔR cut provides an IBD signal inefficiency of 0.3 % and allows to reduce the accidental background by a factor seven in comparison with no ΔR cut [137].

Additional cuts

In order to further reduce the background contamination, several additional cuts were developped w.r.t. the analysis performed in [40].

F_V veto cut When reconstructing the vertex position of an event, the vertex position reconstruction algorithm gives a variable called F_V. It corresponds to the minimized negative log-likelihood which is given in equation (3.16). F_V remains small when reconstructing point-like events but becomes large for events which have different hit pattern such as stopping muons. We use it only on delayed signals as follows:

- $E_{vis} > 0.068 \times \exp(F_V/1.23)$

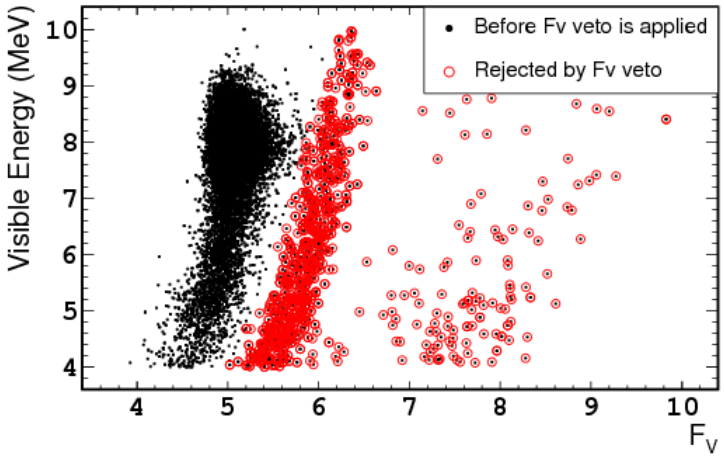

Figure 5.2: Correlations between the F_V variable and the visible energy for the delayed signals. Black points show the data before the cut, and red circles on top of the black points the rejected events after the cut.

This variable helps to discriminate stopping muons as well as remaining light noise. Indeed, the variable becomes larger if the light source does not match a point-like energy deposition, rejecting most of the stopping muons. Figure 5.2 shows the correlation which exists between the variable and the visible energy. The red circles illustrates the events rejected by the cut. The red shape corresponds to the stopping muon component whereas the events at higher F_V correspond to remaining light noise events. Before using this variable, a study pointed out an increase of the accidental background rate. It has been shown that this increase was due to the emission of light noise from PMT #263. Applying light noise cuts did not allow to remove it whereas the F_V veto cut did, leading to the back of a stable accidental background rate.

With this powerful tool, it has been decided to lower the ΔT cut used in [40] from 2 µs to 0.5 µs. At that time, asking ΔT to be lower than 2 µs would bring additional systematic

uncertainty due to the stopping muons contamination, which is not anymore the case.

Inner Veto (IV) veto cut Whereas the IV was used only to tag mainly fast neutrons in [40], it is used as a veto for this analysis. Events which satisfy the following criteria are rejected [138]:

- IV PMT multiplicity ≥ 2
- Total charge in IV > 400 charge units
- $-110 < \Delta t_{\text{ID-IV}} < -10$ ns
- $\Delta d_{\text{ID-IV}} < 3.7$ m

$\Delta t_{\text{ID-IV}}$ corresponds to the time difference between recorded signals in the ID and the IV. $\Delta d_{\text{ID-IV}}$ corresponds to the distance between the vertices position reconstruction calculated in the ID and in the IV. The new IV vertex position reconstruction algorithm is based on a neural network approach [139]. Since neutron capture on Gd leads to high energetic γ which can cross the whole ID to interact in the IV, the IV veto is only applied on prompt signals.

Outer Veto (OV) veto cut As for the IV veto cut, the OV veto cut is only applied on prompt signals. The coincidence with an OV trigger causes the rejection of the event.

^{9}Li + ^{8}He veto cut Here again, the ^{9}Li + ^{8}He veto cut is only applied on prompt signals. A dedicated likelihood function has been developed which takes into account the distance between the vertex position reconstruction of the event and the last muon track position as well as the number of neutrons following the muon within 1 ms. Events which satisfy the following criterium are rejected:

- ^{9}Li + ^{8}He likelihood > 0.4

The ^{9}Li + ^{8}He veto cut allows to reject 1.12 ± 0.05 events per day, *i.e.* 55 % of the ^{9}Li + ^{8}He background expectation. Energy spectrum as well as ΔT distribution of the rejected events are consistent with the behavior of ^{9}Li + ^{8}He candidates. A summary of the inefficiency of IBD signals due to these additional cuts are shown in Table 5.1.

Table 5.1: Inefficiency of IBD signals.

Cut	Inefficiency
F_V	0.06 ± 0.11 %
IV veto	0.058 ± 0.001 %
OV veto	0.035 ± 0.014 %
^{9}Li + ^{8}He veto	0.504 ± 0.018 %

A tremendous work on the background reduction has been done since the previous publication [40]. The F_V cut, the IV veto cut, the OV veto cut and the $^9Li + ^8He$ veto cut allow to considerably reduce the background w.r.t. the previous analysis.

Figure 5.3 (*left*) shows the prompt energy spectrum using two different selection methods and the ratio between them. The yellow histogram represents the selection from the previous analysis [40] and the black points the one from this new analysis [42]. One can appreciate the reduction of the fast neutron and stopping muon components at high energy, as well as the reduction of the accidental component at low energy. Figure 5.3 (*right*) illustrates the different vetoes behavior. The F_V cut, OV veto and IV veto are rejecting respectively 71 %, 64 % and 24 % of the events above 12 MeV, range we know to be free of $\bar{\nu}_e$. Together, these three sets of cuts allow to reject 90 % of these high energy events.

Figure 5.4 (*left*) shows the delayed energy spectrum. Background reduction w.r.t. the selection from [40] is visible below 5.5 MeV and above 9 MeV. Figure 5.4 (*right*) indicates that, here again, the F_V veto and the OV veto are the vetoes which reject the most of events.

Figure 5.5 (*left*) shows the correlation time distribution between the prompt and delayed signals. The ratio between the two selection methods appears to be low at low ΔT. This is due to the reduction of the stopping muon component. The accidental component is also reduced at higher ΔT. Figure 5.5 (*right*) allows to observe a special behavior of the events rejected by the $^9Li + ^8He$ veto. In the previous analysis [40], a longer cut after energetic muons was applied, resulting in an increase of 4.8 % of the dead time. This strategy has been removed in this new analysis [42], replacing it by a likelihood-based cut. The ΔT distribution we can observe from this veto is consistent with the expectation.

Table 5.2: Predicted values of neutrino and background signals in absence of neutrino oscillation.

Source	**Reactor-on**	**Reactor-off**
Neutrinos	17530 ± 320	1.57 ± 0.47
$^9Li + ^8He$	447^{+189}_{-74}	$7.0^{+3.0}_{-1.2}$
FN + SM	278 ± 23	3.83 ± 0.64
Accidentals	32.3 ± 1.2	0.508 ± 0.019
Total	18290^{+370}_{-330}	$12.9^{+3.1}_{-1.4}$

This active background rejection allows to increase the signal over background ratio from 15.6 to 22. With this selection, we end with 17351 neutrino candidates when considering reactor-on periods only. 7 additional neutrino candidates come from the reactor-off period. These 17358 neutrino candidates are below the prediction of 18290^{+370}_{-330} neutrino candidates when taking into account the background and considering an absence of neutrino oscillation. Table 5.2 summarizes the observed and predicted values of neutrino and background signals.

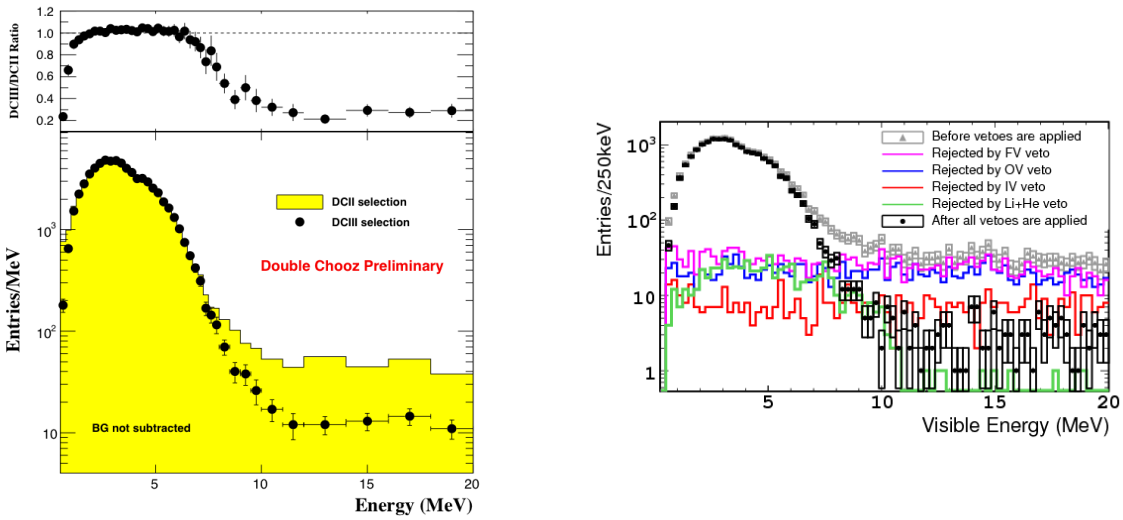

Figure 5.3: (*left*) Visible energy distribution of the prompt signals using selection made in [40] and this selection. (*right*) Visible energy distribution of the prompt signals for this analysis. Points and boxes show the data with their statistical uncertainty before (grey, triangle) and after (black, circle) all analysis vetoes are applied.

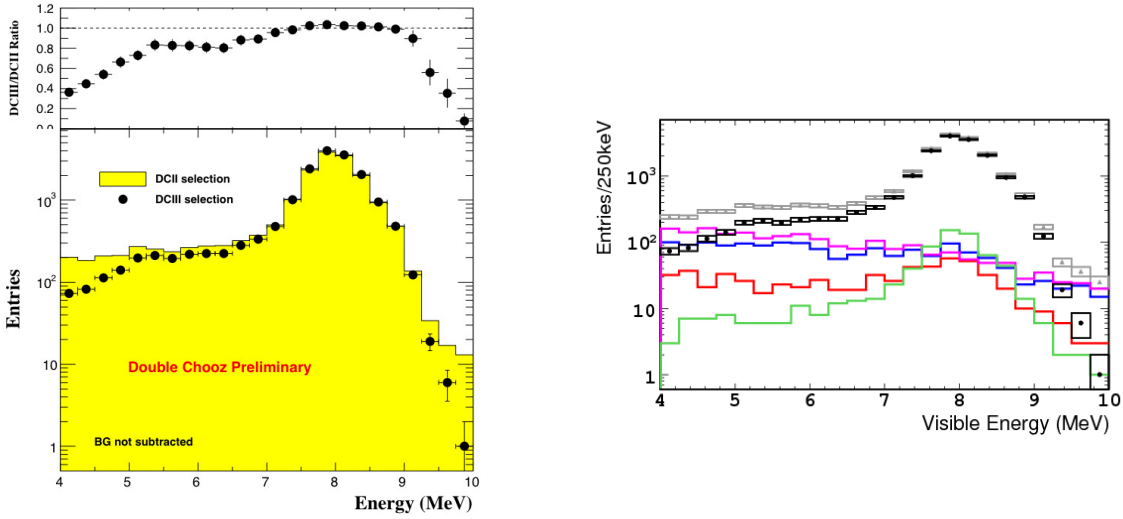

Figure 5.4: (*left*) Visible energy distribution of the delayed signals using selection made in [40] and this selection. (*right*) Visible energy distribution of the delayed signals for this analysis. Points and boxes show the data with their statistical uncertainty before (grey, triangle) and after (black, circle) all analysis vetoes are applied.

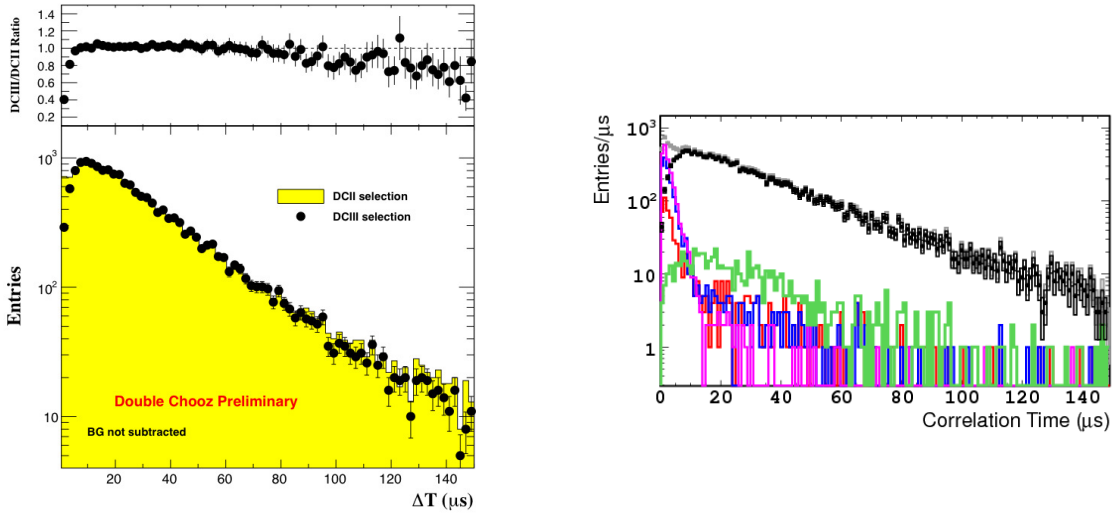

Figure 5.5: (*left*) Correlation time of the prompt and delayed signals using selection made in [40] and this selection. (*right*) Correlation time of the prompt and delayed signals for this analysis. Points and boxes show the data with their statistical uncertainty before (grey, triangle) and after (black, circle) all analysis vetoes are applied.

5.1.2 H-capture sample selection

IBD signals with neutron capture on H have also been investigated in order to provide an independent measurement of θ_{13}. Systematic uncertainties as well as background characteristics differ from the Gd analysis. Since there is no special need to restrict the volume investigation to the target, IBD signals which take place in the γ-catcher have also been taken into account. Nevertheless, due to the presence of Gd in the target, only 13 % of the IBD interations in the target are followed by a neutron capture on H. It results that 95 % of the investigated $\bar{\nu}_e$ candidates come from the γ-catcher [41].

For this analysis, we run from April 13, 2011, to March 15, 2012, for a live time of 240.1 days. The live time is a bit different from the 227.9 days live time used in [40] since we use different analysis cuts. This live time is also two times less than the live time used in [42] since this analysis was performed with an older data set. An analysis running over the same period than [42] is on-going. Figure 5.6 illustrates the neutrino candidates rate per day of data taking.

First of all, the reader must be aware that the light noise strategy used in this H analysis differs from the one we explained in the previous chapter. The variables which take into account the charge deposition were not yet developed at that time. The light noise cuts used in this H analysis are:

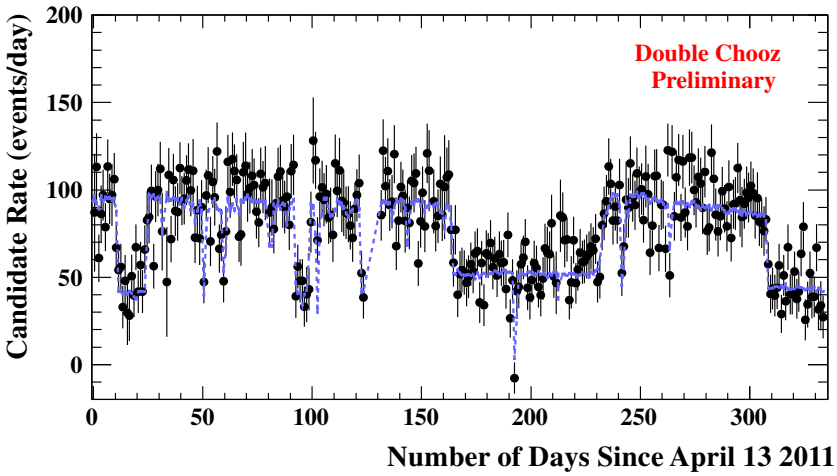

Figure 5.6: Neutrino candidates rate per day of data taking. Black dots show data with accidental background substracted whereas the dashed line shows the MC prediction.

- $RMS(T_{start}) < 40$ ns
- $Q_{max}/Q_{tot} < 0.09$

$RMS(T_{start})$ corresponds to the standard deviation of the distribution of the PMTs hit time, Q_{max} is the maximum charge recorder by a PMT for a given event and Q_{tot} is the total charge of this event. It was shown in the previous chapter why these cuts have been replaced by the ones we are using today.

As for the Gd analysis, a multiplicity cut has been applied, requiring no trigger neither in the 600 µs before the prompt signal nor in the 1000 µs following the prompt signal, except the delayed signal. The visible energy of the prompt candidate is required to stand in the range [0.7, 12.2 MeV] and the visible energy of the delayed candidate in the range [1.5, 3.0 MeV] since the neutron capture on H produces a characteristic 2.2 MeV γ ray. Concerning the coincidence cuts, both time and distance cuts between the prompt and delayed signals are applied. The delayed signal should happen in the range [10, 600 µs] after the prompt signal and the distance between them can not exceed 90 cm.

Figure 5.7 shows the correlation time and the correlation distance of the prompt and delayed signals. Even with a correlation distance cut fixed at 90 cm, an important contamination comes from the accidental background. A tremendous work is going on in order to reduce this accidental background for the next publication.

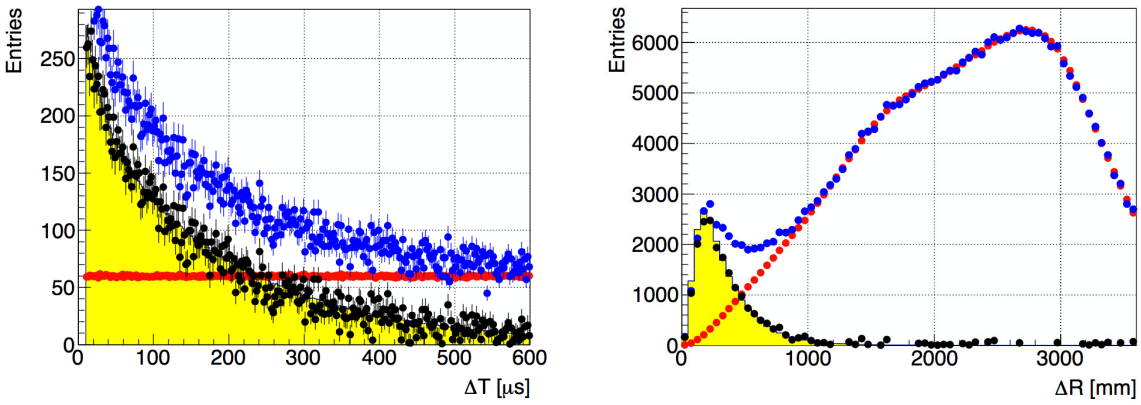

Figure 5.7: Correlation time (*left*) and correlation distance (*right*) of the prompt and delayed signals, from [140]. The red points correspond to the off-time spectrum, *i.e.* the accidental spectrum, the blue points to the on-time spectrum, and the black points denote the off-time subtracted spectrum. The yellow histogram is the MC spectrum.

5.2 Systematic uncertainties

Except for the reactor $\bar{\nu}_e$ rate uncertainties, the Gd and H-capture samples have to deal with different systematics uncertainties since the Gd analysis runs on target events only whereas the H analysis runs on both target and γ-catcher events. The reactor flux uncertainty is summarized in Table 5.3. The uncertainty on the fractional fission rate of the ^{238}U $\bar{\nu}_e$ rate decreased between the release of the H analysis [41] and the release of the new Gd analysis [42] due to a new method explained in Section 3.1.1.

Table 5.3: Reactor $\bar{\nu}_e$ rate uncertainties.

Source	**Uncertainty (%)**
Bugey-4 measurement	1.4
Fractional fission rate of each isotope	0.8 (Gd) / 0.9 (H)
Thermal power	0.5
IBD cross section	0.2
Mean energy released per fission	0.2
Distance to reactor core	< 0.1

5.2.1 Gd-capture systematics

Selection cuts are optimized in order to provide a high efficiency detection together with a low background contamination. Whereas the prompt signal detection efficiency is close to 100 % thanks to a low dead time data acquisition system and a high trigger efficiency, one has to more carefully investigate the delayed signal detection efficiency. Systematics on the neutron

detection efficiency were investigated using neutrino candidates as well as ^{252}Cf calibration source. Data were then compared to MC in order to extract the correction factor which holds three independent contributions:

$$c = c_{\text{Gd}} \times c_{\text{IBD}} \times c_{\text{Spill-in/out}}, \tag{5.1}$$

where c_{Gd} corrects for the Gd fraction, c_{IBD} for the selection efficiency and $c_{\text{Spill-in/out}}$ for the spill-in/out effects.

Gd fraction systematic uncertainty

In the target, neutrons can be mainly captured on Gd or H. The proportion of neutron captures on Gd, f_{Gd}, depends on the Gd concentration in the liquid scintillator. This is estimated using a ^{252}Cf calibration source. Spontaneous fissions of ^{252}Cf lead to the emission of γ and 3.8 neutrons in average [141]. γ and neutrons are respectively recorded as prompt and delayed signals. We investigated the ratio of the number of neutron captures on Gd with the combined number of neutron captures on Gd and H from the delayed energy spectrum:

$$f_{\text{Gd}} = \frac{N(\text{Gd})}{N(\text{Gd+H})} = \frac{N(3.5 < \text{E}_{\text{vis}} < 10 \text{ MeV})}{N(0.5 < \text{E}_{\text{vis}} < 10 \text{ MeV})} \tag{5.2}$$

Whereas the numerator should contain only neutron captures on Gd and a small fraction of neutron captures on C, the denominator holds neutron captures on H in addition. Background contamination is removed by requesting the prompt visible energy to stand above 4 MeV and to have more than one neutron detected after the prompt signal.

Gd fraction has been measured to be 85.30 ± 0.08 % for the data and 87.49 ± 0.04 % for the MC. The Gd fraction correction factor is then:

$$c_{\text{Gd}} = \frac{f_{\text{Gd}}^{\text{Data}}}{f_{\text{Gd}}^{\text{MC}}} = 0.9750 \pm 0.0011\,(\text{stat}) \pm 0.0041\,(\text{syst}) \tag{5.3}$$

Selection efficiency

The goal here is to provide a normalization factor between data and MC in order to ensure that the selection efficiency in MC matches the one in data. Cuts are simultaneously evaluated in an inclusive way. It allows to account for possible correlation between them. The correction factor for the selection efficiency has been calculated using two different methods. The first one uses ^{252}Cf calibration source and the second one neutron capture signals from the neutrino candidates.

Efficiency from ^{252}Cf calibration source Efficiency of neutron capture signals has been measured using a ^{252}Cf calibration source deployed at different positions along the z-axis. Since we do not yet have the articulated arm, we can not deployed calibration source in the (x, y) plane of the target. The ρ-dependence of the efficiency has then be handled by assuming it to be the same as the z-dependence. This approximation has been investigated through a

dedicated MC study [142].

The efficiency of neutron capture signals is defined as:

$$\epsilon_{\text{IBD}} = \frac{N\,(0.5 < \Delta\text{T} < 150\ \mu\text{s}\ \cap\ 4 < \text{E}_{\text{vis}} < 10\ \text{MeV}\ \cap\ \Delta\text{R} < 1\ \text{m})}{N\,(0.25 < \Delta\text{T} < 1000\ \mu\text{s}\ \cap\ 3.5 < \text{E}_{\text{vis}} < 10\ \text{MeV})}, \tag{5.4}$$

where N corresponds to the number of selected events.

This efficiency definition depends on both z and ρ:

$$\epsilon(z,\rho) = \epsilon_0 \times f_1(z) \times f_2(\rho), \tag{5.5}$$

where ϵ_0 stands for the efficiency at the target center and $f_1(z)$ and $f_2(\rho)$ for the spatial dependence functions.

Over the whole target volume, the averaged efficiency has been found to be 98.29 ± 0.06 % for the data and 98.26 ± 0.03 % for the MC. The correction factor corresponds to the ratio between averaged efficiency of data and MC:

$$c_{\text{IBD}} = \frac{\epsilon_{\text{IBD}}^{\text{Data}}}{\epsilon_{\text{IBD}}^{\text{MC}}} = 1.0003 \pm 0.0032 \tag{5.6}$$

Efficiency from neutrino candidates Since neutrino candidates are homogeneously distributed in the whole target volume, the measurement of the efficiency takes into account the ρ dependence. Nevertheless, we have to deal with a lower statistics and a higher background contamination in comparison to the ^{252}Cf method. In order to reduce this background contamination, stronger cuts were applied to the prompt candidates, in addition to the usual cuts:

- $0.5 < \text{E}_{\text{vis}} < 8$ MeV
- $\text{F}_{\text{V}} < 5.8$

Accidental background contamination was also removed by using the off-time window method. The efficiency of neutron capture signals in this case is defined as:

$$\epsilon_{\text{IBD}} = \frac{N\,(0.5 < \Delta\text{T} < 150\ \mu\text{s}\ \cap\ 4 < \text{E}_{\text{vis}} < 10\ \text{MeV}\ \cap\ \Delta\text{R} < 1\ \text{m})}{N\,(0.25 < \Delta\text{T} < 200\ \mu\text{s}\ \cap\ 3.5 < \text{E}_{\text{vis}} < 10\ \text{MeV}\ \cap\ \Delta\text{R} < 1.7\ \text{m})}, \tag{5.7}$$

where N corresponds to the number of selected events.

Efficiencies have been measured to be 98.58 ± 0.19 % for the data and 98.62 ± 0.02 % for the MC. Figure 5.8 shows the efficiency maps for data and MC. By comparing data and MC, we can access the correction factor:

$$c_{\text{IBD}} = \frac{\epsilon_{\text{IBD}}^{\text{Data}}}{\epsilon_{\text{IBD}}^{\text{MC}}} = 0.9996 \pm 0.0021 \tag{5.8}$$

The correction factor to the MC normalization is calculated from a combination of the ones found with the two methods:

$$c_{\text{IBD}} = 1.0000 \pm 0.0019 \tag{5.9}$$

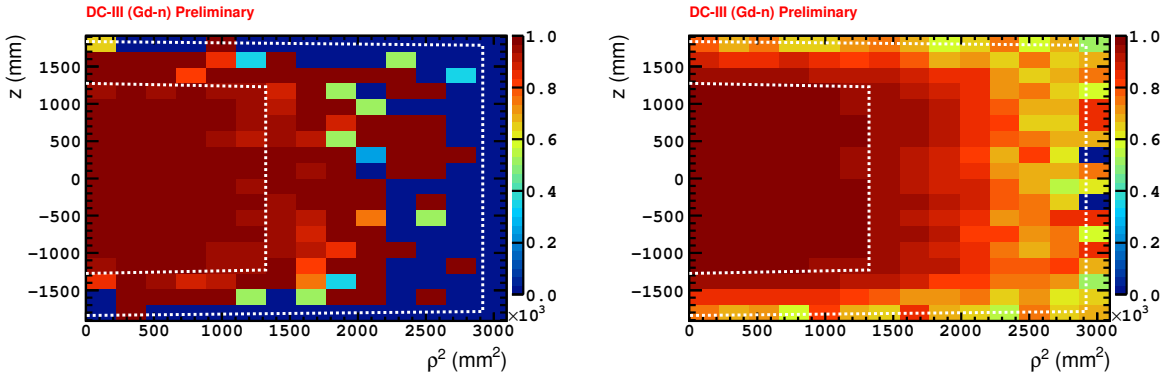

Figure 5.8: Efficiency maps for data (*left*) and MC (*right*).

Spill-in/out systematic uncertainty

Since the target volume is finite, one can expect edge effects. The positron signal can for instance take place in the γ-catcher whereas the neutron can cross the acrylic and be captured in the target. This feature is called spill-in effect. *A contrario*, when the prompt signal takes place in the γ-catcher and the delayed signal in the target, this is called spill-out. These effects do not cancelled and affect the prediction of the number of detected interactions. We can define the spill current as [143]:

$$\Phi_{\text{Spill-in/out}} = \frac{1}{N_{\bar{\nu}_e}^{\text{target}}} \times \left(\frac{N_{\text{Spill-in}}^{\text{det}} + N_{\text{Spill-out}}^{\text{det}}}{\epsilon_{\text{IBD}}} - N_{\text{Spill-out}} \right), \tag{5.10}$$

where $N_{\bar{\nu}_e}^{\text{target}}$ is the number of IBD interactions in the target volume, $N_{\text{Spill-in}}^{\text{det}}$ the number of detected spill-in events, $N_{\text{Spill-out}}^{\text{det}}$ the number of detected spill-out events where the neutron is captured on ^{12}C in the γ-catcher, ϵ_{IBD} the efficiency of neutron capture signals using neutrino candidates as defined previously and $N_{\text{Spill-out}}$ the number of spill-out events.

The net spill current has been found to be 2.08 % from the NeutronTH-Geant4 model and 2.36 % from the Tripoli model. Whereas NeutronTH-Geant4 includes molecular bonds from analytical calculation, Tripoli uses experimental data. The systematic uncertainty on spill-in/out effects comes from this discrepancy. The correction factor has been found to be:

$$c_{\text{Spill-in/out}} = 1.0000 \pm 0.0027 \tag{5.11}$$

Summary of Gd-capture systematics

The final correction factor to be applied is given by equation (5.1) as a combination of the three correction factors we investigated:

$$c = 0.9750 \pm 0.0053 \tag{5.12}$$

Table 5.4 summarizes the input for the MC correction factor as well as the fractional uncertainties. The selection correction factor is different from the one reported in equation (5.9) since it takes into account inefficiencies due to multiplicity and light noise cuts. Table 5.5

summarizes the uncertainties on signal and backgrounds to the MC normalization.

Table 5.4: Correction factors to the MC normalization.

Source	Correction factor	Uncertainty (%)
DAQ & Trigger	1.000	< 0.1
Veto after muons	0.955	< 0.1
F_V, IV, OV, ^{9}Li + ^{8}He	0.993	0.1
Proton number	1.000	0.3
Gd fraction	0.975	0.4
Selection	0.989	0.2
Spill-in/out	1.000	0.3
Total	0.915	0.6

Table 5.5: Signal and backgrounds uncertainties to the MC normalization. Gd-III/Gd-II represents the evolution of the uncertainty between this publication [42] and the previous one [40].

Source	Uncertainty (%)	Gd-III/Gd-II
Reactor $\bar{\nu}_e$ rate	1.7	1.0
Detection efficiency	0.6	0.6
^{9}Li + ^{8}He background	+1.1, -0.4	0.5
FN + SM background	0.1	0.2
Statistics	0.8	0.7
Total	+2.3, -2.0	0.8

5.2.2 H-capture systematics

In order to evaluate the fraction of neutron captures on H within the selection criteria on the delayed visible energy, E_{delayed}, the correlation time, ΔT, and the correlation distance, ΔR, calibration runs using a ^{252}Cf radioactive source have been investigated. It allows to evaluate biases in the neutron selection criteria and to estimate their contribution to the systematic uncertainties.

Since the H analysis considers not only the target but also the γ-catcher, the neutron detection efficiency has to be estimated in these two different volumes. While ^{252}Cf can be inserted in the target using the Z-Axis Deployment System (ZADS), one can use the Guide Tube (GT) to deploy the source inside the γ-catcher. The H-capture fraction was found to be 0.1342 $\pm$ 0.0015 in the target and 0.983 $\pm$ 0.003 in the γ-catcher. Table 5.6 summarizes the neutron detection efficiency.

Table 5.6: Efficiencies from ^{252}Cf radioactive source deployment in taget and γ-catcher.

Efficiency	Target	γ-catcher
H-capture fraction	0.1342 ± 0.0015	0.983 ± 0.003
$\epsilon_{E_{\text{delayed}}}$	0.9679 ± 0.0028	0.9220 ± 0.0021
$\epsilon_{\Delta T}$	0.6955 ± 0.0124	0.9041 ± 0.0015
$\epsilon_{\Delta R}$	0.9361 ± 0.0048	0.9584 ± 0.0018
Total	0.0846 ± 0.0018	0.7853 ± 0.0036

The systematic uncertainty in the detection efficiency over the whole volume has been estimated to 1.0 %. A spill-in/out effect has also been taken into account, with a systematic uncertainty of 1.2 %. Adding in quadrature these two systematic uncertainties leads to a total detection efficiency uncertainty of 1.6 %. An energy scale systematic uncertainty has also been investigated. One has to take into account the time variation, the non-linearity and the non-uniformity in the detector response. While the two first effects have been treated in the same way that [40], the third effect has to be more investigated due to the use of both the target and the γ-catcher volumes. The energy scale systematic uncertainty has been estimated to 1.7 %. Table 5.7 summarizes the uncertainties on signal and background to the MC normalization.

Table 5.7: Signal and background uncertainties to the MC normalization.

Source	Uncertainty (%)
Reactor $\bar{\nu}_e$ rate	1.8
Detection efficiency	1.6
Energy scale	0.3
^{9}Li + ^{8}He background	1.6
FN + SM background	0.6
Accidental background	0.2
Light Noise	0.1
Statistics	1.1
Total	3.1

5.3 Reactor-off data analysis

Double Chooz has the unique opportunity to deal with periods where the two nuclear reactors can be simultaneously off. Having reactor-off data is a real chance to measure the backgrounds. 7.24 days live time of reactor-off data taken in two different periods have been

investigated using a Gd-capture analysis.

5.3.1 Signal prediction

It is not because the reactors are off that they do not still emit $\bar{\nu}_e$. One has to remember that the $\bar{\nu}_e$ are created from the β^- decay of fission products inside the reactors, which are still present even if the nuclear chain reaction is stopped. This residual power is responsible for about 6 % of the total initial power just after the shutdown and exponentially decay because of the fission product exponential decays later on.

The way we are calculating the expected number of $\bar{\nu}_e$ for the θ_{13} analysis relies on the fission rate, as seen in Section 3.1.1. We then have to evaluate the residual emission spectrum using another method. It has been done using a dedicated simulation performed with FISPACT, which is in charge to solve the Bateman equations, together with a spectrum computation performed with BESTIOLE [43].

Even if most of the fission products have a lifetime of the order of a few minutes or a few hours, others can have a longer lifetime, of the order of days. This kind of fission products will then continue to produce $\bar{\nu}_e$ during an off period. We remind that these $\bar{\nu}_e$ can interact in the detector only if they have an energy higher than 1.806 MeV as calculated in equation (3.6). Two fission products fulfill these criteria, the ^{106}Ru and ^{144}Ce decay series:

$$^{106}\mathrm{Ru} \xrightarrow[371.8\ \mathrm{days}]{\beta^-} {}^{106}\mathrm{Rh} \xrightarrow[30.1\ \mathrm{sec}]{\beta^-(3.5\ \mathrm{MeV})} {}^{106}\mathrm{Pd} \tag{5.13}$$

$$^{144}\mathrm{Ce} \xrightarrow[284.9\ \mathrm{days}]{\beta^-} {}^{144}\mathrm{Pr} \xrightarrow[17.3\ \mathrm{min}]{\beta^-(3.0\ \mathrm{MeV})} {}^{144}\mathrm{Nd} \tag{5.14}$$

The amount of short lifetime fission products remains stable when the reactor is running whereas long lifetime fission products such as ^{106}Ru or ^{144}Ce accumulate in the reactor. Because of its long lifetime and thanks to the fact that it emits $\bar{\nu}_e$ which can later on be detected, ^{144}Ce is an excellent candidate for investigating a possible new neutrino oscillation at short baseline.

The amount of remaining $\bar{\nu}_e$ was found to be 1.57 $\pm$ 0.47. The signal prediction is then a sum of these remaining $\bar{\nu}_e$ together with the background model. For the period considered, one should expect $12.93^{+3.07}_{-1.41}$ events.

5.3.2 Reactor-off measurement

The neutrino selection applied for this reactor-off period led to 54 events before applying background vetoes. Once applying those vetoes, we are left with 7 candidates, which corresponds to a 9.0 % ($1.7\,\sigma$) deficit w.r.t. the prediction. This reactor-off data set allows an improvement in the precision of the Reactor Rate Modulation (RRM) analysis while the effect is limited when considering the rate and spectral shape analysis.

5.4 θ_{13} measurements

Two different oscillation analyses allow to extract θ_{13}. The "conventional" one is based on a combined fit of rate and spectral shape whereas the Reactor Rate Modulation (RRM) analysis compares observed and predicted rates at different reactor powers.

5.4.1 Rate and spectral shape analysis

After the selection of the $\bar{\nu}_e$ candidates, the data are compared to the MC together with the background model. This fit is performed using RooFit and Minuit packages. Since we still do not know the mass hierarchy, separate fits using Δm^2_{31} values for normal and inverted hierarchies have been used.

We construct a standard χ^2 function defined as follows:

$$\begin{aligned}\chi^2 = &\sum_i^B \sum_j^B \left(N_i^{\text{obs}} - N_i^{\text{pred}}\right) M_{ij}^{-1} \left(N_j^{\text{obs}} - N_j^{\text{pred}}\right) + \sum_{k=1}^{5} \frac{\epsilon_k^2}{\sigma_k^2} \\ &+ (\epsilon_a, \epsilon_b, \epsilon_c) \times \begin{pmatrix} \sigma_a^2 & \rho_{ab}\sigma_a\sigma_b & \rho_{ac}\sigma_a\sigma_c \\ \rho_{ba}\sigma_b\sigma_a & \sigma_b^2 & \rho_{bc}\sigma_b\sigma_c \\ \rho_{ca}\sigma_c\sigma_a) & \rho_{cb}\sigma_c\sigma_b & \sigma_c^2 \end{pmatrix}^{-1} \times \begin{pmatrix} \epsilon_a \\ \epsilon_b \\ \epsilon_c \end{pmatrix} \\ &+ 2\left(N_{\text{off}}^{\text{obs}} \times \ln\left(\frac{N_{\text{off}}^{\text{obs}}}{N_{\text{off}}^{\text{pred}}}\right) + N_{\text{off}}^{\text{pred}} - N_{\text{off}}^{\text{obs}}\right), \end{aligned} \tag{5.15}$$

where B stands for the number of bins considered and N_i^{obs} and N_i^{pred} refer respectively to the number of observed and predicted events.

The last term of the first line holds the normalization uncertainty on the ^{9}Li $+\,^8$He background rate, the uncertainty on the fast neutron and stopping muon background rate, the systematic component of the uncertainty on the accidental background rate, the uncertainty on Δm^2_{31} and the uncertainty on the number of residual $\bar{\nu}_e$ emitted during the reactors-off period:

$$\begin{aligned}\sum_{k=1}^{5} \frac{\epsilon_k^2}{\sigma_k^2} = &\frac{(\epsilon_{\text{Li+He}} - 1)^2}{\left(\sigma_{\text{Li+He}}^{[\text{up,down}]}\right)^2} + \frac{(\epsilon_{\text{FN+SM}} - 1)^2}{(\sigma_{\text{FN+SM}})^2} + \frac{(\epsilon_{\text{acc}} - 1)^2}{(\sigma_{\text{acc}})^2} \\ &+ \frac{\left(\Delta m^2 - \Delta m^2_{31}\right)^2}{\left(\sigma_{\Delta m^2_{31}}^{[\text{up,down}]}\right)^2} + \frac{(\epsilon_{\text{res}} - 1)^2}{(\sigma_{\text{res}})^2} \end{aligned} \tag{5.16}$$

The first line of equation (5.15) contains the number of predicted events, N_i^{pred}, which can be written as:

$$N_i^{\text{pred}} = \sum_{R=1,2} N_i^{\bar{\nu}_e,R} + \sum_b N_i^b, \tag{5.17}$$

where $N_i^{\bar{\nu}_e,R} = P(\bar{\nu}_e \to \bar{\nu}_e)\, N_i^R$ with $P(\bar{\nu}_e \to \bar{\nu}_e)$ the survival probability in a two neutrino oscillation hypothesis and N_i^R the expected number of $\bar{\nu}_e$ in the energy bin i from equation (3.4).

R runs over the number of nuclear reactors and b over the three backgrounds to be considered.

$N_i^{\bar{\nu}_e,R}$ holds the $\sin^2 2\theta_{13}$ and Δm^2 parameters as well as the ϵ_a, ϵ_b and ϵ_c energy scale parameters whereas N_i^b holds the $\epsilon_{\text{Li+He}}$, $\epsilon_{\text{FN+SM}}$ and ϵ_{acc} parameters. N_i^{pred} is then a function which holds all the free parameters from the χ^2 definition, except the ϵ_{res} parameter.

Systematic and statistical uncertainties are propagated to the fit through the covariant matrix M_{ij} which accounts for correlations between energy bins. It can be expressed as the sum of several covariant matrices:

$$M_{ij} = M_{ij}^{\text{stat}} + M_{ij}^{\text{react}} + M_{ij}^{\text{eff}} + M_{ij}^{\text{Li+He (shape)}} + M_{ij}^{\text{acc (stat)}}, \tag{5.18}$$

where M_{ij}^{stat} is a diagonal matrix which takes into account the statistical uncertainty on the observed events. M_{ij}^{react} accounts for the uncertainty on the $\bar{\nu}_e$ emission prediction. M_{ij}^{eff} can also be written as $\sigma_{\text{eff}}^2 N_i^{\text{pred}} N_j^{\text{pred}}$ where σ_{eff}^2 corresponds to the uncertainty on the normalization of the MC. $M_{ij}^{\text{Li+He (shape)}}$ accounts for the uncertainty on the spectral shape of the Li+He spectrum. $M_{ij}^{\text{acc (stat)}}$ accounts for the statistical uncertainty of the accidental background rate.

The second line of equation (5.15) brings the energy scale model. It has been developed in order to take into account uncertainties on the discrepancy between data and MC:

$$\text{E}_{\text{vis}}^{\text{MC}} \rightarrow a + b \times \text{E}_{\text{vis}}^{\text{MC}} + c \times \left(\text{E}_{\text{vis}}^{\text{MC}}\right)^2, \tag{5.19}$$

where a, b and c are parameters which appear in equation (5.15) through $\epsilon_a = a - a_{\text{CV}}$, $\epsilon_b = b - b_{\text{CV}}$ and $\epsilon_c = c - c_{\text{CV}}$.

Constraints on ϵ_a, ϵ_b and ϵ_c are given by the matrix in which the correlation parameters ρ_{ab}, ρ_{bc} and ρ_{ac} were investigated through dedicated stability, uniformity and non-linearity systematics studies.

Finally, the third line of equation (5.15) brings the contribution of residual $\bar{\nu}_e$ emitted during the reactors-off period. Since the statistics remains low, $N_{\text{off}}^{\text{obs}}$ is compared to $N_{\text{off}}^{\text{pred}}$ through a log-likelihood based on Poisson statistics.

Results on the Gd-capture analysis

There are different ways to use the χ^2 function from equation (5.15) in order to extract $\sin^2 2\theta_{13}$. One of them is to compare the predicted and observed spectra on the whole range of the prompt energy spectra, without taking care of the binning. This is what we call rate-only analysis. Reactor-on and reactor-off periods are separetely used in the fit. We end with:

$$\sin^2 2\theta_{13} = 0.090^{+0.036}_{-0.037} \tag{5.20}$$

It is also possible to account for the spectral behavior of the prompt energy spectra. This is the preferred option of the Double Chooz collaboration, which is called rate+shape analysis. A special binning has been used to do so which is described in Table 5.8. The use of this binning allows to gain additional informations on backgrounds rates since we know that between 12 and 20 MeV there is no space for IBD events. B from equation (5.15) is then running over 40 bins whereas $B = 1$ in the case of the rate-only analysis.

Table 5.8: Bins distribution for the rate and spectral shape analysis with neutron capture on Gd.

Range	**Bin width**	**Number of bins**
0.5 - 8 MeV	250 keV	30 bins
8 - 10 MeV	500 keV	4 bins
10 - 12 MeV	1 MeV	2 bins
12 - 20 MeV	2 MeV	4 bins
0.5 - 20 MeV		40 bins

Assuming a normal hierarchy with $\Delta m^2_{31} = 2.44^{+0.09}_{-0.10} \times 10^{-3}$ eV^2 taken from MINOS [83] in agreement with T2K [84], the minimization of the χ^2 function leads to the best fit value for $\sin^2 2\theta_{13}$:

$$\sin^2 2\theta_{13} = 0.090^{+0.032}_{-0.029}, \tag{5.21}$$

with $\chi^2_{\text{min}}/\text{d.o.f.} = 52.2/40$.

Table 5.9 summarizes the best fit values of the fit parameters. Considering an inverted hierarchy with $|\Delta m^2_{31}| = 2.38^{+0.09}_{-0.10} \times 10^{-3}$ eV^2 [83] leads to $\sin^2 2\theta_{13} = 0.092^{+0.033}_{-0.029}$ with $\chi^2_{\text{min}}/\text{d.o.f.} = 52.2/40$.

Removing the constraints on the ^{9}Li + ^{8}He background rate and the fast neutron and stopping muon background rate allows to cross-check these results. It gives $\sin^2 2\theta_{13} = 0.088^{+0.030}_{-0.031}$ with a Li+He rate of $0.49^{+0.16}_{-0.14}$ events per day and a FN+SM rate of $0.541^{+0.052}_{-0.048}$ events per day. This results is compatible with the one obtained when applying constraints on these two backgrounds.

Figure 5.9 represents the visible energy spectrum of the prompt signals after substraction of the background. This spectrum is superimposed on the best fit prediction and on the non-oscillation hypothesis. The ratio of the data to the non-oscillation prediction shows a clear deficit below 4 MeV, consistent with a neutrino oscillation expectation.

Above 4 MeV, one can observe a spectrum distortion as it can be better seen in Figure 5.10. An excess around 5 MeV as well as a deficit around 7 MeV are clearly visible and are not yet understood. Even if it does not affect the θ_{13} measurement, this unexpected behavior has been deeply investigated by the Double Chooz collaboration before releasing these observa-

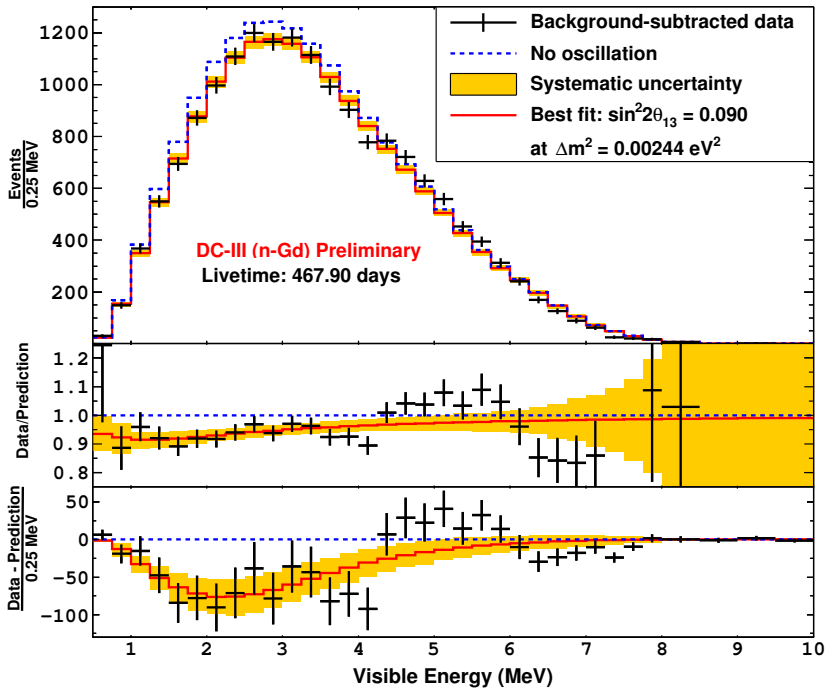

Figure 5.9: Visible energy spectrum of the prompt signals together with the ratio and the substraction of the data with the MC which assumes no oscillation. The points correspond to the background substracted data.

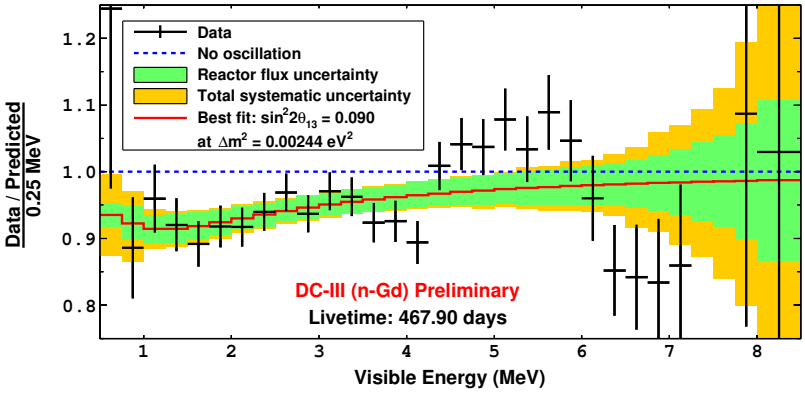

Figure 5.10: Ratio of the data with the MC which assumes no oscillation. The points correspond to the background substracted data. The red line stands for the best fit to the non-oscillation prediction. The reactor flux uncertainty as well as the total systematic uncertainty are represented.

Table 5.9: Input parameters values for the fit and the obtained output parameters values from [144]. These results assume a normal neutrino mass hierarchy.

Parameter	Input	Input error	Output	Output error
Energy scale a	-0.027	0.006	-0.026	+0.006, -0.005
Energy scale b	1.012	0.008	1.011	+0.004, -0.006
Energy scale c	-0.0001	0.0006	-0.0006	+0.0007, -0.0005
^{9}Li + ^{8}He rate (day^{-1})	0.97	+0.41, -0.16	0.74	0.13
FN+SM rate (day^{-1})	0.604	0.051	0.568	+0.038, -0.037
Accidentals rate (day^{-1})	0.0701	0.0026	0.0703	0.0026
Residual $\bar{\nu}_e$	1.57	0.47	1.48	0.47
Δm^2 (10^{-3} eV^2)	2.44	+0.09, -0.010	2.44	+0.09, -0.010
$\sin^2 2\theta_{13}$			0.090	+0.032, -0.029
χ^2_{min}/d.o.f.			52.2/40	

tions [145, 146, 147]. The RENO collaboration reported this same excess at the Neutrino 2014 conference [148] and the Daya Bay collaboration later on at the ICHEP 2014 conference [149].

The energy scale as cause of this distortion is disfavored from spallation neutron with capture on carbon studies. Due to the smaller capture cross section on carbon compared to the one on Gd, the events to be considered take place in the γ-catcher and result in an energy peak at 5 MeV. Both data and MC agree within 0.5 %. The energy scale has further been investigated through the study of β decays of ^{12}B collected in the data, without finding any distortion. This excess is not limited to the Gd-capture sample and depends on the nuclear reactor power, disfavoring the possibility of unknown backgrounds. A deviation from reactor flux prediction seems to be the preferred hypothesis and may find an answer from the calculation of the fission and β decay processes [150].

Results on the H-capture analysis

The extraction of the θ_{13} mixing angle follows the method used in [39, 40]. The visible energy spectrum of the prompt signals has been compared to the MC which assumes no oscillation. The rate and spectral shape analysis runs over 31 variably sized energy bins in the range [0.7, 12.2 MeV]. As for the results on the Gd-capture sample described above, the pull parameters are allowed to vary in the fit and are shown in Table 5.10.

The best fit value gives:

$$\sin^2 2\theta_{13} = 0.097 \pm 0.034\,(\text{stat}) \pm 0.034\,(\text{syst}), \tag{5.22}$$

with χ^2_{min}/d.o.f. = 38.9/30.

Table 5.10: Input parameters values for the fit and the obtained output parameters values from [41]. The Δm^2 input parameter is taken from [151].

Parameter	Input	Output
^{9}Li + ^{8}He rate (day^{-1})	2.8 ± 1.2	3.9 ± 0.6
FN+SM rate (day^{-1})	2.5 ± 0.5	2.6 ± 0.4
Energy scale	1.00 ± 0.02	0.99 ± 0.01
Δm^2 (10^{-3} eV^2)	2.32 ± 0.12	2.31 ± 0.12
$\sin^2 2\theta_{13}$		0.097 ± 0.034 (stat) ± 0.034 (syst)
χ^2_{min}/d.o.f.		38.9/30

The statistical error corresponds to the $1\,\sigma$ error which can be further reduced by collecting more data whereas the systematic error corresponds to the uncertainty which can not be reduced by collecting more data. This analysis exclude $\sin^2 2\theta_{13} = 0$ at 97.4 % ($2.0\,\sigma$). The rate only analysis leads to $\sin^2 2\theta_{13} = 0.044 \pm 0.022\,(\text{stat}) \pm 0.056\,(\text{syst})$.

Figure 5.11 represents the visible energy spectrum of the prompt signals after substraction of the background. The ratio of the data to the non-oscillation prediction does not show a spectrum distortion at 5 MeV even if one can guess a hint of a structure. At that time the statistics was too low to discriminate between a physics effect and a statistical effect. The release of the next H-capture sample analysis, with twice more statistics w.r.t. [41], should confirm the behavior observed previously.

5.4.2 Reactor Rate Modulation (RRM) analysis

The Reactor Rate Modulation (RRM) is based on the comparison of observed and predicted rates at different reactor powers. The strength of this analysis is to provide a background model independent measurement of θ_{13} since both the total background rate and the θ_{13} mixing angle are determined simultaneously. This analysis differs from conventional analysis based on background model used by Daya Bay and RENO which extract θ_{13} through a rate analysis. Double Chooz is so far the only reactor experiment that published such results [152, 42].

Since the Double Chooz far detector is exposed to only two reactors, the $\bar{\nu}_e$ flux changes dramatically when one of these two reactor turns off. It also happens that both reactors turn off in the same time, leading to an almost $\bar{\nu}_e$-free background measurement [111]. Two reactors on (2-On), one reactor off[1] (1-Off) and two reactors off (2-Off) configurations can then be set. The data set is distributed into seven bins of the reactor thermal power, three for the 2-On case, three for the 1-Off case and one for the 2-Off case. The fit procedure can be performed using only reactor-on data but can also include reactor-off data in order to

[1] One reactor off or two reactors on with low power.

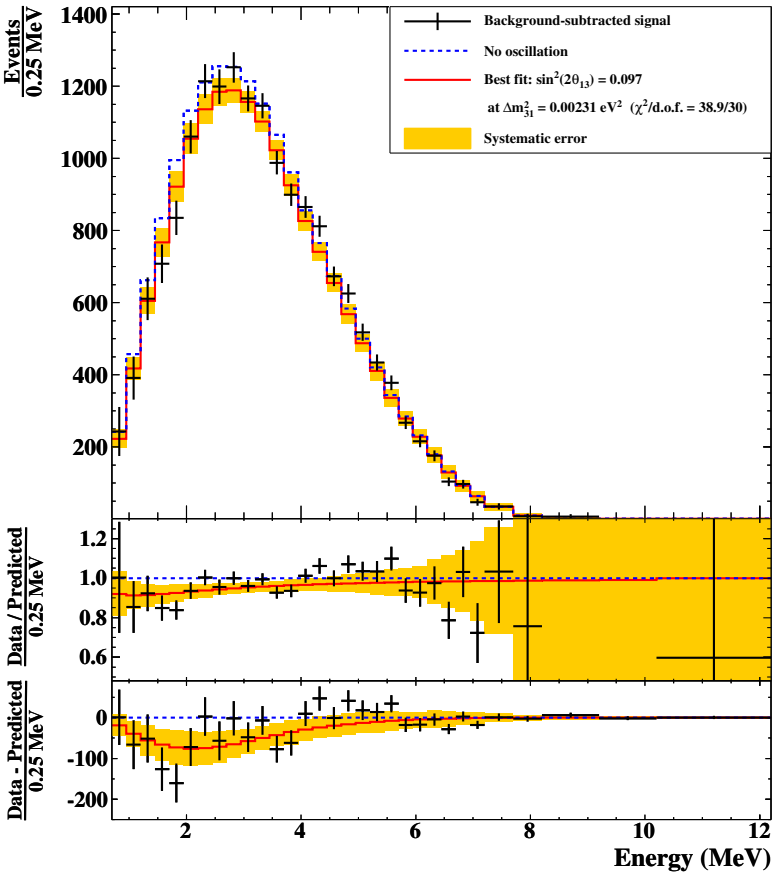

Figure 5.11: Visible energy spectrum of the prompt signals together with the ratio and the substraction of the data with the MC which assumes no oscillation. The points correspond to the background substracted data.

improve background constraint.

The comparison of observed and predicted rates, R^{obs} and R^{pred}, yields to a correlation between $\sin^2 2\theta_{13}$ and the total background rate B:

$$R^{\text{obs}} = B + R^{\text{pred}} = B + (1 - \eta_{\text{osc}} \sin^2 2\theta_{13}) R^{\bar{\nu}_e}, \tag{5.23}$$

where $R^{\bar{\nu}_e}$ refers to the expected $\bar{\nu}_e$ rate when considering an absence of neutrino oscillation and η_{osc} is the average disappearance coefficient $\langle \sin^2(\Delta m^2 L/4E) \rangle = 0.55$.

The RRM analysis has to deal with three sources of systematics uncertainties:

- Detection efficiency ($\sigma_d = 0.6$ %)
- Residual $\bar{\nu}_e$ prediction ($\sigma_{\bar{\nu}_e} = 30$ %)
- Reactor flux prediction (σ_r) which depends on the reactor power for a given configuration (2-On or 1-Off)

A standard χ^2 function has been built:

$$\chi^2 = \sum_{i=1}^{6} \frac{\left(R_i^{\rm obs} - R_i^{\rm pred} - B\right)^2}{\left(\sigma_i^{\rm stat}\right)^2} + \frac{\epsilon_d^2}{\sigma_d^2} + \frac{\epsilon_{\bar{\nu}_e}^2}{\sigma_{\bar{\nu}_e}^2} + \frac{\epsilon_r^2}{\sigma_r^2} + 2\left(N_{\rm off}^{\rm obs} \times \ln\left(\frac{N_{\rm off}^{\rm obs}}{N_{\rm off}^{\rm pred}}\right) + N_{\rm off}^{\rm pred} - N_{\rm off}^{\rm obs}\right) + \frac{\left(B - B^{\rm pred}\right)^2}{\left(\sigma_b\right)^2}, \tag{5.24}$$

where $R_i^{\rm obs}$ and $R_i^{\rm pred}$ are respectively the observed and predicted rate and B the total background rate. Systematics are handled through the ϵ_d, $\epsilon_{\bar{\nu}_e}$ and ϵ_r parameters.

$N_{\rm off}^{\rm obs}$ and $N_{\rm off}^{\rm pred}$ are respectively the observed and predicted number of neutrino candidates during the reactors-off period. $N_{\rm off}^{\rm pred}$ accounts for the residual $\bar{\nu}_e$ and background rates. It can be written as follows:

$$N_{\rm off}^{\rm pred} = \left(R_{\rm off}^{\bar{\nu}_e} + B\right) \times T_{\rm off}, \tag{5.25}$$

where $T_{\rm off}$ corresponds to the 7.24 days of reactors-off period.

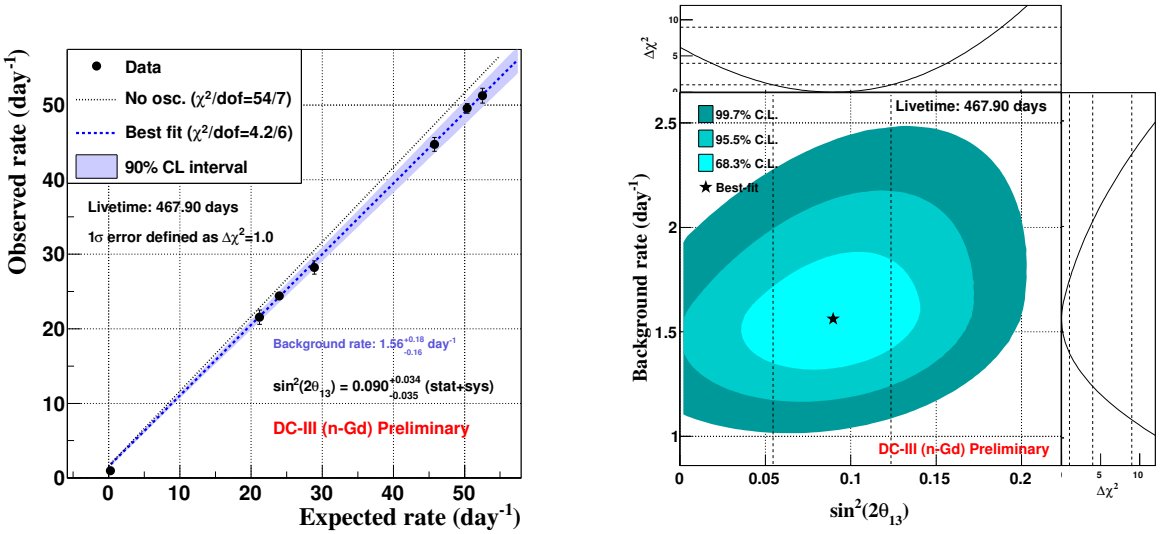

Figure 5.12: (*left*) Two parameters fit with reactor-on data, reactor-off data and background model. (*right*) 68.3 %, 95.5 % and 99.7 % C.L. contour plot.

Using both reactor-on and reactor-off data, as well as the background model, we get the best fit value for $\sin^2 2\theta_{13}$:

$$\sin^2 2\theta_{13} = 0.090^{+0.034}_{-0.035}, \tag{5.26}$$

with $\chi^2_{\rm min}/{\rm d.o.f.} = 4.2/6$ and a background rate of $1.56^{+0.18}_{-0.16}$ per day.

Figure 5.12 (*left*) shows the two parameters fit when using reactor-on, reactor-off and background model. There is a clear correlation between the observed and predicted rates

when considering different reactor powers. Figure 5.12 (*right*) shows the allowed regions on the $(\sin^2 2\theta_{13}, B)$ plane for this configuration.

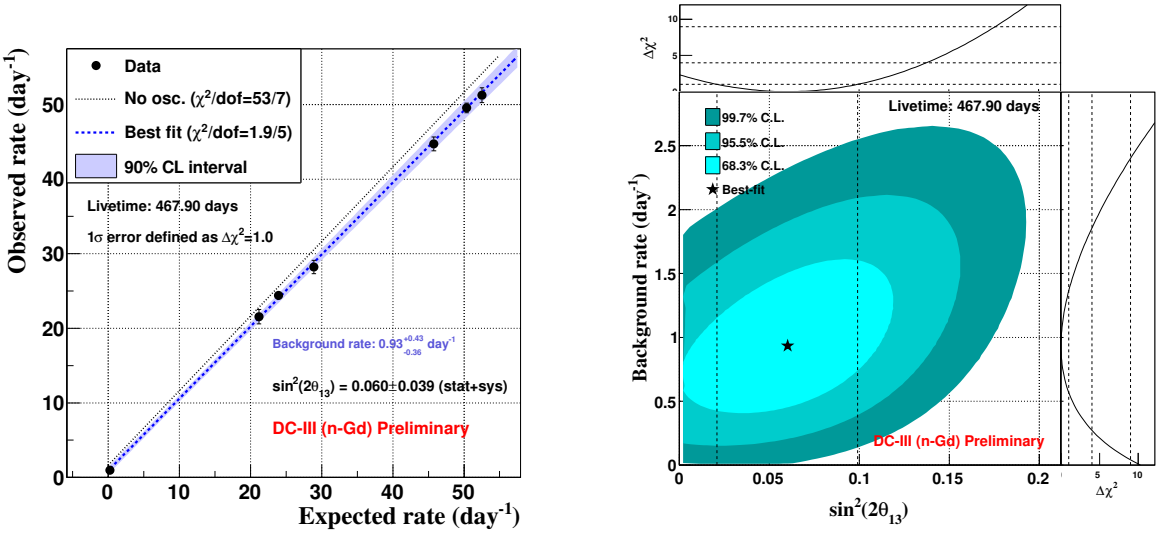

Figure 5.13: (*left*) Two parameters fit with reactor-on and reactor-off data. (*right*) 68.3 %, 95.5 % and 99.7 % C.L. contour plot.

We now remove the background model by suppressing the last line of equation (5.24). B is now treated as a free parameter, allowing a background model independent of $\sin^2 2\theta_{13}$. The best fit value for $\sin^2 2\theta_{13}$ becomes:

$$\sin^2 2\theta_{13} = 0.060 \pm 0.039, \tag{5.27}$$

with $\chi^2_{\text{min}}/\text{d.o.f.} = 1.9/5$ and a background rate of $0.93^{+0.43}_{-0.36}$ per day.

Removing the background model allows to cross-check and provides a background model independent measurement of θ_{13}. Figure 5.13 shows the two parameters fit for this configuration, as well as the allowed regions on the $(\sin^2 2\theta_{13}, B)$ plane.

We finally remove the reactor-off period from the fit, which leaves us with only the first line of the χ^2 definition from equation (5.24). The best fit value for $\sin^2 2\theta_{13}$ becomes:

$$\sin^2 2\theta_{13} = 0.089 \pm 0.052, \tag{5.28}$$

with $\chi^2_{\text{min}}/\text{d.o.f.} = 1.3/4$ and a background rate of 1.56 ± 0.86 per day.

Removing both the background model and the reactor-off period allows to test the impact of the data taken during the reactor-off period. Figure 5.14 shows the two parameters fit for this configuration, as well as the allowed regions on the $(\sin^2 2\theta_{13}, B)$ plane.

The three $\sin^2 2\theta_{13}$ values are compatible among the different configurations. Table 5.11 summarizes the values of $\sin^2 2\theta_{13}$ and B for the three configurations.

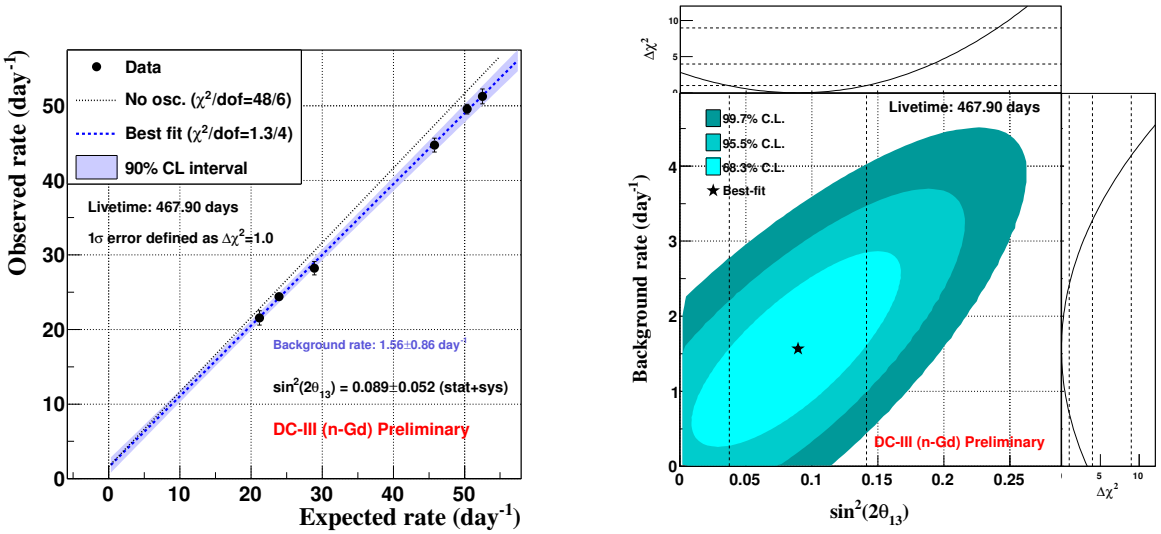

Figure 5.14: (*left*) Two parameters fit with reactor-on data only. (*right*) 68.3 %, 95.5 % and 99.7 % C.L. contour plot.

Table 5.11: Summary of the different configurations of the RRM analysis.

Configuration	$\sin^2 2\theta_{13}$	B	χ^2/d.o.f.
Reactor-on + Reactor-off + Background model	$0.090^{+0.034}_{-0.035}$	$1.56^{+0.18}_{-0.16}$	4.2/6
Reactor-on + Reactor-off	0.060 ± 0.039	$0.93^{+0.43}_{-0.36}$	1.9/5
Reactor-on	0.089 ± 0.052	1.56 ± 0.86	1.3/4

Figure 5.15 illustrates the impact of using the reactor-off data. The measured total background rate from this period allows indeed to better constrain $\sin^2 2\theta_{13}$.

The RRM analysis can help to better understand the 5 MeV excess seen in the rate and spectral shape analysis. Assuming the excess to be due to an unexpected background, the rate should be independent of the reactor power whereas it should be proportional to the reactor power if this excess is due to a deviation from reactor flux prediction. An energy binned RRM fit, called eRRM fit, has been developed in order to investigate this excess. Since the eRRM fit is based on a correlation between observed and predicted rates, it is possible to discriminate between an unexpected background and a deviation from reactor flux prediction.

Constraints on the background were removed whereas $\sin^2 2\theta_{13}$ was set to be equal to $0.090^{+0.009}_{-0.008}$ from [88]. Figure 5.16 shows the background rates in agreement with both the background rates estimation and the observed rates in the reactor-off period. The reactor flux normalizations are found to be larger than expected in the [4.25, 6 MeV] region and lower in the [6, 8 MeV] region. It turns out that this excess is better explained by a deviation from reactor flux prediction than an unexpected background.

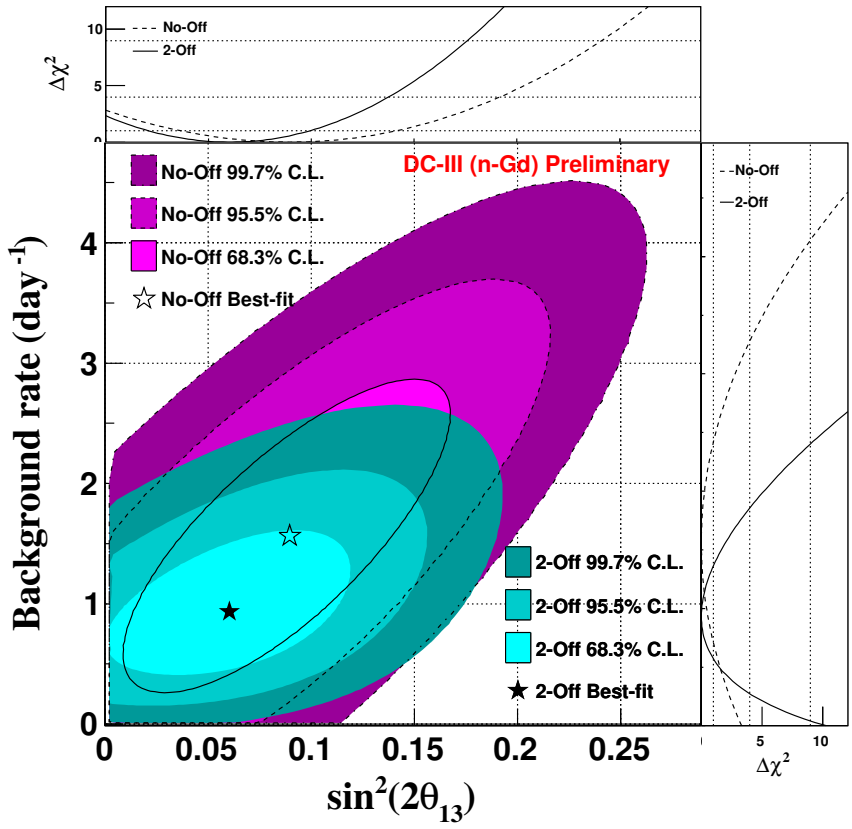

Figure 5.15: 68.3 %, 95.5 % and 99.7% C.L. contour plot. The red plot illustrates the fit when considering the reactor-on period only whereas the green plot takes into account both reactor-on and reactor-off periods.

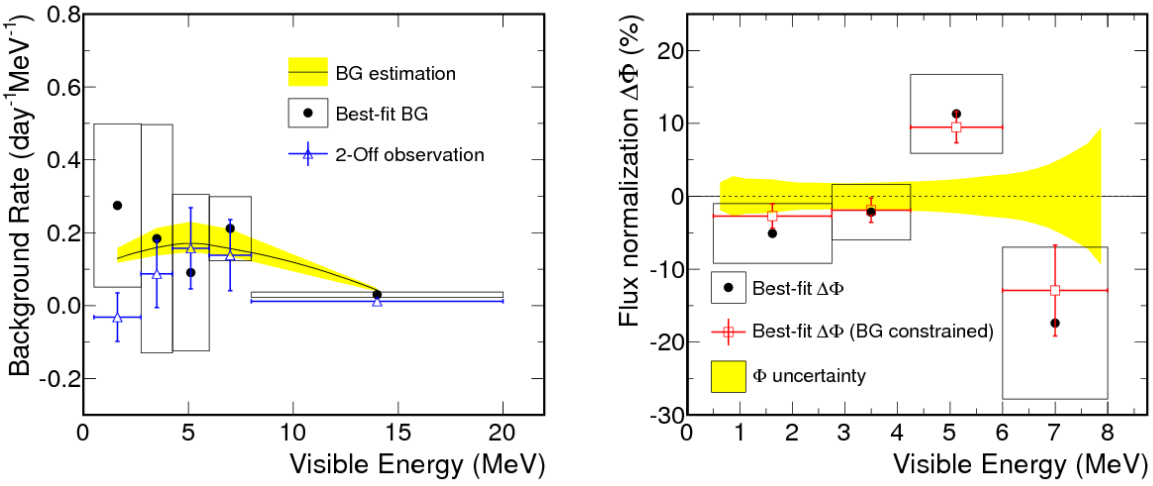

Figure 5.16: Background rates (*left*) and reactor flux normalizations (*right*) through eRRM fits for five visible energy regions. Constraints on the background were removed whereas a constraint on $\sin^2 2\theta_{13}$ was added.

Chapter

6 Looking for geo-neutrinos with Borexino

Les Italiens sont des Français de bonne humeur.
Jean Cocteau

Contents

The knowledge of the Earth is limited by indirect measurements. While seismology constrains the density profile, geochemistry allows to study the chemical composition of rocks which can be accessed. Chondritic meteorites as well as the photosphere of the Sun are also under investigation. The interdisciplinar field of neutrino geoscience aims to take advantage of the neutrino experiments skills to study the Earth interior with direct messengers, the geo-neutrinos.

6.1 Borexino: from the Sun to the Earth

The Borexino experiment was designed to observe solar neutrinos. In particular, the main goal was to measure the flux of neutrinos coming from electron capture on ^{7}Be in the Sun, with 5 % precision. Thanks to its low level of radioactivity background, Borexino succeeded [153]. Borexino can also investigate other solar components, such as ^{8}B and *pep* solar neutrino rate [154, 155]. Due to its position in a nuclear free country, Italy, Borexino is also sensitive to geo-neutrinos [156, 157].

6.1.1 Experimental site and detector design

The Borexino detector is located in the Laboratory Nazionali del Gran Sasso (LNGS), a deep underground laboratory close to L'Aquila in Italy. This laboratory holds several other neutrino experiments. Due to its specific location under a mountain, this laboratory is protected from cosmic rays thanks to a rock shielding equivalent to 3800 meter water equivalent (m.w.e.).

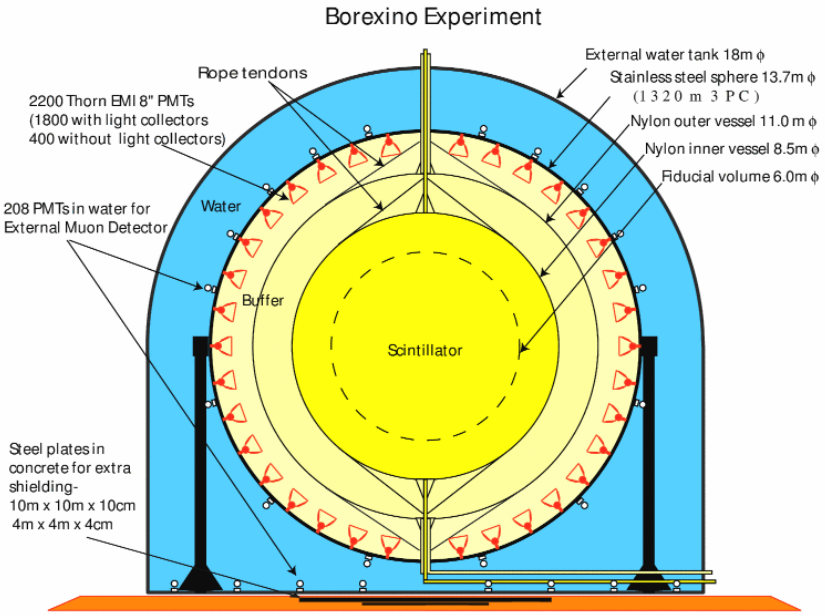

Figure 6.1: Scheme of the Borexino detector.

Borexino was born as a prototype of the BOREX experiment. BOREX was planned to be a liquid scintillator detector filled with several kilotons of trimethyl borate, an organoboron compound. It was then realized that a 100 ton detector would be enough to achieve measurements of low energy solar neutrino fluxes. A smaller BOREX detector was investigated, giving birth to the Borexino detector. A 4 tons prototype, the Counting Test Facility (CTF) was first built to demonstrate the feasibility of liquid scintillator purification needed for solar neutrino studies. The Borexino detector construction began in 1998 and on May 15, 2007,

data taking started.

The Borexino target consists of a thin nylon vessel of 4.25 m nominal radius filled with 278 tons of pseudocumene doped with 1.5 g/L of PPO, a fluorescent dye. Two buffers of 323 and 567 tons of liquid scintillator surround it and act as a shield. They are separated by another thin nylon vessel. A 13.7 m stainless steel sphere support the 2212 8-inch photomultiplier tubes which look at the target. This vessel is finally enclosed in a 18 m diameter by 16.9 m high domed water tank filled with 2100 tons of ultrapure water to detect muons which can enter the target. Figure 6.1 represents a scheme of the Borexino detector.

In order to reduce systematic errors, several calibration campaigns were performed between 2008 and 2011 [158]. They led to a better understanding of the Borexino detector response and allowed to optimize several input parameters values of the Monte Carlo (MC).

6.1.2 Solar neutrinos in sight

As for water Čerenkov experiments, solar neutrinos are detected inside Borexino through the elastic scattering (ES) reaction:

$$\nu_\alpha + e^- \to \nu_\alpha + e^- \qquad \text{(ES)}, \tag{6.1}$$

where α stands for e, μ or τ.

Since the cross section for ν_e with this reaction is about six times higher than the ones for ν_μ and ν_τ, the Borexino detector misses solar neutrinos which oscillate from ν_e to ν_μ or ν_τ, leading to a deficit when comparing with the predictions.

^{7}Be neutrinos

In order to improve the knowledge about the Sun and the fusion reactions which take place inside, the Borexino experiment is looking for monochromatic neutrinos emitted at 862 keV from the electron capture on ^{7}Be process:

$$^7_4\mathrm{Be} + e^- \to {}^7_3\mathrm{Li} + \nu_e \qquad \left(^7\mathrm{Be}\right) \tag{6.2}$$

According to Figure 1.4, this process gives the second most important solar neutrino flux, behind the *pp* process. With a 153.6 ton·year fiducial exposure, the ^{7}Be solar neutrino rate in Borexino, R, was measured to be:

$$R = 46.0 \pm 1.5\,(\text{stat}) \,^{+1.5}_{-1.6}\,(\text{syst}) \quad \text{counts/(day} \times \text{100 tons)} \tag{6.3}$$

It corresponds to a flux of $(3.10 \pm 0.15) \times 10^9$ cm^{-2} s^{-1} when one should expect 4.77×10^9 cm^{-2} s^{-1}, according to Table 1.1. The non-oscillation hypothesis was then excluded at $5.0\,\sigma$ [153].

Thanks to the stability of the detector, a day–night asymmetry was also investigated [159]. Since the solar neutrinos have to cross the Earth during the night and not during the day, one can think there will be a difference in the rate when comparing day data with night data. Whereas the Mikheyev-Smirnov-Wolfenstein (MSW) neutrino oscillations with Large Mixing Angle (LMA) oscillation parameters do not predict any change between day and night, the LOW oscillation parameters allows a large day-night effect. In 2012, Borexino measured a day-night asymmetry, $A_{\rm dn}$, to be:

$$A_{\rm dn} = 0.001 \pm 0.012\,(\text{stat}) \pm 0.007\,(\text{syst}) \tag{6.4}$$

With this result, Borexino was able to exclude the LOW region of the MSW parameter space.

^{8}B neutrinos

While the neutrinos emitted in ^{7}Be process are monochromatic, one has to deal with a three body decay and then with a continuous energy spectrum in the case of the neutrinos emitted from the β^+ radioactivity process of ^{8}B:

$$^8_5\text{B} \rightarrow {}^8_4\text{Be}^* + e^+ + \nu_e \qquad (^8\text{B}) \tag{6.5}$$

In 2010, Borexino reported the first observation of ^{8}B solar neutrino rate with a liquid scintillator detector [154]:

$$R = 0.22 \pm 0.04\,(\text{stat}) \pm 0.01\,(\text{syst})\,\text{counts}/(\text{day} \times 100\ \text{tons}) \tag{6.6}$$

It corresponds to a flux of $(2.4 \pm 0.4\,(\text{stat}) \pm 0.1\,(\text{syst})) \times 10^6\ \text{cm}^{-2}\ \text{s}^{-1}$ for a 3 MeV energy threshold, in good agreement with the Super-Kamiokande result illustrated in Table 1.1.

pep neutrinos

With an uncertainty of 1.2 % thanks to luminosity constraint, the Standard Solar Model (SSM) provides an accurate flux prediction for neutrinos emitted in the *pep* process:

$$p + e^- + p \rightarrow d + \nu_e \qquad (pep) \tag{6.7}$$

The *pep* solar neutrino rate was measured to be [155]:

$$R = 3.1 \pm 0.6\,(\text{stat}) \pm 0.3\,(\text{syst})\,\text{counts}/(\text{day} \times 100\ \text{tons}) \tag{6.8}$$

Figure 6.2 shows the solar rate measurements made by a given type of experiment together with the predictions.

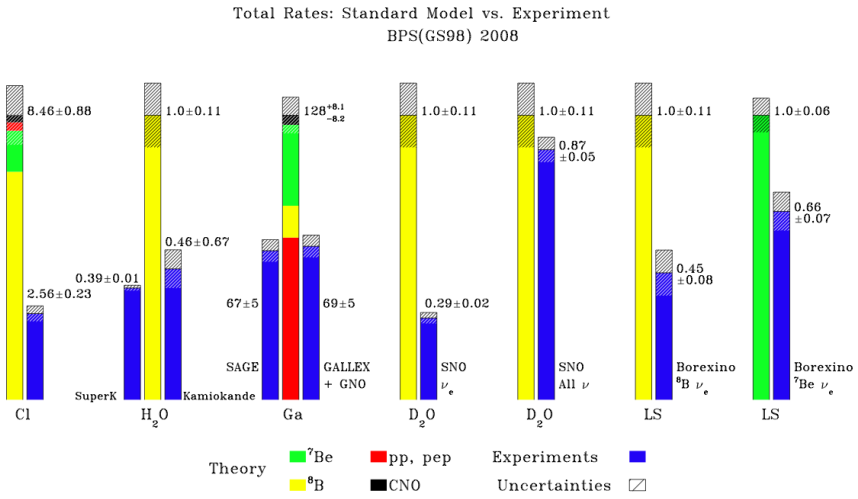

Figure 6.2: Solar rate measurements and predictions for a given type of experiment.

6.2 A unique opportunity to study geo-neutrinos

Geo-neutrinos are neutrinos emitted from the decay of radioactive isotopes present in the interior of the Earth. Since the chemical composition of our planet is not yet perfectly known, having a new source of information will help to better constrain how our planet works. The idea of using geo-neutrinos as a direct messenger was suggested in 1965 by G. Eder [160] and in 1968 by G. Marx [161] before being reviewed by L.M. Krauss, S.L. Glashow and D.N. Schramm in 1984 [162]. So far, only the KamLAND experiment in Japan [163] and the Borexino experiment in Italy [156, 157] have reported an observation of geo-neutrinos. New up-coming projects plan also to study geo-neutrinos, such as SNO+ [164], as well as projects under the design phase like JUNO, LENA [165] or Hanohano [166].

6.2.1 A look at the Earth

Let us have a look at our planet. This 4.54 billion year old lady is composed of three main regions. A metallic core in its center is surrounded by a mantle which is itself covered by a crust.

The innermost part of our planet is mainly composed of a Fe-Ni alloy. This part of the Earth is responsible for the terrestrial magnetism. The core can not be accessed directly, its study relies on the analysis of meteorites such as carbonaceous chondrite and in the measurement of travel time of seismic waves. This measurement allows to know that with a radius of 2890 km, about 45 % of the Earth radius, the core is in fact separated in two cores. The inner core has a 1220 km radius and is solid whereas the outer core was discovered thanks to the study of P and S waves. Since S waves do not go through liquid whereas P waves do, the outer core is believed to be liquid.

The mantle is located between the core and the crust. Even if it is solid, the mantle is

convective. This convection is responsible for plate tectonics and earthquakes. The mantle is, as the core, divided in two regions, the lower mantle and the upper mantle. The lower mantle, which is close to the core, has lost most of its radioactive components to the upper mantle and the crust during the differentiation with the core. The mantle composition can be accessed through the study of mid-ocean ridge basalts which are formed due to plate tectonics.

Since it is directly accessible, the crust is the most known region of the Earth. It appears that there is not only one type of crust but several. One has to make a difference between the continental crust and the oceanic crust. The oceanic crust is thiner and much more younger than the continental crust for instance. Indeed, since the oceanic crust is constantly renewed by being recycling in the mantle when it falls in it at subduction zones, the oceanic crust is around 80 million years old, whereas the continental crust is around 2 billion years old.

Bulk Silicate Earth (BSE) models describe both the crust and the mantle. There are different types of BSE models. Whereas geochemical BSE models study carbonaceous chondrites, cosmochemical BSE models focus on enstatite chondrites. There is also geodynamical BSE models which are not based on meteorite compositions but on the mantle convection. Nevertheless, BSE models allow all to describe both the crust and mantle of the Earth before the differentiation between the crust and the mantle which took place during the Earth formation. BSE models are consistent with most observations. They also allow to estimate the composition of the mantle when making a difference between the mass abundances predicted by the BSE models and the ones measured in the crust. This helps to determine the portion of radioactive elements inside the mantle which can not be directly accessible [167].

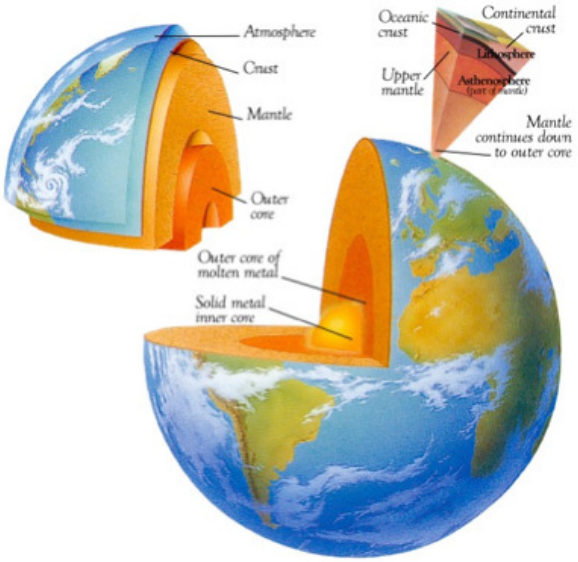

Figure 6.3: Scheme of the different layers of the Earth.

6.2.2 Geo-neutrinos production

Over the last decades, several studies on the total heat released from the surface of the Earth were conducted. It consists in the measurement of temperature gradients of drill holes. With 38347 heat flow measurements, J.H. Davies and D.R. Davies provided in 2010 an estimated rate of 47 ± 2 TW [168], compatible with previous studies led by C. Jaupart in 2007 and by H.N. Pollack in 1993 for estimated rates of 46 ± 3 TW [169] and 44 ± 1 TW [170].

The radiogenic heat is due to radioactive decays inside the Earth and it is admitted that radioactive elements belong only to the crust and the mantle of our planet. These different decays produce neutrinos with a flux which varies in time. The radiogenic heat was therefore much larger in the early Earth than today. Four main decay series are involved:

- ^{238}U decay series
- ^{235}U decay series
- ^{232}Th decay series
- ^{40}K decay

Isotopes in the ^{235}U decay series ($\tau_{1/2} = 0.70 \times 10^9$ year) are not much involved in the radiogenic heat production because of a small isotopic abundance. An even smaller fraction is coming from isotopes in the ^{87}Rb decay series ($\tau_{1/2} = 48.1 \times 10^9$ year), ^{138}La decay series ($\tau_{1/2} = 102 \times 10^9$ year) and ^{176}Lu decay series ($\tau_{1/2} = 37.6 \times 10^9$ year).

In order to access the geo-neutrino luminosity *i.e.* the number of neutrinos produced in the Earth per unit of time, one has to investigate the different decay series.

^{238}U decay series

Isotopes from ^{238}U decay series produce 6 $\bar{\nu}_e$ and release 51.7 MeV according to:

$$^{238}\mathrm{U} \rightarrow {}^{206}\mathrm{Pb} + 8\,\alpha + 6\,e^- + 6\,\bar{\nu}_e + 51.7 \text{ MeV} \tag{6.9}$$

^{238}U does not decay directly to ^{206}Pb but makes a succession of alpha and beta decays, illustrated in Table 6.1. The $\bar{\nu}_e$ production rate per unit of mass of the ^{238}U decay series can be calculated:

$$\mathcal{R}_{\bar{\nu}_e}(^{238}\mathrm{U}) = N_{\bar{\nu}_e} \frac{\mathcal{N}_\mathrm{A}}{M(^{238}\mathrm{U})\,\tau} = 7.46 \times 10^4 \ \bar{\nu}_e \,/\, (\mathrm{g{\cdot}s}), \tag{6.10}$$

where $N_{\bar{\nu}_e}$ is the number of $\bar{\nu}_e$ produced in reaction (6.9), $\mathcal{N}_\mathrm{A}$ the Avogadro number, $M(^{238}\mathrm{U}) = 238.05$ g/mol and $\tau = \tau_{1/2}/\ln 2$ with $\tau_{1/2} = 4.47 \times 10^9$ years.

We can also calculate the heat production rate per unit of mass of the ^{238}U decay series carried by the $\bar{\nu}_e$, which is linked to $\mathcal{R}_{\bar{\nu}_e}(^{238}\mathrm{U})$ through:

$$\mathcal{P}_{\bar{\nu}_e}(^{238}\mathrm{U}) = \mathcal{R}_{\bar{\nu}_e}(^{238}\mathrm{U}) \frac{Q_{\bar{\nu}_e}(^{238}\mathrm{U})}{N_{\bar{\nu}_e}} = 7.88 \text{ nW/g}, \tag{6.11}$$

where $Q_{\bar{\nu}_e}(^{238}\mathrm{U}) = 0.634$ pJ is extracted from [171].

Nevertheless, this heat production rate can not be measured and one would prefer to know the radiogenic heat production rate which can be accessed by subtracting $Q_{\bar{\nu}_e}(^{238}\mathrm{U})$ from the decay Q value of 51.7 MeV:

$$Q_{\mathrm{heat}}(^{238}\mathrm{U}) = Q - Q_{\bar{\nu}_e}(^{238}\mathrm{U}) = 47.74 \text{ MeV}, \tag{6.12}$$

leading to:

$$\mathcal{P}_{\mathrm{heat}}(^{238}\mathrm{U}) = \mathcal{R}_{\bar{\nu}_e}(^{238}\mathrm{U})\frac{Q_{\mathrm{heat}}(^{238}\mathrm{U})}{N_{\bar{\nu}_e}} = 95.12 \text{ nW/g} \tag{6.13}$$

Table 6.1 presents the ^{238}U decay series. Mainly two isotopes, ^{234}Pa and ^{214}Bi, are able to provide $\bar{\nu}_e$ which can later on interact in a detector through Inverse Beta Decay (IBD) interactions [172]. The other isotopes provides $\bar{\nu}_e$ with energy lower than the threshold energy of 1.806 MeV we have calculated in equation (3.6).

Table 6.1: ^{238}U decay series, from [173]. Only the β^- decays of ^{234}Pa and ^{214}Bi provide $\bar{\nu}_e$ susceptible to interact through IBD interactions in a detector.

Step	Parent	Half-life	Decay	Daughter
1	^{238}U	4.47×10^9 y	Alpha	^{234}Th
2	^{234}Th	24.1 d	Beta	^{234}Pa
3	**^{234}Pa**	**1.17 m**	**Beta**	**^{234}U**
4	^{234}U	2.44×10^5 y	Alpha	^{230}Th
5	^{230}Th	7.7×10^4 y	Alpha	^{226}Ra
6	^{226}Ra	1.60×10^3 y	Alpha	^{222}Rn
7	^{222}Rn	3.82 d	Alpha	^{218}Po
8	^{218}Po	3.05 m	Alpha	^{214}Pb
9	^{214}Pb	26.8 m	Beta	^{214}Bi
10	**^{214}Bi**	**19.8 m**	**Beta**	**^{214}Po**
11	^{214}Po	1.64×10^{-4} s	Alpha	^{210}Pb
12	^{210}Pb	22.3 y	Beta	^{210}Bi
13	^{210}Bi	5.01 d	Beta	^{210}Po
14	^{210}Po	138.4 d	Alpha	^{206}Pb (stable)

^{235}U decay series

Isotopes from ^{235}U decay series produce 4 $\bar{\nu}_e$ and release 46.4 MeV:

$$^{235}\mathrm{U} \rightarrow {}^{207}\mathrm{Pb} + 7\,\alpha + 4\,e^- + 4\,\bar{\nu}_e + 46.4 \text{ MeV} \tag{6.14}$$

The $\bar{\nu}_e$ production rate and the radiogenic heat production rate per unit of mass of the ^{235}U decay series can be calculated:

$$\mathcal{R}_{\bar{\nu}_e}(^{235}\mathrm{U}) = N_{\bar{\nu}_e}\frac{\mathcal{N}_\mathrm{A}}{M(^{235}\mathrm{U})\,\tau} = 3.20\times10^5\ \bar{\nu}_e\,/\,(\mathrm{g{\cdot}s}), \tag{6.15}$$

$$\mathcal{P}_\mathrm{heat}(^{235}\mathrm{U}) = \mathcal{R}_{\bar{\nu}_e}(^{235}\mathrm{U})\frac{Q_\mathrm{heat}(^{235}\mathrm{U})}{N_{\bar{\nu}_e}} = 568.36\ \mathrm{nW/g}, \tag{6.16}$$

with $M(^{235}\mathrm{U}) = 235.04\ \mathrm{g/mol^{-1}}$, $\tau_{1/2} = 7.04\times10^8$ years and $Q_{\bar{\nu}_e}(^{235}\mathrm{U}) = 0.325$ pJ is extracted from [171].

^{232}Th decay series

Isotopes from ^{235}U decay series produce 4 $\bar{\nu}_e$ and release 42.7 MeV:

$$^{232}\mathrm{Th} \rightarrow {}^{208}\mathrm{Pb} + 6\,\alpha + 4\,e^- + 4\,\bar{\nu}_e + 42.7\ \mathrm{MeV} \tag{6.17}$$

As for ^{238}U and ^{235}U, ^{232}Th does not decay directly to ^{208}Pb. Table 6.2 illustrates the succession of decays ^{232}Th goes through. The $\bar{\nu}_e$ production rate and the radiogenic heat production rate per unit of mass of ^{232}Th can be calculated:

$$\mathcal{R}_{\bar{\nu}_e}(^{232}\mathrm{Th}) = N_{\bar{\nu}_e}\frac{\mathcal{N}_\mathrm{A}}{M(^{232}\mathrm{Th})\,\tau} = 1.63\times10^4\ \bar{\nu}_e\,/\,(\mathrm{g{\cdot}s}), \tag{6.18}$$

$$\mathcal{P}_\mathrm{heat}(^{232}\mathrm{Th}) = \mathcal{R}_{\bar{\nu}_e}(^{232}\mathrm{Th})\frac{Q_\mathrm{heat}(^{232}\mathrm{Th})}{N_{\bar{\nu}_e}} = 26.41\ \mathrm{nW/g}, \tag{6.19}$$

with $M(^{232}\mathrm{Th}) = 232.04\ \mathrm{g/mol^{-1}}$, $\tau_{1/2} = 1.40\times10^{10}$ years and $Q_{\bar{\nu}_e}(^{232}\mathrm{Th}) = 0.358$ pJ is extracted from [171].

Table 6.2 presents the ^{232}Th decay series. Two isotopes, ^{228}Ac and ^{212}Bi, are able to provide $\bar{\nu}_e$ which can later on interact in a detector through an IBD interaction [172].

^{40}K decay

Finally, let us have a look at the ^{40}K decay series. ^{40}K can decay to ^{40}Ca through β^- decay or can become ^{40}Ar through an electron capture:

$$^{40}\mathrm{K} \rightarrow {}^{40}\mathrm{Ca} + e^- + \bar{\nu}_e + 1.311\ \mathrm{MeV} \qquad (89.3\ \%) \tag{6.20}$$

$$^{40}\mathrm{K} + e^- \rightarrow {}^{40}\mathrm{Ar} + \nu_e + 1.505\ \mathrm{MeV} \qquad (10.7\ \%) \tag{6.21}$$

Both ^{40}Ca and ^{40}Ar are stable, there is no succession of decays as for the previous elements. When considering the first reaction which produces $\bar{\nu}_e$, we can calculate the $\bar{\nu}_e$ production rate and the radiogenic heat production rate par unit of mass of ^{40}K:

$$\mathcal{R}_{\bar{\nu}_e}(^{40}\mathrm{K}) = 0.893\times N_{\bar{\nu}_e}\frac{\mathcal{N}_\mathrm{A}}{M(^{40}\mathrm{K})\,\tau} = 2.31\times10^5\ \bar{\nu}_e\,/\,(\mathrm{g{\cdot}s}), \tag{6.22}$$

Table 6.2: ^{232}Th decay series, from [173]. Only the β^- decays of ^{234}Pa and ^{214}Bi provide $\bar{\nu}_e$ susceptible to interact through IBD interactions in a detector.

Step	Parent	Half-life	Decay	Daughter
1	^{232}Th	1.40×10^{10} y	Alpha	^{228}Ra
2	^{228}Ra	5.75 y	Beta	^{228}Ac
3	**^{228}Ac**	**6.13 h**	**Beta**	**^{228}Th**
4	^{228}Th	1.913 y	Alpha	^{224}Ra
5	^{224}Ra	3.66 d	Alpha	^{220}Rn
6	^{220}Rn	55.6 s	Alpha	^{216}Po
7	^{216}Po	0.15 s	Alpha	^{212}Pb
8	^{212}Pb	10.64 h	Beta	^{212}Bi
9a	**^{212}Bi**	**60.6 m**	**Beta**	**^{212}Po** (64%)
9b	^{212}Bi	60.6 m	Alpha	^{208}Tl (36%)
10a	^{212}Po	2.98×10^{-7} s	Alpha	^{208}Pb (stable)
10b	^{208}Tl	3.053 m	Beta	^{208}Pb (stable)

$$\mathcal{P}_{\text{heat}}(^{40}\text{K}) = \mathcal{R}_{\bar{\nu}_e}(^{40}\text{K})\frac{Q_{\bar{\nu}_e}(^{40}\text{K})}{N_{\bar{\nu}_e}} = 24.72 \text{ nW/g}, \tag{6.23}$$

with $M(^{40}\text{K}) = 39.96$ g·mol^{-1}, $\tau_{1/2} = 1.28 \times 10^9$ years and $Q_{\bar{\nu}_e}(^{40}\text{K}) = 0.103$ pJ is extracted from [171].

From all these decay series we can now provide the total geo-neutrino luminosity $\mathcal{L}$, as well as the total radiogenic heat production rate $\mathcal{H}$:

$$\mathcal{L} = \sum_i \mathcal{R}_i \times m_i \tag{6.24}$$

$$\mathcal{H} = \sum_i \mathcal{P}_i \times m_i \tag{6.25}$$

where $\mathcal{R}_i$ represents the $\bar{\nu}_e$ or the ν_e production rate per unit of mass, $\mathcal{P}_i$ the radiogenic heat production rate per unit of mass and m_i the mass of ^{238}U, ^{235}U, ^{232}Th and ^{40}K.

We summarize in Table 6.3 the properties of the different decay series we investigated. In particular, when looking at the maximal energy the emitted neutrinos can carry, we notice that $\bar{\nu}_e$ from ^{235}U decay series and ^{40}K decay are below the threshold of 1.806 MeV required to create the positron and the neutron in an IBD interaction. The maximal energy carried by ν_e from ^{40}K decay is also too small to be detected. The geo-neutrinos which can be studied

will then only be the $\bar{\nu}_e$ coming from the ^{238}U and ^{232}Th decay series.

Considering only the ^{238}U and ^{232}Th decay series, the effective luminosity is given by:

$$\mathcal{L}_{\text{eff}} = \mathcal{R}_{\bar{\nu}_e}(^{238}\text{U}) \times m(^{238}\text{U}) + \mathcal{R}_{\bar{\nu}_e}(^{232}\text{Th}) \times m(^{232}\text{Th}) \tag{6.26}$$

Table 6.3: ^{238}U, ^{235}U, ^{232}Th and ^{40}K decay series properties.

	^{238}U	^{235}U	^{232}Th	^{40}K($\bar{\nu}_e$)	^{40}K(ν_e)
$\tau_{1/2}$ (year)	4.47×10^9	7.04×10^8	1.40×10^{10}	1.28×10^9	1.28×10^9
Q (MeV)	51.7	46.4	42.7	1.311	1.505
$Q_{\bar{\nu}_e}$ (pJ)	0.634	0.325	0.358	0.103	-
# $\bar{\nu}_e$	6	4	4	1	-
$\mathcal{R}_{\bar{\nu}_e}$ ($\bar{\nu}_e/(\text{g}\cdot\text{s})$)	7.46×10^4	3.20×10^5	1.63×10^4	2.31×10^5	-
# ν_e	-	-	-	-	1
$\mathcal{R}_{\nu_e}$ ($\nu_e/(\text{g}\cdot\text{s})$)	-	-	-	-	2.77×10^4
E_{max} (MeV)	3.26	1.23	2.25	1.311	0.044

From Table 6.3, one can also notice that if the Sun is a ν_e emitter, the Earth is mainly an $\bar{\nu}_e$ emitter. It is then possible to make both studies and to discriminate between them since their interactions in a detector such as Borexino will differ.

6.2.3 Geo-neutrino signal prediction

It is now of importance to precisely know $m(^{238}\text{U})$ and $m(^{232}\text{Th})$ from equation (6.26) in order to obtain the geo-neutrino signal prediction. Let us take a portion of the Earth, of mass $\text{d}m$, located at a distance r from the center of the Earth. We can expressed $\text{d}m$ as $\text{d}m = \rho \text{d}V$ where ρ is the density of the portion considered and $\text{d}V$ its volume. As a first step, we will only focus on ^{238}U and we will see how we can extract information on ^{232}Th.

The $\bar{\nu}_e$ flux coming from the decay series of the ^{238}U present inside this piece of Earth when being at the surface of the Earth is:

$$\text{d}\phi(^{238}\text{U}) = \mathcal{R}_{\bar{\nu}_e}(^{238}\text{U})\, P_{ee}\, \frac{a(r)\rho(r)\text{d}^3 r}{4\pi|R_\otimes - r|^2}, \tag{6.27}$$

where $a(r)$ stands for the mass abundance of ^{238}U, $R_\otimes = 6371$ km is the Earth radius and $P_{ee} = P(\bar{\nu}_e \to \bar{\nu}_e)$ is the survival probability of the geo-neutrinos.

P_{ee} can be expressed as:

$$P_{ee} = \cos^4\theta_{13}\left(1 - \sin^2(2\theta_{12})\sin^2\left(1.27\,\frac{\Delta m^2_{21}(\text{eV}^2)L(\text{m})}{E(\text{MeV})}\right)\right) + \sin^4\theta_{13}, \tag{6.28}$$

with an oscillation length L_0:

$$L_0 = 2.48 \, \frac{E}{\Delta m^2_{21}} \simeq 66 \text{ km}, \tag{6.29}$$

when considering $E = 2$ MeV and $\Delta m^2_{21} = 7.54 \times 10^{-5}$ eV^2.

With an oscillation length $L_0 \ll R_\otimes$, we can make the reasonable assumption of an averaged survival probability for geo-neutrinos:

$$\langle P_{ee} \rangle = \cos^4 \theta_{13} \left(1 - \frac{1}{2} \sin^2(2\theta_{12}) \right) + \sin^4 \theta_{13} = 0.55 \pm 0.03, \tag{6.30}$$

where mixing angles and mass square differences are taken from [110].

We access ϕ through an integration which gives us:

$$\phi(^{238}\text{U}) = \mathcal{R}_{\bar{\nu}_e}(^{238}\text{U}) \, \langle P_{ee} \rangle \int_0^{R_\otimes} \frac{a(r)\rho(r)\text{d}^3 r}{4\pi |R_\otimes - r|^2} \tag{6.31}$$

The abundance $a(r)$ differs when considering different layers of the Earth we call reservoirs. The crust and the mantle do not contain the same amount of ^{238}U and we have to take this into account:

$$\phi(^{238}\text{U}) = \mathcal{R}_{\bar{\nu}_e}(^{238}\text{U}) \, \langle P_{ee} \rangle \sum_{\text{res}} a_{\text{res}} \int_{r_{\text{low}}}^{r_{\text{up}}} \frac{\rho(r)\text{d}^3 r}{4\pi |R_\otimes - r|^2} \tag{6.32}$$

Whereas models do not always agree on the determination of the reservoirs composition, they reach a consensus on the mass abundance ratio between uranium and thorium:

$$\frac{\text{Th}}{\text{U}} = 3.9 \tag{6.33}$$

We can then express the $\bar{\nu}_e$ flux from ^{232}Th with the one from ^{238}U:

$$\begin{aligned} \phi(^{232}\text{Th}) &= \frac{\mathcal{R}_{\bar{\nu}_e}(^{232}\text{Th}) \, \langle P_{ee} \rangle \, \sum_{\text{res}} a_{\text{res}} \int_{r_{\text{low}}}^{r_{\text{up}}} \frac{a(r)\rho(r)\text{d}^3 r}{4\pi |R_\otimes - r|^2}}{\mathcal{R}_{\bar{\nu}_e}(^{238}\text{U}) \, \langle P_{ee} \rangle \, \sum_{\text{res}} a_{\text{res}} \int_{r_{\text{low}}}^{r_{\text{up}}} \frac{a(r)\rho(r)\text{d}^3 r}{4\pi |R_\otimes - r|^2}} \, \phi(^{238}\text{U}) \\ &= 3.9 \, \frac{\mathcal{R}_{\bar{\nu}_e}(^{232}\text{Th})}{\mathcal{R}_{\bar{\nu}_e}(^{238}\text{U})} \, \phi(^{238}\text{U}) \\ &= 0.85 \times \phi(^{238}\text{U}) \end{aligned} \tag{6.34}$$

The total geo-neutrino flux is then:

$$\phi_{\text{tot}} = \phi(^{238}\text{U}) + 0.85 \times \phi(^{238}\text{U}) \tag{6.35}$$

In order to evaluate the total geo-neutrino flux, one can think to use a Bulk Silicate Earth (BSE) model we described previously. Nevertheless, several BSE models exist and they can vary by a factor 3 in the ^{238}U content. We will use the BSE model described in [174] since it takes into account the specificities of the Borexino site. The $\bar{\nu}_e$ flux for ^{238}U is $\left(4.34^{+0.96}_{-0.75}\right) \times 10^6$ cm^{-2}s^{-1} and is $\left(4.23^{+1.26}_{-0.80}\right) \times 10^6$ cm^{-2}s^{-1} for ^{232}Th around Borexino.

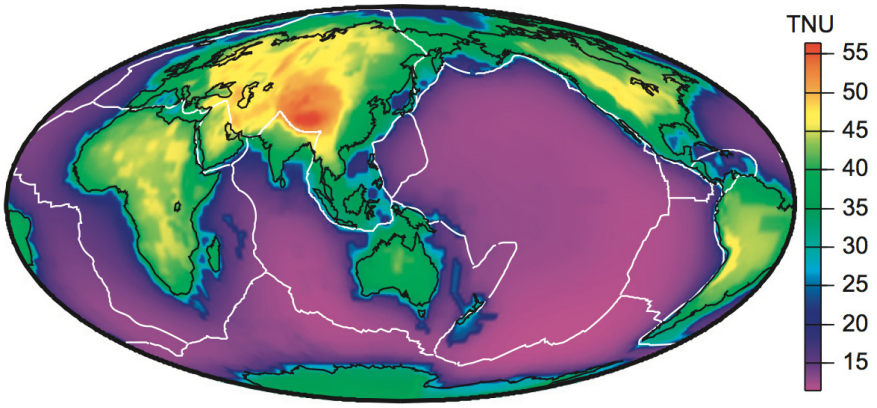

Figure 6.4: Global map of the total geo-neutrino flux prediction, from [167].

These fluxes are given without taking into account the averaged survival probability of the geo-neutrinos calculated in equation (6.30). By introducing it, we finally obtain:

$$\phi(^{238}\mathrm{U}) = \left(2.37^{+0.96}_{-0.75}\right) \times 10^6 \text{ cm}^{-2}\text{s}^{-1} \tag{6.36}$$

$$\phi(^{232}\mathrm{Th}) = \left(2.31^{+1.26}_{-0.80}\right) \times 10^6 \text{ cm}^{-2}\text{s}^{-1} \tag{6.37}$$

A more useful flux unit named TNU for Terrestrial Neutrino Unit allows to convert these fluxes in order to take into account the detector size, the experiment duration and the detection efficiency. One TNU corresponds then to one event detected over one year exposure of 10^{32} target protons at 100 % efficiency. One TNU differs when considering $\bar{\nu}_e$ fluxes emitted from the ^{238}U or the ^{232}Th decay series. One TNU corresponds to a flux of 7.67×10^4 cm^{-2}s^{-1} in the case of ^{238}U and 2.48×10^5 cm^{-2}s^{-1} in the case of ^{232}Th [167]. We can then express $\phi(^{238}\mathrm{U})$ and $\phi(^{232}\mathrm{Th})$ in terms of TNU unit, $\mathcal{S}(^{238}\mathrm{U})$ and $\mathcal{S}(^{232}\mathrm{Th})$:

$$\mathcal{S}(^{238}\mathrm{U}) = 30.95^{+12.52}_{-9.78} \text{ TNU} \tag{6.38}$$

$$\mathcal{S}(^{232}\mathrm{Th}) = 9.33^{+5.08}_{-3.23} \text{ TNU}, \tag{6.39}$$

which leads to the total geo-neutrino rate:

$$\mathcal{S}_{\mathrm{tot}} = \mathcal{S}(^{238}\mathrm{U}) + \mathcal{S}(^{232}\mathrm{Th}) = 40.3^{+13.5}_{-10.3} \text{ TNU} \tag{6.40}$$

6.3 Chasing the geo-neutrinos

6.3.1 Detection

The detection of geo-neutrinos, which are $\bar{\nu}_e$ from what we saw previously, relies on the signature of the IBD interactions $\bar{\nu}_e + p \rightarrow e^+ + n$ where the positron scintillation and annihilation, the "prompt" signal, is followed by the neutron capture on hydrogen (H), the "delayed" signal. The prompt and delayed signals are correlated in space and time, which allows to apply specific cuts determined by neutron capture physics.

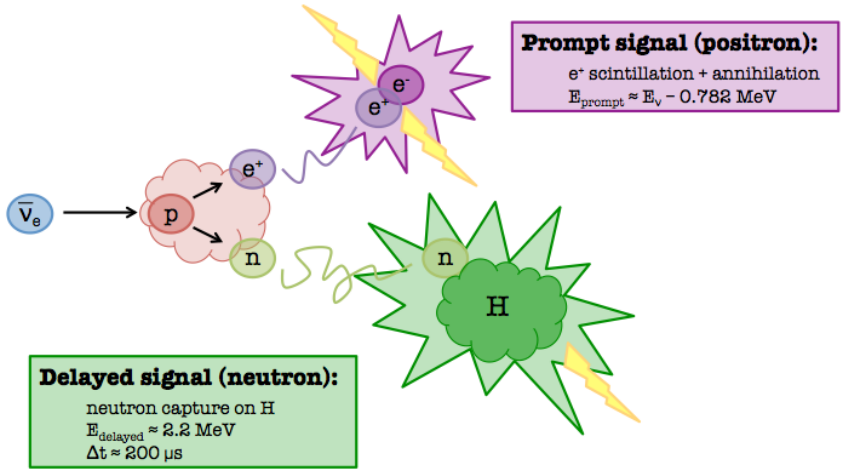

Figure 6.5: Scheme of an IBD interaction with neutron capture on H.

6.3.2 Selection

Even if I run my analysis on the total available data taking period, I will focus in this analysis on the exact same data taking period than the one released in [157], in order not to be in conflict with a future Borexino paper.

Data have then been taken from December 9, 2007 to August 26, 2012. It corresponds to a live time of 1323.26 days live time. This live time is a bit less than the 1353 days live time published in [157]. This is due to the removal of some runs which had hardware issue. The cuts used for the neutrino selection in Borexino are:

- **Prompt**:
  - $Q_{prompt} > 408$ p.e.
  - Fiducial Volume (FV) cut asking to have a distance greater than 25 cm from the target vessel
  - No neutron-like event in the 2 ms preceding the prompt signal

- **Delayed**:
  - $860 < Q_{delayed} < 1300$ p.e.
  - No neutron-like event in the 2 ms following the delayed signal

- **Coincidence** (prompt and delayed):
  - Time coincidence: $20 < \Delta t < 1280$ μs
  - Space coincidence: $\Delta R < 100$ cm

Q_{prompt} and $Q_{delayed}$ stand for the PMTs light yields of the prompt and the delayed signals respectively. 1 MeV corresponds to approximatively 500 photoelectrons (p.e.). The FV cut is required in order to avoid to take into account radioactive components present on the target vessel made of nylon. Since this vessel is not perfectly spherical and changes in time, an algorithm based on the position reconstruction of identified radioactive components allows to

calculate the vessel shape on a weekly basis. We ask then the prompt position reconstruction to be at least 25 cm away from this vessel shape. The precision is about 1.6 % and was calibrated using a dedicated LED calibration system [158].

A 2 s dead time window has been applied after each identified internal muon and a 2 ms dead time window has been applied after each identified external muon. This induces a 10.41 % dead time leading to a 1185.56 days effective live time.

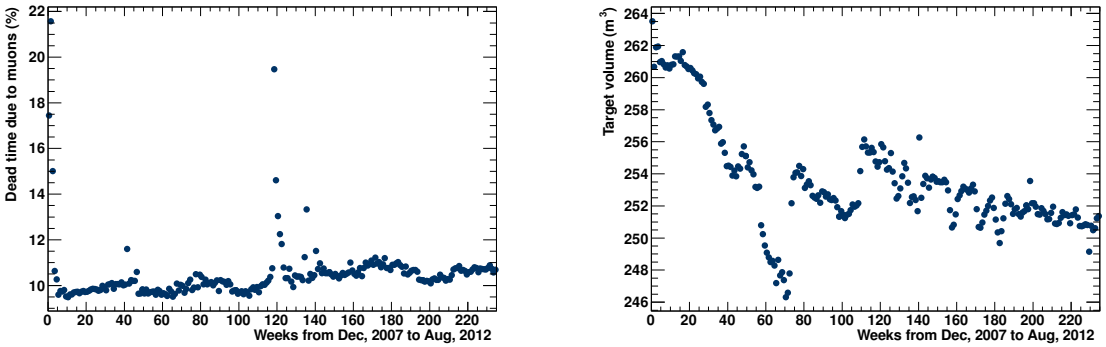

Figure 6.6: Dead time variation due to muons (*left*) and target volume variation (*right*) as a function of time from December 9, 2007 to August 26, 2012.

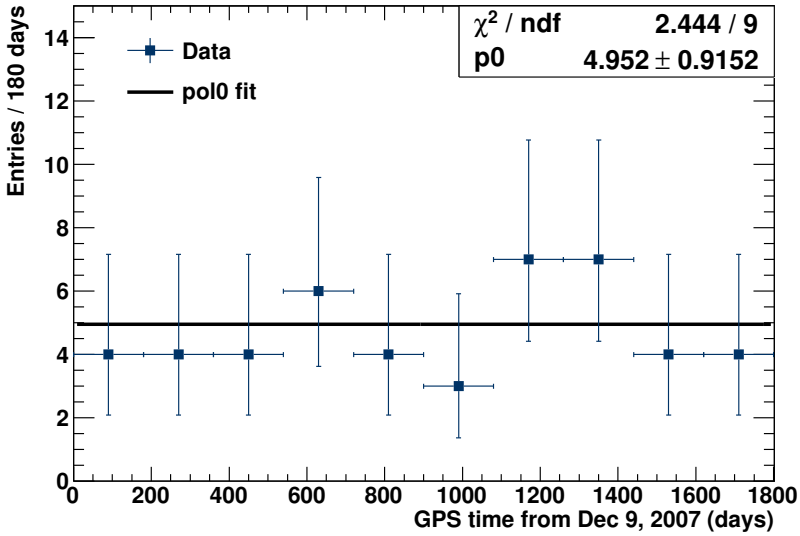

Figure 6.7: Distribution of the 47 $\bar{\nu}_e$ candidates as a function of time from December 9, 2007 to August 26, 2012.

Figure 6.6 (*left*) shows the dead time variation due to muons from December 9, 2007 to August 26, 2012. The peak which can be seen around the week 120 is probably due to a hardware issue and is still under investigation. Figure 6.6 (*right*) shows the target volume

variation for the same period. An important decrease at the beginning of the period can be seen. It was due to a leakage of the liquid scintillator on the top of the target.

Figure 6.7 shows the distribution of the 47 $\bar{\nu}_e$ candidates from December 9, 2007 to August 26, 2012. Each bin indicates the number of observed $\bar{\nu}_e$ candidates within 6 months. The distribution is flat, as expected. We should detect around 10 $\bar{\nu}_e$ candidates per year. Some of the 47 $\bar{\nu}_e$ candidates we found in this analysis are different from the 46 ones reported in [157]. Due to an improvement of the algorithm for the FV cut, three $\bar{\nu}_e$ candidates passed our selection when one was removed from it. Another $\bar{\nu}_e$ candidate was removed since we found an additional signal between the prompt and the delayed signals. We then added three $\bar{\nu}_e$ candidates and removed two.

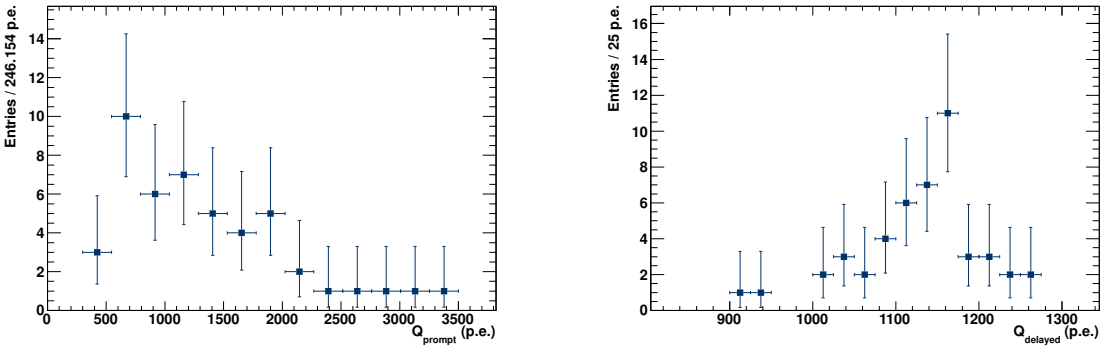

Figure 6.8: Q_{prompt} (*left*) and $Q_{delayed}$ (*right*) light yield spectra of the 47 $\bar{\nu}_e$ candidates.

Figure 6.8 corresponds to the Q_{prompt} and the $Q_{delayed}$ light yield spectra. Since the maximum energy a geo-neutrino can carry is 3.26 MeV according to Table 6.3, the corresponding maximum visible energy we can measure in the detector is:

$$E_{\text{vis}} \simeq E_{\bar{\nu}_e} - 0.782 \text{ MeV} \simeq 2.48 \text{ MeV} \tag{6.41}$$

The geo-neutrino candidates stand then in the $Q_{prompt} < 1300$ p.e. region. Above this end-point, only $\bar{\nu}_e$ from nuclear reactors are seen. We observe 21 neutrino candidates when requesting $Q_{prompt} > 1300$ p.e. while we should expect 22.0 $\pm$ 1.6 and 39.9 $\pm$ 2.7 $\bar{\nu}_e$ candidates with and without oscillation. The observation is then matching the prediction when considering an oscillation hypothesis. The averaged survival probability is found to be:

$$\langle P_{ee} \rangle = 0.55 \pm 0.06, \tag{6.42}$$

in excellent agreement with 0.55 ± 0.03 we found previously in equation (6.30).

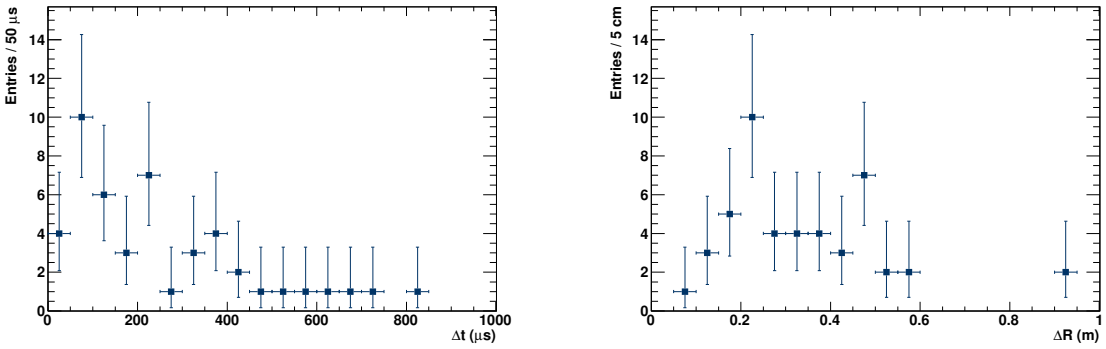

Figure 6.9: Correlation time (*left*) and correlation distance (*right*) between the prompt and the delayed signals of the 47 $\bar{\nu}_e$ candidates.

6.4 Background studies

6.4.1 Reactor background

Even if Borexino is located in a nuclear free country, it is nonetheless sensitive to $\bar{\nu}_e$ emitted from nuclear reactors which lay on our planet. Since one can not discriminate between $\bar{\nu}_e$ from nuclear reactors and geo-neutrinos, this background is the main one. Nevertheless, it is possible to estimate the expected number of events, N_{react}, which can be registered:

$$N_{\text{react}} = \sum_{r=1}^{R} \sum_{m=1}^{M} \frac{\eta_m}{4\pi L_r^2} P_{rm} \times \int \mathrm{d}E_{\bar{\nu}_e} \sum_{i=1}^{4} \frac{f_i}{E_i} \phi_i(E_{\bar{\nu}_e}) \sigma(E_{\bar{\nu}_e}) P_{ee}(E_{\bar{\nu}_e}, L_r), \tag{6.43}$$

where r runs over the number of nuclear reactors R considered, m runs over the number of months M considered, η_m stands for the exposure in month m and includes detector efficiency, L_r is the detector-reactor distance, P_{rm} is the effective thermal power of reactor r in month m, i runs over the spectral components of ^{235}U, ^{238}U, ^{239}Pu and ^{241}Pu, f_i is the power fraction of component i, E_i the average energy released per fission of component i, $\phi_i(E_{\bar{\nu}_e})$ the $\bar{\nu}_e$ spectrum per fission of component i, $\sigma(E_{\bar{\nu}_e})$ the IBD cross section and $P_{ee}(E_{\bar{\nu}_e}, L_r)$ the survival probability of the emitted $\bar{\nu}_e$ of energy $E_{\bar{\nu}_e}$ created at distance L_r.

MC have been developed in order to take into account the 446 nuclear reactors running during the period of interest. The effective thermal power of each of these reactors has been calculated as a product of the nominal thermal power times the monthly load factor provided by the International Atomic Energy Agency (IAEA). $\phi_i(E_{\bar{\nu}_e})$ has been extracted from [43] and $\sigma(E_{\bar{\nu}_e})$ from [175].

6.4.2 Accidental background

Accidentals are one of the main background when looking for $\bar{\nu}_e$. It is an uncorrelated background which corresponds to an accidental coincidence of single events. Such events mimic $\bar{\nu}_e$ events with both prompt and delayed signals, but there is no correlation between them

in this case. Applying correlation time and distance cuts, Δt and ΔR, allows to reduce the accidental background but one has to evaluate the remaining amount of these events in the geo-neutrino candidates sample.

The general way to evaluate this background is to look for off-time coincidences between the prompt-like and the delayed-like signals. The procedure is:

1. Looking for a prompt signal, with the exact same cuts described in the geo-neutrino selection section.
2. Opening a dead time windows of 2 s after the prompt signal.
3. Looking for a delayed signal, with the exact same cuts described in the geo-neutrino selection section, in the [2, 20 s] time window after the prompt signal.
4. Registering the event if $\Delta R < 100$ cm.

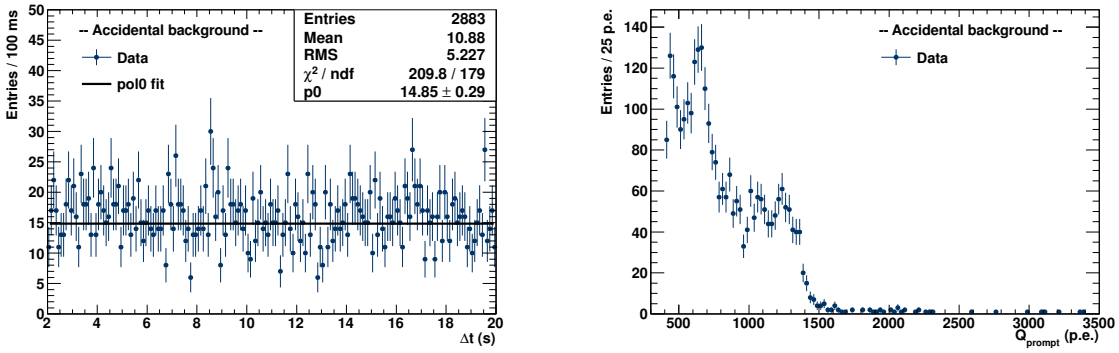

Figure 6.10: (*left*) Correlation time of the prompt and delayed signals of accidentals. (*right*) Q_{prompt} light yield spectrum of accidentals.

Figure 6.10 (*left*) corresponds to the Δt distribution between prompt and delayed signals when looking for accidentals with the procedure described above. Since this distribution is flat, one can then extrapolate in the region of interest when looking for $\bar{\nu}_e$, *i.e.* [20, 1280 µs]. The remaining events within our geo-neutrino candidates sample is then:

$$N_{\mathrm{Acc}} = 0.202 \pm 0.004 \tag{6.44}$$

Figure 6.10 (*right*) shows that the accidental background lives at low energy. This contribution has then to be taken carefully into account since the geo-neutrino candidates stand in this part of the energy spectrum.

6.4.3 Cosmogenic background

Another important source of background is due to ^{9}Li and ^{8}He produced by muons which interact in the scintillator. These elements can decay inside the detector, leading to the emission of electrons and neutrons and therefore can be registered as $\bar{\nu}_e$ events. These events are left untouched by the usual cuts we apply on the prompt and delayed signals but can be

rejected by applying a 2 s veto after each identified internal muon.

We evaluate the remaining events which fall into our $\bar{\nu}_e$ selection by first looking at the candidates which are produced in the [2 ms, 2 s] range after an internal muon identification. We apply the same prompt and delayed selections, as well as the same coincidence cuts, that the ones for the geo-neutrino analysis except that we ask the prompt signal to fall in the [2 ms, 2 s] range of interest. We report the observation of 130 events which satisfy these conditions.

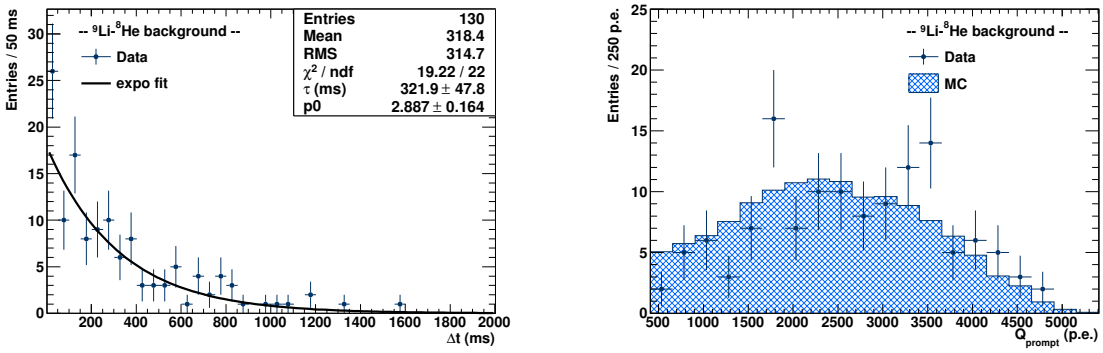

Figure 6.11: (*left*) Correlation time of the prompt and delayed signals of ^{9}Li + ^{8}He candidates. (*right*) Q_{prompt} light yield spectrum of ^{9}Li + ^{8}He candidates.

Figure 6.11 (*left*) corresponds to the Δt distribution between an identified internal muon and a prompt signal. We can fit this distribution using an exponential function. We found $\tau = 321.9 \pm 47.8$ ms. We can then calculate the fraction $\mathcal{R}_{out}$ of ^{9}Li + ^{8}He candidates which are contained in the [2 ms, 2 s] time window:

$$\mathcal{R}_{out} = \exp\left(-\frac{2}{\tau}\right) - \exp\left(-\frac{2000}{\tau}\right) = 99.18\,\% \tag{6.45}$$

By applying a 2 s cut after each identified internal muon, we are left with a fraction $\mathcal{R}_{in}$ of ^{9}Li + ^{8}He candidates inside our geo-neutrino candidates sample:

$$\mathcal{R}_{in} = \exp\left(-\frac{2000}{\tau}\right) = 0.20\,\%, \tag{6.46}$$

which corresponds to the number of events:

$$N_{\mathrm{Li+He}} = 0.260 \pm 0.023 \tag{6.47}$$

6.5 Maximum likelihood analysis

In order to access the number of both geo-neutrinos and $\bar{\nu}_e$ from nuclear reactors which can not be distinguished from the cuts we applied to the selection, we use an unbinned maximum likelihood method.

Let us consider a random variable x which is distributing following a probability density function (p.d.f.) named $f(x,\theta)$. The functional form of $f(x,\theta)$ is known but at least one parameter θ is not. The method of the maximum likelihood allows to approach the value of these parameters considering a measurement of x repeated n times. If the p.d.f. and parameters value are correct, one should expect a high probability for the real data. *A contrario*, if the parameters value do not match the true value, this probability will be low. The so-called likelihood function can be expressed as:

$$L(\theta) = \prod_{i=1}^{n} f(x_i,\theta) \tag{6.48}$$

The number of observations n is a Poisson random variable with a mean value ν. The likelihood function can then be expressed as the Poisson probability to have n times the likelihood function for the n measurements of x:

$$L(\nu,\theta) = \frac{\nu^n}{n!}e^{-\nu}\prod_{i=1}^{n} f(x_i,\theta) = \frac{e^{-\nu}}{n!}\prod_{i=1}^{n}\nu f(x_i,\theta) \tag{6.49}$$

Equation (6.49) is known as the extended likelihood function [176]. n is now one of the experimental results and for our geo-neutrino analysis, it will correspond to our number of geo-neutrino candidates, *i.e.* 47. Assuming that ν is a function of θ, we have then the expression of the extended log-likelihood:

$$\begin{aligned}\ln L(\theta) &= n\ln\nu(\theta) - \nu(\theta) + \sum_{i=1}^{n}\ln f(x_i,\theta)\\ &= -\nu(\theta) + \sum_{i=1}^{n}\ln(\nu(\theta)f(x_i,\theta)),\end{aligned} \tag{6.50}$$

where terms which do not depend on θ have been removed.

The variable x is actually $E \equiv \mathrm{Q}_{\mathrm{prompt}}$, since we are interesting in the prompt energy of our geo-neutrino candidates. We can then define $\nu(\theta)$ and $f(x_i,\theta)$ such that:

$$\nu(\theta) = \int_{E_1}^{E_2}\frac{\mathrm{d}N}{\mathrm{d}E}(E,\theta)\,\mathrm{d}E \tag{6.51}$$

$$f(x_i,\theta) = f(E_i,\theta) = \frac{1}{\nu}\frac{\mathrm{d}N}{\mathrm{d}E}(E_i,\theta) \tag{6.52}$$

The log-likelihood from equation (6.50) finally becomes:

$$\ln L(\theta) = -\int_{E_1}^{E_2}\frac{\mathrm{d}N}{\mathrm{d}E}\,\mathrm{d}E + \sum_{i=1}^{n}\ln\frac{\mathrm{d}N}{\mathrm{d}E}(E_i,\theta) \tag{6.53}$$

Let us now have a look at the parameters θ involved in our geo-neutrino analysis. We have on one side the geo-neutrino component and on the other side the reactor neutrino component. Their energy spectra differ such that we can define $g \cdot f_{\mathrm{geo}}(E)$ for the geo-neutrino component and $r \cdot f_{\mathrm{react}}(E)$ for the reactor neutrino component where g and r are

the number of candidates involved. We also add as parameters the uncertainty on the reactor flux, σ_r, which is of the order of 5.8 % as well as the uncertainty on the volume of the Borexino target, σ_v, of the order of 1.5 % since we remind that it moves with time. The log-likehood becomes:

$$\ln L(\theta) = -\int_{E_1}^{E_2}(1+\sigma_v)\frac{\mathrm{d}N}{\mathrm{d}E}(E,g,r,\sigma_r)\,\mathrm{d}E + \sum_{i=1}^{n}\ln\left((1+\sigma_v)\frac{\mathrm{d}N}{\mathrm{d}E}(E_i,g,r,\sigma_r)\right) - \frac{1}{2}\left(\frac{\sigma_r}{5.8\ \%}\right)^2 - \frac{1}{2}\left(\frac{\sigma_v}{1.5\ \%}\right)^2, \tag{6.54}$$

with:

$$\frac{\mathrm{d}N}{\mathrm{d}E}(E,g,r,\sigma_r) = g\cdot f_{\mathrm{geo}}(E) + r\cdot f_{\mathrm{react}}(E)\,(1+\sigma_r) \tag{6.55}$$

g and r are left as free parameters and allow us to access the number of geo-neutrinos, N_{geo}, as well as the number of $\bar{\nu}_e$ from nuclear reactors, N_{react}. Our best fit values are $N_{\mathrm{geo}} = 14.1^{+5.2}_{-4.5}$ and $N_{\mathrm{react}} = 32.4^{+6.9}_{-6.1}$. Figure 6.12 shows the $-2\,\Delta\ln L$ profiles for N_{geo} and N_{react}.

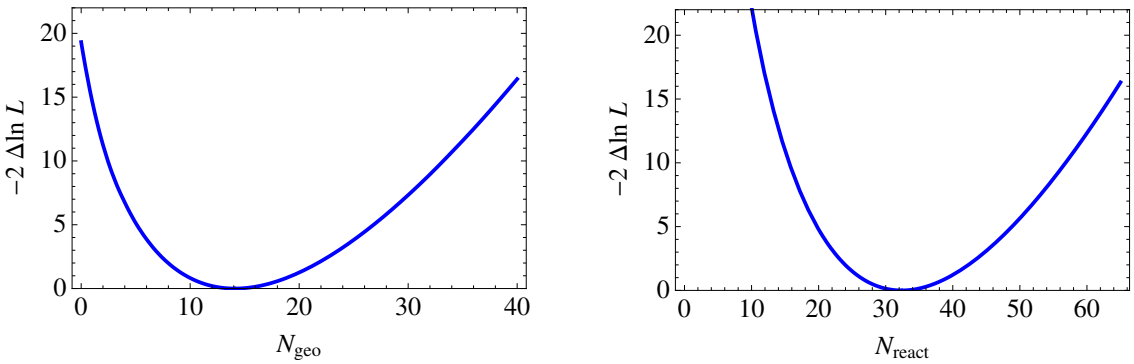

Figure 6.12: $-2\,\Delta\ln L$ profiles for N_{geo} (*left*) and N_{react} (*right*). Our best fit values are $N_{\mathrm{geo}} = 14.1^{+5.2}_{-4.5}$ and $N_{\mathrm{react}} = 32.4^{+6.9}_{-6.1}$.

We can go from N_{geo} and N_{react} to the signal rates S_{geo} and S_{react}, which are expressed in TNU. We first have to extract the number of protons × year:

$$N_p = N_p(\mathrm{C_9H_{12}})\frac{\mathcal{E}\times\mathcal{N}_{\mathrm{A}}}{M(\mathrm{C_9H_{12}})} = 3.65\times10^{31}\ \text{protons}\times\text{year}, \tag{6.56}$$

where $N_p(\mathrm{C_9H_{12}}) = 12$ corresponds to the number of free protons in a pseudocumene molecule, $\mathcal{E} = 606.28$ ton × year is the total exposure which also takes into account the 84 % efficiency of the Borexino detector, $\mathcal{N}_{\mathrm{A}}$ is the Avogadro number and $M(\mathrm{C_9H_{12}}) = 120.19$ g/mol.

We finally access $\mathcal{S}_{\mathrm{geo}}$ and $\mathcal{S}_{\mathrm{react}}$:

$$\mathcal{S}_{\mathrm{geo}} = N_{\mathrm{geo}}\frac{10^{32}}{N_p} = 38.6^{+14.2}_{-12.3}\ \text{TNU} \tag{6.57}$$

$$\mathcal{S}_{\text{react}} = N_{\text{react}} \frac{10^{32}}{N_p} = 88.8^{+18.9}_{-16.7} \text{ TNU} \tag{6.58}$$

These values are in agreement with the best fit values reported in [157]. The null geo-neutrino signal rate hypothesis is excluded at $4.4\,\sigma$.

Figure 6.13 and 6.14 show respectively the contour plots for the numbers and the signal rates of geo-neutrinos and $\bar{\nu}_e$ from nuclear reactors. The dashed lines in Figure 6.14 symbolizes the prediction of the total geo-neutrino rate from equation (6.40).

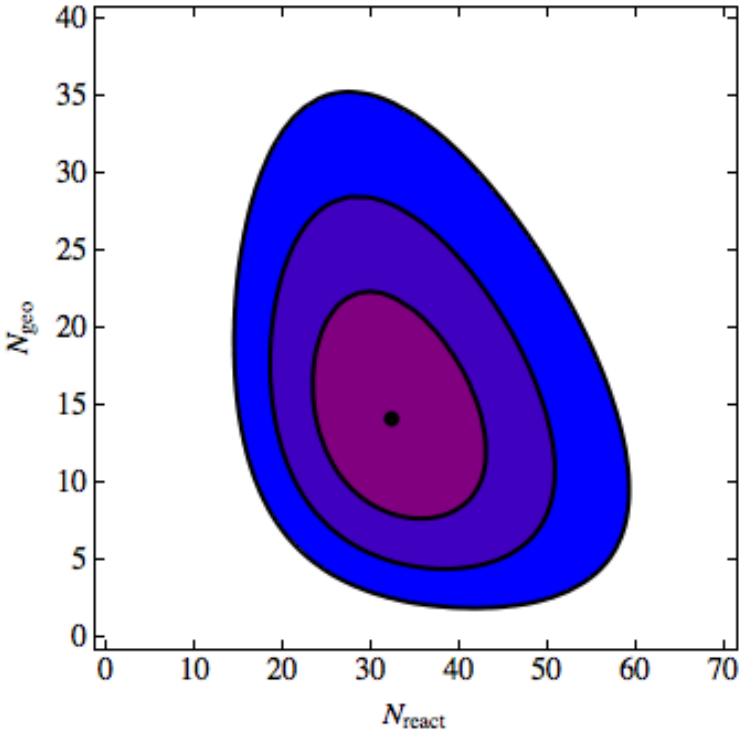

Figure 6.13: Contour plots for the number of geo-neutrinos and $\bar{\nu}_e$ from nuclear reactors. The 68.27 %, 95.45 % and 99.73 % C.L. are represented. The black point indicates the best fit value.

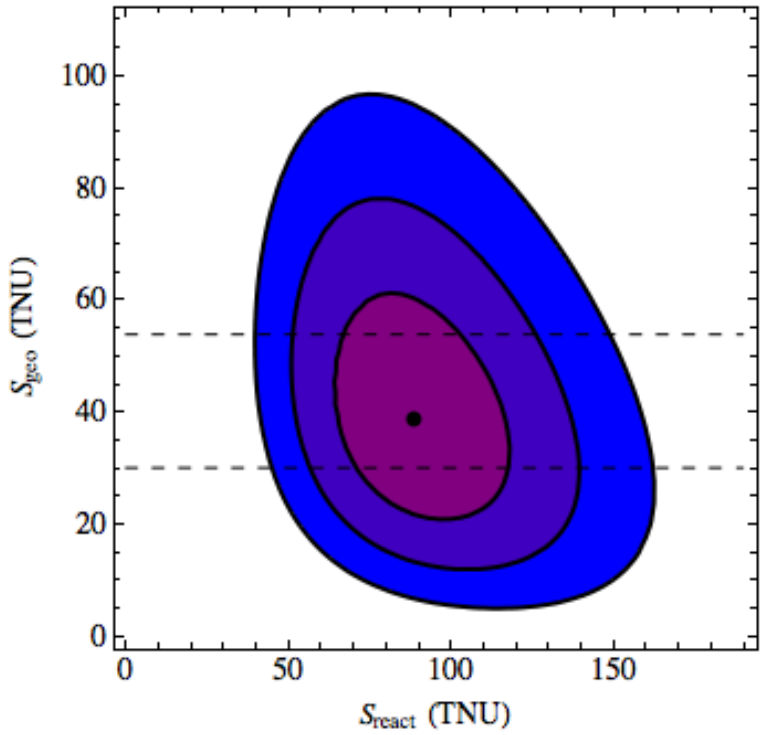

Figure 6.14: Contour plots for the signal rates of geo-neutrinos and $\bar{\nu}_e$ from nuclear reactors. The 68.27 %, 95.45 % and 99.73 % C.L. are represented. The black point indicates the best fit value whereas the dashed lines correspond to the interval of the total geo-neutrino rate from equation (6.40).

Chapter

7 Neutrino directionality studies

L'expérience est une observation provoquée dans le but de faire naître une idée.
Claude Bernard

Contents

The neutrino directionality information could, in principle, be applied when looking for particular sources such as core-collapse supernovae, when searching for geo-neutrinos, with the possibility to discriminate between crust and mantle, or for nuclear monitoring. Liquid scintillator detectors such as Double Chooz or Borexino can use the angular distribution of the positron and the neutron created in Inverse Beta Decay (IBD) interactions in order to retrieve the initial neutrino direction.

7.1 Neutrino directionality motivations

At the end of the last millenium, neutrinos started to be considered as an additional source of information when looking for core-collapse supernovae [177]. Indeed, whereas neutrinos can

easily escape from the core and travel directly to neutrino detectors on Earth, electromagnetic radiation is delayed before escaping this space region. Neutrinos will arrive on Earth a couple of hours before the light. If the detection of these neutrinos allows to know where they were coming from, then neutrino detectors can inform the community to point its telescopes in the space region of interest. This warning is a precious information for astronomical observations but need to have an on-time neutrino directionality measurement.

Neutrino directionality could also help the International Atomic Energy Agency (IAEA) to carry out its missions, among them the monitoring of nuclear reactor activities and the detection of attempts to divert fissile materials which are needed for nuclear weapon programs. In the case for instance of a clandestine nuclear reactor, neutrino directionality could allow to reveal its position on Earth [178].

7.2 Neutrino directionality principle

The feasibility of neutrino directionality measurement by liquid scintillator detectors is not obvious. Whereas water detectors can retrieve the initial ν_e direction thanks to the Čerenkov radiation emitted by the recoil of the electron in the elastic scattering reaction, this is not the case for $\bar{\nu}_e$ in liquid scintillator detectors such as Double Chooz or Borexino. We remind the reader that for these experiments, the $\bar{\nu}_e$ detection relies on the signature of the IBD interactions $\bar{\nu}_e + p \rightarrow e^+ + n$ where the positron is followed by the neutron capture on gadolinium (Gd) for Double Chooz or hydrogen (H) for both Double Chooz and Borexino. Since the emitted neutron preserves some information on the initial $\bar{\nu}_e$ direction, the $\bar{\nu}_e$ direction can be deduced from the reconstructed positions of the prompt and delayed vertices. Up to now, only the CHOOZ experiment provided neutrino directionallity measurement with $\bar{\nu}_e$. The analysis of about 2500 $\bar{\nu}_e$ candidates allowed to locate the source with an uncertainty of 18° [179].

7.2.1 Angular distributions

When we study neutrino directionality with $\bar{\nu}_e$, we have to take into account the physics related to the angular distributions of the positron and the neutron emitted through an IBD interaction. We then have to carefully investigate the behavior of these two signals.

Prompt signal angular distribution

The prompt signal corresponds to the positron scintillation and annihilation. Assuming the proton target to be at rest, the angular distribution of the outgoing positron can be described at zeroth order through the average cosine [107]:

$$\langle \cos(\theta_e) \rangle = \frac{1}{3} v_e \, a \simeq -0.034 \, v_e, \tag{7.1}$$

where θ_e is the angle between the $\bar{\nu}_e$ and the positron directions, v_e the positron velocity and a an asymmetry coefficient.

One can then conclude that the angular distribution of the positron is slightly backward. Nevertheless, since the positron will immediately annihilate with an electron or form a positronium with a longest lifetime of the order of 3 ns for the orthopositronium [180], we can neglect this weak backward. Indeed, Double Chooz and Borexino do not have an accurate enough spatial resolution to measure the few millimeters the positron will do in the backward direction. We will then safely assume that the positron vertex is the $\bar{\nu}_e$ vertex.

Delayed signal angular distribution

The delayed signal corresponds to the neutron capture on Gd or H. This process is longer than the positron one, the neutron capture on Gd takes about 30 µs whereas it is about 200 µs when considering the neutron capture on H. The physics between the neutron capture on Gd or H is also different since the neutron needs to thermalize before being captured on Gd whereas this thermalization is not needed for the neutron capture on H.

Since the positron is emitted slightly backward, the neutron has to be emitted forward in order to keep the momentum conservation. There is an angular correlation between the neutron direction and the initial $\bar{\nu}_e$ direction:

$$\cos\left(\theta_n\right)_{\max} = \frac{\sqrt{2E_{\bar{\nu}_e}\Delta - (\Delta^2 - m_e^2)}}{E_{\bar{\nu}_e}}, \tag{7.2}$$

with $\Delta = M_n - M_p$.

The neutron thermalization consists of a succession of elastic scatterings. This process allows the neutron to quickly decrease its energy, which impacts also its mean free path. The travel distance from the production point is then determined by the first scatterings. The average cosine for each scattering is given by [179]:

$$\langle\cos\left(\theta_n\right)\rangle = \frac{2}{3A}, \tag{7.3}$$

where θ_n is the angle between the incoming neutron and the outgoing neutron directions and A the atomic number of the scattering nucleus.

The neutron directionality is best preserved for low atomic number nuclei. Since the neutron will scatter with a higher probability on H because of a larger elastic scattering cross section, this process allows to memorize the initial neutron direction, and therefore the initial $\bar{\nu}_e$ direction.

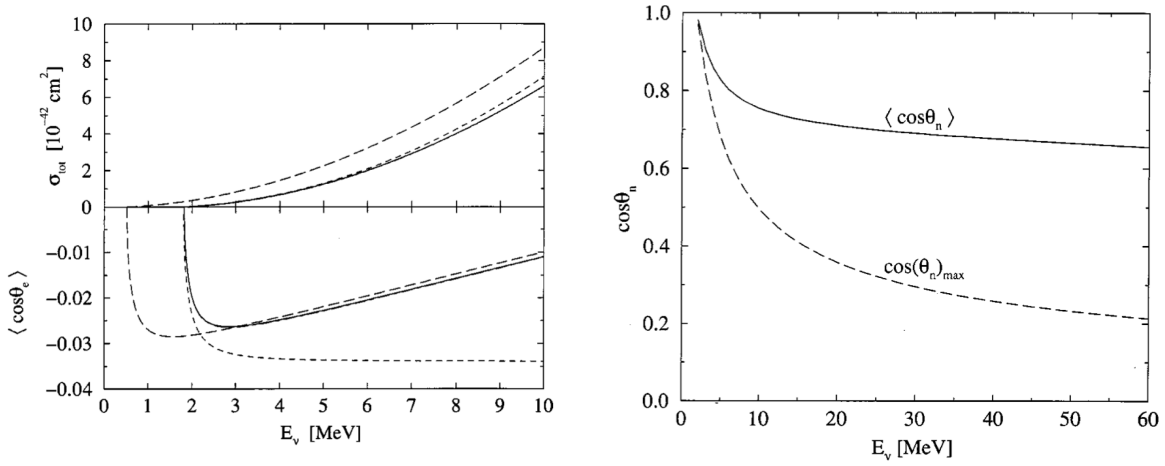

Figure 7.1: (*left*) Total cross section and average positron cosine for $\bar{\nu}_e + p \rightarrow e^+ + n$. (*right*) Average neutron cosine and cosine of the maximum neutron angle as a function of $\bar{\nu}_e$ energy, from [107].

7.2.2 Vectors and angles definition

For each neutrino candidate, we have both prompt and delayed signals. In order to measure the neutrino directionality, one has to focus on the spatial position of these two signals. It is indeed the most relevant information. From the reconstructed prompt and delayed vertices, we can define the signal vector $\vec{\mathrm{X}}_{\mathrm{Signal}}$ as:

$$\vec{\mathrm{X}}_{\mathrm{Signal}} = \vec{\mathrm{X}}_{\mathrm{prompt}} - \vec{\mathrm{X}}_{\mathrm{delayed}} \tag{7.4}$$

This vector has its origin at the reconstructed neutron capture vertex and is pointing the reconstructed positron vertex. In other words, this vector indicates where the neutrino candidate is coming from. We also need to build the unit signal vector:

$$\hat{\mathrm{X}}_{\mathrm{Signal}} = \frac{\vec{\mathrm{X}}_{\mathrm{Signal}}}{|\vec{\mathrm{X}}_{\mathrm{Signal}}|} \tag{7.5}$$

We can then calculate the $\vec{p}$ vector defined as the average of the unit signal vectors over all the neutrino candidates:

$$\vec{p} = \frac{1}{\mathrm{N}} \sum_{i=1}^{\mathrm{N}} \hat{\mathrm{X}}^i_{\mathrm{Signal}} \tag{7.6}$$

The direction of the $\vec{p}$ vector corresponds to the average neutrino wind, pointing to the source where they are coming from. We can finally deduce the azimuthal and zenithal angles, ϕ and θ, from the average neutrino wind $\vec{p}$.

Taking the $\vec{p}$ vector coordinates p_x, p_y and p_z, we have:

$$\phi = \tan^{-1} \frac{p_y}{p_x} \tag{7.7}$$

$$\theta = \tan^{-1} \frac{\sqrt{p_x^2 + p_y^2}}{p_z} \tag{7.8}$$

One of the most delicate points is the definition of the uncertainty on the measured direction. We use the CHOOZ method to compute it. Assuming the neutrino wind to lie along the z-axis, we have $\vec{p} = (0, 0, |\vec{p}|)$. We also assume that the normalised p_x, p_y and p_z distributions are uniform between -1 and +1 and therefore have $\sigma = 1/\sqrt{3}$. From the central limit theorem, it follows that the p_x, p_y and p_z distributions are gaussians with $\sigma = 1/\sqrt{3N}$ centered at respectively 0, 0 and $|\vec{p}|$. We then determine the uncertainty on the direction by generating a random gaussian generator and looking for the half-angle δ of the cone which contains 68 % of the simulated events.

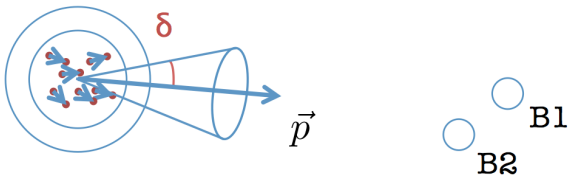

Figure 7.2: Sketch of the way the uncertainty on the measured direction is calculated.

7.3 Studies with Double Chooz

In the case of the Double Chooz experiment, we know where our neutrino candidates are coming from. We are then able to verify the precison of the method. Moreover, since the neutron can be captured either on Gd or H, with a completely different neutron capture physics, we can demonstrate the validity of the method in both cases.

A crucial point for Double Chooz is to perfectly understand the coordinate system and the distances between the two nuclear reactors and the Double Chooz far detector. In order to improve this knowledge, the Fit-Esic company conducted in January, 2013, a survey of the Double Chooz layout providing precise measurements of the two nuclear reactors and the Double Chooz far detector coordinates [181].

Table 7.1: Distance, azimuthal and zenithal angles of the reactors seen from the far detector frame, from [181].

Reactor	**Distance (m)**	ϕ **(°) (azimuthal)**	θ **(°) (zenithal)**
B1	1114.656 ± 0.015	87.190 ± 0.072	88.379 ± 0.001
B2	997.838 ± 0.015	80.929 ± 0.072	88.188 ± 0.001

Thanks to GPS measurements, the coordinates of several reference pillars allowed to connect different places of the Chooz nuclear power plant, including one at the Double Chooz far laboratory entrance. Figure 7.3 shows the laser-based polygonation method which was used to connect this last reference pillar to the far laboratory markers whose positions are

accurately known in the far detector framework. The combination of these two steps allows to precisely know the positions of the two nuclear reactors in the far detector framework, as summarizes in Table 7.1.

Figure 7.3: (*left*) GPS acquisition of the reference pillar #3 at the Chooz nuclear power plant. (*right*) A step of the polygonal route to the far laboratory, from [181].

7.3.1 Gd-capture sample analysis

Neutrino candidates with neutron capture on Gd have been investigated. We use the neutrino candidates from [42]. We first remind the selection that has been done before looking at the neutron displacement and finally at the neutrino directionality measurement.

Antineutrino selection

The cuts used for the antineutrino selection are:

- Not a muon event:
  - Total charge in IV < 30000 charge units
  - Visible energy in ID < 20 MeV
- Not a light noise event:
  - $\mathrm{RMS}(T_{\mathrm{start}}) < 36$ ns or $\mathrm{RMS}(Q) < 464 - 8 \times \mathrm{RMS}(T_{\mathrm{start}})$
  - $Q_{\mathrm{max}}/Q_{\mathrm{tot}} < 0.12$
  - $Q_{\mathrm{diff}} < 30000$ charge units
- **Prompt**:
  - $0.5 < E_{\mathrm{vis}} < 20$ MeV

- OV veto:
  - Candidates whose prompt signal is coincident with an OV trigger are rejected.
- IV veto:
  - IV PMT multiplicity ≥ 2
  - Total charge in IV > 400 charge units
  - ID-IV time coincidence: $-110 < \Delta t < -10$ ns
  - ID-IV space coincidence: $\Delta d < 3.7$ m
- $^{9}Li + ^{8}He$ veto:
  - $^{9}Li + ^{8}He$ likelihood < 0.4

- **Delayed**:
  - $4 < E_{vis} < 10$ MeV
  - F_V veto:
    - $E_{vis} > 0.068 \times \exp(F_V/1.23)$

- **Coincidence** (prompt and delayed):
  - Time coincidence: $0.5 < \Delta T < 150$ µs
  - Space coincidence: $\Delta R < 100$ cm

A 1 ms dead time veto is applied after each identified muon. An isolation cut is also applied, requesting no trigger in the 200 µs preceding the prompt candidate. The time window from 0.5 µs to 600 µs following the prompt candidate can contain only one valid trigger, the delayed candidate. Any other valid trigger in the 0.5 µs following the prompt candidate causes the rejection of the event. The number of neutrino candidates surviving to these cuts is 17358.

Neutron displacement

Since we assume the positron vertex to be the neutrino vertex, looking for the neutron vertex will allow us to access the average displacement between the interaction and capture vertices, *i.e.* the mean free path. In the case of a neutron capture on Gd, the neutron needs first to thermalize. Several collisions with the liquid scintillator atoms lead to a reduction of its energy. Hopefully, this thermalization phase is a non-isotropic process and allows the neutron to memorize the initial neutron direction. The average time for a neutron to be captured on Gd is estimated to be around 30 µs.

Figure 7.4 shows the neutron displacement w.r.t. the positron along the x, y and z-axis, as measured in Double Chooz. A fit made of a convolution of a gaussian together with an exponential has been performed. Due to the Double Chooz layout, one should expect $\mu_y > \mu_x$ since we know that the y-axis is almost pointing the reactors. Also, since the reactors are located above the detector, one should expect a positive value of μ_z, which is not the case here. It will have consequences on the measurement of the zenithal angle θ.

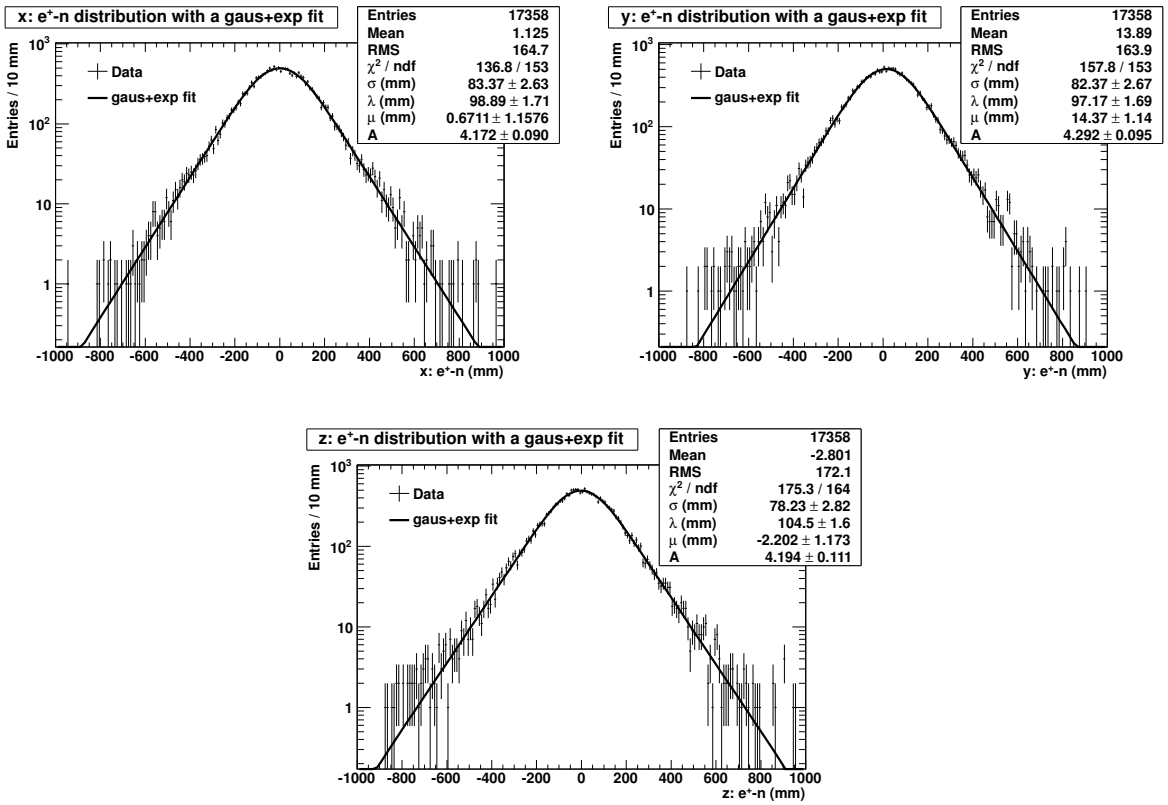

Figure 7.4: Positron-neutron displacement distribution along the x, y and z-axis.

Due to the uncertainty on the reconstruction of the neutron and positron vertices, only the average displacement is of interest [182]. It is obtained by adding the mean values of the fits in quadrature:

$$l_{\text{Data}} = \sqrt{\mu_x^2 + \mu_y^2 + \mu_z^2} = 14.55 \pm 1.14 \text{ mm} \tag{7.9}$$

This value is in agreement with the one obtained with the MC:

$$l_{\text{MC}} = 14.27 \pm 0.11 \text{ mm} \tag{7.10}$$

From the cylindrical geometry of the detector, we expect the RMS of the positron-neutron displacement distribution to be the same along the x and y-axis and to be a bit worth along the z-axis, which is the case.

Neutrino directionality measurement

With the selection of the 17358 neutrino candidates, we can proceed to the calculation of the ϕ and θ angles. The $\vec{p}$ vector coordinates are obtained from the mean value of the normalised p_x, p_y and p_z distributions:

$$\vec{p} = (0.0039, 0.0540, -0.0077) \tag{7.11}$$

The third coordinate is a bit disturbing since we know that the reactors are located above the detector. We should obtain a positive coordinate. This will be discussed later on. From

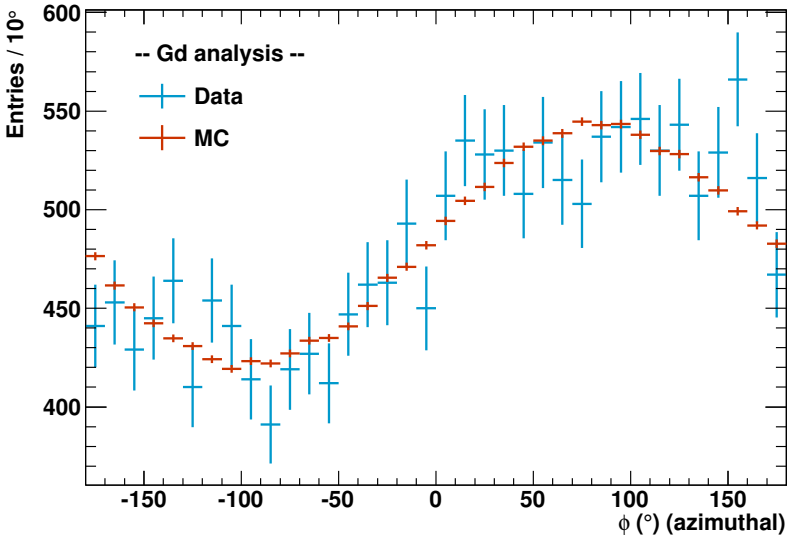

Figure 7.5: ϕ distribution of the 17358 neutrino candidates with neutron capture on Gd. Both data and MC are shown.

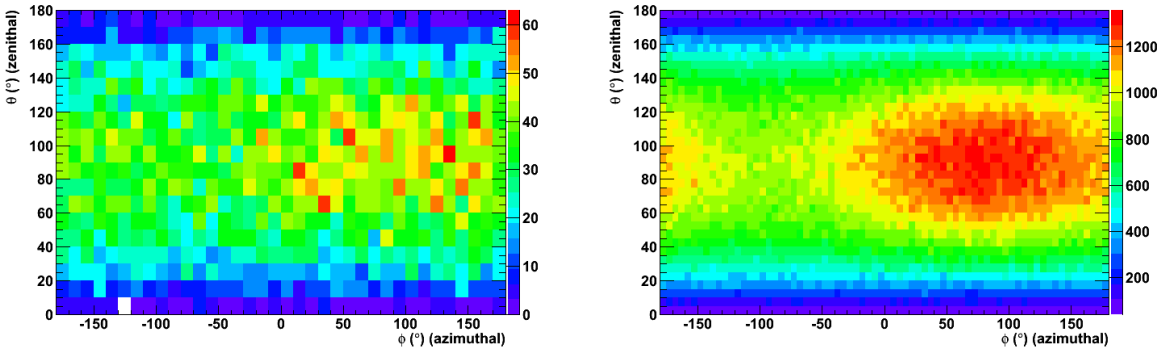

Figure 7.6: θ vs ϕ distribution for both data (*left*) and MC (*right*).

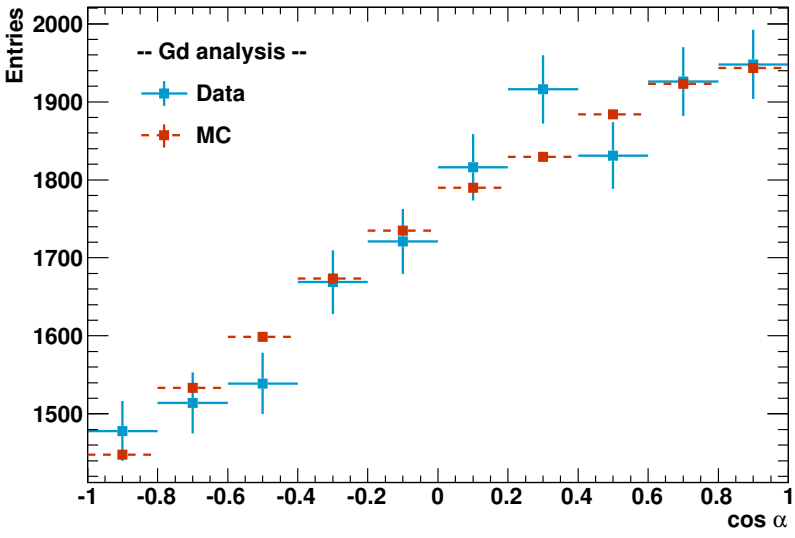

Figure 7.7: $\cos\alpha$ distribution for both data and MC. α is the angle between the signal vectors and the detector-reactors vector.

the $\vec{p}$ vector coordinates, we can extract the average neutrino wind direction. Table 7.2 summarizes the values of the angles for both data and MC.

Table 7.2: Azimuthal, zenithal and uncertainty angles for the Gd analysis with both data and MC.

Gd analysis	ϕ (°)	θ (°)	δ (°)
Data	85.8	98.1	7.0
MC	84.0	89.6	0.7

Figure 7.5 illustrates the azimuthal angle distribution for both data and MC. Data and MC are matching, leading to a bump around 84° which is expected from the layout described in Table 7.1. Figure 7.6 (*left*) shows the distribution of the neutrino candidates in the (ϕ, θ) plane. For comparison, Figure 7.6 (*right*) shows the same distribution for MC. A clear concentration of events can be seen around $\phi = 84°$ and $\theta = 88°$.

A way to access the performance of neutrino directionality measurement is to evaluate the α angle between the reconstructed and true directions of the incoming neutrinos. In particular, the scalar product between each signal vector and the true detector-reactors vector should point more $+1$ than -1. Figure 7.7 represents this scalar product through the $\cos\alpha$ distribution. Data and MC are in agreement and both distributions point $\cos\alpha = +1$, which means that there is an alignement between the reconstructed and true directions.

7.3.2 H-capture sample analysis

Studies in literature focused on scintillators doped with high neutron capture cross section elements, such as Gd, which should minimize neutron diffusion. Nevertheless, directionality studies using neutron capture on H is possible and is potentially very interesting for future large-scale neutrino detectors, such as LENA, JUNO or RENO-50 which will use un-doped scintillators. H analysis allows also to cross-check the method and the results from Gd analysis.

Antineutrino selection

The cuts used for the antineutrino selection are:

- Not a muon event:
  - Total charge in IV < 30000 charge units
  - Visible energy in ID < 20 MeV
- Not a light noise event:
  - RMS(T_{start}) < 36 ns or RMS(Q) $< 464 - 8 \times$ RMS(T_{start})

- $Q_{max}/Q_{tot} < 0.12$
- $Q_{diff} < 30000$ charge units

- **Prompt**:
  - $0.7 < E_{vis} < 20$ MeV
  - OV veto:
    - Candidates whose prompt signal is coincident with an OV trigger are rejected.
  - IV veto:
    - IV PMT multiplicity ≥ 2
    - Total charge in IV > 400 charge units
    - ID-IV time coincidence: $-110 < \Delta t < -30$ ns
    - ID-IV space coincidence: $\Delta d < 4$ m
  - ^{9}Li $+ ^{8}$He veto:
    - ^{9}Li $+ ^{8}$He likelihood < 0.4

- **Delayed**:
  - $1.8 < E_{vis} < 2.6$ MeV
  - F_V veto:
    - $E_{vis} > 0.2208 \times \exp(F_V/1.818)$

- **Coincidence** (prompt and delayed):
  - Time coincidence: $0.5 < \Delta T < 300$ μs
  - Space coincidence: $\Delta R < 60$ cm

A 1250 μs dead time veto is applied after each identified muon. An isolation cut is also applied, requesting no trigger in the 600 μs preceding the prompt candidate. The time window from 0.5 μs to 900 μs following the prompt candidate can contain only one valid trigger, the delayed candidate. Any other valid trigger in the 0.5 μs following the prompt candidate causes the rejection of the event. The number of neutrino candidates surviving to these cuts is 34630.

Table 7.3: Summary of the number of observed IBD candidates and the predictions for signal and background contributions used as input for the oscillation fit analysis performed in [41].

Source	**Predicted/Observed events**
$\bar{\nu}_e$ prediction (no osc.)	17690
Accidentals	17630
Cosmogenic isotopes	680
Fast neutrons	600
Light noise	80
Total prediction	36680
Observed IBD candidates	36284

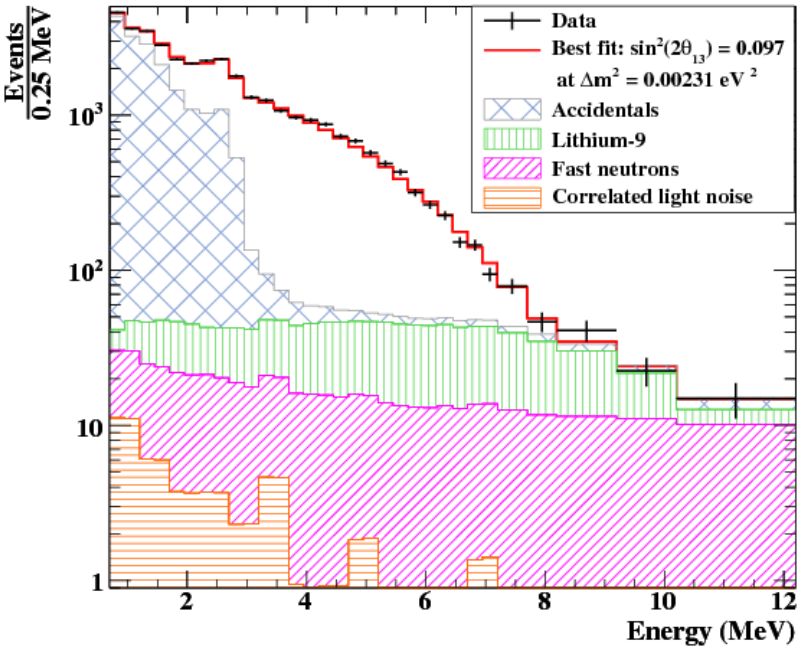

Figure 7.8: Visible energy spectrum of the prompt signals together with the different background contributions. Accidental background dominates at low energy.

Nevertheless, a non-negligible amount of these neutrino candidates are accidental background which dominates the prompt visible energy spectrum at low energy. Table 7.3 and Figure 7.8 are extracted from [41] and illustrate the different contributions at that time. An important work has been done since this publication which now allows a huge decrease of the accidental background. Preliminary cuts have been enhanced, the delayed visible energy range has been reduced from [1.5, 3.0 MeV] to [1.8, 2.6 MeV], ΔR from 90 cm to 60 cm and ΔT from [10, 600 µs] to [0.5, 300 µs].

Since it is known that accidental background dominates at low energy, we decided to apply an additional cut to select a purer sample. Since ΔT and ΔR are correlated with the directionality measurement, we decided not to implement cuts on these two variables and to focus on an additional visible energy cut on prompt signals.

We investigated the signal over accidentals ratio in order to find the minimal prompt energy cut which allows us to have the highest ratio. We took MC and accidentals samples used in [41] and made the normalization according to Table 7.3. Figures 7.9 show that the signal over accidentals ratio is maximal for $E_{cut} > 3.5$ MeV. For this visible energy cut on the prompt signal, we keep 40.5 % of neutrino candidates and 1.1 % of accidentals. We verified that this cut does not affect the behavior of ϕ and θ from MC studies.

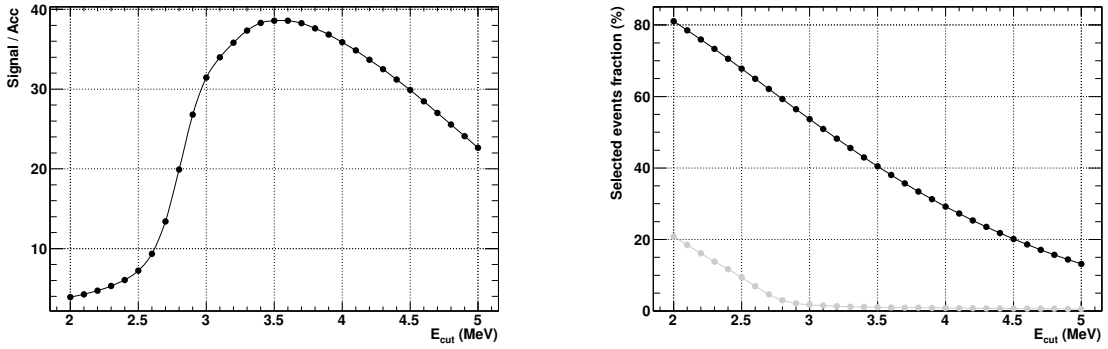

Figure 7.9: (*left*) Signal over accidentals ratio when applying minimal visible energy cuts on the prompt signal. (*right*) Selected events fraction when applying minimal visible energy cuts on the prompt signal.

Neutrino directionality measurement

With the selection of these 13048 neutrino candidates, we can proceed to the calculation of the ϕ and θ angles. The $\vec{p}$ vector coordinates are obtained from the mean value of the normalised p_x, p_y and p_z distributions:

$$\vec{p} = (0.0143, 0.0469, 0.0013) \tag{7.12}$$

From the $\vec{p}$ vector coordinates, we can extract the average neutrino wind direction. Table 7.4 summarizes the values of the angles for both data and MC.

Table 7.4: Azimuthal, zenithal and uncertainty angles for the H analysis with both data and MC.

H analysis	ϕ (°)	θ (°)	δ (°)
Data	73.0	88.5	8.9
MC	84.4	87.3	1.1

Figure 7.10 illustrates the azimuthal angle distribution for both data and MC. As for the Gd analysis, data and MC are matching, leading to a bump around 84°. Figure 7.11 (*left*) shows the distribution of the neutrino candidates in the (ϕ, θ) plane. For comparison, Figure 7.11 (*right*) shows the same distribution for MC. A clear concentration of events can be seen around $\phi = 84°$ and $\theta = 88°$.

As for the Gd analysis, we access the performance of neutrino directionality measurement with neutron capture on H by looking at the scalar product between each signal vector and the true detector-reactors vector. Figure 7.12 represents this scalar product through the $\cos\alpha$ distribution. Data and MC are in agreement and both distributions point $\cos\alpha = +1$, which means that there is an alignement between the reconstructed and true directions.

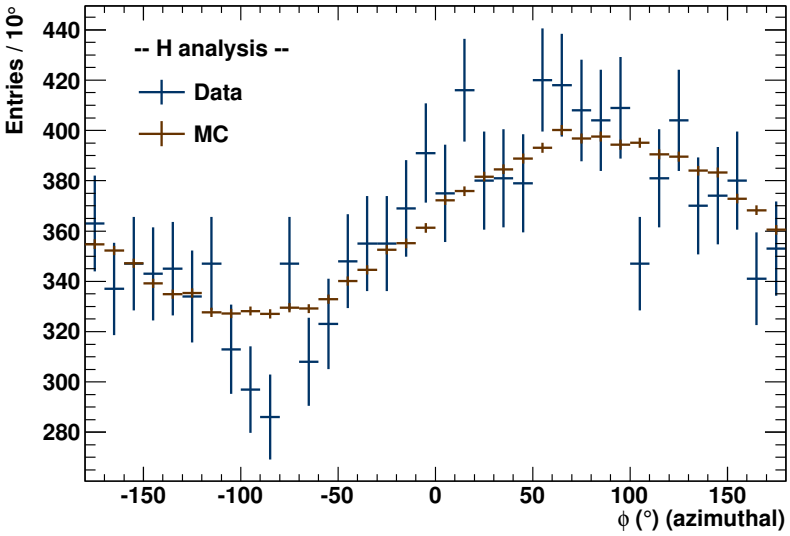

Figure 7.10: ϕ distribution of the 13048 neutrino candidates with neutron capture on H. Both data and MC are shown.

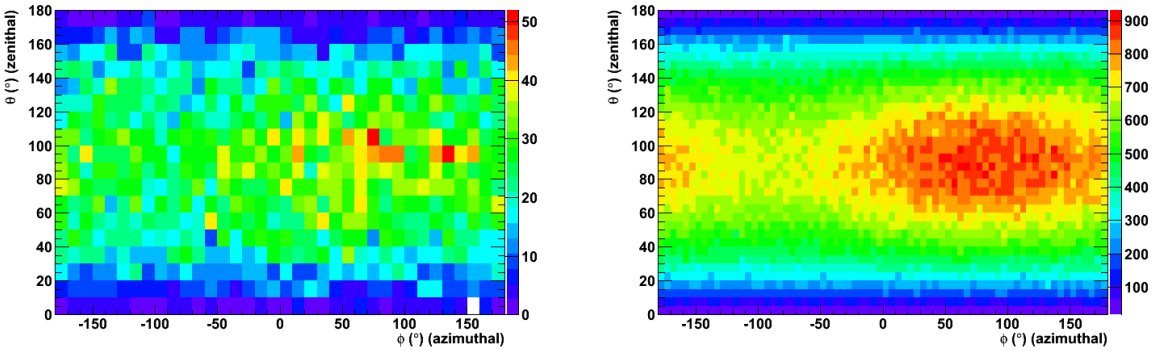

Figure 7.11: θ vs ϕ distribution for both data (*left*) and MC (*right*).

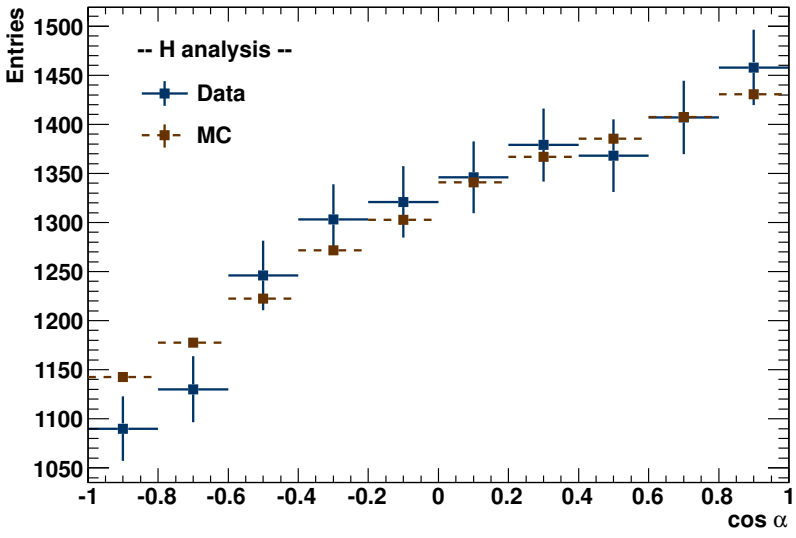

Figure 7.12: $\cos\alpha$ distribution for both data and MC. α is the angle between the signal vectors and the detector-reactors vector.

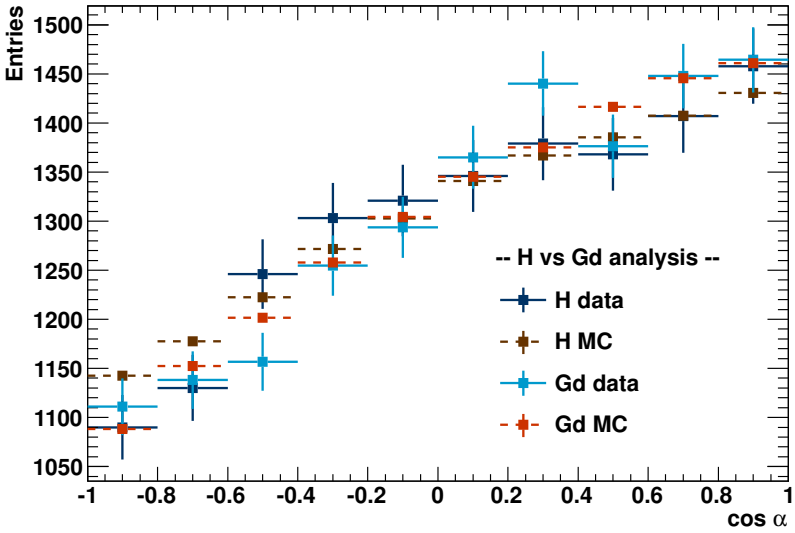

Figure 7.13: $\cos\alpha$ distribution for both Gd and H analysis. α is the angle between the signal vectors and the detector-reactors vector.

Figure 7.13 shows the behavior of both the Gd-capture sample and the H-capture sample. There is a good agreement between the two analyses.

7.3.3 Only one reactor on

Double Chooz has the possibility to deal from time to time with only one reactor on. Since the present resolution is comparable to the angular distance between the two nuclear reactors, it is of interest to investigate these periods and see if we end with a narrower distribution.

Runs with reactor off for more than 48 h were selected from the reactor database. The selection was made in a conservative way, meaning that few runs before and after one given period could also be used.

Reactor B1 was off for the following periods:

- From September 24 to November 28, 2011, for a total of 1239 runs
- From September 15 to September 17, 2012, for a total of 43 runs

Reactor B2 was off for the following periods:

- From April 24 to May 07, 2011, for a total of 217 runs
- From July 14 to July 19, 2011, for a total of 100 runs
- From February 15 to August 25, 2012, for a total of 3432 runs

From Table 7.1, the true values when reactor B2 is the only reactor on are $\phi = 80.9°$ and $\theta = 88.2°$ and the true values when reactor B1 is the only reactor on are $\phi = 87.2°$ and

$\theta = 88.4°$. Tables 7.5 and 7.6 summarize the number of events as well as the values of the angles in the cases where only one reactor is on. Results for Gd and H analyses are presented in both cases. The present statistics is not sufficient to provide a good conclusion. With much more statistics, the Double Chooz near detector will help to deconvolute the two reactors.

Table 7.5: Azimuthal, zenithal and uncertainty angles for Gd and H analyses in the case of B2 running alone.

B1 off	**Events**	ϕ (°)	θ (°)	δ (°)
Gd analysis	1432	86.3°	109.8°	26.1°
H analysis	1142	81.0°	101.7°	26.4°

Table 7.6: Azimuthal, zenithal and uncertainty angles for Gd and H analyses in the case of B1 running alone.

B2 off	**Events**	ϕ (°)	θ (°)	δ (°)
Gd analysis	3464	95.2°	95.7°	13.5°
H analysis	2620	73.2°	94.6°	15.3°

7.4 Vertex position reconstruction correction

Neutrino directionality measurement relies on the precision of the vertex position reconstruction. It is the key of such a study. This vertex position reconstruction is performed through a package which takes into account charge and time informations from each PMT, as explained in Section 3.3.2. The zenithal angle, θ, for the Gd analysis has be found to be 98.1° when one should expect a value around 88°. We first investigate this unexpected behavior.

7.4.1 Investigation of the θ bias

Let us have a look at the detector response w.r.t. to the vertex position reconstruction of the event. One can think to separate the detector volume into several smaller volumes and to look for any unexpected behavior. We separate the target volume into three smaller volumes in order to check a possible bias along the z-axis:

- Top area: $\bar{\nu}_e$ candidates which satisfy $z_{\text{prompt}} > 410$ mm
- Center area: $\bar{\nu}_e$ candidates which satisfy $-410 < z_{\text{prompt}} < 410$ mm
- Bottom area: $\bar{\nu}_e$ candidates which satisfy $z_{\text{prompt}} < -410$ mm

Figure 7.14 shows the zenithal distribution for the three volumes considered. A clear shift of the θ central value can be observed. It is shifted to a positive value when considering the

top of the detector and is shifted to a negative value when considering the bottom of the detector. We now investigate the MC data in order to check whether we have to look for a physics reason or if we have to deal with a reconstruction effect.

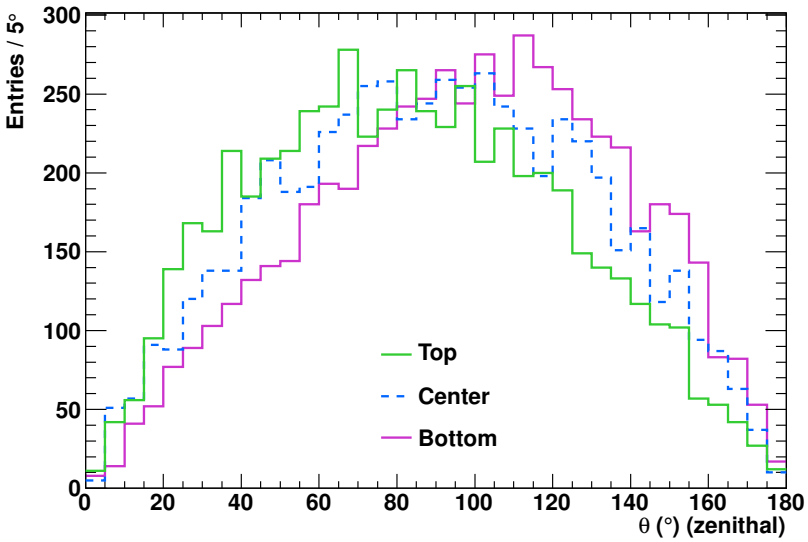

Figure 7.14: θ distributions when considering different volumes in the target.

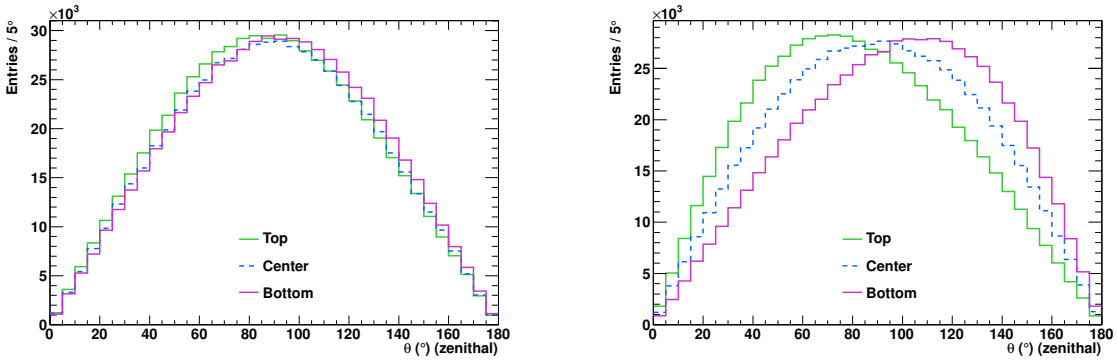

Figure 7.15: θ distributions of the true MC (*left*) and the reconstructed MC (*right*) when considering different volumes in the target.

Figures 7.15 show the zenithal distributions for the true and the reconstructed positions of the vertices. When applying the reconstruction algorithm, we are left with the response of the detector, *i.e.* the way the detector is seeing these events. There should not be such a difference, whatever the section of the target we are considering.

Since the algorihm tends to reconstruct the events closer to the center of the detector than they are really, one can think about a saturation effect of the PMTs. Indeed, if a fraction of the total amount of charges which should be seen by the PMTs is missing, then the

algorithm will reconstruct an event further than it is really. This saturation hypothesis has been investigated using MC.

Electrons have been generated along the z-axis. Three different positions have been chosen in order to check the behavior of the detector response when having an energy deposition in the top, the center or the bottom of the target. If the amplitude of a waveform reaches the dynamic range of the FADC, then the waveform is cutted. It means that a part of the signal has not been reconstructed, leading to a mis-reconstruction of the true position of the event vertex. An event is said saturated if at least one PMT is saturated.

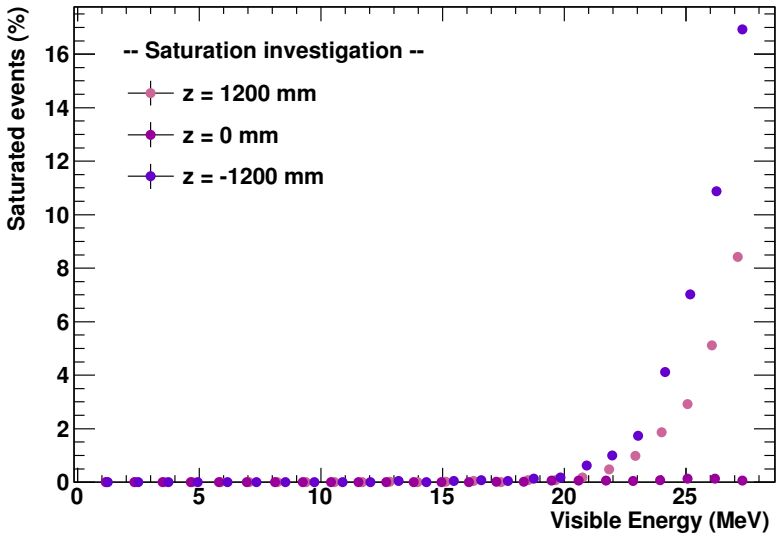

Figure 7.16: Saturation variation as a function of the visible energy.

Figure 7.16 shows the saturation variation as a function of the visible energy. Whereas events generated in the center of the target do not saturate the PMTs, events in the top and the bottom of the target start to sature the PMTs around 20 MeV. This is safe enough neither to affect the θ_{13} analysis nor the neutrino directionality analysis. The origin of the bias remains unexplained. In the following, we will developed corrections based on MC and calibration sources deployments.

7.4.2 Position reconstruction correction for MC

In order to estimate the z position reconstruction correction on MC, samples of electrons are generated with an initial energy which ranges from 1 MeV to 10 MeV by steps of 1 MeV. They are generated along the z-axis in order to check later on with calibration sources located at the same positions. The positions along the z-axis are 0, $\pm$160, $\pm$320, $\pm$480, $\pm$640, $\pm$800, $\pm$960, $\pm$1105 and $\pm$1250 mm.

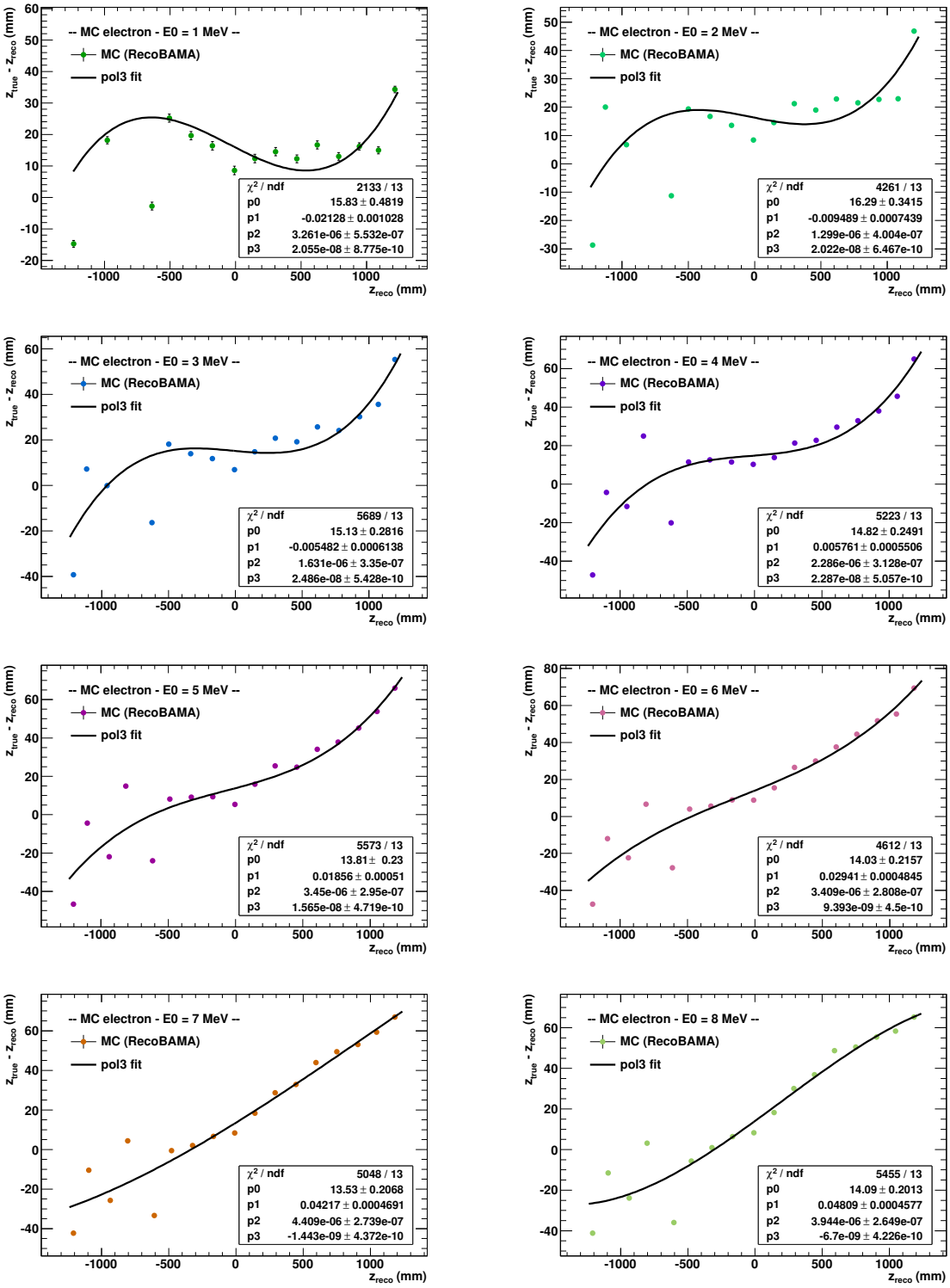

Figure 7.17: Differences between true and reconstructed z position, $z_{\text{true}} - z_{\text{reco}}$, as a function of z_{reco}, for different electron energies in MC.

Figure 7.17 shows the difference between the z coordinate of the true vertices of generation and their reconstructed vertices. The events are reconstructed closer to the center of the detector than they really are. This difference depends on the reconstructed z position and can be fitted by a third-degree polynomial:

$$f(z_{\text{reco}}) = z_{\text{true}} - z_{\text{reco}} = \text{p0} + \text{p1} \times z_{\text{reco}} + \text{p2} \times z_{\text{reco}}^2 + \text{p3} \times z_{\text{reco}}^3 \tag{7.13}$$

Figure 7.18 shows a dependence of the p0, p1, p2 and p3 parameters on the energy:

$$\text{p0} = 15.58 - 0.1806 \times \text{E}_{\text{vis}} \tag{7.14}$$

$$\text{p1} = -0.02974 + 0.008117 \times \text{E}_{\text{vis}} \tag{7.15}$$

$$\text{p2} = 1.21 \cdot 10^{-6} + 3.105 \cdot 10^{-7} \times \text{E}_{\text{vis}} \tag{7.16}$$

$$\text{p3} = 3.946 \cdot 10^{-8} - 4.778 \cdot 10^{-9} \times \text{E}_{\text{vis}} \tag{7.17}$$

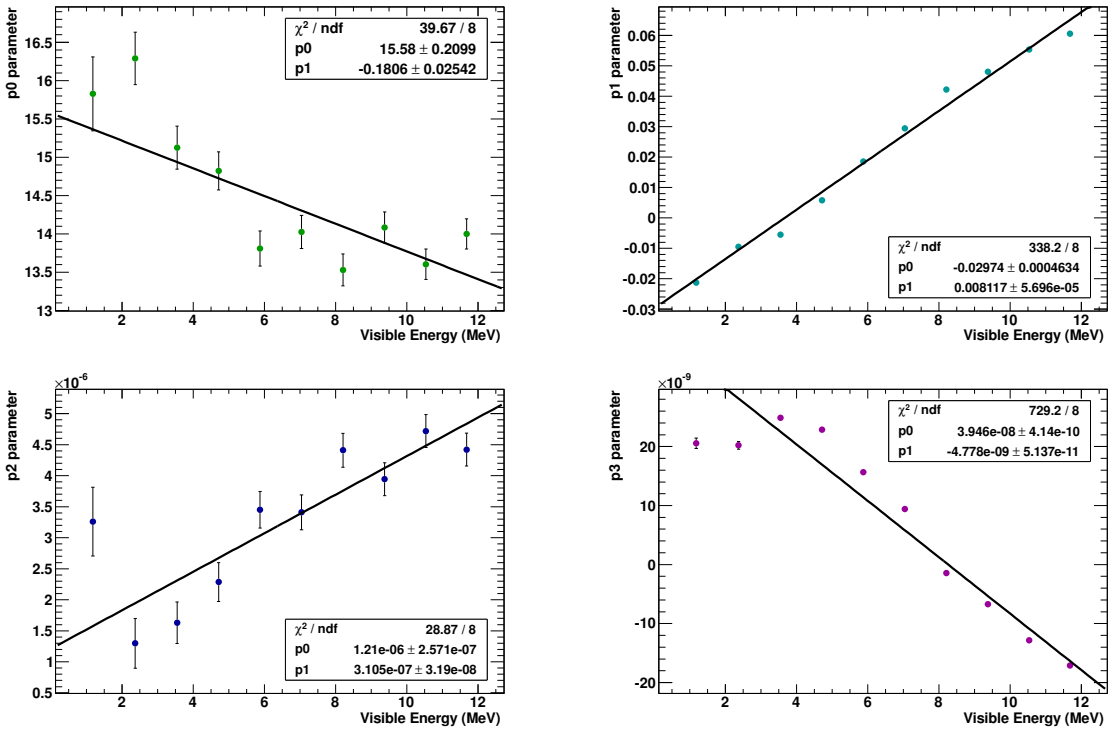

Figure 7.18: Fit results of the different parameters from electron sample generated with different electron energies in MC.

Including 7.14, 7.15, 7.16 and 7.17 in 7.13, we obtain the z position correction formula for MC:

$$\begin{aligned} f_{\text{MC}}(z_{\text{reco}}) = {} & 15.58 - 0.1806 \times \text{E}_{\text{vis}} \\ & + (-0.02974 + 0.008117 \times \text{E}_{\text{vis}}) \times z_{\text{reco}} \\ & + (1.21 \cdot 10^{-6} + 3.105 \cdot 10^{-7} \times \text{E}_{\text{vis}}) \times z_{\text{reco}}^2 \\ & + (3.946 \cdot 10^{-8} - 4.778 \cdot 10^{-9} \times \text{E}_{\text{vis}}) \times z_{\text{reco}}^3 \end{aligned} \tag{7.18}$$

7.4.3 Position reconstruction correction for data

The corrections to be applied on the MC are not necessarily the same as the ones we should apply on the data. In order to evaluate the corrections on data, we use calibration runs taken during the second campaign and we compare the true positions of the deployed radioactive sources and the reconstructed positions given by the reconstruction algorithm.

Table 7.7: Properties of the radioactive sources used in Double Chooz.

Source		Activity (kBq)	Energy (MeV)
γ	^{137}Cs	0.2	662 keV
	^{68}Ge	0.2	2 × 511 keV
	^{60}Co	0.2	1.173 MeV and 1.333 MeV
neutron	^{252}Cf	1	2.2 MeV (H) / 8 MeV (Gd)

Table 7.7 shows the different radioactive sources we use in order to calibrate the detector. We investigate the ^{137}Cs, ^{68}Ge and ^{60}Co calibration sources in order to correct the prompt signal since these sources emit γ. Since the ^{252}Cf source is a neutron emitter, it helps us to investigate the correction to be applied on the delayed signal.

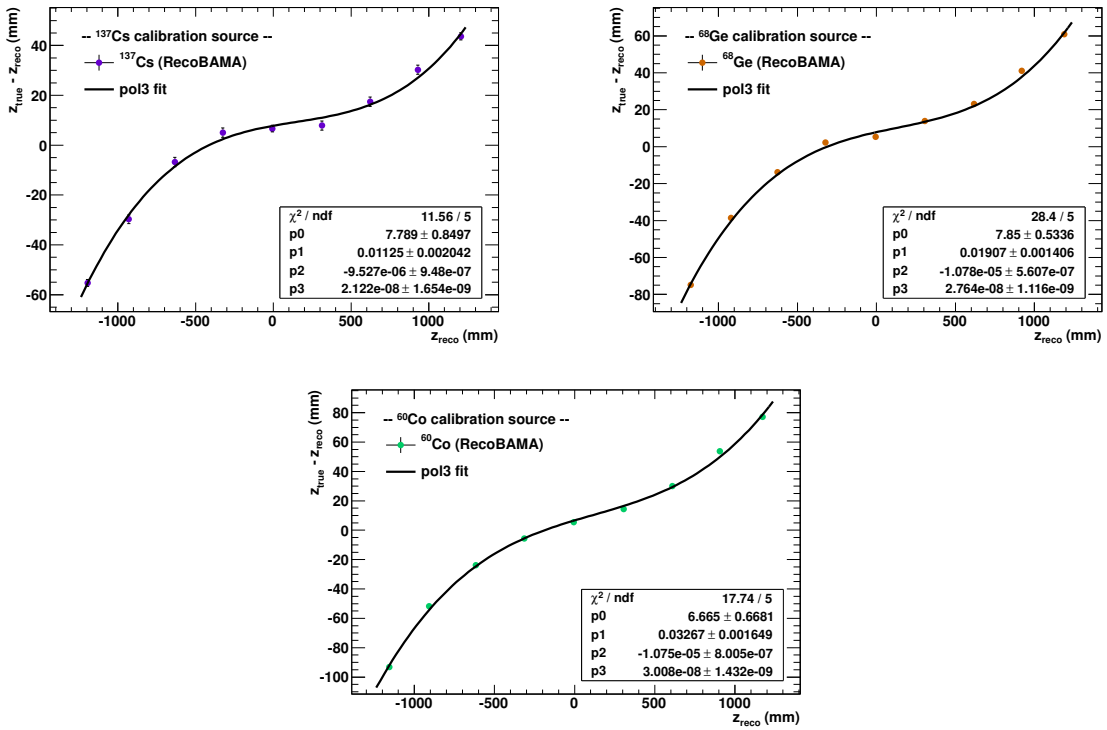

Figure 7.19: Differences between true and reconstructed z position, $z_{\text{true}} - z_{\text{reco}}$, as a function of z_{reco}, for ^{137}Cs (*top left*), ^{68}Ge (*top right*) and ^{60}Co (*bottom*).

Prompt signal z correction

Figure 7.19 illustrates the difference between the z coordinate of the true positions of the calibration sources and their reconstructed positions, as a function of z_{reco}. As for the MC position reconstruction correction, the correction to be applied follows a third-degree polynomial:

$$f(z_{\text{reco}}) = z_{\text{true}} - z_{\text{reco}} = \text{p0} + \text{p1} \times z_{\text{reco}} + \text{p2} \times z_{\text{reco}}^2 + \text{p3} \times z_{\text{reco}}^3 \tag{7.19}$$

The p0, p1, p2 and p3 parameters can be energy dependent, as shown in Figure 7.20, althrough the dependence is less pronounced than on MC:

$$\text{p0} = 7.466 \tag{7.20}$$

$$\text{p1} = 0.008475 + 0.01029 \times \text{E}_{\text{vis}} \tag{7.21}$$

$$\text{p2} = -1.053 \cdot 10^{-5} \tag{7.22}$$

$$\text{p3} = 2.694 \cdot 10^{-8} \tag{7.23}$$

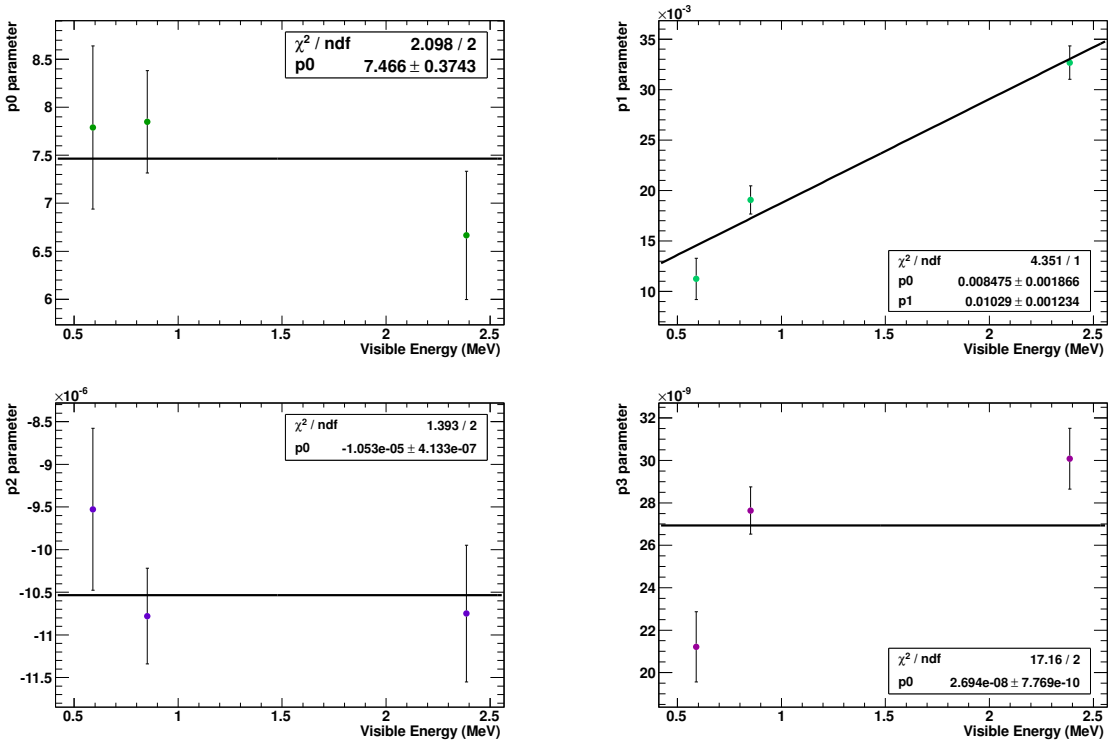

Figure 7.20: Fit results of the different parameters from ^{137}Cs, ^{68}Ge and ^{60}Co.

Including 7.20, 7.21, 7.22 and 7.23 in 7.19, we obtain the z position correction formula for data:

$$\begin{aligned} f_{\text{Data}}(z_{\text{reco}}) = {} & 7.466 \\ & + (0.008475 + 0.01029 \times \text{E}_{\text{vis}}) \times z_{\text{reco}} \\ & - 1.053 \cdot 10^{-5} \times z_{\text{reco}}^2 \\ & + 2.694 \cdot 10^{-8} \times z_{\text{reco}}^3 \end{aligned} \tag{7.24}$$

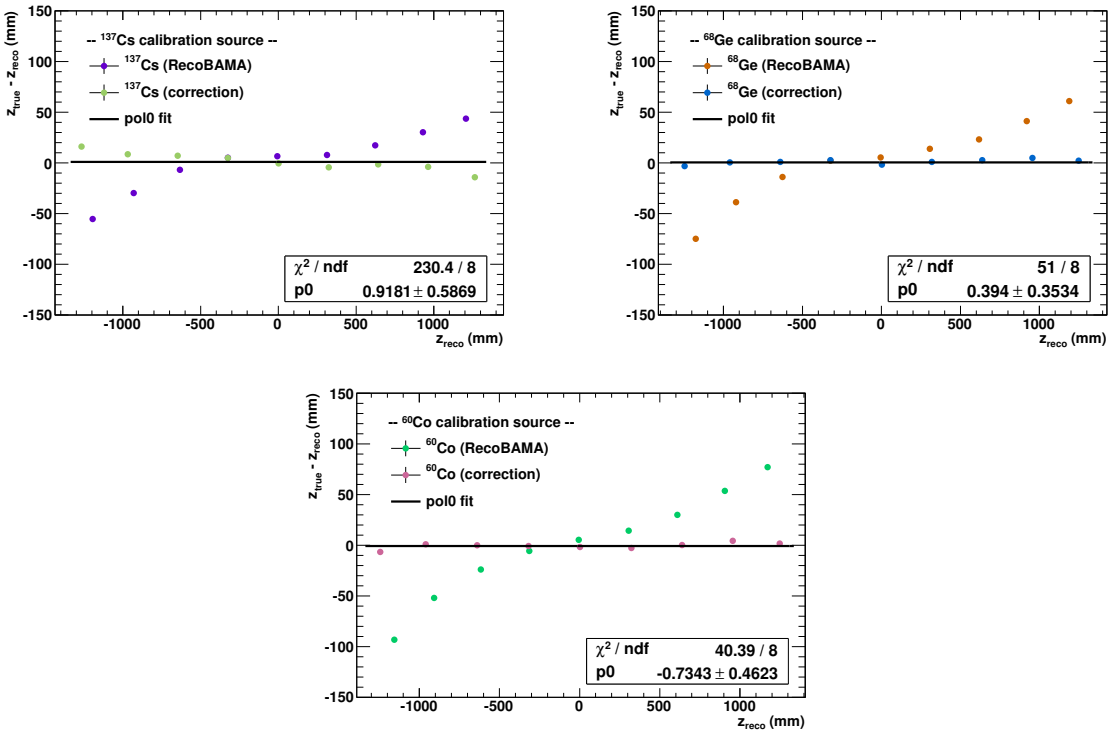

Figure 7.21: Differences between true and reconstructed z position, $z_{\text{true}} - z_{\text{reco}}$, as a function of z_{reco}, for ^{137}Cs (*top left*), ^{68}Ge (*top right*) and ^{60}Co (*bottom*). The position reconstruction correction is applied and is fitted with a zeroth-degree polynomial.

Figure 7.21 represents the $z_{\text{true}} - z_{\text{reco}}$ differences for each calibration source, before and after the corrections. The corrections developed above are the best we can do at present for neutrino candidates, for which nevertheless they have some limitations. First, calibration sources have energies only up to 2.5 MeV and second, we can not guess a possible radial dependence of the corrections.

Delayed signal z correction

The position reconstruction correction of the delayed signal is investigated by looking at the neutron capture produced by the fission of ^{252}Cf. Both neutron capture on Gd and H are studied. The deployement of the ^{252}Cf calibration source took place on June 6 and 7, 2012, during the second campaign. The source was deployed along the z-axis at 0, ±160, ±320, ±480, ±640, ±800, ±960, ±1105 and ±1250 mm. Several cuts are applied in order to access the ^{252}Cf fission signal:

- Not a muon event:
  - Total charge in IV < 30000 charge units
  - $\Delta t_{\mu} > 1$ ms

- Not a light noise event:
  - $RMS(T_{start}) < 36$ ns or $RMS(Q) < 464 - 8 \times RMS(T_{start})$
  - $Q_{max}/Q_{tot} < 0.12$
  - $Q_{diff} < 30000$ charge units

- **Prompt**:
  - $4 < E_{vis} < 30$ MeV
  - $\Delta t_{veto} = 1.5$ ms

- **Delayed**:
  - $0.5 < E_{vis} < 25$ MeV
  - F_V veto:
    - $E_{vis} > 0.068 \times \exp(F_V/1.23)$

- **Coincidence** (prompt and delayed):
  - Time coincidence: $0 < \Delta T < 1$ ms

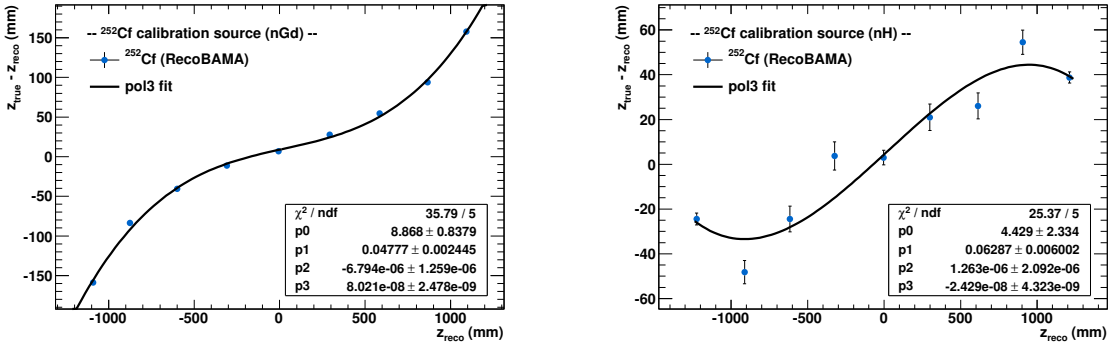

Figure 7.22: Differences between true and reconstructed z position, $z_{true} - z_{reco}$, as a function of z_{reco}, for ^{252}Cf when considering neutron capture on Gd (*left*) and H (*right*).

The delayed energy range is then adapted when looking for neutron capture on Gd or H. It is defined to range in the [7.8, 8.4 MeV] interval for the Gd analysis and in the [1.8, 2.4 MeV] interval for the H analysis. Figure 7.22 shows the reconstruction behavior of the neutron capture on Gd and H. The correction to be applied follows here again a third-degree polynomial which will be directly applied to the delayed signals.

7.4.4 Impact of vertex position reconstruction bias on θ_{13} analysis

Due to the misbehavior in the vertex position reconstruction, it is legitimate to wonder whether this might have an impact on the θ_{13} analyses by altering the correlation distance, ΔR, between prompt and delayed vertices, on which a cut is applied. In order to do so, we applied the corrections on the prompt and delayed signals and we estimate the variation in

terms of number of selected events.

The Double Chooz Gd-capture analysis applies a cut $\Delta R < 100$ cm. Nevertheless, since our sample does not contain events with $\Delta R > 100$ cm, we reduced this cut to 90 cm in order to allow events with $\Delta R > 90$ cm to be able to pass the selection cut after correction. Before correction, we have 17304 neutrino candidates which satisfy $\Delta R < 90$ cm. After correction, we end with 17262 neutrino candidates. We then loose 0.2 % of our initial selection, which remains negligible.

Since most of the neutrino candidates with neutron capture on H take place in the γ-catcher, we can not apply these corrections which focus on the target volume.

7.5 Studies with Borexino

Neutrino directionality can facilitate the discrimination between geo-neutrinos and $\bar{\nu}_e$ from nuclear reactors, the main background in the geo-neutrino analysis. Indeed, whereas geo-neutrinos are generated in the crust and in the mantle of the Earth, nuclear reactors stand at the surface of our planet, leading to a different angular distribution. Directionality of neutrino candidates identified in the previous chapter is investigated in this section.

We remind the cuts used for the antineutrino selection:

- **Prompt**:
  - $Q_{prompt} > 408$ p.e.
  - Fiducial Volume (FV) cut asking to have a distance greater than 25 cm from the target vessel
  - No neutron-like event in the 2 ms preceding the prompt signal
- **Delayed**:
  - $860 < Q_{delayed} < 1300$ p.e.
  - No neutron-like event in the 2 ms following the delayed signal
- **Coincidence** (prompt and delayed):
  - Time coincidence: $20 < \Delta t < 1280$ µs
  - Space coincidence: $\Delta R < 100$ cm

The number of neutrino candidates surviving to these cuts is 47.

In Double Chooz, the $\bar{\nu}_e$ are provided by an almost point-like source, the two nuclear reactors, while, in Borexino, we expect a diffuse angular distribution. For this reason, we implement a different approach. In Borexino, the neutron capture can occur only on H since there is no Gd entering the composition of the liquid scintillator. The prompt and delayed signals are reconstructed and lead to the definition of the signal vector as in equation (7.5):

$$\vec{X}_{Signal} = \vec{X}_{prompt} - \vec{X}_{delayed} \tag{7.25}$$

In the Double Chooz analysis we have defined the $\vec{p}$ vector as the average of the unit signal vectors over all the neutrino candidates. Differently in Borexino, $\vec{p}$ is defined such that $\vec{p} = \hat{\mathrm{X}}_{\mathrm{Signal}}$, on an event-by-event basis. The azimuthal and zenithal angles, ϕ and θ, for each neutrino candidate are defined as in equations (7.7) and (7.8):

$$\phi = \tan^{-1} \frac{p_y}{p_x} \tag{7.26}$$

$$\theta = \tan^{-1} \frac{\sqrt{p_x^2 + p_y^2}}{p_z} \tag{7.27}$$

where p_x, p_y and p_z correspond to the $\vec{p}$ vector coordinates.

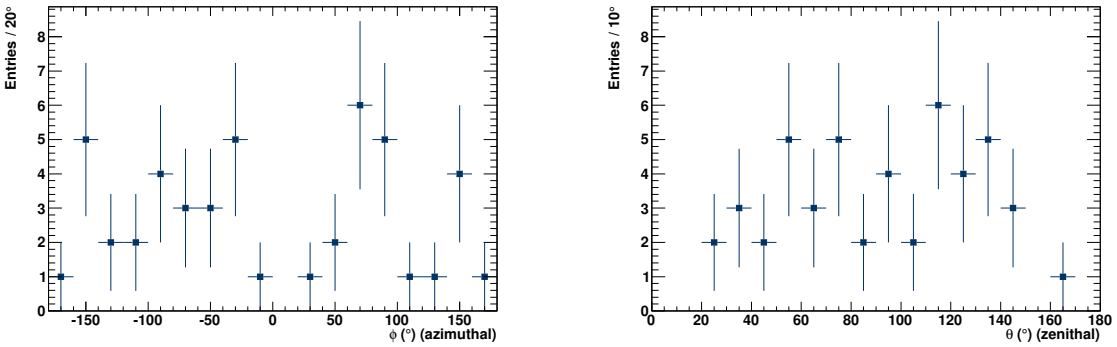

Figure 7.23: ϕ (*left*) and θ (*right*) distributions of the 47 neutrino candidates.

Figure 7.23 shows the azimuthal and zenithal distributions of the 47 neutrino candidates. The zenithal angle is of interest since one can expect the geo-neutrinos to have a zenithal angle larger than 90°, *i.e.* coming from the bottom of the detector, whereas the $\bar{\nu}_e$ from nuclear reactors should have a zenithal angle around 90°, *i.e.* roughly coming from the surface of the Earth.

Figure 7.24 shows the azimuthal angle versus the PMTs light yields of the prompt signals. This sample of 47 neutrino candidates consists of both geo-neutrinos and $\bar{\nu}_e$ from nuclear reactors. From the calculations we made in the previous chapter, we found:

$$N_{\mathrm{geo}} = 14.1^{+5.2}_{-4.5} \tag{7.28}$$

$$N_{\mathrm{react}} = 32.4^{+6.9}_{-6.1} \tag{7.29}$$

Knowing that the geo-neutrino candidates fall in the $\mathrm{Q}_{\mathrm{prompt}} < 1300$ p.e. region from equation (6.41), it is already possible to suppress a fraction of $\bar{\nu}_e$ from nuclear reactors which does not fulfill this condition. It is interesting to notice that we have a better angular resolution at low $\mathrm{Q}_{\mathrm{prompt}}$, according to [107], which corresponds to the region populated by geo-neutrinos.

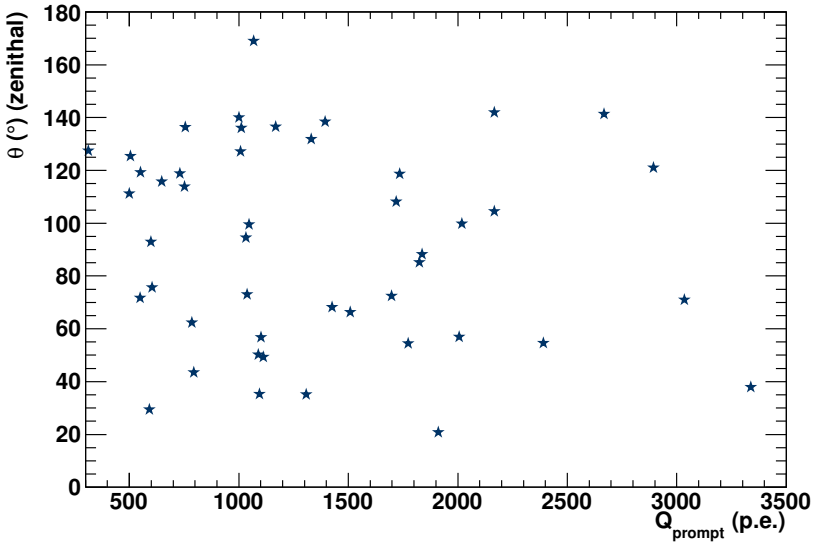

Figure 7.24: θ vs Q_{prompt} of the 47 neutrino candidates.

The azimuthal distribution in this region is shown in Figure 7.25. Among the surviving 26 neutrino candidates, approximately half of them are expected to be geo-neutrinos and therefore with $\theta \gg 90°$, especially for those created in the mantle.

In order to improve the resolution of the directionality, and therefore the geo-neutrino identification, we can have a look at the correlation time, Δt, and correlation distance, ΔR, between the prompt and delayed signals of our events. Whereas in the case of a Gd-capture sample, the neutron has to thermalize before being captured, it is not necessary when considering H-capture sample. Three samples which are illustrated on Figure 7.26 can be considered:

1. Best case (1): high ΔR together with low Δt. The direction information is best preserved when the neutron makes a long path in a short amount of time before being captured.
2. Worst case (2): high Δt together with low ΔR. The neutron is spinning around its initial place of creation for a long time before being captured, leading to the loss of the direction information.
3. Complementary regions (3)

Finally, Figure 7.27 shows the zenithal distribution when considering the best case in terms of direction information, *i.e.* when requesting $\Delta R > 0.2$ m and $\Delta t < 200$ µs. Among the 26 previous neutrino candidates, only 8 of them pass these additional selection cuts. The extremely low statistics does not allow to identify any directionality. In order to understand the needed statistics and systematics to proper discriminate between geo-neutrinos and $\bar{\nu}_e$ from nuclear reactors, a full MC description, not yet available, is required.

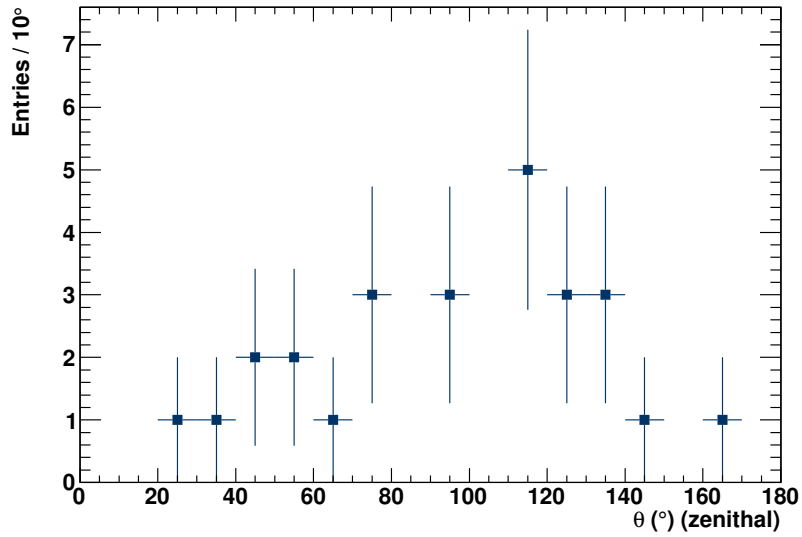

Figure 7.25: θ distribution of the 26 neutrino candidates which satisfy the $Q_{prompt} < 1300$ p.e. condition.

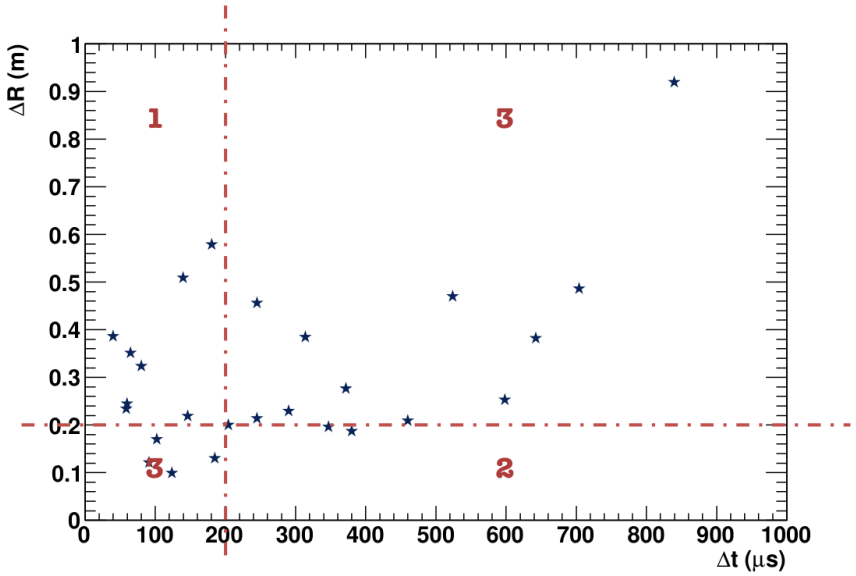

Figure 7.26: ΔR vs Δt of the 26 neutrino candidates which satisfy the $Q_{prompt} < 1300$ p.e. condition.

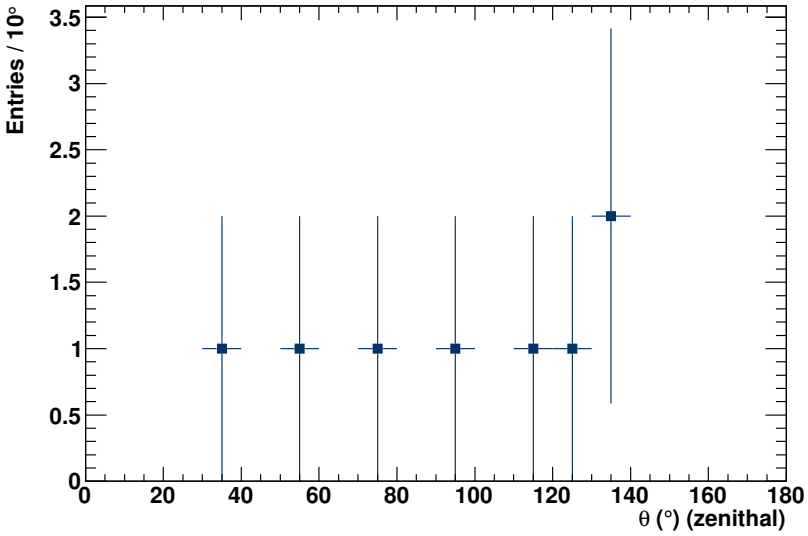

Figure 7.27: θ distribution of the 8 neutrino candidates which satisfy $Q_{prompt} <$ 1300 p.e., $\Delta R > 0.2$ m and $\Delta t < 200$ μs.

Conclusion

The future of neutrino physics is bright
Serguey Petcov

Over the last decades and in particular over the last years, it has been understood that the solar and atmospheric anomalies were due to a quantum mechanical phenomenon called neutrino oscillations. The neutrino oscillation probability can be determined through the knowledge of three mixing angles, two mass-squared differences and a CP-violating phase. We have recently entered the precision era for neutrino oscillations, in particular with θ_{13} for reactor neutrino experiments.

The Double Chooz experiment aims at measuring this mixing angle. With only one detector running, we managed to publish results based on an excellent understanding of our detector. A tremendous work on the backgrounds was carried out, reducing considerably the uncertainties on the cosmogenic, fast neutron and stopping muon backgrounds w.r.t to the previous publication. Nevertheless, Double Chooz has to deal with an unexpected background, the light noise. This background has the highest rate and varies over time. I started my PhD studying this background in order to improve the θ_{13} analysis. I developed an additional variable and implemented a complete strategy in order to remove this unexpected background with an inefficiency of 0.0124 ± 0.0008 %. I cross-checked with MC and ^{252}Cf calibration source and I also investigated a special data set where 14 noisy PMTs normally off were turned back on for a short period. The cuts were able to correctly handle the light noise. The success of this strategy brought the collaboration to decide to turn these PMTs back on. Another achievement concerning this light noise study was its universality. Whereas one had previously to apply different light noise cuts for prompt or delayed events, for neutron capture on Gd or H, the strength of the new set of cuts is to be same for any kind of events considered. Finally, I showed that it would be possible to apply an online cut on the number of hit channels in order to reduce the light noise contamination in the data.

Double Chooz managed to measure θ_{13} using different data sets and methods. Assuming a normal hierarchy with $\Delta m^2_{31} = 2.44^{+0.09}_{-0.10} \times 10^{-3}$ eV^2, we measured $\sin^2 2\theta_{13} = 0.090^{+0.032}_{-0.029}$ from the rate and spectral shape analysis. With a near detector which should soon start taking data, the Double Chooz experiment will be able to reach its full configuration in order to provide a more precise measurement of θ_{13}. Uncertainties on the reactor flux prediction will be suppressed by allowing a direct comparison of the far and near detector data. The Bugey-4 anchor point will be not needed anymore. Within three years of data taking, Double

Chooz should be able to reach a sensitivity of 0.015 on $\sin^2 2\theta_{13}$.

The Borexino experiment is playing a leading part in confirming the observation of geo-neutrinos and can help geoscience to better understand our planet. Due to the low statistics, the geo-neutrino analysis is not yet able to discriminate among proposed geological models. One has to keep in mind that this analysis uses data from December 9, 2007 to August 26, 2012. With two more years of statistics, Borexino alone should be able to reject a null geo-neutrino signal rate above $5\,\sigma$. I participated in the search for geo-neutrinos through the IDAPP exchange program in my third year of PhD. From the selection to the maximum likehood analysis, through the accidental and cosmogenic backgrounds investigation, I made a complete independent analysis to cross-check the already published results and to go beyond by running over the total available data taking period. Nevertheless, in order not to be in conflict with a future Borexino paper, I focused in this thesis on the exact same data taking period than the one released. The selection allowed to discover a hardware issue in the data taking which is still under investigation. A slightly different neutrino candidates sample was selected due to an improvement in the way to calculate the fiducial volume. Finally, the signal rates of geo-neutrinos and $\bar{\nu}_e$ from nuclear reactors were found to be in agreement with the published results.

Retrieving the initial direction of $\bar{\nu}_e$ in IBD interactions with neutron capture on Gd or on H is a promising study which can improve the signature of future neutrino experiments. I was involved in this neutrino directionality analysis for both Double Chooz and Borexino. Here are the main outcomes of my studies:

- **Double Chooz**:
  - Neutrino directionality using IBD interactions is possible since the emitted neutron preserves some information on the initial $\bar{\nu}_e$ direction. Using neutrino candidates with neutron capture on Gd, it is possible to locate the source. Three-dimensional resolution on the direction gave 7.0° with 17358 events.
  - While studies in literature focused on scintillators doped with high neutron capture cross-section elements, such as Gd, we showed that measurement of the directionality of neutrino candidates with neutron capture on H is feasible. This is potentially interesting for future large-scale neutrino detectors which will use un-doped scintillators. I developed the analysis based on a preliminary selection of neutrino candidates with neutron capture on H and I selected the neutrino candidates of interest by investigating the accidental contribution. Three-dimensional resolution on the direction gave 8.9° with 13048 events.
  - Since the present resolution is comparable to the angular distance between the two nuclear reactors of the Chooz power plant, one can think to end with a narrower distribution when only one reactor is on. We did not have enough statistics yet to answer this question. With much more statistics, the Double Chooz near detector will help to deconvolute the two reactors.
  - The vertex position reconstruction is the key of the success of a neutrino directionality study. Unfortunately, the Double Chooz algorithm is biased. After finding a

misbehavior, I investigated and provided corrections for both data and MC. Nevertheless, we had some limitations since we did not have access to calibration sources with energies above 2.5 MeV and we did not have the possibility to investigate a possible radial dependence of the corrections. In my opinion, it would be better to correct the algorithm instead of applying corrections after the algorithm. "*Le mieux est l'ennemi du bien*" as we would say in French.

- **Borexino**:
  - The main background in the geo-neutrino analysis is the $\bar{\nu}_e$ from nuclear reactors. Neutrino directionality can facilitate the discrimination since geo-neutrinos and $\bar{\nu}_e$ from nuclear reactors have a different angular distribution. Nevertheless, due to the low statistics, it is not yet possible to reach a conclusion on the discrimination power.

Appendices

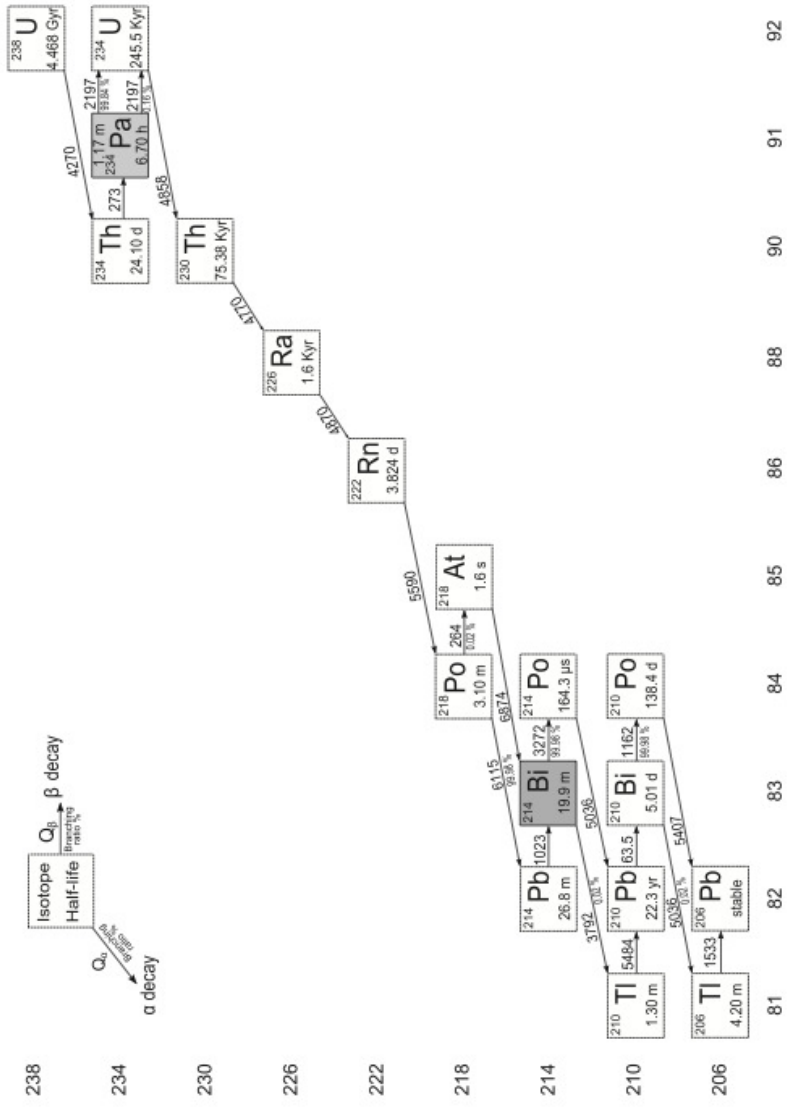

Figure 7.28: Scheme of the ^{238}U decay series, from [172]. Only the β^- decays of ^{234}Pa and ^{214}Bi provide $\bar{\nu}_e$ susceptible to interact through IBD interactions in a detector.

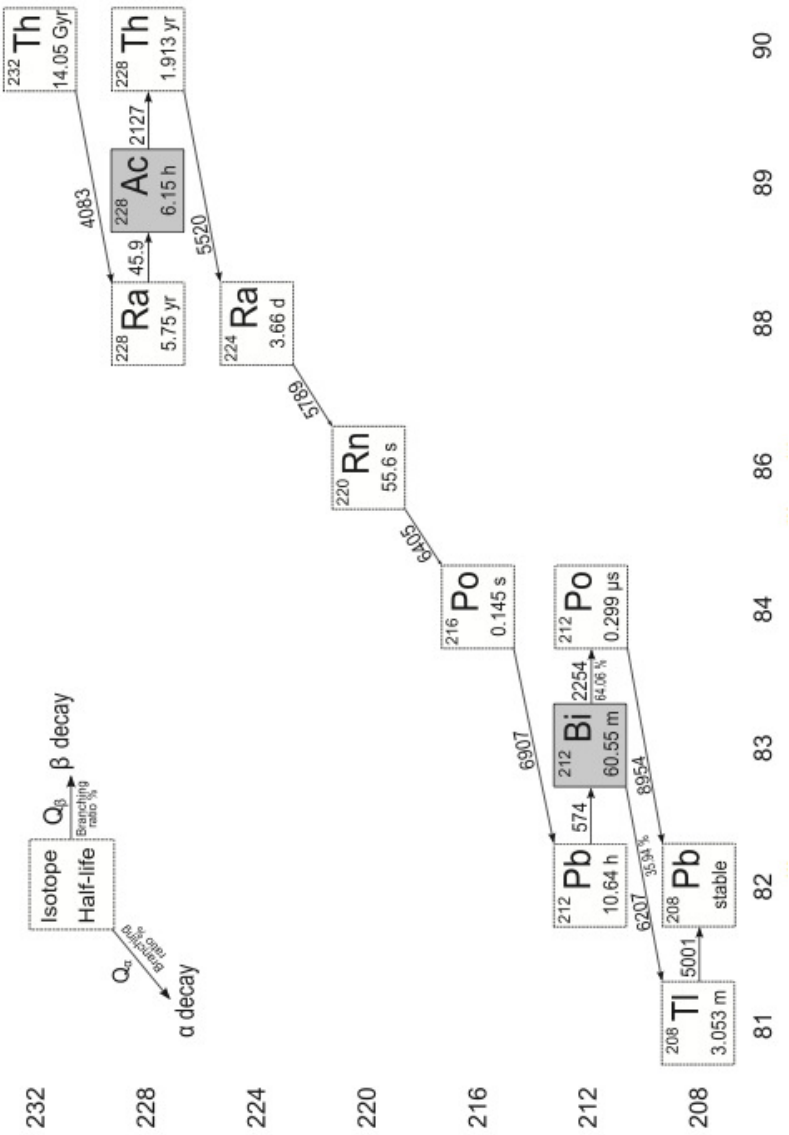

Figure 7.29: Scheme of the ^{232}Th decay series, from [172]. Only the β^- decays of ^{228}Ac and ^{212}Bi provide $\bar{\nu}_e$ susceptible to interact through IBD interactions in a detector.

List of Tables

List of Figures

Bibliography

[1] C.D. Ellis and W.A. Wooster. "The Continuous Spectrum of β-Rays". *Nature*, **119**:563–564, 1927.

[2] J. Chadwick. "Possible Existence of a Neutron". *Nature*, **129**:312, 1932.

[3] E. Fermi. "Versuch einer Theorie der β-Strahlen". *Z.Phys.*, **88**:161–177, 1934.

[4] H. Bethe and R. Peierls. "The "Neutrino"". *Nature*, **133**:532, 1934.

[5] F. Reines and C.L. Cowan. "Detection of the Free Neutrino". *Phys.Rev.*, **92**:830–831, 1953.

[6] C.L. Cowan, F. Reines, F.B. Harisson, H.W. Kruse, and A.D. McGuire. "Detection of the Free Neutrino: a Confirmation". *Science*, **124**:103–104, 1956.

[7] F. Reines and C.L. Cowan. "The Neutrino". *Nature*, **178**:446–449, 1956.

[8] F. Reines and C.L. Cowan. "Free Antineutrino Absorption Cross Section. I. Measurement of the Free Antineutrino Absorption Cross Section by Protons". *Phys.Rev.*, **113**:273–279, 1959.

[9] B. Pontecorvo. "Electron and Muon Neutrinos". *Sov.Phys.JETP*, **10**:1236–1240, 1959.

[10] M. Schwartz. "Feasibility of Using High-Energy Neutrinos to Study the Weak Interactions". *Phys.Rev.Lett.*, **4**:306–307, 1960.

[11] C. Giunti and C.W. Kim. *Fundamentals of Neutrino Physics and Astrophysics*. Oxford University Press, 2007.

[12] G. Danby, J-M. Gaillard, K. Goulianos, L.M. Lederman, N. Mistry, et al. "Observation of High-Energy Neutrino Reactions and the Existence of Two Kinds of Neutrinos". *Phys.Rev.Lett.*, **9**:36–44, 1962.

[13] E.J. Konopinski and H.M. Mahmoud. "The Universal Fermi Interaction". *Phys.Rev.*, **92**:1045–1049, 1953.

[14] M.L. Perl, G.S. Abrams, A.M. Boyarski, M. Breidenbach, D.D. Briggs, et al. "Evidence for Anomalous Lepton Production in $e^+ - e^-$ Annihilation". *Phys.Rev.Lett.*, **35**:1489–1492, 1975.

[15] K. Kodama et al. "Observation of tau neutrino interactions". *Phys.Lett.*, B**504**:218–224, 2001.

[16] S. Schael et al. "Precision electroweak measurements on the Z resonance". *Phys.Rept.*, **427**:257–454, 2006.

[17] M. Salaris and S. Cassisi. *Evolution of Stars and Stellar Populations*. John Wiley & Sons, 2005.

[18] J.N. Bahcall. *Neutrino Astrophysics*. Cambridge University Press, 1989.

[19] J.N. Bahcall, A.M. Serenelli, and S. Basu. "New Solar Opacities, Abundances, Helioseismology, and Neutrino Fluxes". *Astrophys.J.*, **621**:L85–L88, 2005.

[20] J.N. Bahcall and A.M. Serenelli. "How Do Uncertainties in the Surface Chemical Composition of the Sun Affect the Predicted Solar Neutrino Fluxes?". *Astrophys.J.*, **626**:530–542, 2005.

[21] R. Davis Jr., D.S. Harmer, and K.C. Hoffman. "Search for Neutrinos from the Sun". *Phys.Rev.Lett.*, **20**:1205–1209, 1968.

[22] J.N. Bahcall, N.A. Bahcall, and G. Shaviv. "Present Status of the Theoretical Predictions for the ^{37}Cl Solar-Neutrino Experiment". *Phys.Rev.Lett.*, **20**:1209–1212, 1968.

[23] B.T. Cleveland, T. Daily, R. Davis Jr., J.R. Distel, K. Lande, et al. "Measurement of the Solar Electron Neutrino Flux with the Homestake Chlorine Detector". *Astrophys.J.*, **496**:505–526, 1998.

[24] M. Altmann et al. "Complete results for five years of GNO solar neutrino observations". *Phys.Lett.*, B**616**:174–190, 2005.

[25] J.N. Abdurashitov et al. "Solar Neutrino Flux Measurements by the Soviet-American Gallium Experiment (SAGE) for Half the 22-Year Solar Cycle". *J.Exp.Theor.Phys.*, 95:181–193, 2002.

[26] J.N. Bahcall, M.H. Pinsonneault, and S. Basu. "Solar Models: Current Epoch and Time Dependences, Neutrinos, and Helioseismological Properties". *Astrophys.J.*, **555**:990–1012, 2001.

[27] W. Hampel et al. "Final results of the ^{51}Cr neutrino source experiments in GALLEX". *Phys.Lett.*, B**420**:114–126, 1998.

[28] J.N. Abdurashitov et al. "Measurement of the response of a gallium metal solar neutrino experiment to neutrinos from a ^{51}Cr source". *Phys.Rev.*, C**59**(4):2246–2263, 1999.

[29] J. Beringer et al. "Review of Particle Physics (RPP)". *Phys.Rev.*, D**86**:010001, 2012.

[30] J. Hosaka et al. "Solar neutrino measurements in super-Kamiokande-I". *Phys.Rev.*, D**73**:112001, 2006.

[31] Q.R. Ahmad et al. "Direct Evidence for Neutrino Flavor Transformation from Neutral-Current Interactions in the Sudbury Neutrino Observatory". *Phys.Rev.Lett.*, **89**:011301, 2002.

[32] G. Domokos and S. Kovesi Domokos. *Neutrinos in the Next Millennium*. World Scientific Publishing Company, Incorporated, 2000.

[33] K.S. Hirata et al. "Experimental study of the atmospheric neutrino flux". *Phys.Lett.*, B**205**:416–420, 1988.

[34] R. Becker-Szendy et al. "Electron- and muon-neutrino content of the atmospheric flux". *Phys.Rev.*, D**46**:3720–3724, 1992.

[35] W.W.M. Allison et al. "Measurement of the atmospheric neutrino flavour composition in Soudan 2". *Phys.Lett.*, B**391**:491–500, 1997.

[36] Y. Fukuda et al. "Evidence for Oscillation of Atmospheric Neutrinos". *Phys.Rev.Lett.*, **81**:1562–1567, 1998.

[37] Y. Fukuda et al. "Study of the atmospheric neutrino flux in the multi-GeV energy range". *Phys.Lett.*, B**436**:33–41, 1998.

[38] Y. Ashie et al. "Measurement of atmospheric neutrino oscillation parameters by Super-Kamiokande I". *Phys.Rev.*, D**71**:112005, 2005.

[39] Y. Abe et al. "Indication of Reactor $\bar{\nu}_e$ Disappearance in the Double Chooz Experiment". *Phys.Rev.Lett.*, **108**:131801, 2012.

[40] Y. Abe et al. "Reactor $\bar{\nu}_e$ disappearance in the Double Chooz experiment". *Phys.Rev.*, D**86**:052008, 2012.

[41] Y. Abe et al. "First measurement of θ_{13} from delayed neutron capture on hydrogen in the Double Chooz experiment". *Phys.Lett.*, B**723**:66–70, 2013.

[42] Y. Abe et al. "Improved measurements of the neutrino mixing angle θ_{13} with the Double Chooz detector". *arXiv:1406.7763*, 2014.

[43] T.A. Mueller, D. Lhuillier, M. Fallot, A. Letourneau, S. Cormon, et al. "Improved predictions of reactor antineutrino spectra". *Phys.Rev.*, C**83**:054615, 2011.

[44] G. Mention, M. Fechner, T. Lasserre, T.A. Mueller, D. Lhuillier, et al. "Reactor antineutrino anomaly". *Phys.Rev.*, D**83**:073006, 2011.

[45] C. Zhang, X. Qian, and P. Vogel. "Reactor antineutrino anomaly with known θ_{13}". *Phys.Rev.*, D**87**:073018, 2013.

[46] J.N. Abdurashitov, V.N. Gavrin, S.V. Girin, V.V. Gorbachev, P.P. Gurkina, et al. "Measurement of the response of a Ga solar neutrino experiment to neutrinos from a ^{37}Ar source". *Phys.Rev.*, C**73**:045805, 2006.

[47] A. Aguilar et al. "Evidence for neutrino oscillations from the observation of $\bar{\nu}_e$ appearance in a $\bar{\nu}_\mu$ beam". *Phys.Rev.*, D**64**:112007, 2001.

[48] A.A. Aguilar-Arevalo et al. "Improved Search for $\bar{\nu}_\mu \to \bar{\nu}_e$ Oscillations in the MiniBooNE Experiment". *Phys.Rev.Lett.*, **110**:161801, 2013.

[49] S.L. Glashow. Partial-symmetries of weak interactions. *Nucl.Phys.*, **22**:579–588, 1961.

[50] S. Weinberg. "A Model of Leptons". *Phys.Rev.Lett.*, **19**:1264–1266, 1967.

[51] P.W. Higgs. "Broken symmetries, massless particles and gauge fields". *Phys.Lett.*, **12**:132–133, 1964.

[52] F. Englert and R. Brout. "Broken Symmetry and the Mass of Gauge Vector Mesons". *Phys.Rev.Lett.*, **13**:321–323, 1964.

[53] V.N. Aseev et al. "Upper limit on the electron antineutrino mass from the Troitsk experiment". *Phys.Rev.*, D**84**:112003, 2011.

[54] K. Assamagan, C. Bronnimann, M. Daum, H. Forrer, R. Frosch, et al. "Upper limit of the muon-neutrino mass and charged-pion mass from momentum analysis of a surface muon beam". *Phys.Rev.*, D**53**:6065–6077, 1996.

[55] R. Barate et al. "An upper limit on the τ neutrino mass from three- and five-prong tau decays". *Eur.Phys.J.*, C**2**:395–406, 1998.

[56] G. Aad et al. "Observation of a new particle in the search for the Standard Model Higgs boson with the ATLAS detector at the LHC". *Phys.Lett.*, B**716**:1–29, 2012.

[57] S. Chatrchyan et al. "Observation of a new boson at a mass of 125 GeV with the CMS experiment at the LHC". *Phys.Lett.*, B**716**:30–61, 2012.

[58] K. Winter. *Neutrino Physics*. Cambridge University Press, 2000.

[59] E. Majorana. "Teoria simmetrica dell'elettrone e del positrone". *Nuovo Cim.*, **14**:171–184, 1937.

[60] B. Kayser, F. Gibrat-Debu, and F. Perrier. *The Physics of Massive Neutrinos*. World Scientific Publishing Company, Incorporated, 1989.

[61] A. Osipowicz et al. "KATRIN: A next generation tritium beta decay experiment with sub-eV sensitivity for the electron neutrino mass". 2001.

[62] C. Kraus et al. "Final results from phase II of the Mainz neutrino mass search in tritium β decay". *Eur.Phys.J.*, C**40**:447–468, 2005.

[63] G.J. Feldman and R.D. Cousins. "Unified approach to the classical statistical analysis of small signals". *Phys.Rev.*, D**57**:3873–3889, 1998.

[64] S.R. Elliott and P. Vogel. "Double Beta Decay". *Ann.Rev.Nucl.Part.Sci.*, **52**:115–151, 2002.

[65] W.H. Furry. "On Transition Probabilities in Double Beta-Disintegration". *Phys.Rev.*, **56**:1184–1193, 1939.

[66] M. Agostini et al. "Results on Neutrinoless Double-β Decay of ^{76}Ge from Phase I of the GERDA Experiment". *Phys.Rev.Lett.*, **111**:122503, 2013.

[67] M. Auger et al. "Search for Neutrinoless Double-Beta Decay in ^{136}Xe with EXO-200". *Phys.Rev.Lett.*, **109**:032505, 2012.

[68] A. Gando et al. "Limit on Neutrinoless $\beta\beta$ Decay of ^{136}Xe from the First Phase of KamLAND-Zen and Comparison with the Positive Claim in ^{76}Ge". *Phys.Rev.Lett.*, **110**:062502, 2013.

[69] H.V. Klapdor-Kleingrothaus, I.V. Krivosheina, A. Dietz, and O. Chkvorets. "Search for neutrinoless double beta decay with enriched ^{76}Ge in Gran Sasso 1990-2003". *Phys.Lett.*, B**586**:198–212, 2004.

[70] Z. Maki, M. Nakagawa, and S. Sakata. "Remarks on the Unified Model of Elementary Particles". *Prog.Theor.Phys.*, **28**:870–880, 1962.

[71] N. Cabibbo. "Unitary Symmetry and Leptonic Decays". *Phys.Rev.Lett.*, **10**:531–533, 1963.

[72] M. Kobayashi and T. Maskawa. "CP-Violation in the Renormalizable Theory of Weak Interaction". *Prog.Theor.Phys.*, **49**:652–657, 1973.

[73] B. Pontecorvo. "Mesonium and Antimesonium". *Sov.Phys.JETP*, **6**:429–431, 1957.

[74] C. Giunti. "Phenomenology of Absolute Neutrino Masses". *Nucl.Phys.Proc.Suppl.*, **145**:231–236, 2005.

[75] L. Wolfenstein. "Neutrino oscillations in matter". *Phys.Rev.*, D**17**:2369–2374, 1978.

[76] S.P. Mikheev and A.Y. Smirnov. "Resonance Amplification of Oscillations in Matter and Spectroscopy of Solar Neutrinos". *Sov.J.Nucl.Phys.*, **42**:913–917, 1985.

[77] V. Barger, K. Whisnant, S. Pakvasa, and R.J.N. Phillips. "Matter effects on three-neutrino oscillations". *Phys.Rev.*, D**22**:2718, 1980.

[78] A. Gando et al. "Reactor on-off antineutrino measurement with KamLAND". *Phys.Rev.*, D**88**:033001, 2013.

[79] S. Abe et al. "Precision Measurement of Neutrino Oscillation Parameters with KamLAND". *Phys.Rev.Lett.*, **100**:221803, 2008.

[80] A. Gando et al. "Constraints on θ_{13} from a three-flavor oscillation analysis of reactor antineutrinos at KamLAND". *Phys.Rev.*, D**83**:052002, 2011.

[81] M.H. Ahn et al. "Measurement of neutrino oscillation by the K2K experiment". *Phys.Rev.*, D**74**:072003, 2006.

[82] D.G. Michael et al. "Observation of Muon Neutrino Disappearance with the MINOS Detectors in the NuMI Neutrino Beam". *Phys.Rev.Lett.*, **97**:191801, 2006.

[83] P. Adamson et al. "Combined Analysis of ν_μ Disappearance and $\nu_\mu \to \nu_e$ Appearance in MINOS Using Accelerator and Atmospheric Neutrinos". *Phys.Rev.Lett.*, **112**:191801, 2014.

[84] K. Abe et al. "Precise Measurement of the Neutrino Mixing Parameter θ_{23} from Muon Neutrino Disappearance in an Off-Axis Beam". *Phys.Rev.Lett.*, **112**:181801, 2014.

[85] P. Adamson et al. "Measurement of Neutrino and Antineutrino Oscillations Using Beam and Atmospheric Data in MINOS". *Phys.Rev.Lett.*, **110**:251801, 2013.

[86] K. Abe et al. "Measurement of Neutrino Oscillation Parameters from Muon Neutrino Disappearance with an Off-Axis Beam". *Phys.Rev.Lett.*, **111**:211803, 2013.

[87] M. Apollonio et al. "Search for neutrino oscillations on a long base-line at the CHOOZ nuclear power station". *Eur.Phys.J.*, C**27**:331–374, 2003.

[88] F.P. An et al. "Spectral Measurement of Electron Antineutrino Oscillation Amplitude and Frequency at Daya Bay". *Phys.Rev.Lett.*, **112**:061801, 2014.

[89] F.P. An et al. "Observation of Electron-Antineutrino Disappearance at Daya Bay". *Phys.Rev.Lett.*, **108**:171803, 2012.

[90] F.P. An et al. "Improved measurement of electron antineutrino disappearance at Daya Bay". *Chin.Phys.*, C**37**:011001, 2013.

[91] F.P. An et al. "Independent Measurement of the Neutrino Mixing Angle θ_{13} via Neutron Capture on Hydrogen at Daya Bay". 2014.

[92] J.K. Ahn et al. "Observation of Reactor Electron Antineutrinos Disappearance in the RENO Experiment". *Phys.Rev.Lett.*, **108**:191802, 2012.

[93] K. Abe et al. "Indication of Electron Neutrino Appearance from an Accelerator-Produced Off-Axis Muon Neutrino Beam". *Phys.Rev.Lett.*, **107**:041801, 2011.

[94] K. Abe et al. "Observation of Electron Neutrino Appearance in a Muon Neutrino Beam". *Phys.Rev.Lett.*, **112**:061802, 2014.

[95] P. Adamson et al. "Electron Neutrino and Antineutrino Appearance in the Full MINOS Data Sample". *Phys.Rev.Lett.*, **110**:171801, 2013.

[96] P.A.R. Ade et al. "Planck 2013 results. XVI. Cosmological parameters". 2013.

[97] K.N. Abazajian et al. "Light Sterile Neutrinos: A White Paper". 2012.

[98] V.I. Kopeikin, L.A. Mikaelyan, and V.V. Sinev. "Reactor as a Source of Antineutrinos: Thermal Fission Energy". *Phys.Atom.Nucl.*, **67**:1892–1899, 2004.

[99] X.B. Ma, W.L. Zhong, L.Z. Wang, Y.X. Chen, and J. Cao. "Improved calculation of the energy release in neutron-induced fission". *Phys.Rev.*, C**88**:014605, 2013.

[100] P. Huber and T. Schwetz. "Precision spectroscopy with reactor antineutrinos". *Phys.Rev.*, D**70**:053011, 2004.

[101] F. von Feilitzsch, A.A. Hahn, and K. Schreckenbach. "Experimental beta-spectra from ^{2}39Pu and ^{2}35U thermal neutron fission products and their correlated antineutrino spectra". *Phys.Lett.*, B**118**:162–166, 1982.

[102] K. Schreckenbach, G. Colvin, W. Gelletly, and F. von Feilitzsch. "Determination of the antineutrino spectrum from ^{235}U thermal neutron fission products up to 9.5 MeV". *Phys.Lett.*, B**160**:325–330, 1985.

[103] A.A. Hahn, K. Schreckenbach, W. Gelletly, F. von Feilitzsch, G. Colvin, et al. "Antineutrino spectra from ^{241}Pu and ^{239}Pu thermal neutron fission products". *Phys.Lett.*, B**218**:365–368, 1989.

[104] N. Haag, A. Gütlein, M. Hofmann, L. Oberauer, W. Potzel, et al. "Experimental Determination of the Antineutrino Spectrum of the Fission Products of ^{238}U". *Phys.Rev.Lett.*, **112**:122501, 2014.

[105] M. Fallot, S. Cormon, M. Estienne, A. Algora, V.M. Bui, et al. "New Antineutrino Energy Spectra Predictions from the Summation of Beta Decay Branches of the Fission Products". *Phys.Rev.Lett.*, **109**:202504, 2012.

[106] Y. Declais, H. de Kerret, B. Lefièvre, M. Obolensky, A. Etenko, et al. "Study of reactor antineutrino interaction with proton at BUGEY nuclear power plant". *Phys.Lett.*, B**338**:383–389, 1994.

[107] P. Vogel and J.F. Beacom. "Angular distribution of neutron inverse beta decay, $\bar{\nu}_e + p \to e^+ + n$". *Phys.Rev.*, D**60**:053003, 1999.

[108] C. Bemporad, G. Gratta, and P. Vogel. "Reactor-based neutrino oscillation experiments". *Rev.Mod.Phys.*, **74**:297, 2002.

[109] F. Ardellier et al. "Double Chooz: A Search for the Neutrino Mixing Angle θ_{13}". 2006.

[110] F. Capozzi, G.L. Fogli, E. Lisi, A. Marrone, D. Montanino, et al. "Status of three-neutrino oscillation parameters, circa 2013". *Phys.Rev.*, D**89**:093018, 2014.

[111] Y. Abe et al. "Direct measurement of backgrounds using reactor-off data in Double Chooz". *Phys.Rev.*, D**87**:011102, 2013.

[112] V. Durand. "Mesure du paramètre de mélange leptonique θ_{13} auprès de l'expérience d'antineutrinos de réacteur Double Chooz". *PhD thesis*, Université Paris Diderot (Paris 7), 2012.

[113] C. Aberle, C. Buck, B. Gramlich, F.X. Hartmann, M. Lindner, et al. "Large scale Gd-beta-diketonate based organic liquid scintillator production for antineutrino detection". *JINST*, **7**:P06008, 2012.

[114] C. Bauer, E. Borger, R. Hofacker, K. Jänner, F. Kaether, et al. "Qualification tests of 474 photomultiplier tubes for the inner detector of the Double Chooz experiment". *JINST*, **6**:P06008, 2011.

[115] T. Matsubara, T. Haruna, T. Konno, Y. Endo, M. Bongrand, et al. "Evaluation of 400 low background 10-in. photo-multiplier tubes for the Double Chooz experiment". *Nucl.Instrum.Meth.*, A**661**:16–25, 2012.

[116] G. Alimonti et al. "Science and technology of Borexino: a real-time detector for low energy solar neutrinos". *Astropart.Phys.*, **16**:205–234, 2002.

[117] D. Dietrich, D. Greiner, J. Jochum, T. Lachenmaier, M. Röhling, et al. "Monte Carlo aided design of the inner muon veto detectors for the Double Chooz experiment". *JINST*, **7**:P08012, 2012.

[118] A. Cabrera. "The Double Chooz detector". *Nucl.Instrum.Meth.*, A**617**:473–477, 2010.

[119] Y. Abe, T. Akiri, A. Cabrera, B. Courty, J.V. Dawson, et al. "The waveform digitiser of the Double Chooz experiment: performance and quantisation effects on photomultiplier tube signals". *JINST*, **8**:P08015, 2013.

[120] C. Aberle, C. Buck, F.X. Hartmann, S. Schönert, and S. Wagner. "Light output of Double Chooz scintillators for low energy electrons". *JINST*, **6**:P11006, 2011.

[121] C. Aberle, C. Buck, F.X. Hartmann, and S. Schönert. "Light yield and energy transfer in a new Gd-loaded liquid scintillator". *Chem.Phys.Lett.*, **516**:257–262, 2011.

[122] I. Stancu. "The Double Chooz Optical Model". *Double Chooz internal document*, DocDB #**2897**, 2011.

[123] E. Calvo et al. "Toward a better understanding of the Hamamatsu R7081 PMT glowing". *Double Chooz internal document*, DocDB #**3234**, 2011.

[124] F. Suekane et al. "Off-site glow studies". *Double Chooz internal document*, DocDB #**2252**, 2011.

[125] A. Collin. "Etude des antineutrinos de réacteurs : mesure de l'angle de mélange leptonique θ_{13} et recherche d'éventuels neutrinos stériles". *PhD thesis*, Université Paris-Sud, 2014.

[126] R. Roncin, A. Hourlier, and A. Cabrera. "Light Noise discrimination". *Double Chooz internal document*, DocDB #**4164**, 2012.

[127] T. Konno. "Studies for reduction of remaining noise events". *Double Chooz internal document*, DocDB #**4179**, 2012.

[128] R. Roncin, T. Konno, and A. Cabrera. "Light Noise reduction". *Double Chooz internal document*, DocDB #**4935**, 2013.

[129] E. Chauveau. "DATA/MC comparison of LN variables for DC3rdPub". *Double Chooz internal document*, DocDB #**5148**, 2013.

[130] C. Palomares. "Special HV runs". *Double Chooz internal document*, DocDB #**3731**, 2012.

[131] M. Röhling. "Looking for Δt_μ of neutrino candidates". *Double Chooz internal document*, DocDB #**4751**, 2012.

[132] A. Stüken. "Trigger Efficiency Determination for 3rd Pub". *Double Chooz internal document*, DocDB #**5252**, 2013.

[133] R. Carr. "Extended E_{prompt} range sensitivity study". *Double Chooz internal document*, DocDB #**4822**, 2013.

[134] R. Sharankova. "ΔT, E_{del} cuts for DCIII". *Double Chooz internal document*, DocDB #**4978**, 2013.

[135] J. Haser. "DC-III MC-neutrino selection". *Double Chooz internal document*, DocDB #**5087**, 2013.

[136] A. Collin. "Which Upper Value for the ΔT Cut?". *Double Chooz internal document*, DocDB #**5130**, 2013.

[137] A. Cabrera and R. Sharankova. "$\Delta d(p \sim d)$ cut". *Double Chooz internal document*, DocDB #**4959**, 2013.

[138] A. Cabrera. "IV prompt/delay tag/veto". *Double Chooz internal document*, DocDB #**5055**, 2013.

[139] G. Pronost and R. Santorelli. "Inner Veto Vertex Reconstruction - A Neural Network approach". *Double Chooz internal document*, DocDB #**4550**, 2013.

[140] K. Terao, R. Carr, K. Crum, S. Lucht, J. Maeda, et al. "Memo for $\bar{\nu}_e$ Analysis With Neutron Capture on Hydrogen". *Double Chooz internal document*, DocDB #**4156**, 2013.

[141] E.J. Axton and A.G. Bardell. "Neutron Yield from the Spontaneous Fission of ^{252}Cf ($\bar{\nu}$)". *Metrologia*, **21**:59–74, 1985.

[142] J. Haser. "n-Gd Neutron Detection Efficiency Volume Factorization Method using ^{252}Cf". *Double Chooz internal document*, DocDB #**5293**, 2013.

[143] A. Collin. "Impact of the ΔT cut values on spill-in/out systematics". *Double Chooz internal document*, DocDB #**5078**, 2013.

[144] R. Carr and K. Crum. "Gd-III Rate+Shape blessed results for publication". *Double Chooz internal document*, DocDB #**5610**, 2014.

[145] A. Cabrera. "Double Chooz". *Seminar given at LAL*, Orsay (France), May 22, 2014.

[146] H. de Kerret. "Double Chooz". *Talk given at the Neutrino 2014 conference*, Boston (USA), June 3, 2014.

[147] J. Haser. "Current status of the Double Chooz experiment". *Talk given at the ICHEP 2014 conference*, Valencia (Spain), July 4, 2014.

[148] S.H. Seo. "New Results from RENO". *Talk given at the Neutrino 2014 conference*, Boston (USA), June 3, 2014.

[149] W. Zhong. "Measurement of the reactor antineutrino flux and spectrum at Daya Bay". *Talk given at the ICHEP 2014 conference*, Valencia (Spain), July 5, 2014.

[150] D.A. Dwyer and T.J. Langford. "Spectral Structure of Electron Antineutrinos from Nuclear Reactors". *arXiv:1407.1281*, 2014.

[151] P. Adamson et al. "Measurement of the Neutrino Mass Splitting and Flavor Mixing by MINOS". *Phys.Rev.Lett.*, **106**:181801, 2011.

[152] Y. Abe et al. "Background-independent measurement of θ_{13} in Double Chooz". *Phys.Lett.*, B**735**:51–56, 2014.

[153] G. Bellini et al. "Precision Measurement of the ^{7}Be Solar Neutrino Interaction Rate in Borexino". *Phys.Rev.Lett.*, **107**:141302, 2011.

[154] G. Bellini et al. "Measurement of the solar ^{8}B neutrino rate with a liquid scintillator target and 3 MeV energy threshold in the Borexino detector". *Phys.Rev.*, D**82**:033006, 2010.

[155] G. Bellini et al. "First Evidence of *pep* Solar Neutrinos by Direct Detection in Borexino". *Phys.Rev.Lett.*, **108**:051302, 2012.

[156] G. Bellini et al. "Observation of geo-neutrinos". *Phys.Lett.*, B**687**:299–304, 2010.

[157] G. Bellini et al. "Measurement of geo-neutrinos from 1353 days of Borexino". *Phys.Lett.*, B**722**:295–300, 2013.

[158] H. Back et al. "Borexino calibrations: hardware, methods, and results". *JINST*, **7**:P10018, 2012.

[159] G. Bellini et al. "Absence of a day-night asymmetry in the ^{7}Be solar neutrino rate in Borexino". *Phys.Lett.*, B**707**:22–26, 2012.

[160] G. Eder. "Terrestrial neutrinos". *Nucl.Phys.*, **78**:657–662, 1966.

[161] G. Marx. "Geophysics by neutrinos". *Czech.J.Phys.*, B**19**:1471–1479, 1969.

[162] L.M. Krauss, S.L. Glashow, and D.N. Schramm. "Antineutrino astronomy and geophysics". *Nature*, **310**:191–198, 1984.

[163] T. Araki et al. "Experimental investigation of geologically produced antineutrinos with KamLAND". *Nature*, **436**:499–503, 2005.

[164] M.C. Chen. "Geo-neutrinos in SNO+". *Earth Moon Planets*, **99**:221–228, 2006.

[165] M. Wurm et al. "The next-generation liquid-scintillator neutrino observatory LENA. *Astropart.Phys.*, **35**:685–732, 2012.

[166] S.T. Dye, E. Guillian, J.G. Learned, J. Maricic, S. Matsuno, et al. "Earth Radioactivity Measurements with a Deep Ocean Anti-neutrino Observatory". *Earth Moon Planets*, **99**:241–252, 2006.

[167] O. Šrámek, W.F. McDonough, E.S. Kite, V. Lekić, S. Dye, et al. "Geophysical and geochemical constraints on geoneutrino fluxes from Earth's mantle". *Earth and Planet.Sci.Lett.*, **361**:356–366, 2013.

[168] J. H. Davies and D. R. Davies. "Earth's surface heat flux". *Solid Earth*, **1**:5–24, 2010.

[169] C. Jaupart, S. Labrosse, and J.-C. Mareschal. "Temperatures, Heat and Energy in the Mantle of the Earth". *Treatise on geophysics*, **7**:253–303, 2007.

[170] H.N. Pollack, S.J. Hurter, and J.R. Johnson. "Heat flow from the Earth's interior: Analysis of the global data set". *Rev.Geophys.*, **31**:267–280, 1993.

[171] S.T. Dye. "Geoneutrinos and the radioactive power of the Earth". *Rev.Geophys.*, **50**:3007, 2012.

[172] G. Fiorentini, M. Lissia, and F. Mantovani. "Geo-neutrinos and Earth's interior". *Phys.Rept.*, **453**:117–172, 2007.

[173] W.R. Van Schmus. *"Natural Radioactivity of the Crust and Mantle"*. American Geophysical Union, 2013.

[174] Y. Huang, V. Chubakov, F. Mantovani, R.L. Rudnik, and W.F. McDonough. "A reference Earth model for the heat-producing elements and associated geoneutrino flux". *Geochem., Geophys., Geosyst.*, **14**:2003–2029, 2013.

[175] A. Strumia and F. Vissani. "Precise quasielastic neutrino/nucleon cross-section". *Phys.Lett.*, B**564**:42–54, 2003.

[176] G. Cowan. *Statistical Data Analysis*. Clarendon Press, 1998.

[177] J.F. Beacom and P. Vogel. "Can a supernova be located by its neutrinos?". *Phys.Rev.*, D**60**:033007, 1999.

[178] G.R. Jocher, D.A. Bondy, B.M. Dobbs, S.T. Dye, J.A. Georges III, et al. "Theoretical antineutrino detection, direction and ranging at long distances". *Phys.Rept.*, **527**:131–204, 2013.

[179] M. Apollonio et al. "Determination of neutrino incoming direction in the CHOOZ experiment and its application to supernova explosion location by scintillator detectors". *Phys.Rev.*, D**61**:012001, 2000.

[180] D. Franco, G. Consolati, and D. Trezzi. "Positronium signature in organic liquid scintillators for neutrino experiments". *Phys.Rev.*, C**83**:015504, 2011.

[181] M. Vivier, T. Lasserre, and C. Veyssiere. "Double Chooz geodetic survey". *Double Chooz internal document*, DocDB #**4753**, 2013.

[182] K.A. Hochmuth, M. Lindner, and G.G. Raffelt. "Exploiting the directional sensitivity of the Double Chooz near detector". *Phys.Rev.*, D**76**:073001, 2007.

- Résumé - Double Chooz est une expérience d'oscillation de neutrinos de réacteur qui a pour but de mesurer l'angle de mélange θ_{13} grâce à deux détecteurs identiques situés à différentes distances des deux réacteurs de la centrale nucléaire de Chooz, dans les Ardennes françaises. Tandis que le détecteur proche commencera à prendre des données à l'automne 2014 afin de normaliser le flux des neutrinos émis par les réacteurs nucléaires, le détecteur lointain fonctionne depuis avril 2011 et permet d'observer la disparition des neutrinos à travers le phénomène d'oscillation de neutrinos. Cette thèse est également consacrée à l'expérience Borexino qui a été conçue afin d'observer les neutrinos solaires. Du fait d'un très faible bruit de fond ainsi que de son emplacement dans un pays sans réacteur nucléaire, l'Italie, Borexino est également sensible aux geo-neutrinos. Cette thèse présente à la fois les expériences Double Chooz et Borexino, de la description des détecteurs jusqu'aux principaux résultats, avec une attention particulière portée au bruit de fond et à sa réjection. Des études sur la directionalité des neutrinos avec ces deux expériences sont aussi détaillées. Pour Double Chooz, puisque les neutrinos proviennent des réacteurs nucléaires, la précision de la méthode d'analyse peut être évaluée. Cette thèse présente également pour la première fois la possibilité de retrouver la direction initiale des neutrinos quand les neutrons créés dans les réactions inverses de désintégration beta sont capturés sur l'hydrogène. Pour Borexino, l'information sur la directionalité des neutrinos pourrait faciliter la discrimination entre geo-neutrinos et neutrinos de réacteurs nucléaires.

- Mots-clés - Double Chooz, oscillation de neutrinos, angle de mélange θ_{13}, Borexino, geo-neutrinos, directionalité des neutrinos

---

- Abstract - Double Chooz is a reactor neutrino oscillation experiment which aims at measuring the θ_{13} mixing angle thanks to two identical detectors located at different distances from the two reactors of the Chooz nuclear power plant, in the French Ardennes. While the near detector will start taking data in fall 2014 to normalize the flux of the neutrinos emitted by the nuclear reactors, the far detector is running since April 2011 and allows to observe the neutrinos disappearance through the neutrino oscillation phenomenon. This thesis is also dedicated to the Borexino experiment which was designed to observe solar neutrinos. Due to its low background level as well as its position in a nuclear free country, Italy, Borexino is also sensitive to geo-neutrinos. This thesis presents both the Double Chooz and Borexino experiments, from the description of the detectors to the main results, with a special attention to the background and its rejection. Studies on the neutrino directionality with these two experiments are also detailed. In the case of Double Chooz, since the neutrinos are coming from the two nuclear reactors, the precision of the analysis method can be assessed. This thesis presents also for the first time the possibility to retrieve the initial direction of the neutrinos when the neutrons created in the inverse beta decay reactions are captured on hydrogen. In the case of Borexino, neutrino directionality information could facilitate the discrimination between geo-neutrinos and neutrinos from nuclear reactors.

- Keywords - Double Chooz, neutrino oscillation, θ_{13} mixing angle, Borexino, geo-neutrinos, neutrino directionality